Doctoral Dissertations (All Dissertations, All Years)   Electronic Theses and Dissertations

2005-03-10

Vibration Control of Large Scale Flexible Structures Using Magnetorheological Dampers

Wei Liu
Worcester Polytechnic Institute

Follow this and additional works at: https://digitalcommons.wpi.edu/etd-dissertations

Vibration Control of Large Scale Flexible Structures Using Magnetorheological Dampers

by

Wei Liu

A Dissertation

Submitted to the Faculty

of the

WORCESTER POLYTECHNIC INSTITUTE

In partial fulfillment of the requirements for the

Degree of Doctor of Philosophy
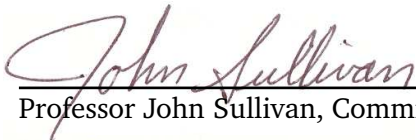
in

Mechanical Engineering
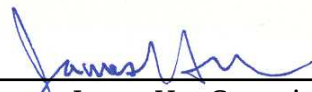
March 2, 2005

Approved:

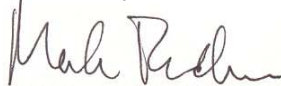Professor Zhikun Hou, Major Advisor

Professor Michael A. Demetriou, Co-advisor

Professor John Sullivan, Committee Member

Professor James Hu, Committee Member
(University of Rhode Island)

Professor Mark Richman, Graduate Committee Representative

Abstract

Structural vibration control (SVC) of large scale structures using the magnetorheological (MR) dampers are studied. Some key issues, i.e. model reduction, suppression of spillover instability, optimal placement of actuators and sensors, modeling of the MR dampers and their applications in SVC system for large scale structures, are addressed in this work.

A new model reduction method minimizing the error of a modal-truncation based reduced order model (ROM) is developed. The proposed method is implemented by using a Genetic Algorithm (GA), and can be efficiently used to find a ROM for a large scale structure. The obtained ROM has a finite $\mathcal{H}_2$ norm and therefore can be used for $\mathcal{H}_2$ controller design. The mechanism of the spillover instability is studied, and a methodology to suppress the spillover instability in a SVC system is proposed. The suggested method uses pointwise actuators and sensors to construct a controller lying in an orthogonal space spanned by the several selected residual modes, such that the spillover instability caused by these residual modes can be successfully suppressed. A GA based numerical scheme used to find the optimal locations for the sensors and actuators of a SVC system is developed. The spatial $\mathcal{H}_2$ norm is used as the optimization index. Because the spatial $\mathcal{H}_2$ norm is a comprehensive index in evaluating the dynamics of a distributed system, a SVC system using the sensors and actuators located on the obtained optimal locations is able to achieve a better performance defined on a distributed domain. An improved model of MR dampers is suggested such that the model can maintain the desired hysteresis behavior when noisy data are used. For the simulation purpose, a numerical iteration technique is developed to solve the nonlinear differential equations aroused from a passive control of a structure using the MR dampers. The proposed method can be used to simulate the response of a large scale structural system with the MR dampers. The methods developed in this work are finally verified using an industrial roof structure. A passive and semi-active SVC systems are designed to attenuate the wind-induced structural vibration inside a critical area on the roof. The performances of the both SVC systems are analyzed and compared. Simulation results show that the SVC systems using the MR dampers have great potentials in reducing the structural vibration of the roof structure.

In Memory of My Grandmothers

To My Beloved Son

故天将降大任于斯人也
必先苦其心志,
劳其筋骨
——《孟子》

Acknowledgments

I am grateful to all people who have contributed towards shaping this dissertation. First of all, I would like to express my sincere gratitude to my advisor, professor Zhikun Hou, for his comprehensive guidance and continuous support. His observations and invaluable advice helped me to establish the overall direction of the research and to move forward smoothly. Withtout his support, this work would never be possible. Financial support from the FM Global® Research Center is gratefully acknowledged.

I would like to express my sincere appreciation to my co-advisor, professor Michael A. Demetriou, for his guidance and assistance in helping me to gain a better understanding in the control theories. His encouragement and advice have substantially helped me out in learning this new discipline.

Gratitude goes to my dissertation committee members, professor Sullivan, professor Richman and professor Hu. Whenever I felt a dead-end in my research, they were there to give me helping hands. I am thankful to professor Sullivan for teaching me both theories and practical techniques in numerical analysis from which my research benefited. I am thankful to professor Richman for teaching me elasticity theories and agreeing to provide me a TA assistantship during the end of my research. I am indebted to professor Hu for his instructive advice on this work.

Thanks also go to professor Dimentberg who gave me valuable help on random and nonlinear vibration. I would like to express my gratitude towards my colleague Adriana for all the enlightening discussions with her. I'd like to thank Edyta for her efforts in keeping our office a clean, comfortable place to work. I also wish to express my appreciation to secretaries of the ME office, Barbara Edilberti, Barbara Furhman, Janice and Pam for all of their assist and cooperation.

I would like to thank my grandfather, my parents, my sister and her husband for their sustained supports. I shall be more obliged to all of them than I can express.

Finally, I owe special thank to my wife, Yiqun Hu, for all what she did in supporting

me in finishing this work. Without her understanding and supports, I would not have made it this far. My lovely son was brought into this world during the writing of my dissertation. His arrival added a lot of joy to my tedious work. As a father, I should have spent more time with him. For this, I felt obliged to him. I therefore dedicate this dissertation to my son, Andrew.

Wei Liu

Worcester, Massachusetts

$$\text{_____}$$

CONTENTS

LIST OF FIGURES

CHAPTER 1

Introduction

1.1 Motivation

Advances in structural technology over the last few decades have enabled the design and application of flexible structures of large scale. A flexible structure could be anything from small to large scale. Examples of flexible structures include: disk drives, high-rising buildings, suspension bridges, and space structures. One of the common characteristics of these structures is that the inherent structural damping to suppress vibrations is very small, and as a result, disturbances applied to these structures may induce long lasting and sometimes severe structural vibrations. The vibration of a structure or structural members not only reduces performances of the structural systems, but also can cause fatigue inside the structure and, in extreme cases, failure of the structure. Therefore, supressing structural vibration is often a quite important issue that should be addressed for a successful application of flexible structures. Structural vibration control (SVC) systems are to serve the vibration reduction purpose by implementation of energy dissipation devices or control systems into structures to reduce excessive structural vibration, enhance structural functionality and safety, and prevent catastrophic structural failure due to vibration caused by various disturbances.

Among the recently developed vibration control devices, those made from Magnetorheological (MR) fluids have found many successful applications in structural vibration control area. The

MR fluids were first found by Winslow [1] in the 1940's. They are typically consisted of micro-sized, magnetically polarized particles (such as iron particles) dispersed in a carrier medium, such as mineral or sillicon oil and characterized by the constitutive material properties which are sensitive to magnetic field. In response to an applied magnetic field, the particles dispersed inside MR fluids align, and interparticle bonds increase the resistance of the fluid, turning the fluid into a semi-solid. This change can be finished within a few milliseconds [2]. To take advantage of the special material properties demonstrated by the MR fluids, various devices have been developed. Because the deformation behavior of the MR fluids is governed by the mechanism that resembles yielding, the forces are primarily dissipative, devices made of the MR fluids are therefore also known as the MR dampers.

MR dampers are able to provide large damping forces using a small amount of external power. For example, a MR damper used in [3] can produce yield stress up to 80 kPa using a $20 \sim 50$ watts of power. Instead of using mechanical valves, the damping force of a MR damper can be adjusted by varying the strength of the magnetic field applied to the MR fluids, as a result, MR dampers are more reliable than other devices that contain mechanical moving parts. All these characteristics make the MR dampers ideal control devices that can be used in various SVC systems.

Altough structural vibration control has been an extensively studied topic for decades, its application to large scale structures is still a task full of challenge, and many issues need to be addressed. This research is devoted to vibration control of large scale flexible structures using MR dampers. In this work, some key issues related to this topic will be studied. In the following section, these issues are identified through an overview of structural vibration control.

1.2   Overview of Structural Vibration Control

SVC systems can be categorized into three types, namely *passive*, *active*, *semi-active* control systems [4]. A passive control system does not require an external power source to operate, and dissipates the vibration energy through a variety of mechanisms including the yielding of mild steel, viscoelastic action in a rubber-like material, and sliding friction, etc. Control forces in a passive control system are developed from the motion of the structure. Usually, the mechanical

properties of a passive control system can not be modified. In contrast, an active control system require external power supply to operate. Control forces could be generated by various types of actuators, such as electro-hydraulic Arcturus, piezoelectric films, etc. A compromise between passive and active SVC systems gives semi-active control systems, which have been developed to take advantage of the best features of both passive and active control systems. A semi-active control system usually requires a small amount of external power to operate. As in an active control system, the mechanical properties of a semi-active control system can be adjusted based on feedback from the structure being controlled. As in a passive control system, semi-active control systems utilize the motion of the structure to develop control forces. By above categorization, a SVC system using MR dampers could be a passive or a semi-active control system.

The major components of a typical active SVC system are: mechanical structure, sensors, actuators, and controller. For a given structure, design of an active SVC system involves various analyses and simulation steps. Figure - 1.1 outlines some of key steps and their interactions involved in a SVC system design. From this figure it can be seen that, design a SVC system is a complicated work, and many issues need to be addressed. For a *large scale* structure, complexity of the structure itself makes some of these issues more challenging. For example, model reduction, placement of sensors/actuators and controller design/simulation, etc. Because the so-called *spillover* [6] has potentials to lead instability in a SVC system, the suppression of spillover instability is another important issue need to be considered for vibration control of a large scale flexible structure. The issues mentioned above will be studied in this research. Additionally, because the MR dampers will be used in this research, dynamics of MR dampers and the issues related to their applications to a SVC system consist another part of this research. In the following few paragraphs, a detailed introduction to the issues that will be studied in this work are presented.

Model Reduction: Most modern control system design methods, such as LQG, $\mathcal{H}_2$, $\mathcal{H}_\infty$ etc., tend to produce a controller of the order comparable to that of the plant, i.e. a structure model, which is usually obtained using the finite element method (FEM). For a large scale structure, its FEM model often has tens of thousands of degree of freedoms. Direct application of a forementioned method to a FEM model of a structure will end up with a controller of higher order, which is difficult to analyze, and from the application point of view, is also difficult
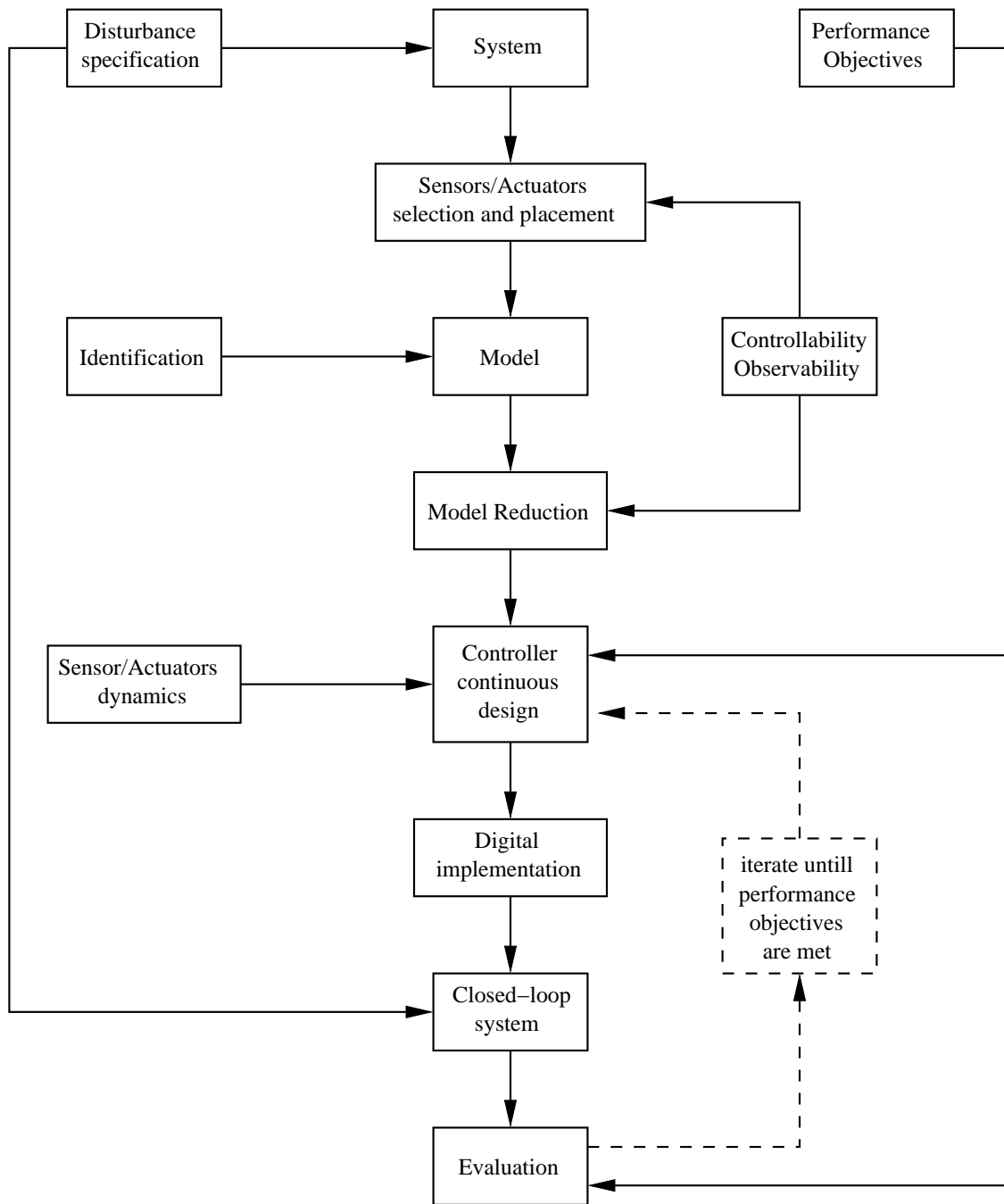
Figure - 1.1: Various steps of an active structure system design (Preumont [5]).

to be implemented in a real time manner. Therefore, a lower controller is often required. A controller with a tractable order could be obtained by two different ways as shown in Figure - 1.2. In one of the approaches, a reduced order controller is obtained by reducing the order of

4
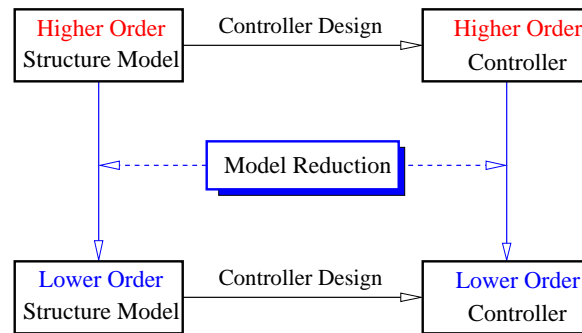
Figure - 1.2: Two approaches to get a lower order controller

a controller designed directly from the high fidelity structural model using the so-called *model reduction* methods. The advantage of this approach is that because an accurate structure model is used, uncertainty faced in the controller design is minimized. However, design a controller directly from a FEM model with a large number of DOFs is computationally difficult. In the second approach, a structure model is first reduced using a model reduction method to obtain a reduced order model (ROM), then a lower order controller can be designed from the obtained ROM. In the second approach, numerical difficulty as seen in the first approach can be avoided, but the effect of uncertainty (or modeling error) due to an inaccurate structure model has to be considered in controller design. Otherwise, a controller based on an inaccurate model is unable to achieve the expected performance, or even worse, may induce instability to the control system. Although a robust controller, e.g. $\mathcal{H}_\infty$ controller, can be used to stabilize a system with uncertainty, the performance of the obtained system are sacrificed. The larger the uncertainty, the worse the performance. In some cases, larger uncertainty makes it impossible to find a stabilizing controller. In order to reduce the uncertainty faced in a controller design, more attention should be paid in minimizing the modeling error caused by the model reduction of a structure model.

Spillover: Spillover happens when a ROM based controller is used to control a higher order system. It deteriorates performance and has potentials to cause instability of a closed-loop system. In an active SVC system for a flexible structure, because the structural damping is usually small, spillover is more likely to induce instability and, as a result, endanger the safety of the structure. Therefore, suppression of the spillover instability is another issue that will be

studied in this reseach.

Optimal Location of Sensors and Actuators: For a SVC system with given number of sensors and actuators (SAs), the system performance is affected significantly by the locations of SAs. In order to achieve the highest performance-expanse ratio, finding the optimal locations for SAs is desirable. For a structure with a simple geometry and smaller number of DOF's, experiences and a trail-and-error approach may suffice to solve the problem. While, for a large scale structure, a systematic and efficient methodology is needed. In finding the optimal locations for SAs, an appropriate type of performance index should be used, such that the performance of the resultant SVC system is able to satisfactorily meet the design requirements. In this research, the methodology used to find optimal locations of SAs for an active SVC system will be studied. Effect of different optimization indices on the performance of the final SVC system will be addressed as well.

Modeling of MR Dampers and Applications: A MR damper can be used in a passive SVC system as a damper. Because the material properties of the MR fluids can be controlled conveniently by changing the applied magnetic filed, it can also be used as an actuator in a semi-active SVC system. To design a SVC system using MR dampers, a mathematical model that is able to reproduce the hysteresis behavior of MR dampers has to be found. Additionally, because the behavior of MR dampers is nonlinear, an appropriate control algorithm that enables a MR damper to be conveniently used in a linear control system also needs to be found. Through decades' research, various MR models and control algorithms have been reported in the literature. In this research, a MR model and a control algorithm will be determined through a comparison study on the previous works. As regarding to this part, emphasis will be put on the application aspects using an established MR model and control algorithm to a SVC system design.

Through the above introduction to various aspects involved in structural vibration control, key issues that will be addressed in this research were identified and briefly introduced, the scope of this research was therefore defined. Addressing these issues will lead to a better understanding of a series problems related to the structural vibration control for a large flexible structure using MR damper.

1.3 Literature Survey

1.3.1 Model Reduction

In the literature, model reduction has been studied both in control engineering and structural analysis. Motivated by different applications, methods from these two areas generally have different subjects and requirements.

In control engineering, model reduction methods were developed to find a ROM for a given finite dimensional system. A good model reduction method should be able to preserve the stability of the original system, and provide an error bound for the obtained ROM. These methods can be divided into the following two categories [7]: singular value decomposition (SVD) based, and moment matching based methods. Both of them can be used to reduce the order of MIMO dynamical systems.

For a n-th order MIMO system $\mathcal{S}$ with p output and q input channels, assume the transfer matrix of the system $\mathcal{S}$ is given by

$$G(s) = C(sI - A)^{-1}B + D = \left[\begin{array}{c|c} A & B \\ \hline C & D \end{array}\right] \in \mathbb{C}^{p \times q}, \tag{1.3.1}$$

where A, B, C and D are system matrices of $G(s)$. The model reduction probelm is usually defined to find a r-th order system,

$$G_r(s) = C_r(sI - A_r)^{-1}B_r + D_r = \left[\begin{array}{c|c} A_r & B_r \\ \hline C_r & D_r \end{array}\right] \in \mathbb{C}^{p \times q}, \tag{1.3.2}$$

such that $r \ll n$ and the difference between the above two systems measured in some norm is minimized, i.e.

$$\min_{G_r} \|G(s) - G_r(s)\|, \tag{1.3.3}$$

where $\|\cdot\|$ denotes an appropriate norm.

One of the popular SVD based methods is the so-called *balanced model reduction*, which is based on the balanced realization theory introduced by Moore [8]. This method finds a ROM for a system by truncating the states (also known as *modes*) that are less observable and less controllable from a balanced system. Because the observability and controllability are equivalent in a balanced system, a less observable mode must be less controllable, or vice versa. Truncation

of a mode from a balanced system does not change the stability property of the obtained ROM. The difference between the original system and the ROM is bounded, and the bound can be found easily using the Hankel singular value of the system. The frequency-weighted balanced model reduction method introduced by Enns [9] is an extension of the balanced model reduction method.

The *Hankel norm approximation* method is another SVD based method. In this method, a reduced model $G_r(s)$ that makes $\|G - G_r\|_H$ minimized is to be found, where $\| \cdot \|_H$ denotes the Hankel norm. The reduced model $G_r(s)$ is constructed using a series of all pass functions. The difference of the two systems in terms of the Hankel norm is proved to be bounded [10]. Another two closely related methods of *singular perturbation approximation*[11, 12] also belong to the SVD based methods.

SVD based methods are able to preserve stability of a system and provide error bound of the obtained ROM, but are not computationally efficient. They may face computational challenges when are used for large scale structures.

On the other hand, moment matching based methods can be implemented in a numerically efficient way, but they are unable to provide error bound. Moment matching based methods work in the frequency domain. For a give system, the transfer matrix $G(s)$ is first expanded in the Laurent series around a given point $s_0 \in \mathbb{C}$ in the complex plane as follows,

$$G(s_0 + \sigma) = \eta_0 + \eta_1\sigma + \eta_2\sigma^2 + \eta_3\sigma^3 + \ldots, \tag{1.3.4}$$

where η_i is known as the *i*-th *moment* of the system at s_0. Then a reduced order system is found by requiring that its Laurent expansion of the transfer matrix at s_0,

$$G_r(s_0 + \sigma) = \hat{\eta}_0 + \hat{\eta}_1\sigma + \hat{\eta}_2\sigma^2 + \cdots + \hat{\eta}_k\sigma^k, \tag{1.3.5}$$

matches with the corresponding terms of the original system, i.e.

$$\eta_i = \hat{\eta}_i, \qquad i = 1, 2, \ldots, k \tag{1.3.6}$$

for an appropriate $k \ll n$.

Both SVD and moment matching based methods were developed to find a ROM for a finite-dimensional system. To use them to a distributed system, e.g. a continuous structure, one has to find a finite-dimensional approximation for the structural system.

In structural engineering, various model reduction methods have also been developed to reduce the computational load involved in static or dynamical analysis of large scale structures. Among the methods that fall into this category are *static condensation* [13], various *dynamic condensation* techniques [14, 15] and *modal truncation* methods. A static condensation method is able to produce a ROM that is exact for a static analysis. The obtained ROM often lacks the required accuracy for a dynamical analysis. Therefore, static condensation methods are not suitable for a control system design purpose. Dynamic condensation methods reduce the order of a FEM model of a structure. The obtained ROM is able to preserve the dynamical characteristics of the original model with certain accuracy within a frequency band, which is usually at the lower end of frequency spectrum. Accuracy of the ROM decreases dramatically with the increase of the frequency. To improve the accuracy of a thus obtained ROM in higher frequency range, iteration techniques [14][16] are usually needed.

Modal truncation is another model reduction method widely used in dynamical analyses in the structural engineering. When the frequency band of excitation to a structure is limited and known in priori, a ROM constructed for the structure by using the modal truncation method can be used to represent the original structure in a dynamical analysis to obtain a sufficiently accurate response in a reduced computational effort. A modal truncation based ROM contains the modes that fall inside the frequency band of the excitation, which are known as *in-bandwidth modes*. All other modes beyond this frequency band, which are known as *out-of-bandwidth* or *residual modes*, are truncated. As long as the modes contributing significantly to the in-bandwidth dynamics are included, the obtained ROM is a good approximation of the original structure from which it was constructed. Although the removal of the out-of-bandwidth modes does not affect the poles of the transfer matrix of a ROM, it shifts the in-bandwidth zeroes [17]. When the ROM is used to design a controller, the error caused by the truncation may propgate to the controller, and finally will deteriorate the performance or lead to instability of the closed-loop system [18].

To compensate the error due to modal truncation, *mode acceleration method* [19] adds a DC (or feedthrough) term, which includes all contributions from the truncated modes, to the ROM. However, this method can only reduce the truncation error at zero frequency. The error in higher frequency could still be large. Furthermore, it is also not clear how the multivariable

systems should be dealt with [20].

Another approach to minimize the truncation error in a structural system with zero damping was reported by Moheimani [21]. By minimizing a weighted $\mathcal{H}_2$ norm of truncation error associated with a modal-truncation based ROM, the authors found a closed form of an optimal feedthrough term that can be added to the ROM to correct the truncation error. The proposed method can be used to multivariable pintwise systems. In [20], this method was further explored and extended to a damped system, and a closed form of an optimal feedthrough term was found by minimizing either a weighted $\mathcal{H}_2$ or a spatial $\mathcal{H}_2$ norm of the truncation error. Essentially, these two related methods followed the same idea as that of the mode acceleration method by adding a constant term to a ROM to account for the in-bandwidth contribution of the truncated modes. Because the error due to modal truncation is frequency denpendent, adding a constant (i.e. feedthrough) term to a ROM is not adequate to reduce the errors in higher frequency range. Furthermore, because a ROM compensated using these methods has an infinite $\mathcal{H}_2$ norm, they can not be used in a case where a $\mathcal{H}_2$ controller is desired [22].

1.3.2 Suppression of Spillover Instability

Spillover phenomena were first studied by Balas [23], and many research efforts have been put on this topic since then. To suppress the spillover instability, one popular approach as suggested by Balas [23] is to use LPFs (low pass filter) with output channels [6] to reject the signals from residual modes. The order of the LPF should be determined such that the undesired spillover signals can be effectively blocked, and the in-bandwidth signals are able to pass undisturbed. When the gap between a controller's cutoff frequency and lower frequency of the spillover signals is not big enough to allow the use of a traditional LPF, a phase locked filter is required [6]. However, incorporating a filter in a control system increases the order of the system, and as a side-effect, also causes time delay to the filtered signal. Furthermore, the filter could perturb the closed-loop system eigenvalues. This perturbation can reduce the stability margin and jeopardize the convergence of an observer [24]. To avoid the problems caused by a filter, Chait and Radcliffe [24] suggested a method where observer equations are augmented to include dynamics of a first-order filter. Numerical simulation showed that this method introduced very small perturbation on the closed-loop system eigenvalues.

Nagarkatti et al. [25] studied the spillover on a plate structure, and proposed that the spillover instability could be eliminated by using a distributed measurement feedback. The distributed measurements of displacement and velocity were obtained by processing the plate deformation image acquired through a high speed video camera. The method appeared effective in a plate experiment. To use this method, however, ability of high speed image processing is required. For large scale structures, real time distributed measurement and the ability of processing large amount of measurement data, are both difficult and expensive.

Kim and J. [26], Smyser and Chandrashekhara [27], Chang et al. [28], Kim et al. [29], Baz [30] proposed the spillover reduction by using a sliding mode observer. Another approach [31] was to treat the dynamics of the residual modes as norm-bounded uncertainties to a ROM, and designed a $\mathcal{H}_\infty$ robust controller [10] to stabilize the system with the uncertainties. The stability robustness of such a system is achieved by sacrificing the system performance. Additionally, because the $\mathcal{H}_\infty$ controller design always considers the worst scenario, this method usually ends up with a quite conservative design.

Skelton and Likins [32] and Tzou and Hollkamp [33] suggested using spatially distributed actuators that is orthogonal to the unwanted modes to prevent the control spillover. They used piezoelectric actuators, and applied the method to a ring structure. Their results showed the filtering capability of the actuator on the control spillover signals for some selected residual modes. For large scale structures, the piezoelectric based actuators may not be able to provide enough control forces, and even if they can, covering a structure totally by the distributed actuators appears impractical.

In the works surveyed above, questions such as under what condition the spillover can cause instability to a closed-loop system, and how to determine this condition in a SVC system design, were not answered.

1.3.3   Optimal Locations of Sensors and Actuators

Finding optimal locations for sensors and actuators (OLSA) for a SVC system design, involves solving a complicated nonlinear optimization problem. By looking at the performance index used in solving this problem, the methods developed in the previous works can roughly divided into two categories: some of them used open-loop performance indices, and the others used

closed-loop performance indices in solving this optimization problem.

Among the methods that fall in the first category was the method proposed by Lim [34], in which a non-dimensional open-loop index, which was defined in an intersection subspace of the observability and controllability spaces, was used to evaluate the importance of each sensor and actuator (SA) pair. Importance of a SA pair was evaluated using this open-loop performance index. The larger the index, the more important the corresponding SA pair in the sense of the both controllability and observability. In the similar fashion, Gawronski [35] solved a SA selection problem by using performance indices measured in terms of various norms, which could be $\mathcal{H}_2$, $\mathcal{H}_\infty$ or Hankel norms, of an open-loop system. The SAs corresponding to larger norms were more important than the those corresponding to smaller norms, and the locations corresponding to those SAs were the optimal locations. In the approach proposed by Skelton and DeLorenzo [36, 37], an input/output cost index, which was defined as the RMS contribution of each sensor and actuator to the overall closed-loop system performance metric, was used to select an optimal subset of SAs from a given candidate set.

Limitations of the above mentioned methods are: first, the optimality of the obtained solution is dependent on the originally given set of SA, and secondly, by optimizing the performance of an open-loop system, the performance of the associated closed-loop system can be improved, but can not be guaranteed.

Fahroo and Demetriou [38] used a quadratic performance index of a closed-loop system in solving an OLSA problem for a noise reduction problem. The obtained nonlinear optimization problem was solved iteratively by using a gradient-based method. Demetriou [39] solved a SA placement problem for a flexible structure subjected to a worst case spatiotemporal disturbance variation, where both LQG and $\mathcal{H}_2$ norm performance indices were used. In this work, an actuator-switching policy was proposed to achieve the better performance when the disturbances are moving randomly on the structure.

Li et al. [40] solved a problem of finding both the optimal number and locations for actuators in an actively controlled structure using a two-level genetic algorithm (GA). A closed-loop performance index, which included the displacement responses of the structure and the control efforts, was used and minimized by the GA method. Arabyan and Chemishkian[41, 42] used a GA method in solving a problem of optimal locations for SAs in the sense of a $\mathcal{H}_\infty$ norm. To

reduce computational overhead, in each GA iteration step, the lower limit of the $\mathcal{H}_\infty$ norm of the transfer function from disturbance to controlled output was evaluated first, and a $\mathcal{H}_\infty$ controller would be designed only when this lower limit was below a predefined threshold value.

The performance indices used in the methods mentioned above are all defined based on a point input and point output manner, such as conventional $\mathcal{H}_2$ and $\mathcal{H}_\infty$ etc. Different from the above works, Halim and Moheomani [43] solved an OLSA problem using a *spatial controllability* index, which was based on the spatial $\mathcal{H}_2$ norm theory developed by Moheimani and Fu [44, 45]. As an extention of the standard $\mathcal{H}_2$ norm to the distributed system, the spatial $\mathcal{H}_2$ norm takes into account the spatial characteristics of a distributed system by introducing an additional integration over the spatial domain of interest. A performance index based on the spatial $\mathcal{H}_2$ norm is a more comprehensive measurement than an index based on the standard $\mathcal{H}_2$ norm in describing the behavior of a structural system.

1.3.4 Modeling and Control of MR Damper

Due to their excellent properties as introduced above, MR dampers have found many applications in structural vibration control area since 1940's. Typical applications include, vibration control of bridges [46–48], buildings [49–51], and vehicle suspension system [52], etc.. Through these research, various MR models have been developed. Shames and Cozzarelli [53] proposed a Bingham viscoplastic model to describe the hysteresis behavior of MR dampers. Compared with the experiment results, this model did not exhibit the nonlinear force-velocity response when the acceleration and the velocity have opposite signs [54]. While this model may be adequate for response analysis, it is not good for the control analysis. Another extensively used model for modeling hysteretic system is the Bouc-Wen model [55]. The Bouc-Wen model is extremely versatile and is able to emulate a variety of hysteretic behaviors. However, similar to the Bingham model, the nonlinear force-velocity response obtained from this model does not match experimental results in the region where the acceleration and velocity have opposite signs and the magnitude of the velocities are small [54]. To improve the above mentioned models, Spencer Jr. et al. [54] proposed a modified Bouc-Wen model. Their experiments showed that the proposed model was able to accurately predict the response of atypical MR damper over a wide range of operating conditions under various input voltage levels.

Because the hysteresis behavior of MR dampers can be controlled by changing the applied magnetic field, besides can be used as traditional dampers, MR dampers can also be used as actuators in a semi-active control system. In a semi-active control system, nonlinearity of MR dampers should be considered in the controller design.

To avoid the complexity of a nonlinear controller design, the *inverse dynamics* of the MR dampers could be used. Because the input/output relationship of a combination of the inverse and forward dynamics of the MR dampers are linear, using the inverse dynamics of the MR dampers make it possible to use a linear controller in a SVC system with the MR dampers. In this case, various linear control theories can be applied. However, due to the complicated nonlinear relationships of the forward dynamics of the MR dampers, a closed form of the inverse dynamics appear to be difficult to obtain. To work around this problem, some researchers proposed that the inverse dynamics of MR dampers could be numerically represented by neural networks (NN), which are well known for their ability to approximate arbitrary functions with arbitrary accuracy [56]. Chang and Roschke [57] showed that the nonlinear behavior of a MR damper can be satisfactorily reproduced by a trained feedforward NN model with one hidden layer. Hidaka et al. [58] used an adaptive NN control system that was composed of a forward NN for system identification and NN to control an electrorheological damper. Chang and Zhou [59] employed a recurrent NN to emulate the inverse dynamics of a MR damper. Although a trained NN can produce satisfactory outputs for the training inputs set, but there is no guarantee that it can produce the same satisfactory results for the inputs outside of training set. This inherent property makes NN-representations of the inverse dynamics of the MR dampers unreliable in predicting the behavior of the MR dampers in a real application.

In the work done by Yokoyama et al. [60], a nonlinear controller, i.e. a sliding mode controller, was used with the MR dampers in a semi-active control system to control the vibration of the suspension system of a vehicle. McClamroch and Gavin [61] proposed a decentralized bang-bang controller to control the seismically excited vibration using electrorheological material, which demonstrates the similar hysteresis behaviors as the MR fluids. The controller was obtained by using the Lyapunov direct method. Dyke et al. [62] proposed a clipped-optimal control algorithm based on acceleration feedback. In their works, a linear optimal controller combined with a force feedback loop was designed to adjust the command voltage of the MR

damper. The command signal was set to either zero or the maximum level, depending on how the damper's force compared with the target optimal control force. Analytical and experimental studies demonstrated that the MR damper, used in conjunction with the clipped-optimal control algorithm, was effective for controlling a multistory building structure.

1.4 Objectives of the Dissertation

Through the literature survey it can be seen that, for the topics involved in this research, there are more or less limitations exist in the previous works. Therefore, there are room for the further improvement for some of the previous works. Furthermore, complexities associated with the *large scale* structures considered in this research also warrant additional considerations on these issues.

Given the subjects that will be studied in this research, and considering the amount of research that has been done, this work is aimed at further exploring the issues involved in the structural vibration control of large scale structures using the MR dampers. Through this research, the following objectives are expected:

1. Model reduction method based on the direct modal truncation will be developed. The method should be able to compensate the in-bandwidth error due to the modal truncation, such that the zero shift of the transfer matrix of the obtained ROM is minimized. The obtained ROM should be able to avoid the difficulty of an infinite $\mathcal{H}_2$ norm as experienced in the method suggested in [20]. Furthermore, the developed method should be able to be implemented efficiently for large scale structures;

2. A method to suppress the spillover instability in a SVC system using pointwise actuators and sensors will be developed. The method to determine whether or not the spillover will cause the instability to a SVC system will be explored;

3. Develop an efficient numerical scheme to find the optimal locations for sensors and actuators in a SVC system for a large scale structure using the spatial $\mathcal{H}_2$ norm performance index.

4. Determine an appropriate model and the control algorithm for MR dampers such that

MR dampers can be used in a linear control system. Study related issues involved in the application of MR dampers in SVC systems for large scale structures;

5. Using the methodologies developed in the research , design a SVC system for an industrial roof structure subjected to wind loading such that the structural vibration of the roof structure can be reduced. The emphasis on this part of work will be put on the verification of the above developed methodologies.

Because a plate structure is among one of the most common building blocks of flexible structures, furthermore, the roof structure used in this research can be modeled as a plate structure, plate structures are considered throughout this research. All the methods developed in this work will be verified on plate structures. It should be noted that except small damping, the development of the methods presented in this research does not make any assumption on the structure to which they can be used.

1.5   Overview of the Dissertation

In the previous sections, some key issues that will be addressed in this research were identified through an introduction to the structural vibration control, and the objectives of this work were clarified. The rest parts of the dissertation are arranged as follows:

Chapter 2 introduces some background on flexible structures modeling and control system design. In this chapter, the Mindlin-Reissener plate theory are introduced. Finite element method and modal analysis that commonly used in the structural analysis are briefly reviewed. Finally, two closely related and commonly used controller design methods, i.e. the LQG and the $\mathcal{H}_2$ controller design, are introduced.

Chapter 3 studies the problem of model reduction for structural systems. The method constructing a ROM for a structure using the direct model truncation method is first outlined. The in-bandwidth truncation error associated with the obtained ROM is then analyzed. A parametric study on the effect of changing the modal parameters of the transfer function of a modal-truncation-based ROM is performed. Based on this parametric study, a modal reduction method that can minimizes the truncation error is developed. A GA method is introduced and used to

solve the obtained optimization problem. The effectiveness of the proposed method is demonstrated through an illustrative example.

Chapter 4 considers the suppression of the spillover instability. In this chapter, the mechanism of spillover and the spillover instability in a SVC system are first analyzed. Based on these analyses, a method to suppress the spillover instability using pointwise actuators and sensors is developed. A quantitative condition used to determine whether or not the spillover instability will happen to a SVC system is proposed. The internal structure of a controller designed from the proposed method is revealed. Finally, the effectiveness of the proposed method is verified via a numerical example.

Chapter 5 develops a numerical scheme used to find optimal locations of sensors and actuators for a SVC system using the spatial $\mathcal{H}_2$ norm as a performance index. Spatial $\mathcal{H}_2$ theory and the corresponding controller design method are introduced. In order to be implemented efficiently for a large scale structure, a GA algorithm is proposed to solve the optimization problem. In the proposed numerical scheme, the optimality of a set of locations for SAs is evaluated by the spatial $\mathcal{H}_2$ norm of the transfer function of the closed-loop system formed by a spatial $\mathcal{H}_2$ controller using these sensors and actuators. A numerical example is used to demonstrate the effectiveness of the proposed scheme.

Chapter 6 deals with modeling of the MR dampers, and the issues involved in application of the MR dampers in a SVC system. In this chapter, a MR model and a related control algorithm are determined through a comparison study on the works reported in the literature. Hysteresis behavior of the selected MR model are investigated through a series numerical experiments. An improvement is made to the selected model to help to preserve the desired hysteretic behaviors in a situation of noisy input data. A numerical technique is developed to enable an efficient simulation on large scale structural systems with the MR dampers being attached. Semi-active control using the selected control algorithm is then studied.

Chapter 7 verifies the methodologies developed in this work through designing a SVC system for an industrial roof structure subjected to wind loading. The roof structure is modeled as a plate structure, and its FEM model is build. Wind load data obtained from a wind tunnel experiment [1] is analyzed, statistical properties and frequency characteristics of the wind load

---

[1]The experiment was done in a separated research sponsored by the FM Global®

are obtained. Through a transient analysis of the roof structure, a critical area on the roof is identified. Passive and semi-active control systems using MR dampers to attenuate the vibration in the critical area are designed, and their performances are compared.

Chapter 8 summarizes the works that have been presented in this dissertation. The main contributions of this research are outlined. Finally, some recommendations for future work are suggested.

Modeling of Flexible Structures and Controller Design

2.1 Introduction

In order to design a controller for a structure, a mathematical model describing the dynamics of the structure should be first set up. This process is known as *modeling*. In this chapter, the procedure of modeling of flexible structures are illustrated through deriving the governing equations for plate structures. Numerical techniques, namely the finite element method and modal analysis, that will be used in this research are briefly reviewed. Two controller design methods, i.e. the LQG and the $\mathcal{H}_2$ controller designs, are introduced.

2.2 Mindlin Plate Theory

A plate as shown in Figure - 2.1 is defined as a structure whose thickness h is small as compared with the other two dimensions L_x and L_y. For a plate structure, it can be assumed that the deformation state in the plate can be described by the deformation in its mid-plane, which is defined as the plane midway between the upper and lower surfaces of the plate. A plate is *thin* when its thickness-to-span ratios are significantly smaller than 1, i.e. the following conditions hold,

$$\frac{h}{L_x} \ll 1, \qquad \frac{h}{L_y} \ll 1. \tag{2.2.1}$$

PSfrag replacements
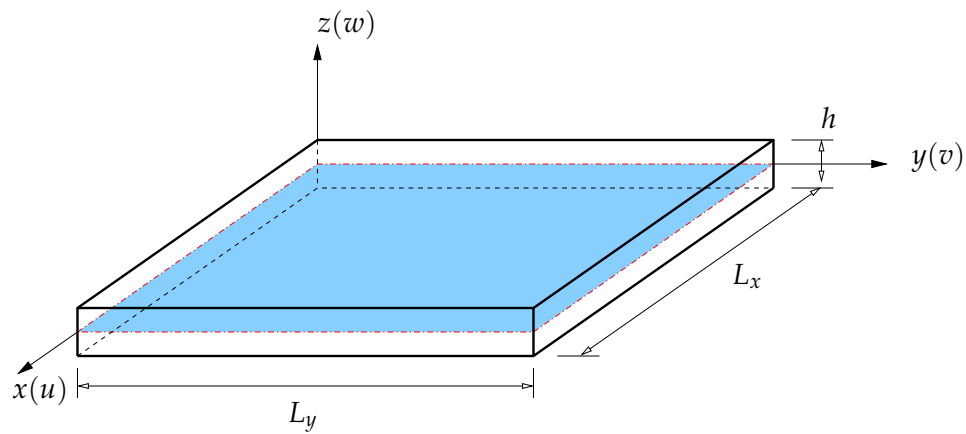
Figure -2.1: Plate geometry and coordinate system

For a thin plate, the so-called *Kirchhoff thin plate theory* [63] is usually used to derive the plate equations. The Kirchhoff plate theory is based on the following assumptions about the deformation state of the plate:

1. There is no in-plane deformation in the thin plate mid-plane;

2. The stress and strain in the direction of the mid-plane normal can be ignored;

3. A normal to the mid-plane of the plate remains normal to the mid-plane after deformation as illustrated in Figure - 2.2;

4. The effect of rotary inertia is negligible.

PSfrag replacements
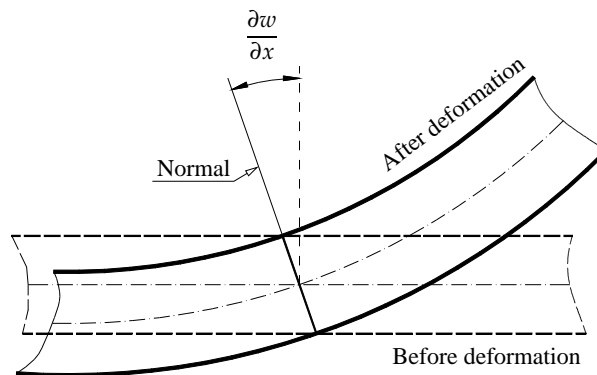
Figure -2.2: Straight normal assumption of the classical Kirchhoff theory (cross-section in the yz plane)

Based on the above assumptions, the displacements field in a thin plate can be determined by the deflection w of the plate in the z direction as follows,

$$u = -z\frac{\partial w}{\partial x}, \quad v = -z\frac{\partial w}{\partial x}, \quad w = w(x,y), \tag{2.2.2}$$

where u, v, w are displacement components in x, y, z directions, respectively, as shown in Figure - 2.1. Using the above defined displacement field and the *Hamilton Principle* [64], the following dynamic plate equation for an isotropic material can be obtained,

$$\frac{\partial^4 w}{\partial x^4} + 2\frac{\partial^4 w}{\partial x^2 \partial y^2} + \frac{\partial^4 w}{\partial y^4} = \frac{q(x,y)}{D} - \rho h \frac{\partial^2 w}{\partial t^2}, \tag{2.2.3}$$

where $q(x,y)$ is the distributed lateral load applied to the surface of the plate, D is the *flexural rigidity* given by

$$D = \frac{Eh^3}{12(1-v^2)}, \tag{2.2.4}$$

in which E is the Young's modulus and v is the Poisson's ratio of the material. The Kirchhoff plate theory was obtained by ignoring the transverse shear effects, i.e. assuming that the rotation of the mid-plane normal is totally determined by the deflection w (see Figure - 2.2). This assumption can accurately reflect the real status of the deformation happend in a thin plate.

When the thickness of the plate is moderately thick, i.e. the conditions (2.2.1) does not hold, the effect of the transverse shear on the deformation can not be ignored anymore, and the above Kirchhoff assumptions need to be modified. Reissener [65] proposed the simplest thick plate theory by introducing the effect of transverse shear deformation through a complementary energy principle. Unlike the Reissener's work, Mindlin [66] presented a first-order theory of plates where he accounted for shear deformation in conjunction with a shear correction factor. In this theory, the first two Kirchhoff assumptions are maintained. To allow for the effect of transverse shear deformation, the theory relaxes the normality assumption so that normals to the undeformed midplane remain straight and unstretched in length but not necessarily normal to the deformed midplane. This assumption is shown in Figure - 2.3. In this figure, the deformation status of a plate in its yx plane is showed, where $\partial w/\partial x$ is the rotation angle of the mid-plane normal assumed in the Kirchoff theory, θ_x denotes the rotation angle assumed in the Mindlin hypothesis. Same as in the Kirchhoff plate theory, the stress component σ_z in the z direction are assumed to be zero in the Mindlin plate theory.
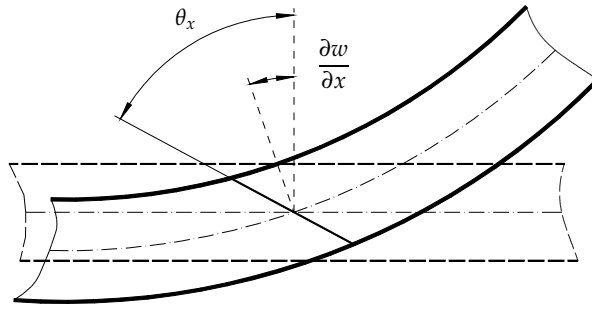
Figure - 2.3: Mindlin thick plate assumption (cross-section in yz plane)

Based on the above assumptions, the displacement field of a thick plate is modified as follows:

$$u = -z\theta_x, \quad v = -z\theta_y, \quad w = w(x,y), \tag{2.2.5}$$

where θ_x and θ_y are rotation angles due to bending in the yz and xz planes, respectively. The strain field of the plate then follows,

$$\{\epsilon\} = \begin{Bmatrix} \epsilon_x \\ \epsilon_y \\ \epsilon_{xy} \\ \epsilon_{xz} \\ \epsilon_{yz} \end{Bmatrix} = \begin{Bmatrix} -z\dfrac{\partial \theta_x}{\partial x} \\ -z\dfrac{\partial \theta_y}{\partial y} \\ -\dfrac{z}{2}\left(\dfrac{\partial \theta_x}{\partial y} + \dfrac{\partial \theta_y}{\partial x}\right) \\ \dfrac{1}{2}\left(\dfrac{\partial w}{\partial x} - \theta_x\right) \\ \dfrac{1}{2}\left(\dfrac{\partial w}{\partial y} - \theta_y\right) \end{Bmatrix}, \tag{2.2.6}$$

The stress field is determined as follows by applying the Hook's law and the assumption $\sigma_z = 0$,

$$\{\sigma\} = \begin{Bmatrix} \sigma_x \\ \sigma_y \\ \sigma_{xy} \\ \sigma_{xz} \\ \sigma_{yz} \end{Bmatrix} = \begin{bmatrix} \dfrac{E}{1-\nu^2} & \dfrac{E\nu}{1-\nu^2} & & & \\ \dfrac{E\nu}{1-\nu^2} & \dfrac{E}{1-\nu^2} & & & \\ & & 2G & & \\ & & & 2G & \\ & & & & 2G \end{bmatrix} \begin{Bmatrix} \epsilon_x \\ \epsilon_y \\ \epsilon_{xy} \\ \epsilon_{xz} \\ \epsilon_{yz} \end{Bmatrix} = \begin{Bmatrix} \dfrac{E}{1-\nu^2}(\epsilon_x + \nu\epsilon_y) \\ \dfrac{E}{1-\nu^2}(\epsilon_y + \nu\epsilon_x) \\ -\dfrac{Ez}{2(1+\nu)}\left(\dfrac{\partial \theta_x}{\partial y} + \dfrac{\partial \theta_y}{\partial x}\right) \\ G\left(\dfrac{\partial w}{\partial x} - \theta_x\right) \\ G\left(\dfrac{\partial w}{\partial y} - \theta_y\right) \end{Bmatrix}, \tag{2.2.7}$$

22

where G is the *shear modulus* given by

$$G = \frac{E}{2(1+\nu)}. \qquad (2.2.8)$$

Based on the stress and strain field defined above, the following equations of motion for a Mindlin (or thick) plate can be obtained by using the Hamilton principle [64],

$$khG\left(\frac{\partial^2 w}{\partial x^2} + \frac{\partial^2 w}{\partial y^2} - \frac{\partial \theta_x}{\partial x} - \frac{\partial \theta_y}{\partial y}\right) + q = \rho h \ddot{w},$$

$$D\left[\frac{\partial^2 \theta_x}{\partial x^2} + \frac{1-\nu}{2}\frac{\partial^2 \theta_x}{\partial y^2} + \frac{1+\nu}{2}\frac{\partial^2 \theta_y}{\partial x \partial y}\right] + khG\left(\frac{\partial w}{\partial x} - \theta_x\right) = \frac{\rho h^3}{12}\ddot{\theta}_x, \qquad (2.2.9)$$

$$D\left[\frac{\partial^2 \theta_y}{\partial y^2} + \frac{1-\nu}{2}\frac{\partial^2 \theta_y}{\partial x^2} + \frac{1+\nu}{2}\frac{\partial^2 \theta_x}{\partial x \partial y}\right] + khG\left(\frac{\partial w}{\partial y} - \theta_y\right) = \frac{\rho h^3}{12}\ddot{\theta}_y,$$

where k is the *shear correction factor* introduced in the Mindlin plate theory to compensate for the error in assuming a constant shear stress throughout the plate thickness. This factor usually takes value of 1.2 in most analyses.

The boundary conditions associated with the above PDE's can be determined from the virtual work done by the forces (moments) along the virtual displacement on the boundary. For an arbitrary boundary as shown in Figure - 2.4, the following boundary conditions should be
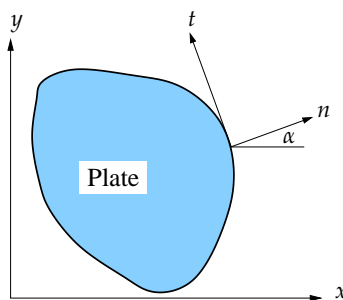
Figure - 2.4: An arbitrary boundary of the plate (cross-section in xy plane)

specified [64]:

$$V_n = 0 \quad \text{or} \quad w \text{ is specified,}$$

$$M_n = 0 \quad \text{or} \quad \theta_n \text{ is specified,} \qquad (2.2.10)$$

$$M_{nt} = 0 \quad \text{or} \quad \theta_t \text{ is specified,}$$

where V is shear force, and M is moment, and subscript n and t denote the normal and tangential directions of the boundary.

In the Mindlin plate theory, the effects of transverse shear deformation was considered through introducing two rotation variables θ_x and θ_y, which are independent of the plate deflection w, in the displacement field of a thick plate. When a thick plate decays to a thin plate, i.e. $\theta_x \to \partial w/\partial x$ and $\theta_x \to \partial w/\partial x$, it can be verified that the Mindlin plate equation (2.2.9) reduces to the thin plate equation (2.2.3). Therefore, the Mindlin plate model as given in (2.2.9) can be used to analyze both thick and thin plates.

For the plate equations obtained above, in most cases, closed form solutions are very difficult to obtain, and numerical solutions are usually sought. Among various numerical methods developed to solve the partial differential equations (PDEs) aroused from structural modeling, the finite element method (FEM) is especially powerful in dealing with complicated structures with arbitrary boundary conditions, and therefore, will be used in this research for the structural modeling purpose.

2.3   Finite element Formulation

In this section, the FEM is introduced through deriving an isoparametric plate element formulation for the Mindlin plate. A typical isoparametric plate element considered here and the notations used in the following derivation are shown in Figure - 2.5. The displacements u inside
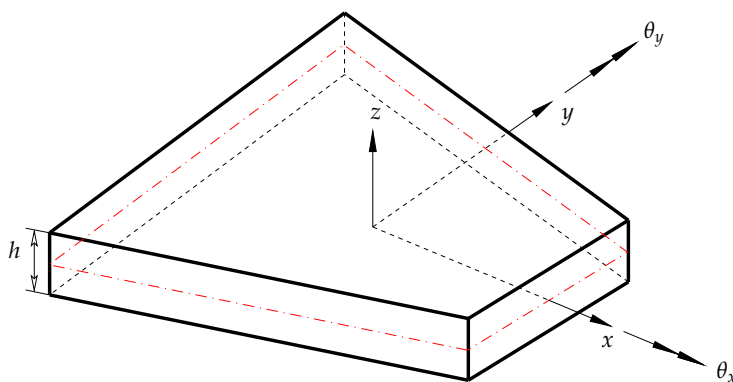
Figure - 2.5: A typical plate element.

an element can be expressed in terms of the nodal displacements using the shape function as

follows,

$$u = \begin{Bmatrix} w(x,y) \\ \theta_x(x,y) \\ \theta_y(x,y) \end{Bmatrix} = \sum_{i=1}^{n} N_i d_i = N d, \qquad (2.3.11)$$

where n is the number of nodes in a typical element, and

$$d_i = \begin{bmatrix} w_i & \theta_{xi} & \theta_{yi} \end{bmatrix}^T \qquad (2.3.12)$$

is the nodal displacement vector of the i-th node, and

$$N_i = N_i \begin{bmatrix} 1 & 0 & 0 \\ 0 & 1 & 0 \\ 0 & 0 & 1 \end{bmatrix}, \qquad (2.3.13)$$

in which N_i is the shape function associated with the node i. In an isoparametric formulation, the shape function is defined in a natural coordinates system (ξ, η). The velocity $\dot{u}$ and acceleration $\ddot{u}$ can be expressed in a similar way as follows,

$$\dot{u} = \sum_{i=1}^{n} N_i \dot{d}_i = N \dot{d},$$
$$\ddot{u} = \sum_{i=1}^{n} N_i \ddot{d}_i = N \ddot{d}. \qquad (2.3.14)$$

The dynamical equations of the element can then be obtained using the principle of virtual work, which states that for any kinematically consisten set of displacemens of a structure system, the virtual work due to deformation must equal to that done by the external forces on virtual displacements irrespective of the material behavior. The principle of virtual work can be mathematically expressed as follows,

$$\int_{v} (\delta \epsilon)^T \sigma \, dv = \int_{S_t} (\delta u)^T t \, ds + \int_{v} (\delta u)^T (b - \rho \ddot{u}) \, dv, \qquad (2.3.15)$$

where δu is virtual displacements vector, $\delta \epsilon$ is the corresponding virtual strains vector, and σ is the vector of stresses, t is the surface traction acting on the portion S_t of the boundary S, vectors b, $\rho \ddot{u}$ are body and inertial forces, respectively, and ρ is the mass density of the material.

For a linear elastic material, the following finite element equation can be obtained by substituting (2.3.11) and (2.3.14) into (2.3.15),

$$M \ddot{d} + C \dot{d} + K d = f, \qquad (2.3.16)$$

25

where M, C and K are mass, damping and stiffness matrices, respectively, and given as follows,

$$
\begin{aligned}
M &= \int_v \rho N^T N dv, \\
K &= \int_v B^T D B dv, \\
f &= \int_{s_t} N^T t ds + \int_v N^T b dv,
\end{aligned}
\tag{2.3.17}
$$

where B is the strain-displacement matrix and D is the elasticity matrix. The structural damping is generally a frequency-dependent variable for most of materials, and is very difficult to determine. Therefore, in most applications, the damping matrix C is determined by assuming

$$
C = \alpha M + \beta K,
\tag{2.3.18}
$$

where α and β are two constants independent of frequency. The structure damping determined in this way is known as *Rayleigh damping*.

The finite element equation (2.3.16) can be solved using either a direct integration method or the method of modal superposition based on the modal analysis. Due to its excellent stability, the Newmark method is one of the most commonly used direct integration methods. A brief description of this method can be found in Appendix A.

The modal superposition method solves (2.3.16) by first transforming the system into a set of uncoupled single degree of freedom (SDOF) systems in the modal space, solving for the modal response for each SDOF system , and then superimposing the modal responses to obtain the response of the original multi-degree of freedom (MDOF) system.

As an essential part of the modal superpostion method, modal analysis is used to find natural frequencies and modal matrix for the linear system (2.3.16) with zero damping, i.e.

$$
M\ddot{d} + K\dot{d} = 0.
\tag{2.3.19}
$$

assume M, $K \in \mathbb{R}^{n \times n}$, and that the solution to the above equation is

$$
d = \phi \sin \omega(t - t_0),
\tag{2.3.20}
$$

where $\phi \in \mathbb{R}^n$ is unknown mode shape vector, ω is the frequency associated with ϕ, t_0 is a constant determined by the initial condition. Substituting (2.3.20) into (2.3.19) gives the following generalized eigenvalue problem,

$$
K\phi - \omega^2 M\phi = 0.
\tag{2.3.21}
$$

There are n eigensolution pairs to the above equation, $(\omega_1, \boldsymbol{\phi}_1)$, ... $(\omega_n, \boldsymbol{\phi}_n)$, where ω_i represents the i-th natural frequency of the system with

$$0 \leq \omega_1 \leq \omega_2 \leq \cdots \leq \omega_n, \tag{2.3.22}$$

and $\boldsymbol{\phi}_i$ is the mode shape vector associated with the i-th mode. Modal shape vectors are usually normalized with respect to the mass matrix as follows

$$\boldsymbol{\phi}_i^T M \boldsymbol{\phi}_i = 1, \quad (i = 1, 2, \ldots, n). \tag{2.3.23}$$

By substituting $\boldsymbol{\phi}_i$ into (2.3.21), the following properties of modal shape vectors can be verified,

$$\boldsymbol{\phi}_i^T M \boldsymbol{\phi}_j = \begin{cases} 1 & \text{when } i = j \\ 0 & \text{otherwise} \end{cases}, \qquad \boldsymbol{\phi}_i^T K \boldsymbol{\phi}_j = \begin{cases} \omega_i^2 & \text{when } i = j \\ 0 & \text{otherwise.} \end{cases} \tag{2.3.24}$$

Furthermore, for the Rayleigh dampig, the following property follows,

$$\boldsymbol{\phi}_i^T C \boldsymbol{\phi}_j = \begin{cases} 2\omega_i \zeta_i & \text{when } i = j \\ 0 & \text{otherwise,} \end{cases} \tag{2.3.25}$$

where ζ_i is the modal damping ratio associated with the i-th mode defined as follows,

$$\zeta_i = \frac{\alpha + \beta \omega_i^2}{2\omega_i}. \tag{2.3.26}$$

Define the modal matrix $\boldsymbol{\Phi} = [\boldsymbol{\phi}_1 \; \boldsymbol{\phi}_2 \; \cdots \; \boldsymbol{\phi}_n]$ and

$$\boldsymbol{\Omega} = \begin{bmatrix} \omega_i & & & \\ & \omega_2 & & \\ & & \ddots & \\ & & & \omega_n \end{bmatrix}, \quad \boldsymbol{\zeta} = \begin{bmatrix} \zeta_i & & & \\ & \zeta_2 & & \\ & & \ddots & \\ & & & \zeta_n \end{bmatrix}, \tag{2.3.27}$$

then the above properties can be rewritten in the following matrix forms

$$\boldsymbol{\Phi}^T M \boldsymbol{\Phi} = I, \quad \boldsymbol{\Phi}^T K \boldsymbol{\Phi} = \boldsymbol{\Omega}^2, \quad \boldsymbol{\Phi}^T C \boldsymbol{\Phi} = 2\boldsymbol{\Omega}\boldsymbol{\zeta}. \tag{2.3.28}$$

In the modal superposition method, the above properties are used to transform (2.3.16) into modal space by introducing

$$\boldsymbol{d}(t) = \boldsymbol{\Phi} \boldsymbol{a}(t), \tag{2.3.29}$$

27

where $a = [a_1 \ a_2 \ \ldots \ a_n]^T$ is modal displacement vector. By (2.3.29) and (2.3.28), the original coupled system equations (2.3.16) can be transformed to n independent SDOF equations in the modal space as follows,

$$\ddot{a}_i(t) + 2\omega_i \zeta_i \dot{a}_i(t) + \omega_i^2 a_i(t) = r_i(t), \quad (i = 1, 2, \ldots, n) \tag{2.3.30}$$

where $r_i(t) = \boldsymbol{\phi}_i^T \boldsymbol{f}(t)$ is the projection of the load vector $\boldsymbol{f}(t)$ on the i-th mode shape $\boldsymbol{\phi}_i$. The solution $a_i(t)$ to each of these SDOF equations can be conveniently obtained by using the Duhamel integral. The displacement responses of the original system (2.3.16) can be obtained by substituting a_i's into (2.3.29). The velocity and acceleration can be obtained similarly as follows,

$$\dot{d} = \boldsymbol{\Phi}\dot{a}, \qquad \ddot{d} = \boldsymbol{\Phi}\ddot{a}. \tag{2.3.31}$$

In some cases[1], the response of a structure subjected to given loads can be approximately obtained as follows,

$$d \approx \sum_{i=1}^{r} \boldsymbol{\Phi}_i a_i, \tag{2.3.32}$$

where $r \leq n$ is the number of modes whose contributions to the system's response are accounted for. In the above equation, the contributions from the modes whose natural frequency $\omega_i > \omega_r$ are neglected. In this case, only the first r of SDOF equations as given in (2.3.30) need to be solved to obtain an approximate response of the original n-DOF systems. When $r \ll n$, a large amount of computation can be saved. Therefore, the modal superposition method is more efficient than the Newmark method if the modal information is available.

2.4 Controller Design

In this section, the state space form of the structure system as given in (2.3.16) is first derived, followed by an introduction of the two related controller design methods, i.e. the LQG (Linear Quadratic Gaussian) and $\mathcal{H}_2$. The differences and connections between these two methods are reviewed.

---

[1]When the frequency band of the external loads is limited.

2.4.1 State Space Form

The equations of motion of a n-DOF structural structural system considered in a SVC system design problem is often written in the following general form

$$M\ddot{d} + C\dot{d} + Kd = B_u f. \tag{2.4.33}$$

Except the right handside, the above equation is a copy of (2.3.16). In the above equation, $B_u \in \mathbb{R}^{n \times p}$ is a constant matrix specifying the locations of p applied loads, which could be external forces or control forces denoted by a vector $f \in \mathbb{R}^p$. For controller design purpose, the above equation is further transformed to a first order ODE (or state space) form as follows,

$$\begin{Bmatrix} \dot{d} \\ \ddot{d} \end{Bmatrix} = \begin{bmatrix} 0 & I \\ -M^{-1}K & -M^{-1}C \end{bmatrix} \begin{Bmatrix} d \\ \dot{d} \end{Bmatrix} + \begin{Bmatrix} 0 \\ M^{-1}B_u \end{Bmatrix} f. \tag{2.4.34}$$

The measurement outputs from the above system could be the displacement d, velocity $\dot{d}$ or any linear combination of the displacement and velocity. Without loss of the generality, the measurement outputs can be written as follows,

$$y = \begin{bmatrix} C_d & C_v \end{bmatrix} \begin{Bmatrix} d \\ \dot{d} \end{Bmatrix}, \tag{2.4.35}$$

where C_d and C_v are measurement matrices associated with displacement and velocity, respectively.

Transforming the above equations into the modal space using the transformations (2.3.29) and (2.3.31) gives,

$$\begin{aligned} \dot{x} &= Ax + Bf \\ y &= Cx \end{aligned} \tag{2.4.36}$$

where $x^T = [a^T \ \dot{a}^T]$ is the state vector, A, B and C are system metrices given as follows

$$A = \begin{bmatrix} 0 & I \\ -\Omega r^2 & -2\Omega\zeta \end{bmatrix}, \quad B = \begin{bmatrix} 0 \\ \Phi^T B_u \end{bmatrix}, \quad C = \begin{bmatrix} C_d \Phi^T & C_v \Phi^T \end{bmatrix} \tag{2.4.37}$$

where

$$\begin{aligned} \Omega &= \text{diag}(\omega_1, \omega_2, \ldots, \omega_n), \quad \zeta = \text{diag}(\zeta_1, \zeta_2, \ldots, \zeta_n) \\ \Phi &= \begin{bmatrix} \phi_1 & \phi_2 & \cdots & \phi_n \end{bmatrix} \end{aligned} \tag{2.4.38}$$

2.4.2 LQG Controller

In structural vibration control, a controller is usually used to help a structure to achieve certain precise positioning or tracking requirements. These requirements should be satisfied for the structure with natural frequencies within the controller bandwidth and within the disturbance spectra [67]. A Linear Quadratic Gaussian (LQG) controller can meet these requirements, and is often used for tracking and disturbance rejection purposes.

A block diagram of a LQG control system is shown in Figure - 2.6. It consists of a plant G,
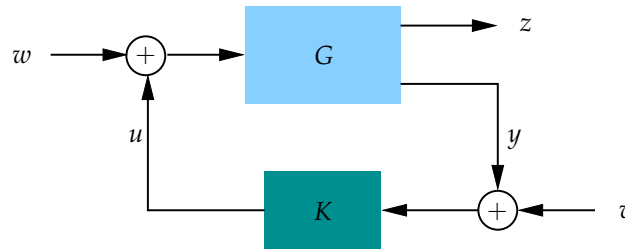
Figure - 2.6: A LQG closed-loop system.

i.e. a structural model in this case, and a controller K. The dynamics of the plant is described by the following state space equations,

$$
\begin{aligned}
\dot{x} &= Ax + B(u + w), \\
y &= Cx + v, \\
z &= Dx,
\end{aligned}
\tag{2.4.39}
$$

where A, B, C and D are given constant matrices, x denotes the plant state vector, y is the measurement output, z is error output (also known as controlled output), w denotes the disturbance applied to the plant, which is usually known as the *process noise*, v is the sensor noise, which is also known as the *measurement noise*. In the LQG controller design, both w and v are assumed to be Gaussian white noise with constant covariance matrices,

$$
W = E(ww^T), \qquad V = E(vv^T),
\tag{2.4.40}
$$

where $E(\cdot)$ denotes the expectation operator. Furthermore, w and v are assumed be uncorrelated, i.e.

$$
E(wv^T) = 0.
\tag{2.4.41}
$$

In the above equations, when the plant is a structural system, A, B and C matrices can be determined as (2.4.37).

A LQG problem is to find a controller such that the performance index J,

$$J^2 = \lim_{t \to \infty} \int_0^t E\left[z^T Q z + u^T R u\right],$$ (2.4.42)

is minimized. In the above equation, Q is a positive semidefinite state weight matrix, and $z^T Q z$ represents the control error. R is a positive definite input weight matrix, and $u^T R u$ represents the control efforts. Without loss of generality, the input weight matrix is usually assumed to be $R = I$. Therefore, by adjusting Q matrix, the tradeoff between the control error and the control effort can be made.

In the closed-loop system shown in Figure‑2.6, the control input u is developed by the controller K according to the plant state x, whose information is contained in the measurement output y. In most applications, the full information about the plant state x is not available directly from the measurement. In this case, the controller needs to estimate the state of the plant from the measurement y. The estimated state, which is denoted by $\hat{x}$, is then used to compute the control input u. Given the estimated state $\hat{x}$, the control input is given by

$$u = -K_c \hat{x},$$ (2.4.43)

where K_c is the controller gain matrix. It is well known [10, 68] that the following gain matrix minimizes the performance index J

$$K_c = B^T X_c,$$ (2.4.44)

where X_c is the solution of the following algebraic Riccati equation

$$A^T X_c + X_x A - X_c B B^T X_c + Q = 0.$$ (2.4.45)

To estimate the plant state from the measurement y, an estimator needs to be incorporated inside the controller. The dynamics of the estimator is governed by the following equation,

$$\dot{\hat{x}} = A\hat{x} + Bu + K_e(y - C\hat{x}),$$ (2.4.46)

where K_e is the estimator gain matrix, which is given by

$$K_e = X_e C^T,$$ (2.4.47)

where X_e is the solution of the following estimator algebraic Riccati equation

$$AX_e + X_eA^T - X_eC^TCX_e + V = 0, \tag{2.4.48}$$

where V is the covariance matrix of the measurement noise as given in (2.4.40).

Combining (2.4.43) and (2.4.46) gives the following state space equations of a typical LQG controller,

$$\dot{\hat{x}} = (A - BK_c - K_eC)\hat{x} + K_ey,$$
$$u = -K_c\hat{x}. \tag{2.4.49}$$

The performance requirements for a SVC system, e.g. root-mean-square (RMS) response to applied disturbances, settling time and overshoot etc., are reflected in a LQG controller design by choosing an appropriate state weighting matrix Q (see (2.4.42)). There is no established method to find such a matrix from the given design requirements, however, experiences and a trial-and-error approach are needed to choose an appropriate Q matrix such that the obtained LQG controller can meet the design requirements.

2.4.3 $\mathcal{H}_2$ Controller

In the LQG design, the control inputs u and disturbances w were assumed collocated, and both the process and the measurement noises are Gaussian [68]. However, in many applications, the control inputs u do not always coincide with the disturbances w, and the disturbances to the system are not necessarily Gaussian. In this case, a $\mathcal{H}_2$ controller is needed.

An $\mathcal{H}_2$ controller is designed for a system with a more general configuration, where the control inputs and disturbances are not required collocated. Moreover, the disturbances, which include process and measurement noises, are not assumed to be Gaussian. A closed-loop system formed by a $\mathcal{H}_2$ controller is shown in Figure - 2.7. In this figure, G and K are the plant and the controller, respectively, y is the measurement output, z is the controlled output, u and w are the control input and the disturbance, respectively. The state space equations of the plant are given by

$$\dot{x} = Ax + B_1w + B_2u,$$
$$z = C_1x + D_{12}u, \tag{2.4.50}$$
$$y = C_2x + D_{21}w.$$
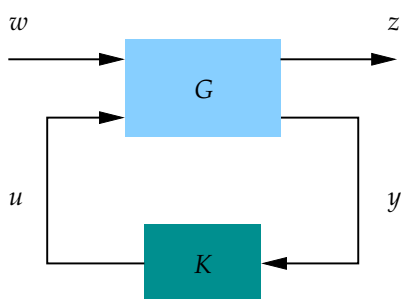
Figure - 2.7: A $\mathcal{H}_2$ closed-loop system.

A controller K is designed such that the performance index J,

$$J = \int_0^\infty \left\{ \begin{matrix} x \\ u \end{matrix} \right\}^T \begin{bmatrix} Q & S \\ S^T & R \end{bmatrix} \left\{ \begin{matrix} x \\ u \end{matrix} \right\} dt, \tag{2.4.51}$$

is minimized for some $Q^T = Q$, S and $R = R^T > 0$. Requiring $R > 0$ emphasizes that the control energy has to be finite. Moreover, it is generally assumed that the weighting matrix used in the above definition is positive semi-definite, i.e.

$$\begin{bmatrix} Q & S \\ S^T & R \end{bmatrix} \geq 0. \tag{2.4.52}$$

Due to the above assumption, it is possible to factorize the weighting matrix as follows

$$\begin{bmatrix} Q & S \\ S^T & R \end{bmatrix} = \begin{bmatrix} C_1^T \\ D_{12}^T \end{bmatrix} \begin{bmatrix} C_1 & D_{12} \end{bmatrix}. \tag{2.4.53}$$

Using (2.4.53), the performance index given in (2.4.51) can be rewritten as

$$J = \|C_1 x + D_{12} u\|_2^2 = \|z\|_2^2, \tag{2.4.54}$$

where $\| \cdot \|_2$ denotes the $\mathcal{H}_2$ norm operator. The $\mathcal{H}_2$ norm of a matrix $g(t)$ is defined as follows,

$$\|g\|_2^2 = \int_0^\infty \text{Trace}\{g^T(t)g(t)\}dt. \tag{2.4.55}$$

Denote the Fourier transform of $g(t)$ by $G(j\omega)$, by the Parseval theorem, the above definition can also be given in the frequency domain as follows,

$$\|g\|_2^2 = \|G\|_2^2 = \frac{1}{2\pi} \int_{-\infty}^\infty \text{Trace}\{G^*(j\omega)G(j\omega)\}d\omega, \tag{2.4.56}$$

where superscript * is a complex conjugate operator.

As mentioned above, in a $\mathcal{H}_2$ design, the disturbance w to the system is not restricted to a Gaussian white noise, it can be any signal with bounded *power spectral density*. For a signal $u(t)$, its power spectral density is given by

$$S_{uu}(j\omega) = \int_{-\infty}^{\infty} R_{uu}(\tau)e^{-j\omega\tau}d\tau, \tag{2.4.57}$$

where $R_{uu}(\tau)$ is the *autocorrelation matrix* of u, and

$$R_{uu}(\tau) = \lim_{T\to\infty} \frac{1}{2T} \int_{-T}^{T} u(t+\tau)u^T(t)dt. \tag{2.4.58}$$

A signal with bounded power spectral density can be generated by passing a white noise signal through a weighting filter. Therefore, the disturbance considered in the LQG design is a special case covered in the $\mathcal{H}_2$ design.

In literature, the performance index for a $\mathcal{H}_2$ controller design is usually defined in terms of the $\mathcal{H}_2$ norm of the closed-loop transfer matrix T_{zw} that relates the disturbance input w to the controlled output z. This definition is consistent with the one defined previously in (2.4.54). In the frequency domain, the controlled output can be written as

$$Z(s) = T_{zw}(s)W(s). \tag{2.4.59}$$

For an unit intensity white noise input w, the power spectral density of the output signal z is given by

$$S_{zz}(j\omega) = T_{zw}(j\omega)S_{ww}(j\omega)T_{zw}^*(j\omega) = T_{zw}(j\omega)T_{zw}^*(j\omega). \tag{2.4.60}$$

Then it follows

$$\begin{aligned}\|z\|_2^2 &= \frac{1}{2\pi} \int_{-\infty}^{\infty} \text{Trace}\{S_{zz}(j\omega)\}d\omega = \frac{1}{2\pi} \int_{-\infty}^{\infty} \text{Trace}\{T_{zw}(j\omega)T_{zw}^*(j\omega)\}d\omega \\ &= \|T_{zw}\|_2^2.\end{aligned} \tag{2.4.61}$$

Therefore, the performance index for a $\mathcal{H}_2$ controller design problem can also be defined as

$$J = \|T_{zw}\|_2, \tag{2.4.62}$$

and it is equivalent to the index defined in (2.4.54).

To ensure that there exist a proper controller minimizing the performance index defined above, the following assumptions about the plant should be made:

- (A, B_2) is stabilizable, and (A, C_2) is detectable;

- $D_{12}^T D_{12}$ and $D_{21} D_{21}^T$ are nonsingular.

For the purpose of simplicity, the following conditions are commonly assumed in the $\mathcal{H}_2$ controller design, i.e.

$$
\begin{aligned}
D_{12}^T \begin{bmatrix} C_1 & D_{12} \end{bmatrix} &= \begin{bmatrix} 0 & I \end{bmatrix} \\
D_{21} \begin{bmatrix} B_1^T & D_{21}^T \end{bmatrix} &= \begin{bmatrix} 0 & I \end{bmatrix}.
\end{aligned}
\tag{2.4.63}
$$

The first condition can be interpreted as the absence of cross terms in the performance index $(D_{12}^T C_1 = 0)$. The second one just assumes that the process noise and the measurement noise are uncorrelated $(D_{21} B_1^T = 0)$. Furthermore, because it is assumed that $D_{12}^T D_{12} = I$, the tradeoff between the error and the control efforts as seen in the performance can be defined in C_1 matrix. Similarly, because $D_{21} D_{21}^T = I$, the process and measurement noise level can be specified by B_1 matrix.

Under the above assumptions, an optimal $\mathcal{H}_2$ controller minimizing the performance index (2.4.62) can be found. Similar to a LQG controller, a $\mathcal{H}_2$ controller contains a state estimator. It has been proved [10, 67] that the minimum of the performance index can be achieved using the following controller and estimator gain matrices

$$
K_c = B_2^T X_{2c}, \qquad K_e = X_{2e} C_2^T,
\tag{2.4.64}
$$

where X_{2c} and X_{2e} are solutions of the following controller and the estimator Riccati equations,

$$
X_{2c} A + A^T X_{2c} + C_1^T C_1 - X_{2c} B_2 B_2^T X_{2c} = 0,
\tag{2.4.65}
$$

$$
X_{2e} A^T + A X_{2e} + B_1 B_1^T - X_{2e} C_2^T C_2 X_{2e} = 0,
\tag{2.4.66}
$$

respectively. A $\mathcal{H}_2$ controller then can be represented by the following state space form,

$$
\begin{aligned}
\dot{\hat{x}} &= (A - B_2 K_c - K_e C_2)\hat{x} + K_e y, \\
u &= -K_c \hat{x},
\end{aligned}
\tag{2.4.67}
$$

which is of similar structure as that of the LQG controller given in (2.4.49).

The closed-loop system formed by the controller given above is proved to minimize the $\mathcal{H}_2$ norm of the the transfer function T_{zw}, and the minimum is found to be [10],

$$
\min \|T_{zw}\|_2^2 = \|G_c X_{2e}\|_2^2 + \|C_1 G_f\|_2^2,
\tag{2.4.68}
$$

35

where G_c and G_f are transfer functions of the following two systems,

$$G_c(s) = \left[\begin{array}{c|c} A - B_2 B_2^T X_{2c} & I \\ \hline C_1 - D_{12} B_2^T X_{2c} & 0 \end{array} \right] \tag{2.4.69}$$

$$G_f(s) = \left[\begin{array}{c|c} A - X_{2e} C_2^T C_2 & B_1 - X_{2e} C_2^T D_{21} \\ \hline I & 0 \end{array} \right] \tag{2.4.70}$$

2.5 Summary

This chapter is intended to introduce some necessary background needed later in this research. The procedure of modeling of flexible structures were introduced through deriving the governing equations for plate structures. Finite element formulation of an isoparametric Mindlin plate element was derived, and modal analysis was introduced. The LQG and the $\mathcal{H}_2$ controller design methods were outlined. Through the introduction to these two controller design methods, it can be seen that a $\mathcal{H}_2$ controller is an extention of a LQG controller, and can be applied to a general system with non-collocated control-inputs and disturbances, and disturbances are not necessarily Gaussian white noise. The $\mathcal{H}_2$ controller will be used in this research to design a SVC system.

Model Reduction

3.1 Introduction

As introduced in Chapter 1 and Chapter 2, to design a controller for a structure, the structural model, which is often obtained through the FEM modeling process, has to be set up in the first place. For a large scale structure, the obtained FEM needs to be reduced in order to obtain a lower order controller that can be conveniently analyzed and implemented. The modal truncation method can be used to construct a reduced order modal (ROM) for the structure. In a modal-truncation based ROM, the vibration modes beyond the frequency band of interest are truncated, and only some in-bandwidth modes are retained. The obtained ROM can be directly used to design a controller for the structure, or be further reduced using a model reduction method, e.g. the balanced model reduction.

The modal truncation process develops errors in the obtained ROM. Whatever the ROM will be used, to design a controller or to obtain another further reduced ROM through a balanced model reduction process, the error exist in the modal-truncation based ROM has to be minimized. Otherwise, the error in the original ROM either increases the uncertainty that will be faced in controller design, or will be propgated or even magnified in the following model reduction process.

In most cases, as long as the frequency band used in constructing a modal-truncation based

ROM is appropriate, significant truncation error can be avoided in the obtained ROM. However, truncating modes from a structural system does affect the zeros of the transfer matrix of the obtained ROM, i.e. shift the frequencies of the zeroes. A controller based on a ROM with zero shift also has potentials to deteriorate the performance and even destabilize the closed-loop system when it is used to control the original structure [18].

In this chapter, the model reduction method aiming at reducing the zero shift observed in a modal-truncation based ROM is studied. As an important part involved in the topic of this chapter, the balanced model reduction method and related backgrounds are also introduced.

3.2 Balanced Realization and Model Reduction

3.2.1 Controllerability and Observability

Assume a finite-dimensional LTI system be described by the following first order ODE:

$$\dot{x} = Ax + Bu, \quad x(0) = x_0,$$
$$y = Cx + Du,$$

(3.2.1)

where $x \in \mathbb{R}^n$ is the state vector of the system, x_0 is the initial condition, $u(t) \in \mathbb{R}^m$ is the system input, and $y(t) \in \mathbb{R}^p$ is the system output, A, B, C and D are appropriately dimensioned real constant matrices. The transfer matrix of the above system is given by

$$G(s) = C(sI - A)^{-1}B + D.$$

(3.2.2)

Sometimes, the transfer matrix (3.2.2) can also be expressed using the following notation

$$G(s) = \left[\begin{array}{c|c} A & B \\ \hline C & D \end{array} \right].$$

(3.2.3)

The dynamical system described by (3.2.1) is controllable if, for any initial state $x(0) = x_0$ and the finial state $x(t_1)$ with $t_1 > 0$, there exists an input $u(\cdot)$ that drives the system (3.2.1) from the initial state to the final state. Otherwise, the system in uncontrollable. A necessary and sufficient condition for the system be controllable is the following controllability matrix has full (row) rank,

$$\mathcal{C} = \left[A \quad AB \quad A^2B \quad \ldots \quad A^{n-1}B \right].$$

(3.2.4)

The system (3.2.1) is observable if, for any $t_1 > 0$, the initial state $x(0) = x_0$ can be determined from the time history of the input $u(t)$ and the output $y(t)$ in the time interval of $[0, t_1]$. Otherwise, the system is unobservable. A necessary and sufficient condition for the system be observable is the following observability matrix has full (column) rank,

$$\mathcal{O} = \begin{bmatrix} A \\ CA \\ CA^2 \\ \dots \\ CA^{n-1} \end{bmatrix}. \tag{3.2.5}$$

Although the controllability and observability a system can be checked by computing the rank of the controllability and observability matrices, respectively, there is a more efficient approach. Associated with the controllability and observability of the system (3.2.1), there are two Lyapunov equations,

$$AW_c + W_c A^T + BB^T = 0 \tag{3.2.6}$$

$$A^T W_o + W_o A + C^T C = 0, \tag{3.2.7}$$

where W_c and W_o are called as *controllability Gramian* and *observability Gramian* matrices of the system, respectively. For a stable A, the system is controllable iff the controllability Gramian is positive definite, i.e. $W_c > 0$, and observable iff the observability Gramian is positive definite $W_o > 0$.

As introduced in section 2.4.3, the $\mathcal{H}_2$ norm of a system can be obtained by evaluating the following integral on the transfer matrix of the system,

$$\|G\|_2^2 = \frac{1}{2\pi} \int_{-\infty}^{\infty} \text{Trace}\{G^*(j\omega)G(j\omega)\} d\omega. \tag{3.2.8}$$

For the system (3.2.1), its $\mathcal{H}_2$ norm can be obtained in a more efficient way as follows,

$$\|G\|_2^2 = \text{Trace}(B^T W_o B) = \text{Trace}(C W_c C^T), \tag{3.2.9}$$

where W_c and W_o are the system's controllability and observability Gramian matrices, respectively.

3.2.2 Balanced Realization

For a given transfer function, there are infinite number of state space realizations. Among them, there is a so-called *balanced realization*. Different from other kind of realizations, in a balanced realization, the controllability and the observability of a system's state are equivalent. This special property makes the balanced realization very useful in many applications, such as finding a ROM for a system.

The balanced realization of a system can be found by applying an appropriate transformation to the system. Suppose the state of the system G as described in (3.2.1) is transformed by a non-singular transformation T to $\hat{x} = Tx$, then the transfer matrix of the system corresponding to the transformed state $\hat{x}$ is given by

$$G' = \left[\begin{array}{c|c} \widehat{A} & \widehat{B} \\ \hline \widehat{C} & \widehat{D} \end{array} \right] = \left[\begin{array}{c|c} TAT^{-1} & TB \\ \hline CT^{-1} & D \end{array} \right]. \tag{3.2.10}$$

Correspondingly, the system Gramians become

$$\widehat{W}_c = TW_cT^T, \quad \widehat{W}_o = (T^{-1})^TW_oT^{-1}. \tag{3.2.11}$$

It can be verified that $G = G'$, i.e. the realization given in (3.2.10) is simply another realization of the original system G.

The balanced realization corresponds to one that is obtained through a transformation T such that, the Gramian matrices are equivalent and diagonalized, i.e.

$$\widehat{W}_c = \widehat{W}_o = \Sigma, \quad \Sigma = \text{diag}(\sigma_1,\ \sigma_2,\ \ldots,\ \sigma_n), \tag{3.2.12}$$

where $\sigma_i \geq 0$ $(i = 1, 2, \ldots, n)$ are called the *Hankel singular values* of the system. The transformation T that balances a system as defined in (3.2.1) can be found as follows:

1. Compute the system controllability and observability Gramians W_c and W_o by solving the Lyapunov equations given in (3.2.6) and (3.2.7)

2. Compute the decompositions P and Q of the Gramian matrices such that

$$W_c = PP^T, \qquad W_o = Q^TQ. \tag{3.2.13}$$

3. Compute the singular value decomposition of matrix $H = QP$,

$$H = V\Sigma U^T, \qquad \text{where } V^T V = I \text{ and } U^T U = I. \qquad (3.2.14)$$

4. The transformation T and its inverse T^{-1} are then given by

$$T = PU\Sigma^{-1/2}, \qquad T^{-1} = \Sigma^{-1/2}V^T Q. \qquad (3.2.15)$$

It is easy to verify that the transformation T obtained above brings the Gramian matrices of the transformed system diagonal. The transformed controllability Gramian matrix $\widehat{W}_c$ is given by

$$\widehat{W}_c = T^{-1}W_c T^{-T} = \Sigma^{-1/2}V^T PP^T Q^T V\Sigma^{-1/2}. \qquad (3.2.16)$$

Introducing $H = QP$ into the above equation yields

$$\widehat{W}_c = \Sigma^{-1/2}V^T HH^T V\Sigma^{-1/2}. \qquad (3.2.17)$$

Then by substituting (3.2.14) into the above equation, it follows

$$\widehat{W}_c = \Sigma{-1/2}V^T V\Sigma U^T U\Sigma V^T V\Sigma^{-1/2} = \Sigma. \qquad (3.2.18)$$

Follow the similar procedure, it can be shown that $\widehat{W}_o = \Sigma$. Therefore, in a balanced realization, both controllability and observability Gramians are diagonal and equivalent, i.e. $\widehat{W}_c = \widehat{W}_o = \Sigma$, which are known as balanced Gramians.

3.2.3 Model Reduction by Balanced Truncation

Because the controllability and observability Gramians are equivalent in a balanced realization, a less controllable state must be less observable, and vice versa. Moreover, because the balanced Gramians are diagonal, the states are uncoupled in terms of input-output relationship. The above nice properties of a balanced realization makes it possible to reduce the order of the corresponding system by deleting those less controllable/observable states from the original system without changing the system input-output dynamics too much. This is a rough idea behind the balanced model reduction method, which is established by the following theorem [69].

Theorem 1. *Suppose system $G(s)$ is stable, and*

$$G = \left[\begin{array}{cc|c} A_{11} & A_{12} & B_1 \\ A_{21} & A_{22} & B_2 \\ \hline C_1 & C_2 & D \end{array} \right]$$

is a balanced realization with Gramian $\Sigma = \text{diag}(\Sigma_1, \Sigma_2)$ with

$$\Sigma_1 = \text{diag}(\sigma_1 I_{s_1}, \ \sigma_2 I_{s_2}, \ \ldots, \ \sigma_r I_{s_r})$$

$$\Sigma_2 = \text{diag}(\sigma_{r+1} I_{s_{r+1}}, \ \sigma_{r+2} I_{s_{r+2}}, \ \ldots, \ \sigma_N I_{s_N})$$

and

$$\sigma_1 > \sigma_2 > \cdots > \sigma_r > \sigma_{r+1} > \sigma_{r+2} > \cdots > \sigma_N,$$

where σ_i has multiplicity s_i, $i = 1, 2, \ldots, N$ and $s_1 + s_2 + \cdots + s_N = n$. Then the truncated system

$$G_r(s) = \left[\begin{array}{c|c} A_{11} & B_1 \\ \hline C_1 & D \end{array} \right]$$

is balanced and asymptotic stable. Furthermore

$$\|G(s) - G_r(s)\|_\infty \leq 2(\sigma_{r+1} + \sigma_{r+2} + \cdots + \sigma_N)$$

and the bound is achieved if $r = N - 1$, i.e.

$$\|G(s) - G_{N-1}(s)\|_\infty = 2\sigma_N.$$

By this theorem, a ROM of a stable finite-dimensional system can be obtained by simply truncating the states corresponding to smaller Hankel singular values from its balanced realization. The bound of the truncation error can be easily estimated using the Hankel singular values corresponding to those truncated states.

From the above introduction, it is seen that the key step in the balanced model truncation method is to find a balanced realization for a given system. Because computing balanced realization is a computational extensive process, the balanced model truncation method is suitable for a small or a moderately large system. To use this method for a large scale structure, the first step is to reduce the FEM model of the structure to tractable size. This can be done by using the modal truncation method that will be introduced in the following section.

3.3 Modal Truncation

Consider a n-DOF structural system described by the following equations

$$M\ddot{d} + C\dot{d} + Kd = B_u u, \tag{3.3.19}$$

$$y = C_d d + C_v \dot{d}, \tag{3.3.20}$$

where $d \in \mathbb{R}^n$ is displacement vector, M, C and K are mass, damping and stiffness matrices, respectively, $B_u \in \mathbb{R}^{n \times p}$ is the control input matrix, $u \in \mathbb{R}^p$ is the control input vector, $y \in \mathbb{R}^q$ is the output from the system, $C_d, C_v \in \mathbb{R}^{q \times n}$ are output matrices corresponding to the displacement and velocity sensors, respectively. As discussed in Chapter 2, the state space form of the above system can be written as (see section 2.4.1 on pp.29)

$$\dot{x} = Ax + Bu, \qquad y = Cx, \tag{3.3.21}$$

using the modal transformation $d = \Phi a$, where Φ is the modal matrix of the structure, and a is the modal displacement vector. In the above equations, $x = [a \ \dot{a}]^T \in \mathbb{R}^{2n}$ is the state vector and

$$A = \begin{bmatrix} 0 & I \\ -\Omega^2 & -2\Omega\zeta \end{bmatrix}, \quad B = \begin{Bmatrix} 0 \\ \Phi^T B_u \end{Bmatrix}, \quad C = \begin{bmatrix} C_d \Phi & C_v \Phi \end{bmatrix}, \tag{3.3.22}$$

in which Ω and ζ are diagonal matrices of natural frequencies and modal damping ratios, i.e.

$$\Omega = \text{diag}(\omega_1, \omega_2, \ldots, \omega_n), \quad \zeta = \text{diag}(\zeta_1, \zeta_2, \ldots, \zeta_n). \tag{3.3.23}$$

The transfer matrix of the system (3.3.21) can be written as

$$G(s) = C(sI - A)^{-1}B = \begin{bmatrix} G_{11}(s) & G_{12}(s) & \ldots & G_{1p}(s) \\ G_{21}(s) & G_{22}(s) & \ldots & G_{2p}(s) \\ \vdots & \vdots & \vdots & \vdots \\ G_{q1}(s) & G_{q2}(s) & \ldots & G_{qp}(s) \end{bmatrix} \in \mathbb{R}^{q \times p}, \tag{3.3.24}$$

where G_{ij} ($i = 1, \ldots q, j = 1, \ldots, p$) is the transfer function from the j-th input to the i-th output. G_{ij} can be expanded by modes as follows,

$$G_{ij}(s) = \sum_{k=1}^{n} G_{ij}^{(k)} = \sum_{k=1}^{n} \frac{(c_{dik} + c_{vik}s)b_{kj}}{s^2 + 2\zeta_k \omega_k s + \omega_k^2}, \tag{3.3.25}$$

43

where $G_{ij}^{(k)}$ is the transfer function associated with the k-th mode on the ij input-output channel, which will be known as *modal transfer function* in sequel, c_{dik} and c_{vik} are (i,k) entries of the matrices $C_d \mathbf{\Phi}$ and $C_v \mathbf{\Phi}$, respectively, B_{kj} is the (k,j) entry of the matrix $\mathbf{\Phi}^T B_u$, ω_k and ζ_k are natural frequency and modal damping ratio of the k-th mode, respectively.

Using the modal truncation, a r-mode ROM of the system (3.3.21) can be obtained by truncating the modes starting from $r+1$ up to n. The transfer matrix of the obtained ROM is given by

$$G'(s) = [G'_{ij}(s)], \quad i = 1, 2, \ldots q, \quad j = 1, 2, \ldots, p, \tag{3.3.26}$$

where

$$G'_{ij}(s) = \sum_{k=1}^{r} \frac{(c_{dik} + c_{vik}s)b_{kj}}{s^2 + 2\zeta_k \omega_k s + \omega_k^2}. \tag{3.3.27}$$

In this case, the frequency band covered by the ROM is $[0, \omega_r]$. All modes inside this frequency band are known as *in-bandwidth* modes, and all other modes are known as *residual* modes. $G'(s)$ governs the in-bandwidth dynamics of the ROM.

3.3.1 Truncation Error

The dynamics of the residual modes (also known as *truncated dynamics*) is given by $G_t(s) = G(s) - G'(s)$. It should be noted that the bandwidth of the truncated dynamics $G_t(s)$ overlaps with that of the original system, i.e. $(0, \omega_n)$. In a ROM obtained from modal truncation, the in-bandwidth contributions of the residual modes are neglected, as a result, the in-bandwidth dynamics are different from that of the full model. This difference is known as the truncation error.

Truncation error has little effect on the poles of the transfer matrix of the ROM, however, it shifts the zeroes. This can be shown by the following simple example. Consider a 5-DOF single input single output (SISO) system, whose modal transfer functions $G_i(s)$ $i = 1, 2, \ldots, 5$ are given as follows,

$$G_1(s) = \frac{50}{s^2 + 0.1s + 100}, \qquad G_2(s) = \frac{120}{s^2 + 0.17s + 300}, \qquad G_3(s) = \frac{140}{s^2 + 0.28s + 800},$$

$$G_4(s) = \frac{130}{s^2 + 0.34s + 1200}, \qquad G_5(s) = \frac{120}{s^2 + 0.49s + 2400}.$$

The transfer function of the full model is then given by $G(s) = G_1(s) + G_2(s) + \cdots + G_5(s)$. A 3-mode ROM is constructed by truncating the last two modes. Figure‑3.1(a) shows the

magnitude of the transfer function of the full model, 3-mode ROM and the truncated modes. It can be seen that the truncation causes the notable zero shift in the ROM: the second zero of the ROM is shifted by about 4Hz. The truncation disturbs the phase angle of the transfer function correspondingly as shown in Figure - 3.1(b).

To check the performance of the balanced truncation method, the balanced model reduction method is used to construct a ROM containing the same modes as the ROM obtained above. First, the balanced realization of the 5-DOF system is computed using the algorithm presented above. The obtained state space equation has 10 states. The balanced Gramian of the system are listed as below,

$$\Sigma = \begin{bmatrix} 25.1 & 24.9 & 20.1 & 19.9 & 8.8 & 8.7 & 5.4 & 5.4 & 2.5 & 2.5 \end{bmatrix}. \tag{3.3.28}$$

Truncating the modes corresponding to the 4 smallest Hankel singular values gives the following balanced model,

$$G' = \left[\begin{array}{cccccc|c} -0.055 & -9.985 & 0.068 & -0.593 & 0.078 & 0.158 & 1.664 \\ 9.985 & -0.045 & 0.582 & -0.063 & 0.149 & 0.070 & -1.504 \\ 0.068 & -0.582 & -0.085 & 17.304 & -0.102 & -0.254 & -1.852 \\ 0.593 & -0.063 & -17.304 & -0.087 & 0.268 & 0.102 & -1.866 \\ 0.078 & -0.149 & -0.102 & -0.268 & -0.145 & -28.271 & -1.597 \\ -0.158 & 0.070 & 0.254 & 0.102 & 28.271 & -0.140 & 1.561 \\ \hline 1.664 & 1.504 & -1.852 & 1.866 & -1.597 & -1.561 & 0.000 \end{array} \right]. \tag{3.3.29}$$

The magnitude and phase angle of transfer function of the obtained ROM are plotted in Figure - 3.2 along with the full model and the model-truncation based ROM. It is seen that balanced model reduction can not avoid the zero shift due to truncation. In this particular example, the balanced truncation caused the same amount of zero shift as the the modal truncation did in the obtained ROM as shown in Figure - 3.2.

To compensate the truncation error, Moheimani [21] proposed a modified balanced model reduction by adding a feed-through term to a ROM experiencing the zero shift. Figure - 3.3 compares the results from the modified balanced ROM and the modal truncation ROM. It is seen that by adding a feed-through (or DC) term, the zero shift due to truncation is reduced. However, thus obtained ROM has an infinite $\mathcal{H}_2$ norm, and can not be used in $\mathcal{H}_2$ controller
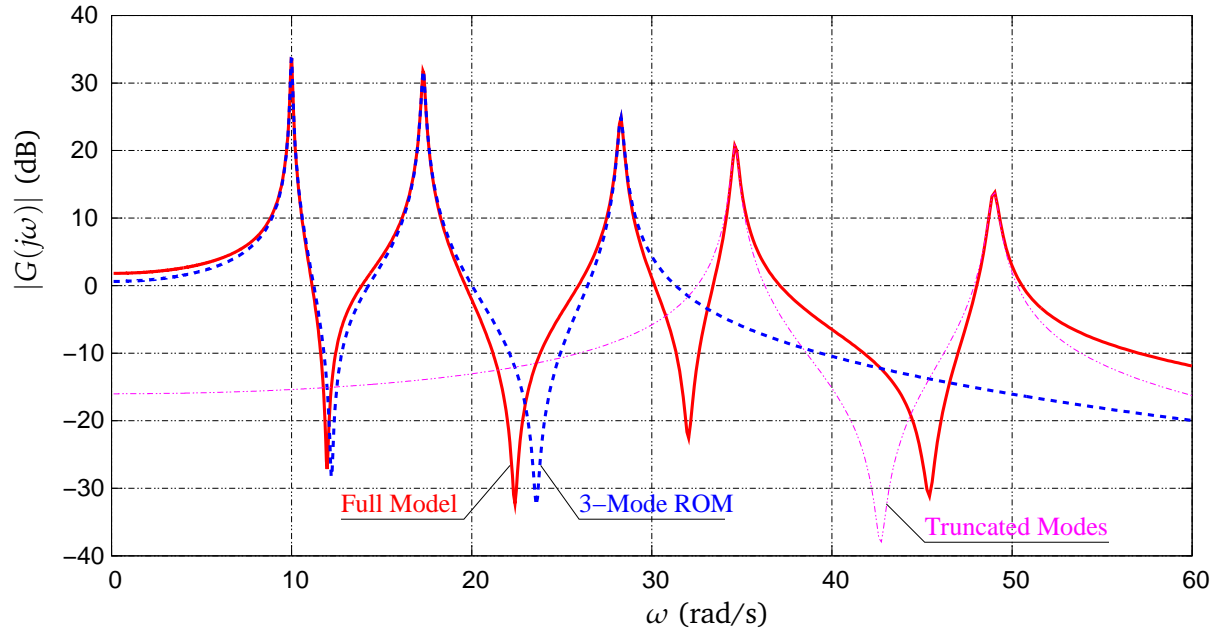
(a) Magnitude
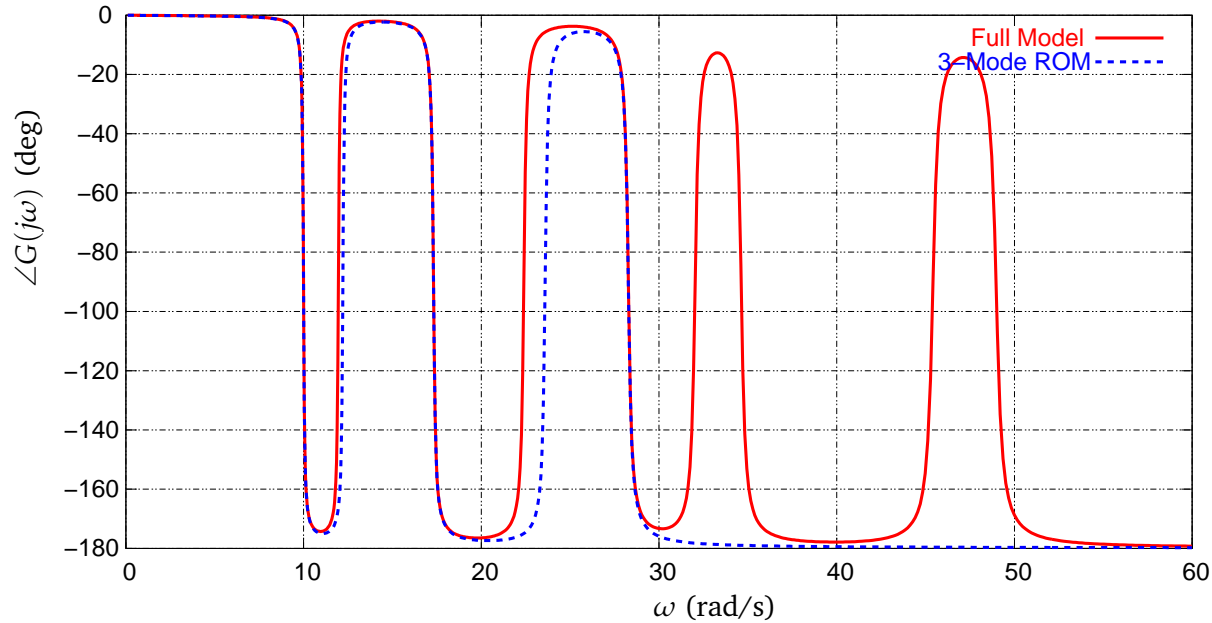
(b) Phase angle

Figure - 3.1: Modal truncation error in a ROM
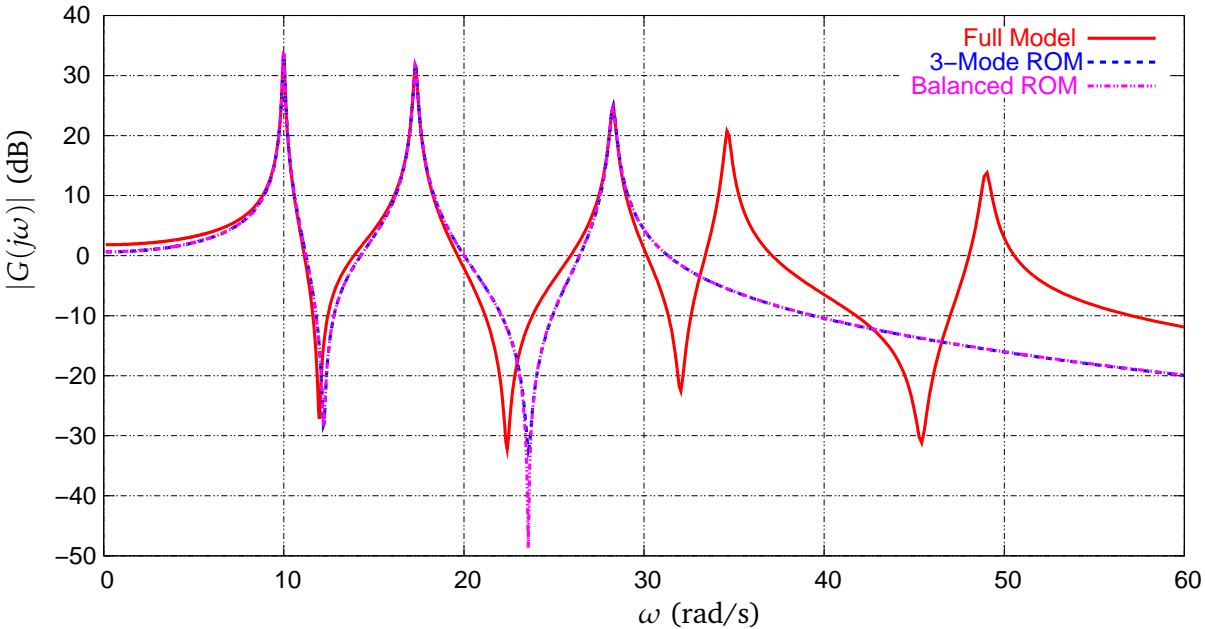
(a) Magnitude
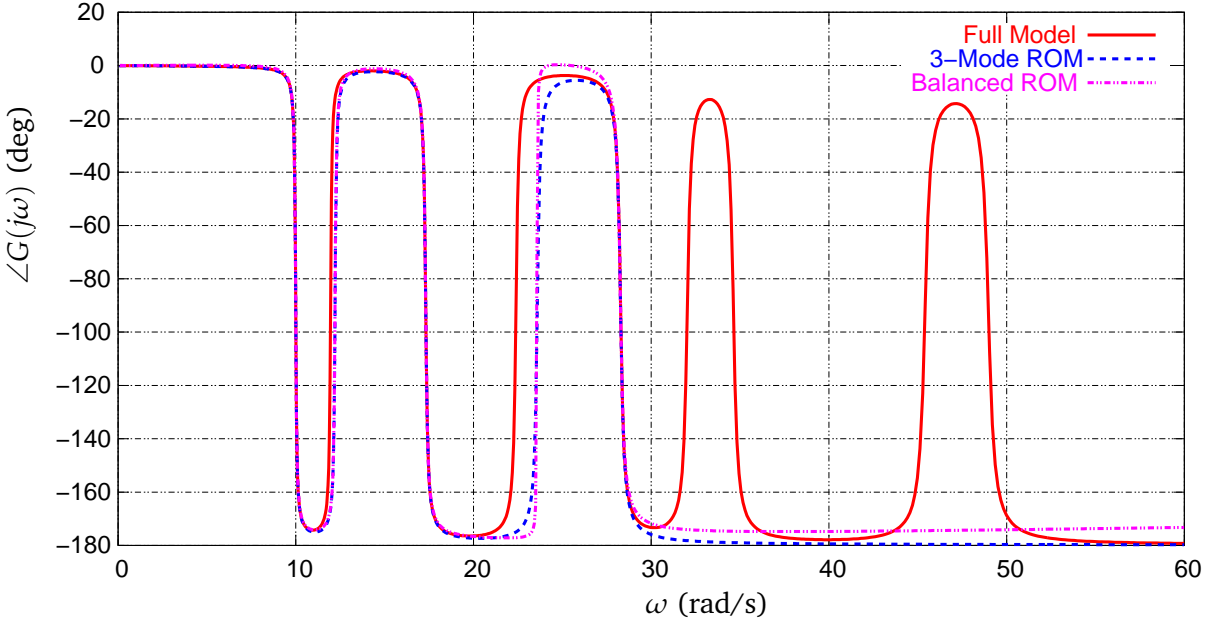
(b) Phase angle

Figure - 3.2: Truncation error in a ROM caused by the balanced model reduction
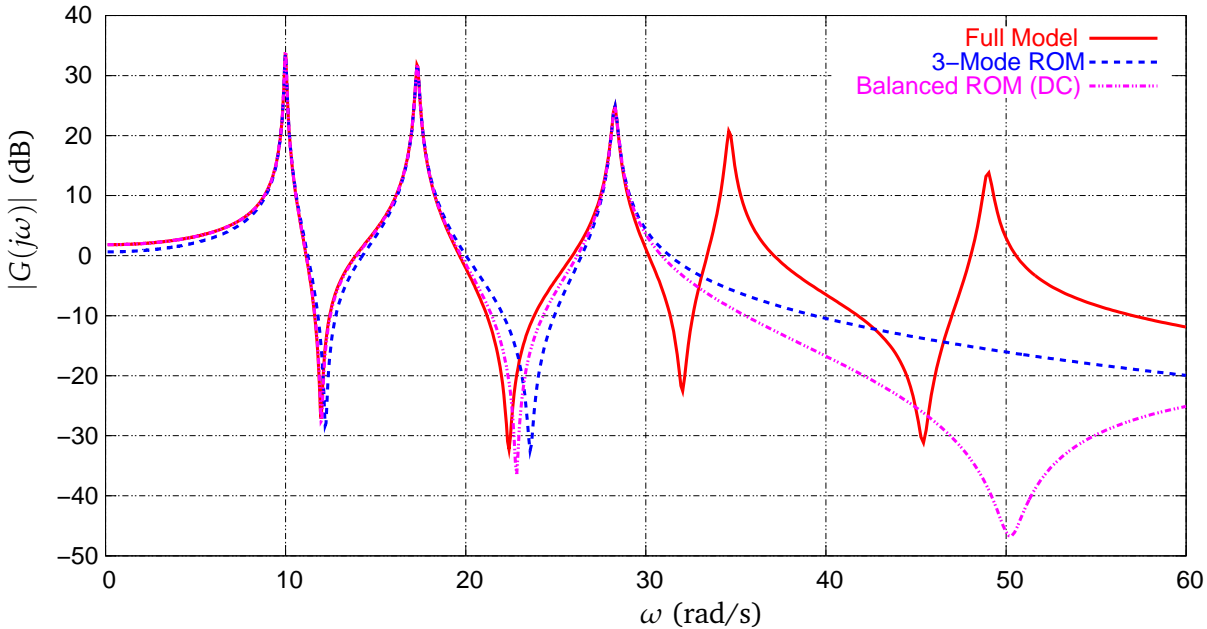
(a) Magnitude
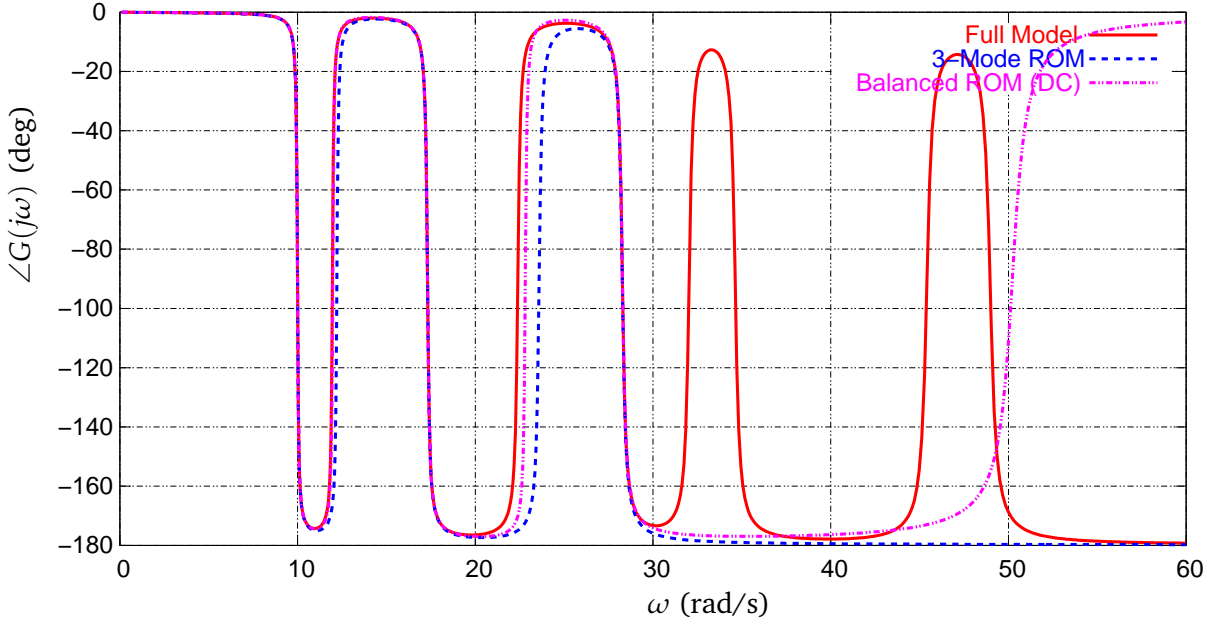
(b) Phase angle

Figure -3.3: Compensation of error using a feedthrough term

design. Therefore, this method can not be used in this research because a $\mathcal{H}_2$ controller will be used. To avoid getting a ROM with an infinite $\mathcal{H}_2$ norm, new approach should be developed.

3.3.2 Parametric Study

If the in-bandwidth contributions of the truncated modes can be compensated by adjusting the parameters of the in-bandwidth modes, then adding a feedthrough term to a ROM and the difficulty associated with this approach can be avoided. In this section, the effect of changing the corresponding modal parameters on the modal transfer function will be studied.

Without loss of generality, the following modal transfer function of a single input single output (SISO) structural system is considered,

$$G(j\omega) = \frac{a + jb\omega}{(\omega_n^2 - \omega^2) + 2j\zeta\omega_n\omega}, \tag{3.3.30}$$

where a and b are parameters associated with the displacement and velocity outputs, respectively, ζ and ω_n are modal damping ratio and natural frequency of the structure's mode. In the sequel, these parameters are refferred as the *modal parameters* associated with the modal transfer function as given in (3.3.30).

Among the modal parameters of a transfer function, the natural frequency ω_n determines the location of the transfer function's pole. In this study, ω_n will be kept unchanged, and the effect of changing a, b and ζ on the tansfer function associated with these parameters is analyzed.

Let these parameters be changed to their new values as shown below,

$$a' = \alpha a \qquad b' = \beta b \qquad \zeta' = \gamma\zeta, \tag{3.3.31}$$

where α, β and γ are *adjusting coefficients* corresponding to the modal parameters a, b and ζ, respectively. Correspondingly, the new transfer function (or perturbed transfer function) becomes

$$G'(j\omega) = \frac{a' + jb'\omega}{(\omega_n^2 - \omega^2) + 2j\zeta'\omega_n\omega} = \frac{\alpha a + j\beta b\omega}{(\omega_n^2 - \omega^2) + 2j\gamma\zeta\omega_n\omega}. \tag{3.3.32}$$

The magnitude of the original and perturbed transfer functions are given by

$$|G(j\omega)|^2 = \frac{a^2 + b^2\omega^2}{(\omega_n^2 - \omega^2)^2 + 4\zeta^2\omega_n^2\omega^2}, \tag{3.3.33}$$

$$|G'(j\omega)|^2 = \frac{\alpha^2 a^2 + \beta^2 b^2\omega^2}{(\omega_n^2 - \omega^2)^2 + 4\gamma^2\zeta^2\omega_n^2\omega^2}, \tag{3.3.34}$$

respectively. Define the ratio between the magnitudes of these two transfer functions as $r(\omega)$, i.e.

$$r(\omega) = \frac{|G'(j\omega)|}{|G(j\omega)|}. \tag{3.3.35}$$

By introducing

$$A = \frac{b\omega}{a}, \qquad B = \frac{\omega}{\omega_n}, \tag{3.3.36}$$

the magnitude ratio can be written as

$$r(\omega) = \sqrt{\left(\frac{\alpha^2 + \beta^2 A^2}{1 + A^2}\right)\left[\frac{(1 - B^2)^2 + 4\zeta^2 B^2}{(1 - B^2)^2 + 4\gamma^2\zeta^2 B^2}\right]} = r_1 \cdot r_2, \tag{3.3.37}$$

where

$$r_1 = \sqrt{\frac{\alpha^2 + \beta^2 A^2}{1 + A^2}}, \quad r_2 = \sqrt{\frac{(1 - B^2)^2 + 4\zeta^2 B^2}{(1 - B^2)^2 + 4\gamma^2\zeta^2 B^2}}. \tag{3.3.38}$$

It is seen that, when A is small (i.e. at low frequency range), r_1 is approximately proportional to α, while when A is large (i.e. at high frequency range), r_1 is approximately proportional to β. Figure - 3.4 visualizes the variation of the coefficient r_1 with respect to (α, A) and (β, A) when α and β are taking constant values around 1, namely $\alpha, \beta = 0.8, 1.0, 1.2$. These plots depict the variation trends of r_1 as a function of α, β and A. From these plots it is observed that, changing α and β affect the magnitude ratio over the whole frequency range, and the variation of r_1 is dominated by α in the lower frequency range, and by β in the higher frequency range. Because r_1 does not depend on the natural frequency ω_n, above observation applies to all modes.

As regarding r_2, it depends on the modal damping ratio ζ, the adjusting coefficient γ and the frequency ratio B. Figure - 3.5 and Figure - 3.6 show the variation of r_2 as a function γ and B when the damping ratio ζ taking four typical values, i.e. $\zeta = 0.005, 0.006, 0.007, 0.008$. It is seen from these plots that, compared with the change of α and β, the change of adjusting coefficient γ of the damping ratio has limited influence range around $B = 1$, i.e. $\omega = \omega_n$. The smaller the damping ratio ζ, the narrower the γ's influence range. Decreasing the modal damping ratio, i.e. $\gamma < 1$, increases the magnitude of the transfer function dramatically around $\omega = \omega_n$. Increasing the modal damping ratio, i.e. $\gamma > 1$, gradually reduces the magnitude around the neighborhood of $\omega = \omega_n$. The larger the γ, the wider this neighborhood. For a typical flexible structural damping, it is found that the width of the influenced neighbor is dependent on γ linearly as follows,

$$\Delta B \approx 1 \pm 0.025\gamma \tag{3.3.39}$$

PSfrag replacements

PSfrag replacements

(a) $\beta = 0.8$

(b) $\alpha = 0.8$

PSfrag replacements

PSfrag replacements

(c) $\beta = 1.0$

(d) $\alpha = 1.0$

PSfrag replacements

PSfrag replacements

(e) $\beta = 1.2$

(f) $\alpha = 1.2$
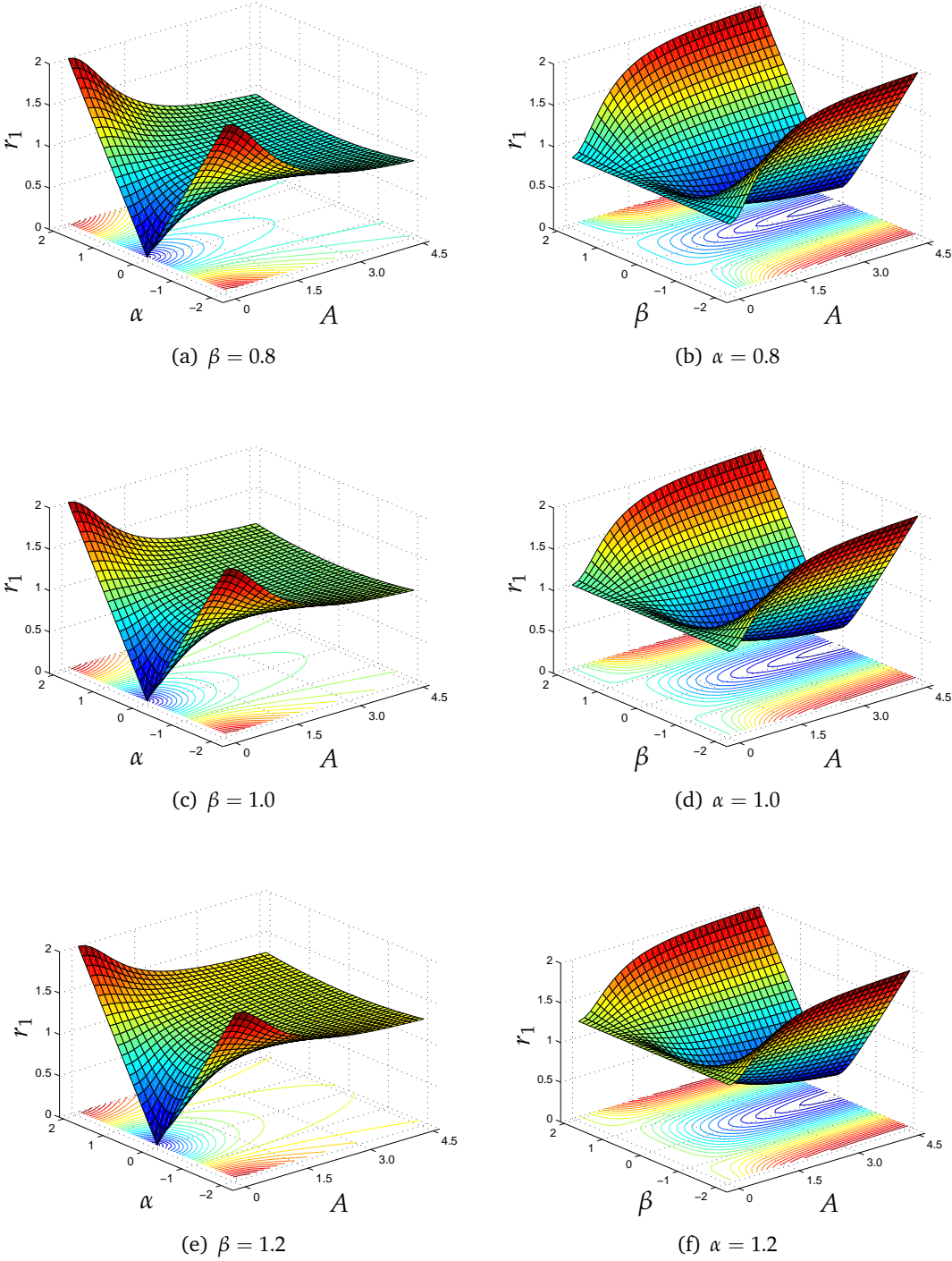
Figure -3.4: Variation of r_1 as a function of α, β and A

PSfrag replacements
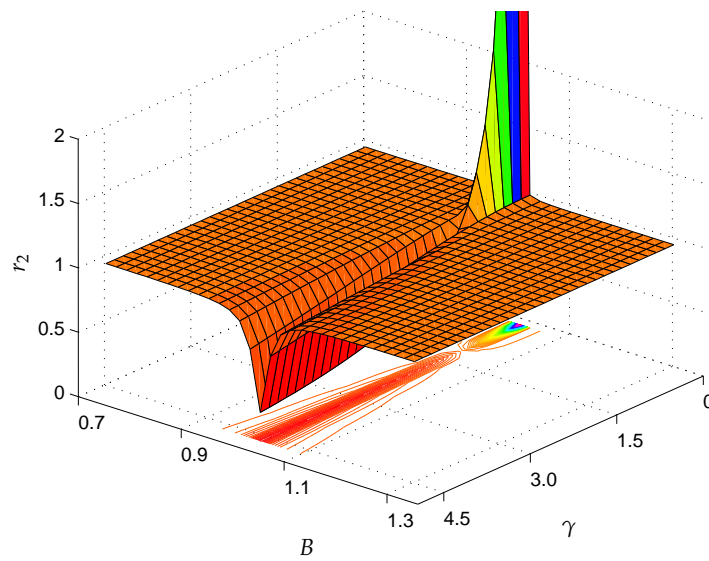
(a) Damping ratio $\zeta = 0.005$

PSfrag replacements
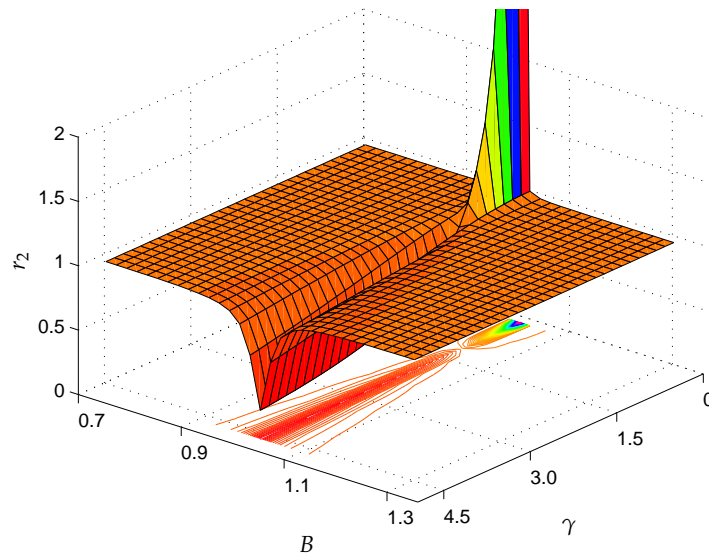
(b) Damping ratio $\zeta = 0.006$

Figure -3.5: Variation of r_2 as function of γ, ζ and B.
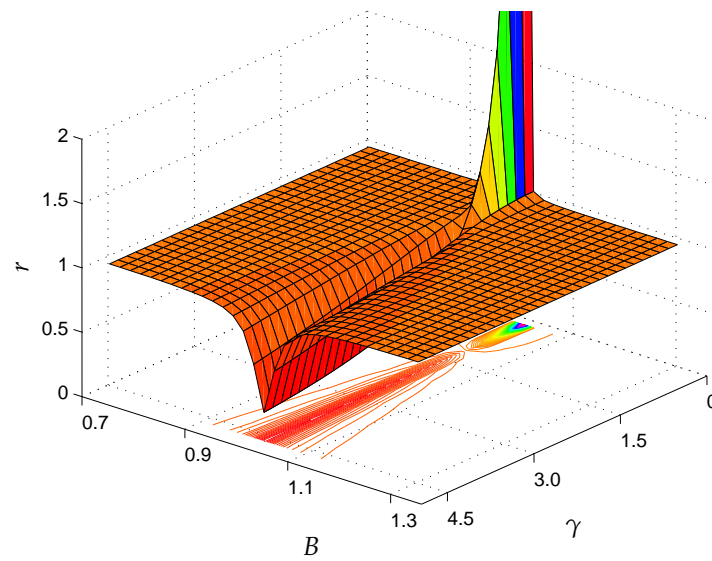
(a) Damping ratio $\zeta = 0.007$
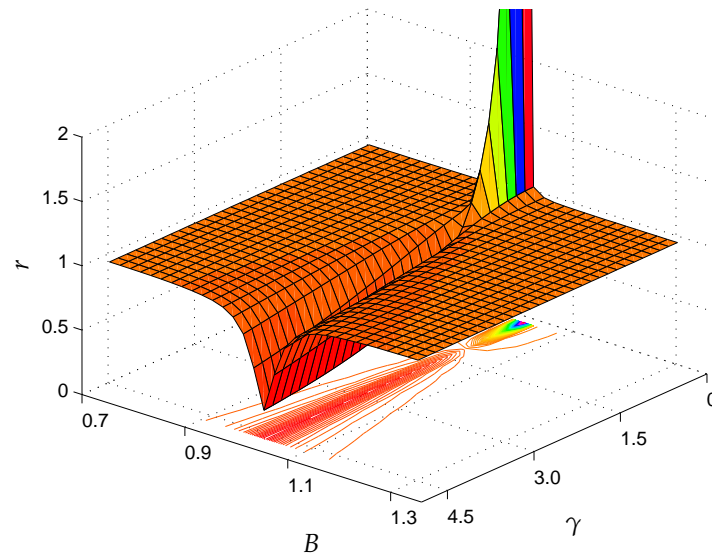
(b) Damping ratio $\zeta = 0.008$

Figure - 3.6: Variation of r_2 as function of γ, ζ and B (cont).

In summary of the above discussion, it was observed that change of the modal parameters α and β has global effects on the magnitude of the corresponding modal transfer function, while the change of damping ratio coefficient γ has local effects in a neighborhood around the resonant frequency ω_n. The width of the neighborhood is approximately proportional to γ.

In the following example, it will be demonstrated that for a system with multiple modes, by changing one or more of the modal transfer functions, the system zeros can be shifted without notable effect on the poles. Consider a 3-DOF system whose transfer function is given by $G(s) = G_1(s) + G_2(s) + G_3(s)$, where $G_i(s)$ $i = 1, 2, 3$ are three modal transfer functions given as follows,

$$G_1(s) = \frac{50}{s^2 + 0.1s + 100}, \quad G_2(s) = \frac{120}{s^2 + 0.17s + 300}, \quad G_3(s) = \frac{140}{s^2 + 0.28s + 800}.$$

Assume the transfer function of the second mode is perturbed as follows,

$$G_2'(s) = \frac{120\alpha}{s^2 + 0.17\gamma s + 300},$$

and the perturbed system is given by $G'(s) = G_1(s) + G_2'(s) + G_3(s)$. Figure - 3.7 plots the magnitudes and phase angles of of the transfer functions of $G(s)$ and $G'(s)$. It can be seen that two

(a) Magnitude   (b) Phase angle
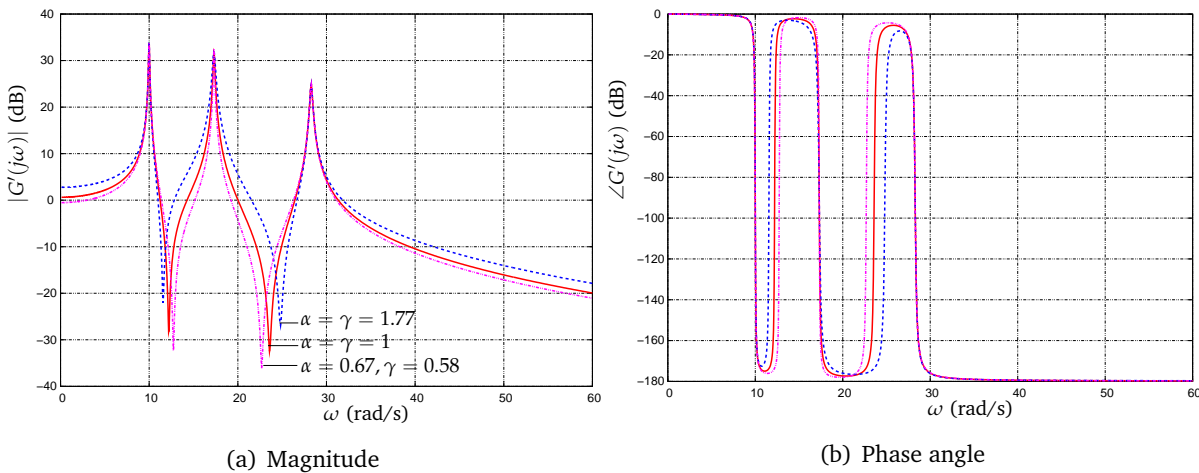
Figure - 3.7: Zero shift by change modal parameters.

zeroes of the transfer function $G'(s)$ can be displaced from their original locations by changing the modal parameters of the second mode. By increasing or decreasing the modal parameters, the direction to which the zeroes are moving can be controlled. In both cases, the magnitudes

of the transfer function poles have been kept unperturbed by ensuring an appropriate ratio between α and γ. In this example, it was assumed that $b = 0$. Similar effect can be observed for a more general case where a and b are both nonzero.

3.4 Model Reduction by Modified Modal Truncation

In the previous section, it has been showed that the zeroes of the transfer function of a ROM can be shifted by changing the modal parameters of the ROM. By adjusting these modal parameters in an appropriate way, it is expected that the truncation error can be minimized. An optimization problem is formulated in this section for this purpose.

For a n-DOF MIMO structural system with p outputs and q inputs, its transfer function is a $p \times q$ complex valued matrix as given in (3.3.24). The (i,j) entry of this matrix is a transfer function $G_{ij}(s)$ describing input-output dynamics from the j-th input to the i-th output, which is given by

$$G_{ij}(s) = \sum_{k=1}^{n} \frac{(c_{dik} + c_{vik}s)b_{kj}}{s^2 + 2\zeta_k \omega_k s + \omega_k^2}, \tag{3.4.40}$$

with $i = 1, 2, \ldots, p$, $j = 1, 2, \ldots, q$. A set of parameters $\alpha_{ijk}, \beta_{ijk}, \gamma_{ijk}$ are seeked such that a r-mode ROM of the following form,

$$G'_{ij}(s) = \sum_{k=1}^{r} \frac{(\alpha_{ijk}c_{dik} + \beta_{ijk}c_{vik}s)b_{kj}}{s^2 + 2\gamma_{ijk}\zeta_k \omega_k s + \omega_k^2}, \tag{3.4.41}$$

minimizes the following error index,

$$\Delta_{ij} = \int_0^\infty |W(\omega)(G_{ij}(j\omega) - G'_{ij}(j\omega))| d\omega, \tag{3.4.42}$$

where $W(\omega)$ is a weighting function defined by

$$W(\omega) = \begin{cases} 1, & \omega \leq \omega_r, \\ 0, & \omega > \omega_r. \end{cases} \tag{3.4.43}$$

The error index Δ_{ij} defined above measures the error that exist in the ij input-output channel of the r-mode ROM due to truncation.

As discussed in the previous section, the error index defined in (3.4.42) can be minimized by finding a set of optimal modal parameters associated with the transfer function of this input-output channel. By introducing the adjusting coefficients as given in (3.3.31), minizing the

truncation error of a ROM can be formulated as an optimization problem that finds a set of optimal adjusting coefficients α^*_{ijk}, β^*_{ijk} and γ^*_{ijk}, such that the truncation error Δ_{ij} given in (3.4.42) is minimized, i.e.

$$(\alpha^*_{ijk}, \beta^*_{ijk}, \gamma^*_{ijk}) = \text{argmin}(\Delta_{ij}) \tag{3.4.44}$$

for $i = 1, 2, \ldots, p$, $j = 1, 2, \ldots, q$ and $k = 1, 2, \ldots, r$. The optimization problem formulated above is a nonlinear optimization problem. It is difficult to find a globally optimal solution to the problem using a gradient based algorithm.

In this research, this optimization problem will be solved using a Genetic Algorithm (GA), which was first proposed by Holland [70] and used as an effective numerical method to find a global optimal (or sub-optimal) solution to a complicated multi-parameter optimization problem. An introduction to the GA method can be found in Appendix C.

For the optimization problem as given in (3.4.44), each of the optimization variables, i.e. α_{ijk}, β_{ijk} and γ_{ijk}, are real numbers. In the GA method, these real variables are represented as follows,

$$\alpha_{ijk} = \frac{R^1_\alpha - R^0_\alpha}{N_{ij}} n_\alpha, \quad \beta_{ijk} = \frac{R^1_\beta - R^0_\beta}{N_{ij}} n_\beta, \quad \gamma_{ijk} = \frac{R^1_\gamma - R^0_\gamma}{N_{ij}} n_\gamma, \tag{3.4.45}$$

where (R^0_α, R^1_α), (R^0_β, R^1_β) and (R^0_γ, R^1_γ) are three set of pre-selected real numbers that define the ranges of the variables α_{ijk}, β_{ijk} and γ_{ijk}, respectively, N_{ij} is an integer number represents the resolution used in the GA method for searching the optimization variables, n_α, n_β and n_γ are three integer variables that encoded in the GA method to represent α_{ijk}, β_{ijk} and γ_{ijk}, respectively. By introducing the relationships given in (3.4.45), the original optimization problem (3.4.44) is transformed to a problem with integer optimization variables, which is solvable using a binary-string-encoded GA method as introduced in Appendix C.

Based on the parametric study presented previously, the following parameters are used in solving the optimization problem defined in (3.4.44),

$$(R^0_\alpha, R^1_\alpha) = (-4, +4), \quad (R^0_\beta, R^1_\beta) = (-4, +4), \quad (R^0_\gamma, R^1_\gamma) = (0, +4), \tag{3.4.46}$$

and $N_{ij} = 2^{16}$, i.e. the length of the binray-string codes used in the GA method is 16. Correspondingly, the resolutions for the optimization variables α_{ijk} and β_{ijk} are 1.2×10^{-4}, and the resolution for γ_{ijk} is 0.6×10^{-4}. Upon the termination of the GA iterations, a set of optimal n_α, n_β and n_γ are found, and the corresponding optimal variables α_{ijk}, β_{ijk} and γ_{ijk} can be obtained from (3.4.45).

3.4.1 Approximation of Real System

To solve the above defined optimization problem, the transfer matrix representing the real dynamics of a MIMO structural system is needed. For a n-DOF MIMO structural system, the transfer function associated with the ij input-output channel is a summation of n modal transfer functions associated with this channel as given in (3.4.40). When n is large, computing the transfer matrix of the full model system using (3.4.40) is expensive and not necessary. In this case, an approximation of the transfer matrix is used to solve the optimization problem defined above. This approximation should include contributions from all dominant modes for the all input-output channels. For a flexible structure, these dominant modes can be found by using the method suggested by Gawronski [67].

For a n-DOF structural system, let $G_i(j\omega) = C_i(j\omega I - A_i)^{-1} B_i$ be the modal transfer function associated with the i-th mode, where A_i is defined as follows,

$$A_i = \begin{bmatrix} 0 & \omega_i \\ -\omega_i & -2\zeta_i\omega_i \end{bmatrix}, \tag{3.4.47}$$

where ω_i is the natural frequency of the i-th mode, and B_i is the i-th row of the matrix B in (3.3.22), C_i is the output matrix given by

$$C_i = \begin{bmatrix} \dfrac{C_{di}}{\omega_i} & C_{vi} \end{bmatrix}, \tag{3.4.48}$$

in which C_{di} and C_{vi} are i-th column of the matrix $C_d\boldsymbol{\Phi}$ and $C_v\boldsymbol{\Phi}$ given in (3.3.22), respectively. When the modal damping ratio is small, the controllability and observability Gramians of G_i are diagonally dominant [67], i.e.

$$W_c \approx \operatorname{diag}(w_{ci}I_2), \quad W_o = \operatorname{diag}(w_{oi}I_2), \tag{3.4.49}$$

where $i = 1, 2, \ldots, n$, I_2 is a 2×2 identity matrix, w_{ci} and w_{oi} are the modal controllability and observability matrices, respectively, given by

$$w_{ci} = \frac{\|B_i\|_2^2}{4\zeta_i\omega_i}, \qquad w_{oi} = \frac{\|C_i\|_2^2}{4\zeta_i\omega_i}. \tag{3.4.50}$$

In the above equations, $\|\cdot\|_2$ denotes the $\mathcal{H}_2$ norm operator, which is defined as in (2.4.55). For a real constant matrix X, the $\mathcal{H}_2$ norm of the matrix can also be obtained as follows

$$\|X\|_2 = \sqrt{\lambda_{max}(X^T X)}, \tag{3.4.51}$$

where $\lambda_{max}(\cdot)$ denote the maximum eigenvalue of a matrix. The $\mathcal{H}_2$ norm of a transfer function is defined in (2.4.56). However, for a lightly damped structure system, the $\mathcal{H}_2$ norm of its i-th modal transfer function can be approximated [67] by

$$\|G_i\|_2 \approx \frac{\|B_i\|_2 \|C_i\|_2}{2\sqrt{\zeta_i \omega_i}}. \tag{3.4.52}$$

Furthemore, the $\mathcal{H}_2$ norm of the whole system is approximately given by the RMS sum of the $\mathcal{H}_2$ norm of all modal transfer functions, i.e.

$$\|G\|_2 = \sqrt{\sum_{i=1}^{n} \|G_i\|_2^2}. \tag{3.4.53}$$

The above relationships provide an efficient way to find the dominant modes of a lightly damped structure. The dominance of a mode can be evaluated using the following index,

$$r_i = \frac{\|G_i\|_2^2}{\|G\|_2^2}, \quad i = 1, 2, \ldots, n, \tag{3.4.54}$$

which gives the percentage of the contribution of the i-th mode to the total system $\mathcal{H}_2$ norm. The lager r_i, the more important this mode is in terms of the input-output gain. Therefore, a mode is defined dominant if the corresponding index r_i is larger than some threshold value.

After the dominant modes are found, the transfer function of the system used in the optimization problem (3.4.44) can be approximated by the summation of the modal transfer functions of these dominant modes. The error caused by this approximation can be controlled by the threshold value used in the definition of a dominant mode.

3.4.2 Algorithm of Modified Modal Truncation Using GA Method

The algorithm described here is to use a GA method to solve a model reduction problem as define in (3.4.44). The algorithm can be outlined as follows:

1. Build a finite element model for the given structure, perform modal analysis to obtain the modal parameters for each mode;

2. Find the dominant modes for the structure using the index given in (3.4.54);

3. Compute the approximation of the transfer matrix $G(s)$ using the obtained dominant modes;

4. Solve the optimization problem (3.4.44) for $(\alpha_{ijk}^*, \beta_{ijk}^*, \gamma_{ijk}^*)$ using the GA method as introduced in Appendix C;

5. Substituting the optimal $(\alpha_{ijk}^*, \beta_{ijk}^*, \gamma_{ijk}^*)$ obtained in the previous step into (3.4.41) gives the transfer function of the ROM.

The flow-chart of the above steps is shown in Figure - 3.8. In this figure, the shaded blocks

PSfrag replacements
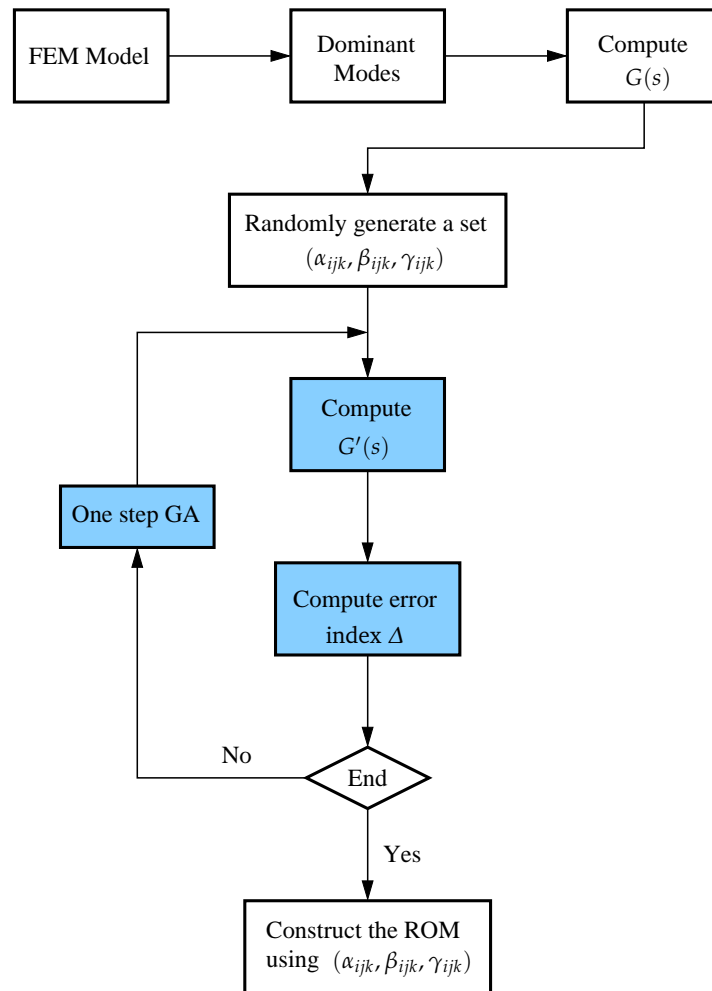
Figure - 3.8: Flow-chart of the model reduction algorithm

constitute a complete GA iterations which are detailed in Appendix C. The obtained ROM is in the form of the transfer matrix, whose state space realization can be found using either the balanced realization method, or the Eigensystem Realization Algorithm (Appendix B).
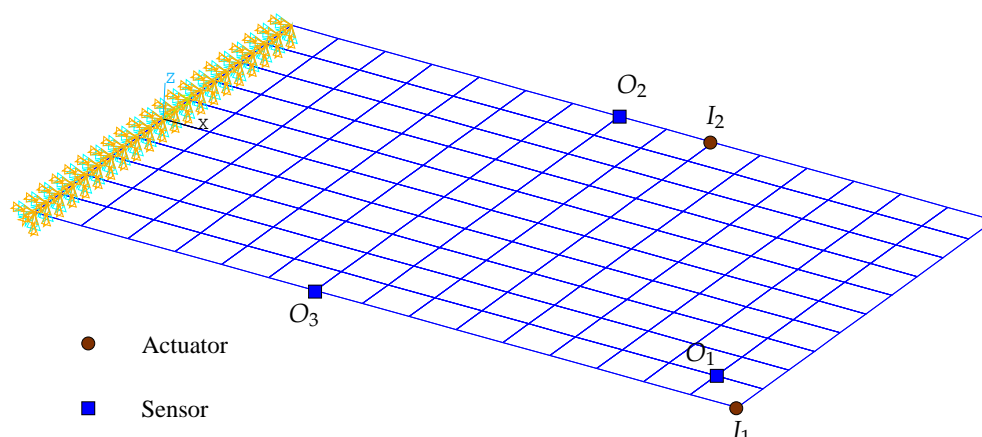
Figure -3.9: A cantilever plate with 2 actuators and 3 displacement sensors.

3.5   Numerical Example

A model reduction problem for a cantilever plate is solved using the proposed algorithm in this section. The plate considered here is shown in Figure - 3.9. The plate is of a dimension $30 \times 20 \times 0.2$ (in), and made of a material with the Young's modulus $E = 30 \times 10^6$ psi, the Possion's ratio $\nu = 0.27$ and the mass density $\rho = 0.0009218$ lb/in^3. There are 2 point actuators (denoted by I_1 and I_2) and 3 point displacement sensors (denoted by O_1, O_2 and O_3) are attached to the plate at the locations as shown in Figure - 3.9.

First, the plate is discretized using the 150 8-node Mindlin plate elements. There are totally 501 nodes, and 1203 DOF's in the FEM model of the plate. Modal matrix and natural frequencies of the plate are obtained via a modal analysis. Figure - 3.10 shows the mode shapes and the corresponding natural frequencies of the first 10 modes.

To find the dominant modes, the modal contribution indices r_i are computed. Let $G(s)$ be the transfer function of the system, $G^{(k)}(s)$ represent the transfer function of the system containing the first k modes. When k is large enough, $\|G^{(k)}(s)\|_2$ converges to $\mathcal{H}_2$ norm of the system. By simulation, it is found that

$$\|G^{(k)}\|_2 \rightarrow 2.4372 \quad \text{when } k > 20,$$

i.e. $\|G\|_2 \approx 2.437$. Figure - 3.11-(a) shows the variation of $\|G^{(k)}\|/\|G\|$ v.s k. Given the system norm $\|G\|_2$, the modal contribution index r_i for $i = 1, 2, \ldots, 40$ are computed. Figure - 3.11-(b) plots these indices. From this figure, it is observed that, except those shaded modes, contribu-

60

(a) 1st mode (6.63 Hz)

(b) 2nd mode (22.60 Hz)

(c) 3rd mode (41.27 Hz)

(d) 4th mode (76.00 Hz)

(e) 5th mode (103.07 Hz)

(f) 6th mode (118.87 Hz)

(g) 7th mode (154.47 Hz)

(h) 8th mode (164.02 Hz)

(i) 9th mode (229.50 Hz)

(j) 10th mode (257.14 Hz)
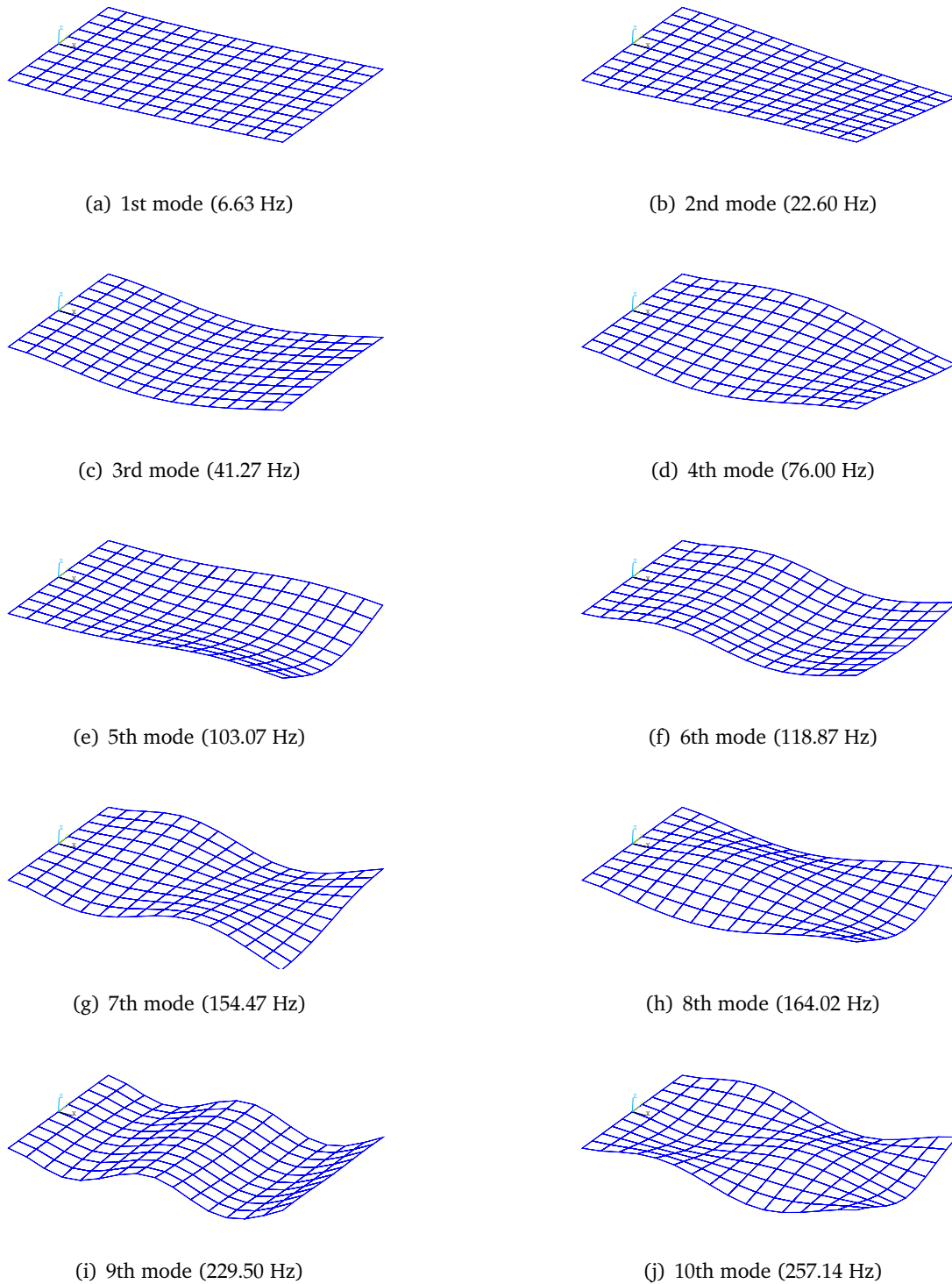
Figure -3.10: The mode shapes of the first 10 modes.

(a) Accumulative contribution   (b) Contribution index
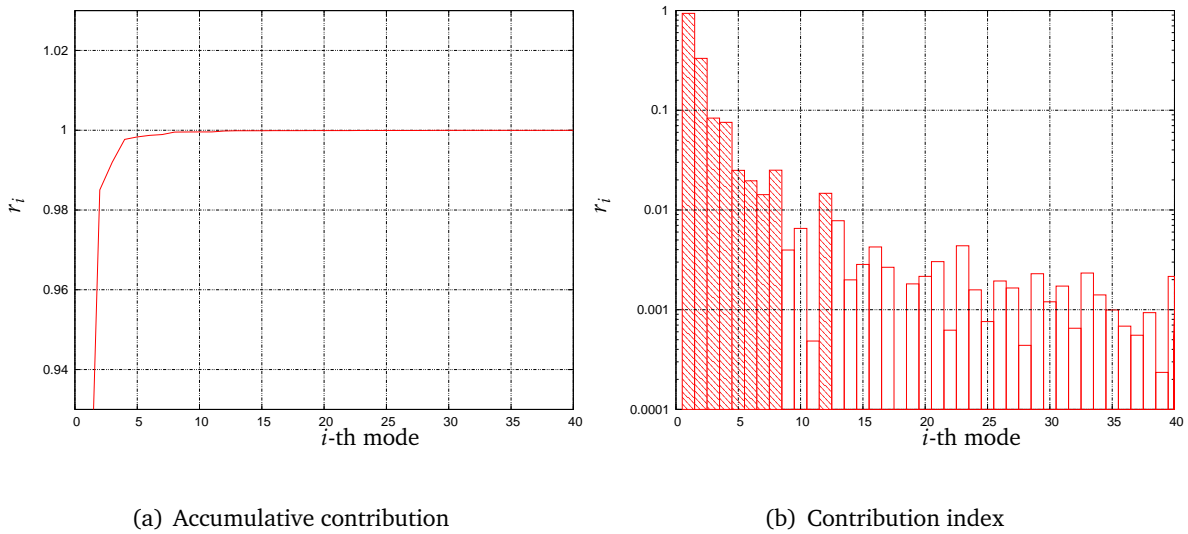
Figure - 3.11: Contributions indices of the first 40 modes.

tions of all other individual modes are less than 1%. Assume that all modes corresponding to $r_i < 1\%$ can be ingorned, then it is adquate to approximate the original 1203-DOF system by its first 20 modes.

Using the algorithm described previously, a 3-mode ROM for the structure system is constructed. The optimal adjusting coefficients corresponding to the modal parameters of the first 3 modes found by using the GA method are listed as follows:

$$
[\gamma_{11k}, \alpha_{11k}] = \begin{bmatrix} 1.64 & 1.02 \\ 1.31 & 1.09 \\ 1.09 & 1.47 \end{bmatrix}, \ [\gamma_{12k}, \alpha_{12k}] = \begin{bmatrix} 1.08 & 1.03 \\ 1.06 & 1.03 \\ 0.95 & 0.81 \end{bmatrix}, \ [\gamma_{21k}, \alpha_{21k}] = \begin{bmatrix} 1.31 & 1.00 \\ 1.02 & 1.11 \\ 1.14 & 0.80 \end{bmatrix},
$$

$$
[\gamma_{22k}, \alpha_{22k}] = \begin{bmatrix} 0.86 & 0.98 \\ 0.87 & 1.06 \\ 0.66 & 1.41 \end{bmatrix}, \ [\gamma_{31k}, \alpha_{31k}] = \begin{bmatrix} 1.02 & 0.99 \\ 0.87 & 0.94 \\ 0.74 & 1.16 \end{bmatrix}, \ [\gamma_{32k}, \alpha_{32k}] = \begin{bmatrix} 0.98 & 0.99 \\ 0.97 & 1.01 \\ 0.97 & 0.94 \end{bmatrix}.
$$

$$(3.5.55)$$

Relative error reduction v.s. GA iteration steps for each channels are shown in Figure - 3.12. For a given channel, the relative error reduction shown in the figure is defined as the ratio of truncation errors of the adjusted ROM and the original 3-mode ROM, which was obtained by the direct modal truncation. After 100 GA iteration steps, the relative errors associated with the

PSfrag replacements

PSfrag replacements

(a) Channel G_{11}

(b) Channel G_{12}

PSfrag replacements

PSfrag replacements

(c) Channel G_{21}

(d) Channel G_{22}

PSfrag replacements

PSfrag replacements

(e) Channel G_{31}

(f) Channel G_{32}
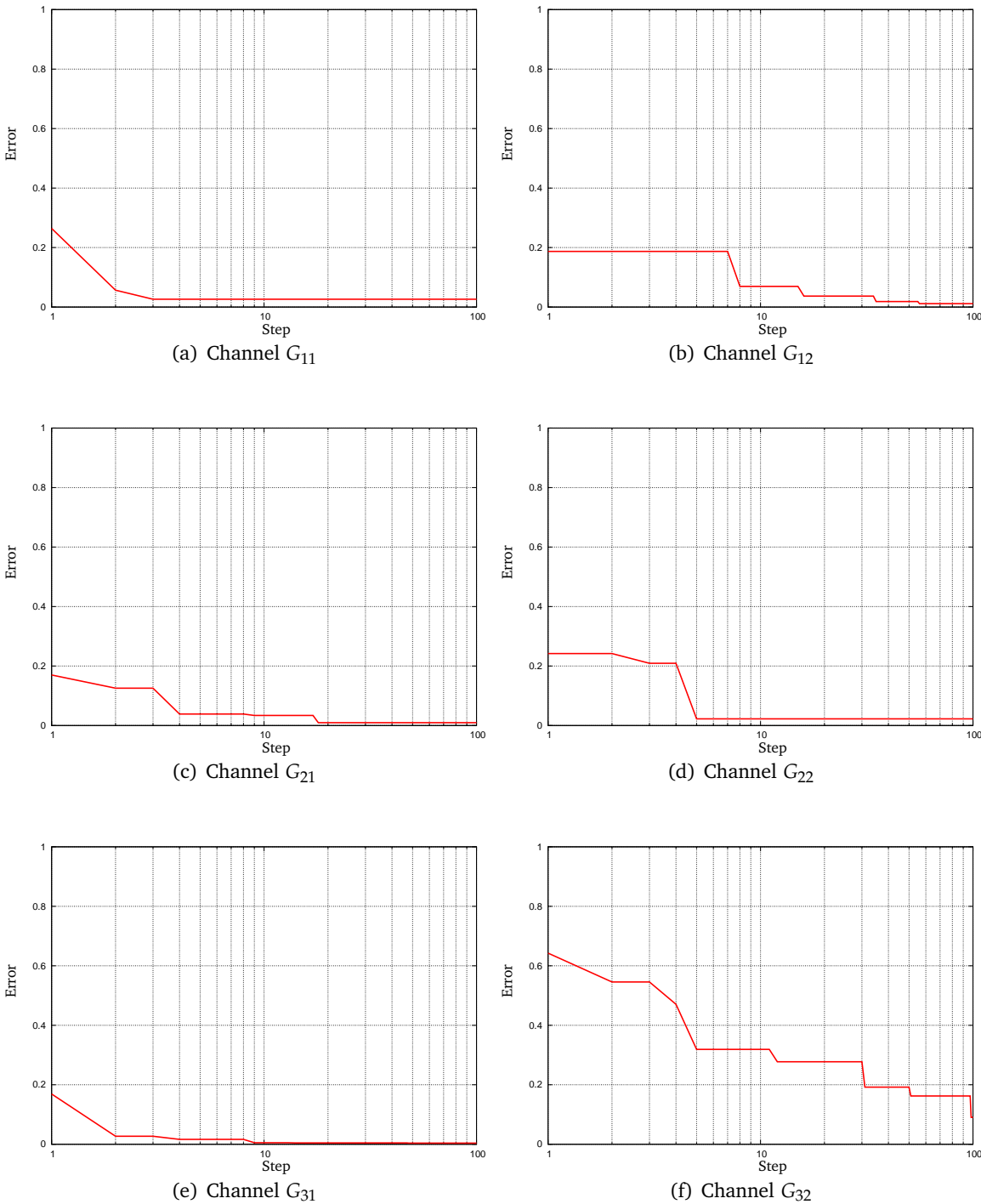
Figure -3.12: Error v.s. GA iteration steps for each input-output channels

3×2 input-output channels are found as follows,

$$
\begin{bmatrix}
3.56\% & 1.71\% \\
1.66\% & 2.37\% \\
0.78\% & 11.38\%
\end{bmatrix} .
\tag{3.5.56}
$$

IN the above, the relative error associated with the ij input-output channel is defined as follows,

$$
\frac{\int_0^\infty |W(\omega)(G_{ij} - G_{ij}^*)|}{\int_0^\infty |W(\omega)(G_{ij} - G_{ij}')|}
\tag{3.5.57}
$$

where G_{ij} is the transfer function of the full model, G_{ij}^* denotes the optimal ROM found by the proposed method, and G_{ij}' denotes the ROM obtained from the traditional modal truncation method.

The adjusted modal parameters can be obtained from (3.3.31) using the optimal adjusting coefficients given in (3.5.55). Figure - 3.13 plots the magnitudes of the transfer matrix of the full model, the optimal ROM, which was constructed using the adjusted modal parameters obtained above, and the ROM obtained from the direct modal truncation. It can be seen that in each of input-output channels, the transfer function curve of the optimal ROM matches that of full model satisfactorily. Especially for the channels G_{11}, G_{12}, G_{21} and G_{22}, the originally large zero shifts caused by the truncation errors have been reduced clearly. For the channels where the original ROM is already close enough to the full model, such as channel G_{32} as shown in Figure - 3.13(f), the improvement on the truncation error is not as good as other channels. Figure - 3.14 plots the corresponding phase angles of the full model, original ROM and the optimal ROM. It can be seen that the agreement of phase angles between the full model and the optimal 3-mode ROM are also improved.

The obtained ROM is in the form of transfer matrix. Its state space form can be found using either the balanced realization method, or the ERA algorithm as introduced in Appendix B.

(a) Channel G_{11}

(b) Channel G_{12}

(c) Channel G_{21}

(d) Channel G_{22}

(e) Channel G_{31}

(f) Channel G_{32}
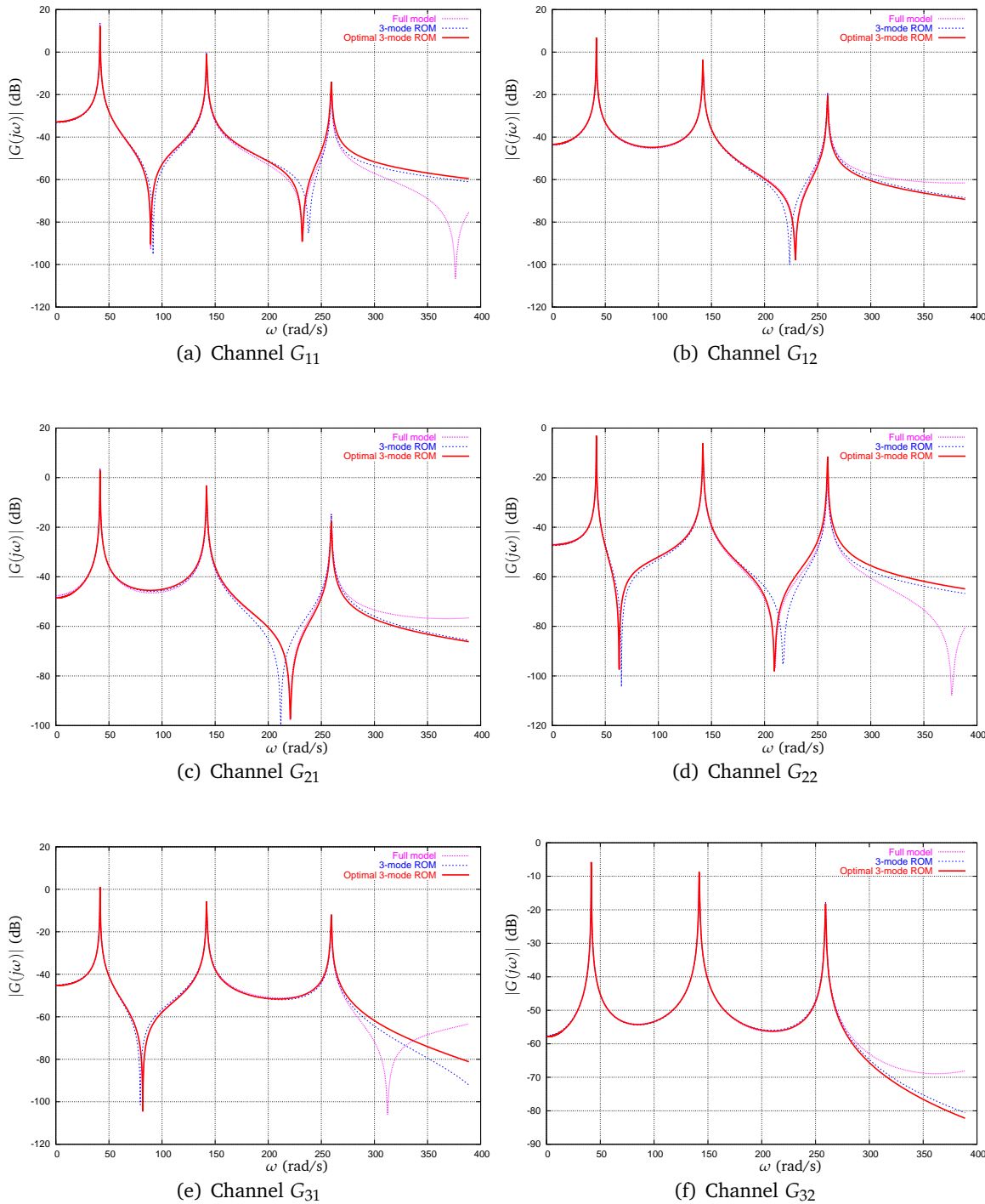
Figure -3.13: Magnitude of the transfer functions for each input-output channels

PSfrag replacements

PSfrag replacements

(a) Channel G_{11}

(b) Channel G_{12}

PSfrag replacements

PSfrag replacements

(c) Channel G_{21}

(d) Channel G_{22}

(e) Channel G_{31}

(f) Channel G_{32}
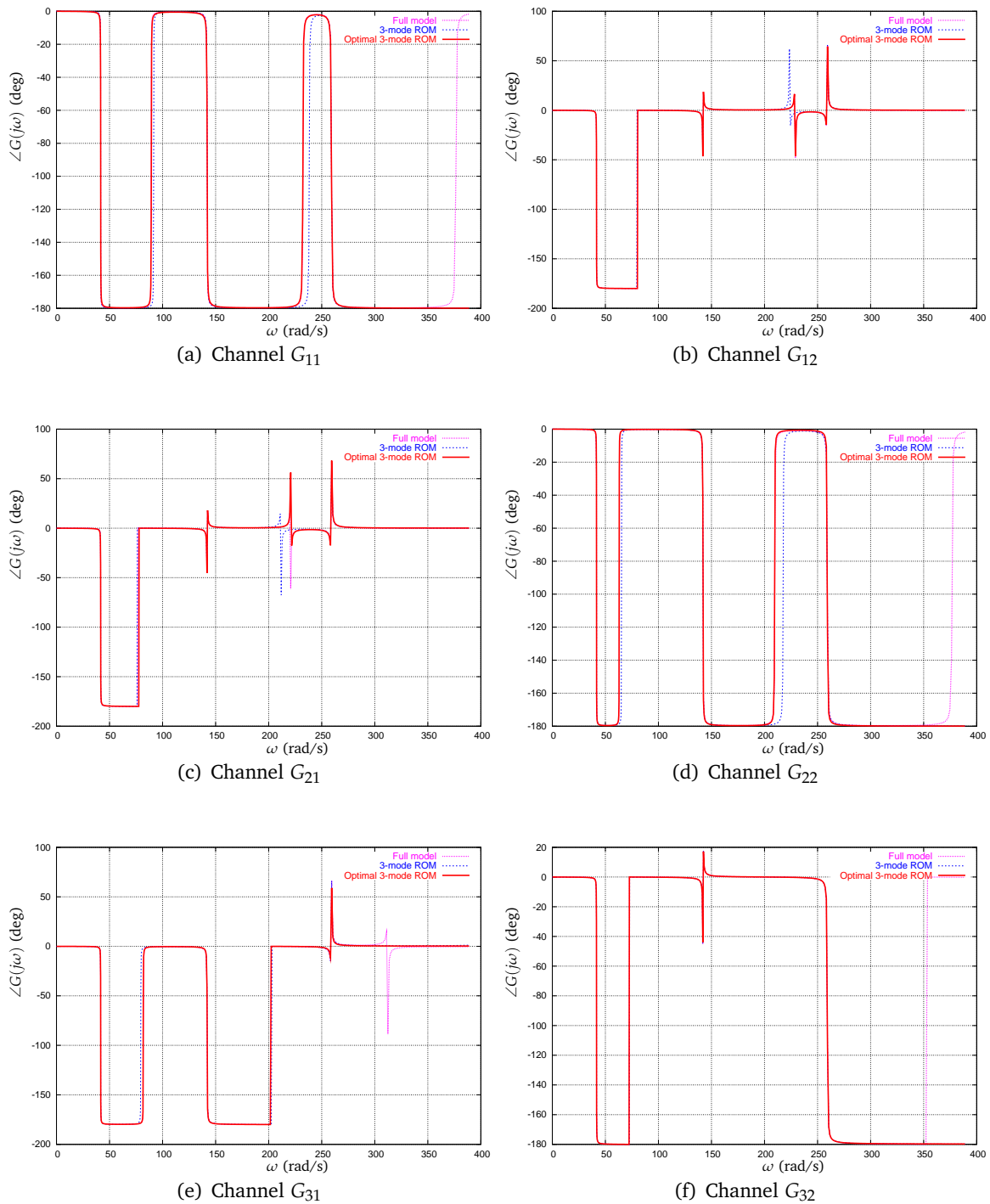
Figure -3.14: Phase angle of the transfer functions for each input-output channels

3.6 Summary

Model reduction problem was studied, and a methodology to compensate the zero shift observed in the transfer matrix of a modal-truncation based ROM was developed. The balanced model reduction and modal truncation methods were introduced. It was showed that zero shift happened to the transfer matrix of a ROM obtained either from balanced model reduction or the direct modal truncation method. Through the parametric study, it was found that the zero shifts, which was caused by the truncation error, observed in a transfer function could be reduced by changing the modal parameters associated with the transfer function. Based on this observation, an innovative approach to minimize the zero shifts by tuning modal parameters of a ROM was proposed. The GA method was used in the proposed method to find a set of optimal modal parameters such that the zero shifts, i.e. the truncation errors, were minimized. The method was verified using a numerical example. Simulation results showed that the agreement between the transfer functions of the full model and the optimal ROM was improved satisfactorily.

It should be noted that, although the method developed in this chapter was aimed at reducing the zero shift observed in a modal-truncation based ROM, no assumption made in the development of the method could prevent the method from being used to other situations. Although the contents discussed in section 3.4.1 is necessary in this research, it is not an essential part of the proposed method itself. Because in a real application, the transfer matrix of a structural system can obtained through experiments, and the approximation of the system as discussed in section 3.4.1 can be skipped.

Suppression of Spillover Instability

4.1 Introduction

Spillover happens when a reduced-order model (ROM) based controller is used to control a higher order system. Consider a system $G(s)$, let $G_r(s)$ be a ROM of the system, $G_t(s)$ be the truncated (or residual) dynamics, and $K(s)$ be a controller based on the ROM $G_r(s)$. Figure - 4.1 shows the closed-loop system when the controller is used to the original system $G(s)$. It can be
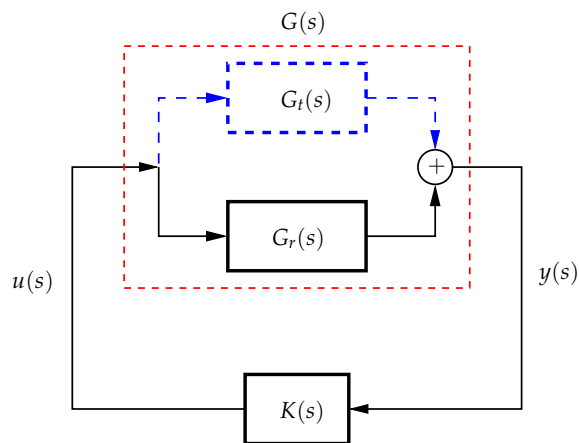
Figure -4.1: Schematic of a closed-loop SVC system.

seen that there exist two closed-loop subsystems: $K(s) \rightleftharpoons G_r(s)$ and $K(s) \rightleftharpoons G_t(s)$. The first closed-loop subsystem is the one that the controller was designed for, while the latter one isn't.

In the closed-loop system as shown in Figure - 4.1, there are some control input energy leaks into the residual dynamics, and this leakage is known as the *control spillover*. Similarly, some output signals due to the residual dynamics are feedback to the controller, which is known as the *observation spillover*. Both control and observation spillovers act as a disturbance to the closed-loop subsystem $K(s) \rightleftharpoons G_r(s)$ degrading the overall performance of the closed-loop system. In some cases, especially when the damping effects are small, the control system could become unstable.

Due to its adverse effects on the performance of a SVC system, and its potentials to induce the instability, the spillover has been studied in many researches. Various methods have been developed aiming at suppressing the spillover instability in a SVC system. However, as discussed in the Chapter 1, there are more or less limitations on the methods developed in the previous works. In this chapter, suppression of spillover instability is studied. Through an investigation on the mechanism of spillover, it is expected that an efficient method to suppress the spillover instability that is suitable for SVC systems design for large scale structures can be developed.

4.2   Mechanism of Spillover

In this section, mechanism of spillover and the spillover-induced instability in a SVC system are studied. The system as shown in Figure - 4.1 is considered here.

Assume a structural system $G(s)$ has n DOFs, p inputs, q outputs consisted of the outputs from q_d displacement and q_v velocity sensors. Let $G(s)$ has the following realization,

$$G(s) = \left[\begin{array}{c|c} A & B \\ \hline C & 0 \end{array} \right], \tag{4.2.1}$$

where $A \in \mathbb{R}^{2n \times 2n}$, $B \in \mathbb{R}^{2n \times p}$ and $C \in \mathbb{R}^{q \times 2n}$ are given as follows

$$A = \begin{bmatrix} 0 & I \\ -\Omega^2 & -2\Omega\zeta \end{bmatrix}, \quad B = \begin{bmatrix} 0 \\ \Phi^T B_f \end{bmatrix}, \quad C = \begin{bmatrix} C_d \Phi^T & C_v \Phi^T \end{bmatrix}, \tag{4.2.2}$$

and

$$\begin{aligned} &\Omega = \mathrm{diag}(\omega_1, \omega_2, \ldots, \omega_n), \quad \zeta = \mathrm{diag}(\zeta_1, \zeta_2, \ldots, \zeta_n), \\ &\Phi = \begin{bmatrix} \phi_1 & \phi_2 & \cdots & \phi_n \end{bmatrix} \end{aligned} \tag{4.2.3}$$

In the above equations, ω_i, ζ_i and $\boldsymbol{\phi}_i \in \mathbb{R}^n$ are natural frequency, modal damping ratio and the mode shape vector of the i-th mode, respectively, $B_f \in \mathbb{R}^{n \times p}$ is input matrix denoting the locations of inputs, $C_d \in \mathbb{R}^{q \times n}$, $C_v \in \mathbb{R}^{q \times n}$ are output matrices denoting the locations of the displacement and velocity sensors, respectively. Let $G_r(s)$ denote a r-mode ROM of the structural system system $G(s)$ defined above.

For simplicity, the partions of the matrices B_d, C_d and C_v that will be repeatedly used in the following derivation are defined here. Assume the number of actuators, displacement sensors and velocity sensors are all less than the number of modes included in the ROM[1], i.e.

$$p < r, \quad q_d < r, \quad q_v < r, \tag{4.2.4}$$

then without loss of generality, the matrix B_f can be partitioned as follows,

$$B_f = \begin{bmatrix} B_{fr} \\ 0 \end{bmatrix}, \tag{4.2.5}$$

where $B_{fr} \in \mathbb{R}^{r \times p}$. Similarly, C_d and C_v are partitioned as follows,

$$\begin{bmatrix} C_d & C_v \end{bmatrix} = \begin{bmatrix} C_{dr} & 0 & C_{vr} & 0 \end{bmatrix}, \tag{4.2.6}$$

where $C_{dr}, C_{vr} \in \mathbb{R}^{q \times r}$. $\boldsymbol{\Omega}$ and $\boldsymbol{\zeta}$ are partitioned such that

$$\boldsymbol{\Omega} = \begin{bmatrix} \boldsymbol{\Omega}_r & 0 \\ 0 & \boldsymbol{\Omega}_t \end{bmatrix}, \quad \boldsymbol{\zeta} = \begin{bmatrix} \boldsymbol{\zeta}_r & 0 \\ 0 & \boldsymbol{\zeta}_t \end{bmatrix}, \tag{4.2.7}$$

with $\boldsymbol{\Omega}_r \in \mathbb{R}^{r \times r}$ and $\boldsymbol{\zeta}_r \in \mathbb{R}^{r \times r}$. Moreover, the modal matrix $\boldsymbol{\Phi}$ is partitioned such that,

$$\boldsymbol{\Phi} = \begin{bmatrix} \boldsymbol{\Phi}_{rr} & \boldsymbol{\Phi}_{tr} \\ \boldsymbol{\Phi}_{rt} & \boldsymbol{\Phi}_{tt} \end{bmatrix}, \tag{4.2.8}$$

where $\boldsymbol{\Phi}_{rr} \in \mathbb{R}^{r \times r}$ and $\boldsymbol{\Phi}_{rt} \in \mathbb{R}^{(n-r) \times r}$.

In Figure - 4.1, $K(s)$ is an output feedback controller based on the ROM $G_r(s)$. Assume the realization for the controller is given by

$$K(s) = \left[\begin{array}{c|c} A_K & B_K \\ \hline C_K & D_K \end{array} \right]. \tag{4.2.9}$$

---

[1]This assumption is made for simplicity purpose, and does not affect the validity of the derivation.

Let $[a_r \ \dot{a}_r]$ and x_K denote the state vectors of the ROM $G_r(s)$ and the controller $K(s)$, respectively. Using the notations defined above, the dynamics of the closed-loop subsystem $K(s) \rightleftharpoons G_r(s)$ formed by the controller and the ROM can be written as follows

$$
\begin{Bmatrix} \dot{a}_r \\ \ddot{a}_r \\ \dot{x}_K \end{Bmatrix} = \begin{bmatrix} 0 & I & 0 \\ -\Omega_r^2 & -2\Omega_r\zeta_r & \Phi_{rr}^T B_{fr} C_K \\ B_K C_{dr}\Phi_{rr} & B_K C_{vr}\Phi_{rr} & A_K \end{bmatrix} \begin{Bmatrix} a_r \\ \dot{a}_r \\ x_K \end{Bmatrix} + \begin{Bmatrix} 0 \\ 0 \\ B_K C_{dr}\Phi_{tr}a_t + B_K C_{vr}\Phi_{rt}\dot{a}_t \end{Bmatrix},
$$
(4.2.10)

where $[a_r \ \dot{a}_r]$ is the state vector of the residual modes. Because the controller was designed to stabilize $G_r(s)$, the subsystem (4.2.10) is guaranteed stable. The right-hand-side term $B_K C_{dr}\Phi_{tr}a_t + B_K C_{vr}\Phi_{tr}\dot{a}_t$ comes from the truncated modes, and acting on the input channel of the controller like a measurement noise. The following equations, i.e.

$$
\begin{Bmatrix} \dot{a}_t \\ \ddot{a}_t \\ \dot{x}_K \end{Bmatrix} = \begin{bmatrix} 0 & I & 0 \\ -\Omega_t^2 & -2\Omega_t\zeta_t & \boxed{\Phi_{tr}^T B_{fr} C_K} \\ \boxed{B_K C_{dr}\Phi_{tr}} & \boxed{B_K C_{vr}\Phi_{tr}} & A_K \end{bmatrix} \begin{Bmatrix} a_t \\ \dot{a}_t \\ x_K \end{Bmatrix} + \begin{Bmatrix} 0 \\ 0 \\ B_K C_{dr}\Phi_{rr}a_r + B_K C_{vr}\Phi_{rr}\dot{a}_r \end{Bmatrix}
$$
(4.2.11)

describe the dynamics of the residual modes, where $\Phi_{tr}^T B_{fr} C_K$ is known as the control spillover term, which represents the leakage of the control forces to the residual modes, $B_K C_{dr}\Phi_{tr}$ and $B_K C_{vr}\Phi_{tr}$ are known as observation spillover terms, which correspond to the perturbations to the controller caused by the displacement and velocity signals from the truncated modes, respectively.

It is through the control and observation spillover terms that the residual dynamics interact with the controller. This interaction could lead to the instability of the residual dynamics. If there is no control spillover, i.e. $\Phi_{tr}^T B_r C_K \equiv 0$, the stability of the residual dynamics is determined by the eigenvalues of the following matrix,

$$
\begin{bmatrix} 0 & I & 0 \\ -\Omega_t^2 & -2\Omega_t\zeta_t & 0 \\ B_K C_{dr}\Phi_{tr} & B_K C_{vr}\Phi_{tr} & A_K \end{bmatrix}.
$$
(4.2.12)

Because the matrix is in a block triangular form, its eigenvalues are same as those of the matrices

$$
\begin{bmatrix} 0 & I \\ -\Omega_t & -2\Omega_t\zeta_t \end{bmatrix} \quad \text{and} \quad A_K.
$$
(4.2.13)

71

As long as the controller $K(s)$ is stable, so is the matrix (4.2.12), and as a result, the residual dynamics are stable. Same result can be obtained when the observation spillover terms vanish. The above discussions can be summarized in the following theorem,

Theorem 2. *A necessary condition for the spillover instability happening to a closed-loop system is that both the control and observation spillover terms present, i.e.*

$$\boldsymbol{\Phi}_{tr}^T B_{fr} C_K \neq 0, \quad B_K C_{dr} \boldsymbol{\Phi}_{tr} \neq 0 \quad \text{and/or} \quad B_K C_{vr} \boldsymbol{\Phi}_{tr} \neq 0.$$

An important implication of the above theorem is that, the spillover instability can be avoided through blocking either the control or the observation spillover in a closed-loop system. Using a low-pass-filter (LPF) to the outputs from sensors is an approach trying to block the observation spillover, and therefore achieve the objective of avoiding the spillover instability. However, as reviewed in Chapter 1, the effect of this approach is compromised when there is no enough frequency gap between the cutoff frequency of the ROM and the lower frequency of the residual modes. Furthermore, introducing a LPF increases the size of the closed-loop system, disturbs the eigenvalues of the observer, and therefore is not favorable.

4.3   A Null Space Approach for Suppressing Spillover Instability

In the above section, it was concluded that the spillover instability can be avoided by eliminating either the control or the observation spillover terms. Utilizing this conclusion, a method to suppress the spillover instability in a SVC system is developed in this section.

Elimination of the control spillover is first discussed. One possible way to reduce the control spillover term $\boldsymbol{\Phi}_{tr}^T B_{fr} C_K$ to zero is to put all actuators on the vibration nodes of the residual modes, i.e. to construct a B_{fr} matrix such that

$$\boldsymbol{\Phi}_{tr}^T B_{fr} = 0. \tag{4.3.14}$$

For a large scale structure, it is generally true that the number of modes included in the ROM is much less than the number of residual modes $R = n - r$, i.e. $r \ll R$. Without loss of generality, it is assumed that the last m' rows of Φ_{tr}^T are all zeros, then it follows

$$\Phi_{tr}^T B_{fr} = \begin{bmatrix} \Phi_{tr1}^T \\ 0 \end{bmatrix} B_{fr}, \quad \text{where } \Phi_{tr1}^T \in {}^{(R-m') \times r}. \tag{4.3.15}$$

In general cases, Φ_{tr1}^T has full (column) rank, therefore $\Phi_{tr}^T B_{fr} = 0$ leads to a trivial solution $B_{fr} = 0$. However, this solution makes the r-mode ROM $G_r(s)$ uncontrollable. Only in some special cases, where $\text{rank}(\Phi_{tr}^T) \leq r$, a non-trivial solution could be obtained. Similar conclusion applies to the observation spillover terms. Through the above discussion it can be seen that, for a large scale structure with a ROM-based controller, it is generally impossible to bring the control spillover and observation spillover terms to zero by placing actuators and sensors at the vibration nodes of the residual modes.

Actually, it is not necessary to reduce the spillover terms mentioned above to zero for all residual modes. Generally, the controller used in a SVC system is a dynamical system with limited frequency bandwidth. Amplification effects of the controller on the signals whose frequency is far beyond the controller's bandwidth will be vanishingly small. For these signals, the second closed-loop subsystem as shown in Figure - 4.1 can not be formed. In other words, the spillover instability due to these signals is unlikely to happen. As a result, to avoid spillover instability, only the spillover terms corresponding to some of the residual modes[2] needs to be brought to zero.

Therefore, although it is impossible to find a control input matrix B_f bringing the corresponding control spillover term $\Phi_{tr}^T B_{fr}$ to zero for the all residual modes, it is possible to find a nontrivial matrix B_f such that the spillover terms $\Phi_{tr}^T B_{fr}$ vanishes for a few selected residual modes as summarized in the following theorem.

Theorem 3. *Given a r-mode ROM of a n-DOF plant, and p actuators, there exist a control input matrix $B_{fr} \in \mathbb{R}^{r \times (p-\ell)}$ with $0 < \ell < p$ such that*

- *control spillover term $\Phi_{tr}^T B_{fr} = 0$ for any ℓ of the residual modes;*

- *the r-mode ROM is controllable.*

Proof. In the control spillover term $\Phi_{tr}^T B_{fr}$, Φ_{tr}^T has dimension of $R \times r$ with $R = n - r$ being the number of residual modes. It can be partitioned as follows,

$$\Phi_{tr}^T = \begin{bmatrix} \Phi_{tr11}^T & \Phi_{tr12}^T \\ \Phi_{tr21}^T & \Phi_{tr22}^T \end{bmatrix} \in \mathbb{R}^{R \times r},$$

---

[2]How to find these modes will be discussed later in this chapter.

where Φ_{tr11}^T has dimension of $\ell \times p$, and other submatrices have compatible dimensions. Because $\ell < p$, a non-trivial null space of Φ_{tr11}^T can always be found. Denote the null space operator by $N(*)$, and define

$$B_{fr} := \begin{bmatrix} N(\Phi_{tr11}^T) \\ 0 \end{bmatrix} \in \mathbb{R}^{r \times (p-\ell)}, \quad \text{where } N(\Phi_{tr11}^T) \in \mathbb{R}^{p \times (p-\ell)}$$

then the spillover term can be written as follows,

$$\Phi_{tr}^T B_{fr} = \begin{bmatrix} \Phi_{tr11}^T & \Phi_{tr12}^T \\ \Phi_{tr21}^T & \Phi_{tr22}^T \end{bmatrix} \begin{bmatrix} N(\Phi_{tr11}^T) \\ 0 \end{bmatrix} = \begin{bmatrix} 0 \\ \Phi_{tr21}^T N(\Phi_{tr11}^T) \end{bmatrix}.$$

By substituting the above control spillover term $\Phi_{tr}^T B_{fr}$ into (4.2.11), it's easy to verify the following relationships,

$$\ddot{a}_i + 2\zeta_i \omega_i \dot{a}_i + \omega_i^2 a_i = 0, \quad \text{for } i = r+1, r+2, \ldots, r+\ell,$$

which indicate that the control spillover term corresponding to the ℓ residual modes starting from $r+1$ has been eliminated.

It is true that $\text{rank}(\Phi_{rr}) = r$, i.e. $N(\Phi_{rr}) = 0 \neq B_{fr}$, therefore, the controllability of the r-mode ROM is guaranteed. $\qquad \square$

In the above proof, the B_{fr} matrix was constructed such that the control inputs are orthogonal to a subspace spanned by the first ℓ residual modes. It should be noted that the above theorem can be applied to any selected ℓ residual modes, which are not necessarily those starting from the $(r+1)$-th mode. Moreover, these ℓ residual modes are not necessarily consecutive.

The observation spillover for some residual modes can be eliminated similarly by constructing an output matrix in a null space spanned by these residual modes as showed in following theorem.

Theorem 4. *Given a r-mode ROM of a n-DOF plant, and $q = q_d + q_v$ (q_d displacement and q_v velocity) sensors, there exist a output matrices $C_{dr} \in \mathbb{R}^{(q-s) \times r}$ and $C_{vr} \in \mathbb{R}^{(q-s) \times r}$ such that*

- *the observation spillover terms $C_{dr}\Phi_{tr}$ and $C_{vr}\Phi_{tr}$ corresponding to s residual modes are zero;*

- *the r-mode ROM is observable.*

where $s = \min\{s_1, s_2 \mid 0 < s_1 < q_d,\ 0 < s_2 < q_v\}$.

Proof. When both displacement and velocity sensors present, $C_{dr}\Phi_{tr}$ denotes the observation spillover due to the displacement sensors, and $C_{vr}\Phi_{tr}$ denotes the the observation spillover due to velocity sensors. First, consider $C_{dr}\Phi_{tr}$ term. Partition $\Phi_{tr}^T \in \mathbb{R}^{R \times r}$ as follows

$$\Phi_{tr}^T = \begin{bmatrix} \Phi_{tr11}^T & \Phi_{tr12}^T \\ \Phi_{tr21}^T & \Phi_{tr22}^T \end{bmatrix},$$

where $R = n - r$ is the number of residual modes, Φ_{tr11}^T has dimension of $s \times q$, and all other submatrices have compatible dimensions. Define

$$C_{dr} := \begin{bmatrix} \left(N(\Phi_{tr11}^T)\right)^T & 0 \end{bmatrix} \in \mathbb{R}^{(q-s) \times r}, \quad \text{where } N(\Phi_{tr11}^T) \in \mathbb{R}^{q \times (q-s)}.$$

Because $s < q$, it follows that $N(\Phi_{tr11}^T) \neq 0$, and $C_{dr} \neq 0$. Then

$$C_{dr}\Phi_{tr} = \left(\Phi_{tr}^T C_{dr}^T\right)^T = \left(\begin{bmatrix} \Phi_{tr11}^T & \Phi_{tr12}^T \\ \Phi_{tr21}^T & \Phi_{tr22}^T \end{bmatrix} \begin{bmatrix} N(\Phi_{tr11}^T) \\ 0 \end{bmatrix}\right)^T = \begin{bmatrix} 0 & \Phi_{tr21}^T N(\Phi_{tr11}^T) \end{bmatrix}.$$

In the above equations, the zero submatrix has dimension of $(q - s) \times s$. Thus, the displacement observation spillover over s residual modes corresponding to Φ_{tr11} has been eliminated.

The similar arguments apply for to the velocity spillover term. By partitioning Φ_{tr}^T as follows

$$\Phi_{tr}^T = \begin{bmatrix} \bar{\Phi}_{tr11}^T & \bar{\Phi}_{tr12}^T \\ \bar{\Phi}_{tr21}^T & \bar{\Phi}_{tr22}^T \end{bmatrix}$$

where $\bar{\Phi}_{tr11}^T \in \mathbb{R}^{s \times q}$. By defining

$$C_{vr} := \begin{bmatrix} \left(N(\bar{\Phi}_{tr11}^T)\right)^T & 0 \end{bmatrix} \in \mathbb{R}^{(q-s) \times r}, \quad \text{where } N(\bar{\Phi}_{tr11}^T) \in \mathbb{R}^{q \times (q-s)},$$

it can be verified that

$$C_{vr}\Phi_{tr} = \left(\Phi_{tr}^T (C_{vr})^T\right)^T = \begin{bmatrix} 0 & \bar{\Phi}_{tr21}^T N(\bar{\Phi}_{tr11}^T) \end{bmatrix}.$$

The zero submatrix in the above equation has dimension of $(q - s) \times s$, i.e. , the velocity observation spillover corresponding to s residual modes has been eliminated. Therefore, when both kind of sensors present, i.e. $s_1 > 0$ and $s_2 > 0$, there are totally $s = \min\{s_1, s_2\}$ residual modes

for which both the displacement observation spillover and the velocity observation spillover can be eliminated.

Because Φ_{rr} is non-singular, it follows $C_{dr}\Phi_{rr} \neq 0$ and $C_{vr}\Phi_{rr} \neq 0$, therefore, the output matrix $[C_d\ C_v]$ guarantees the observability of the r-mode ROM. $\hfill\square$

Again, this theorem applies to any selected s residual modes, not necessarily to those starting from the $(r+1)$-th mode, and these modes need not to be consecutive.

From Theorem 3, Theorem 4 and the discussions therein, it is seen that for a given r-mode ROM with p actuators, q_d displacement sensors and q_v velocity sensors, the possible spillover instability can be suppressed for totally $N = \ell + s$ residual modes, where $\ell < p$ and $s = \min\{s_1, s_2 \mid 0 < s_1 < q_d,\ 0 < s_2 < q_v\}$. This observation can be visualized in Figure - 4.2. It
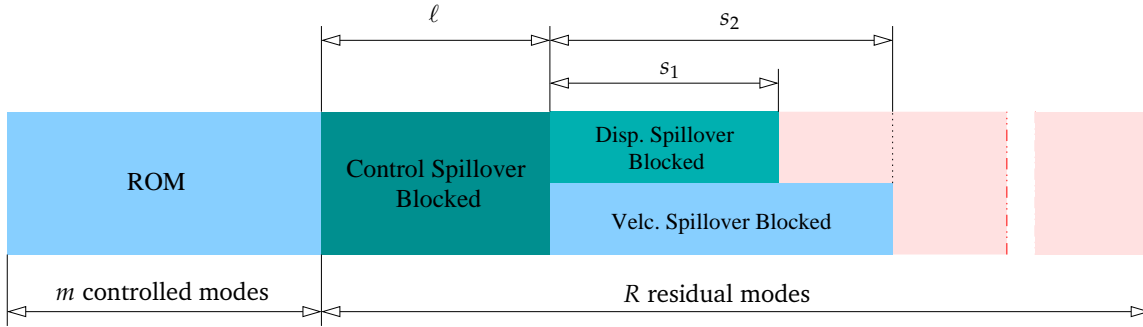
Figure - 4.2: Residual modes where spillover instability is blocked

should be noted that, when only one kind of sensors are used, for example when $q_v = 0$, i.e. only q_d displacement sensors are used, the number of residual modes for which the observation spillover can be eliminated is determined by $s = \{s_1 \mid 0 < s_1 < q_d\}$. Similarly, when $q_d = 0$, s is given by $s = \{s_2 \mid 0 < s_2 < q_v\}$.

Through the process described above, an input matrix B_{fr} and the output matrices C_{dr} and C_{vr} used in a controller design were constructed in a subspace orthogonal to the space spanned by some selected residual modes, such that the resultant controller is able to avoid spillover instability when it is used to control the higher order system.

In the previous section, the assumption (4.2.4) was made. This assumption does not affect the validity of the proposed method. For example, when the number of sensors are greater than the number of in-bandwidth modes, these sensors can be divided into several groups such that

PSfrag replacements

Figure - 4.3: Internal structure of a controller with spillover-suppression capability.

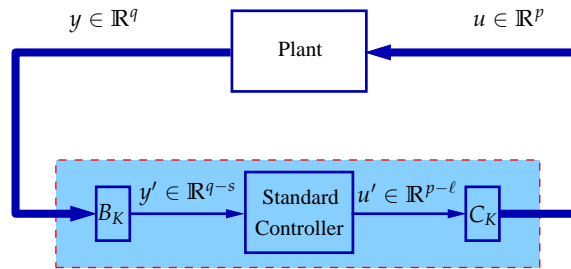each group satisfies that assumption. Alternatively, by following the idea presented above, it's easy to show that more number of residual modes can be blocked for the spillover. Obviously, in this case, favorable results will be obtained.

It should be noted that the controller designed by using the above obtained input and output matrices has a special internal structure different from those designed using a standard approach. Figure - 4.3 shows a closed-loop system formed by a plant and a controller with spillover-suppression capability. In this figure, the internal structure of the controller is shown in the shaded box. The q measurements from the plant are fed into the controller through matrix $B_K \in \mathbb{R}^{(q-s) \times q}$. An embedded standard controller utilizes the output $y' \in \mathbb{R}^{q-s}$ transformed by the matrix B_K to generate an intermediate control input $u' \in \mathbb{R}^{p-\ell}$, which is then transformed by the matrix $C_k \in \mathbb{R}^{p \times (p-\ell)}$ to generate a real control input u applied to the plant. The embedded controller can be obtained using any appropriate control theory, and its transfer matrix has a dimension of $(p - \ell) \times (q - s)$. The controller is able to suppress the spillover instability for the $\ell + s$ residual modes, where ℓ is any integer such that $0 < \ell < p$, and s is an integer number determined by the number of sensors as described previously.

4.4 Discussion

In the previous sections, the method used to suppress the spillover instability in a SVC system was developed. When the developed method is applied to a SVC system, there are two questions need to be answered. As indicated previously, the spillover does not necessarily cause instability in a system. Therefore, the first question is: under what condition the spillover will lead to instability? If it is determined that the spillover instability will happen, then the second question

follows: among all the residual modes, which of them will be unstable such that should be used with the proposed method?

It should be noted that the answers to these questions do not affect the validity of the proposed method. In the development of the method, it was assumed that, the spillover instability will happen and, the residual modes that tend to be unstable under the spillover are known in prior. From the application point of view, these questions have to be answered to implement the proposed method in a SVC system design. In this section, the answers to the questions posed above are explored.

Consider the interconnected system shown in Figure - 4.4, where $\Delta(s)$ and $M(s)$ are two stable transfer matrices. The stability of this system can be determined using the small gain
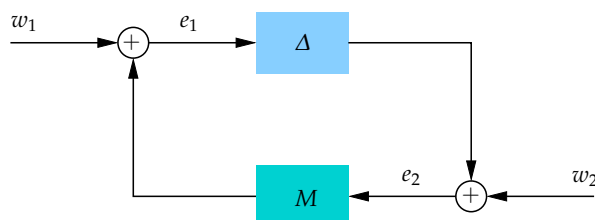
Figure - 4.4: Small gain theorem.

theorem [10] given below.

Theorem 5 (Small Gain Theorem). *Suppose M is stable and let $\gamma > 0$. Then the interconnected system shown in Figure - 4.4 is well-posed and internally stable for all stable $\Delta(s)$ with*

1. *$\|\Delta\|_\infty \leq 1/\gamma$ if and only if $\|M(s)\|_\infty < \gamma$;*

2. *$\|\Delta\|_\infty < 1/\gamma$ if and only if $\|M(s)\|_\infty \leq \gamma$.*

A feedback system said to be *well-posed* is all closed-loop transfer matrices are physically realizable or proper. Let x_1 and x_2 denote the state vectors of the systems Δ and M, respectively, then the interconnected system shown in Figure - 4.4 is said to be *internally stable* if the origin $(x_1, x_2) = (0, 0)$ is asymptotically stable [10].

For the SVC system considered in this chapter (see Figure - 4.1), its topological structure can be equivalently transformed to the one as shown in Figure - 4.5. In this figure, the shaded block $\hat{K}(s)$ represents the closed-loop system formed by the controller $K(s)$ and the ROM $G_r(s)$.

Figure -4.5: Schematic of a closed-loop SVC system.

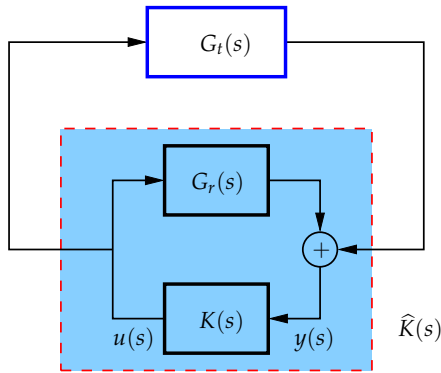Because the controller $K(s)$ was designed to stabilize the ROM $G_r(s)$, therefore, the stability of $\hat{K}(s)$ is guaranteed. Furthermore, the residual dynamics $G_t(s)$ are always stable as long as all residual modes have positive damping. In summary, the small gain theorem can be directly used to determine the stability of the interconnected system shown in Figure - 4.5.

By the small gain theorem, the spillover instability will happen to the system shown in Figure - 4.5 when

$$\|G_t(s)\|_\infty \geq \frac{1}{\|\hat{K}(s)\|_\infty}, \tag{4.4.16}$$

where $\hat{K}(s)$ is the closed-loop system formed by the controller $K(s)$ and the ROM $G_r(s)$. The condition given above can be used to answer the first question as posed in the beginning of this section. In (4.4.16), $\|\cdot\|_\infty$ denotes the $\mathcal{H}_\infty$ norm operator. Given a stable transfer matrix $G(s)$, its $\mathcal{H}_\infty$ norm is defined as [10]

$$\|G(s)\|_\infty = \sup_{\omega \in \mathbb{R}} \overline{\sigma}\{G(j\omega)\}, \tag{4.4.17}$$

where $\overline{\sigma}\{G(j\omega)\}$ denotes the largest singular value of the matrix $G(j\omega)$. To compute the $\mathcal{H}_\infty$ norm of a transfer matrix, an iterative algorithm [10] is often needed. If the Bode plot of the transfer matrix $G(s)$ is available, the $\mathcal{H}_\infty$ norm can also be obtained graphically: it is the maximum peak value on the Bode magnitude plot of $|G(j\omega)|$.

For a lightly damped structure $G(s)$, the $\mathcal{H}_\infty$ norm of $G(s)$ approximately equals to the largest $\mathcal{H}_\infty$ norm of its modal transfer matrices, i.e.

$$\|G\|_\infty \approx \max_i \|G_i\|_\infty, \quad i = 1, 2, \ldots, n, \tag{4.4.18}$$

where $\|G_i\|_\infty$ denotes the $\mathcal{H}_\infty$ norm of the modal transfer matrix associated with the i-th mode, and can be approximated as follows [67]

$$\|G_i\|_\infty \approx \frac{\|B_i\|_2\|C_i\|_2}{2\zeta_i\omega_i}, \tag{4.4.19}$$

where B_i and C_i are same as those defined in section 3.4.1. Therefore, using (4.4.18) and (4.4.19), the $\mathcal{H}_\infty$ norm of the residual dynamics $G_t(s)$ can be obtained as follows,

$$\|G_t\|_\infty \approx \max_{i>r} \frac{\|B_i\|_2\|C_i\|_2}{2\zeta_i\omega_i}. \tag{4.4.20}$$

After the $\mathcal{H}_\infty$ norms of the residual dynamics $G_t(s)$ and the controller $\widehat{K}(s)$ are obtained, whether or not the spillover instability will happen to the system shown in Figure - 4.5 can be determined using the criterion given in (4.4.16).

In the case when the spillover instability happens, to use the proposed method to suppress the spillover instability, the residual modes that tend to be unstable need to be identified. One possible approach is to use the criterion given in (4.4.16) to each mode separately. Beause $\|\widehat{K}(s)\|_\infty$ tends to increase by including the residual modes in $\widehat{K}(s)$, criterion given in (4.4.16) is reduced to a sufficient condition in this case. A more safe way is to check *manually*, i.e. to check the eigenvalues of the system $\widehat{K}(s)$ and pick up all modes corresponding to the eigenvalues that have positive real part. Considering the bandwidth of a controller is limited, only those residual modes that fall inside a frequency range close to the cutoff frequency of the controller need to be considered. The width of this frequency range can be determined in a trial-and-error manner. Whatever approach to be used, a controller with a spillover-suppression capability can be designed using the method described in the previous section, as long as these residual modes are obtained.

4.5 Numerical Example

In this section, the effectiveness of the proposed method is verified using a numerical example, where a controller is designed to stabilize a cantilever plate as shown in Figure - 4.6. The plate has dimension of $15 \times 9 \times 0.01$ inches, and is made of a material with the Young's modulus $E = 30 \times 10^6$ psi/in^4, the mass density $\rho = 0.000728$ lb/in^3, and the Poisson's ratio $\mu = 0.27$. The plate is first discretized using finite element method into 5×3 8-node plate elements with
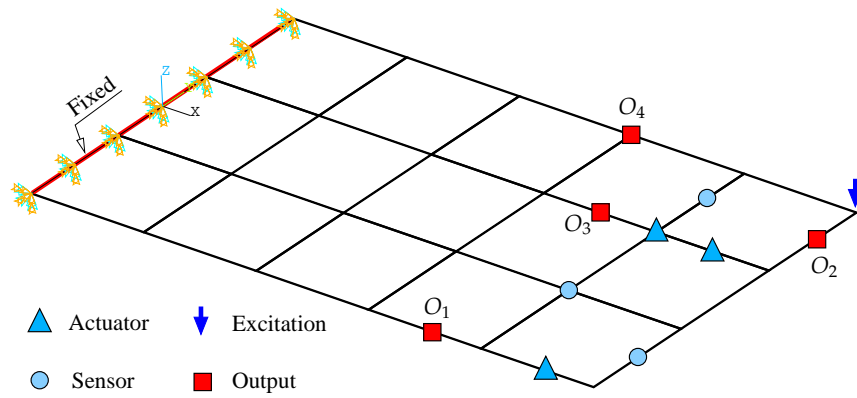
Figure - 4.6: A cantilever plate with sensors, actuators and controlled outputs.

5-DOF at each node. Three point velocity sensors and three point actuators are used in the control system, and their locations as shown in Figure - 4.6. Sensitive direction of sensor and action direction of actuators are all along with z-axis.

Modal matrix and the natural frequencies of the plate are obtained through a modal analysis. The natural frequencies of the first 9 modes are given in Table. 4.1.

Table 4.1: Natural frequencies of the cantilever plate

i-th Mode	1	2	3	4	5
ω_i (rad/s)	9.36	34.87	58.43	115.67	163.68

i-th Mode	6	7	8	9	
ω_i (rad/s)	184.79	231.72	271.12	340.74	

In this example, an optimal $\mathcal{H}_2$ controller is designed to control the vibration of the first 5 modes. For this purpose, a ROM containing the first 5 modes is first constructed. The structure

81

of the ROM is described as follows

$$
G_r(s) = \left[\begin{array}{c|cc} A & B_1 & B_2 \\ \hline C_1 & 0 & D_{12} \\ C_2 & D_{21} & 0 \end{array}\right] = \left[\begin{array}{cc|cc|c} 0 & I & 0 & 0 & 0 \\ -\Omega_r^2 & -2\zeta_r\Omega_r & B_w & 0 & \phi_r^T B_u \\ \hline C_{dw} & C_{vw} & 0 & 0 & 0 \\ 0 & 0 & 0 & 0 & I \\ \hline 0 & C_v\phi_r & 0 & I & 0 \end{array}\right].
\tag{4.5.21}
$$

From the above expression it is seen that, A, B_2 and C_2 matrices can be easily determined using the results from the modal analysis, i.e. the natural frequencies and the modal matrix. The modal damping ratio is assumed to be

$$
\zeta_i = 0.005, \qquad i = 1, 2, \ldots, 5.
\tag{4.5.22}
$$

Because only the velocity sensors are used in the feedback, C_2 matrix only has one nonzero entry of $C_v\phi_r$, which corresponds to the velocity measurement. The process noises are added to the system as modal forces through B_w, which is a 5×5 diagonal matrix given as follows,

$$
B_w = \mathrm{diag}\{\sqrt{W_1},\ \sqrt{W_2},\ \ldots,\ \sqrt{W_5}\},
\tag{4.5.23}
$$

where W_i with $i = 1, 2, \ldots, 5$ denotes the intensity of the process noise associated with the i-th mode. The controlled outputs consist of the modal velocity and the control input u. The weight for the control effort is defined by the identity submatrix included in D_{12}. C_{dw} and C_{vw} are two 5×5 diagonal matrices defining the weights for the controlled outputs of the modal displacement and velocity, respectively, and are given as follows,

$$
\begin{aligned}
C_{dw} &= \mathrm{diag}\{c_{dw1},\ c_{dw2},\ \ldots,\ c_{dw5}\}, \\
C_{vw} &= \mathrm{diag}\{c_{vw1},\ c_{vw2},\ \ldots,\ c_{vw5}\},
\end{aligned}
\tag{4.5.24}
$$

where c_{dwi} and c_{vwi} with $i = 1, 2, \ldots, 5$ are the scalar weights assigned to the i-th modal displacement and velocity, respectively. The larger c_{dwi} (or c_{wi}), the more controll effort will be addressed to control the vibration of the corresponding mode. The measurement noises enters the system through a 3×3 identity submatrix contained in D_{21}.

Based on the 5-mode ROM defined above, a standard $\mathcal{H}_2$ controller and a $\mathcal{H}_2$ controller with spillover suppression capability are designed using $B_w = I$, and

$$
\begin{aligned}
C_{dw} &= \mathrm{diag}\{1.3,\ 0.0,\ 0.0,\ 0.0,\ 0.0\}, \\
C_{vw} &= \mathrm{diag}\{0.0,\ 0.3,\ 0.3,\ 0.3,\ 0.3\}.
\end{aligned}
\tag{4.5.25}
$$

In the sequel, "Controller-A" and "Controller-B" will be used to denote these two controllers, respectively. Because there are 3 actuators and 3 velocity sensors, as described in section 4.3, Controller-B is able to block the spillover for the 4 of residual modes.

Assume for the moment that the first 4 residual modes tend to be unstable under the spillover. Therefore, the mode shapes of the first 4 residual modes are used to compute B_{fr} and C_{vr} matrices used in Controller-B. Using the method presented previously, B_{fr} and C_{vr} are found as follows,

$$B_{fr} = \begin{bmatrix} -5.282 \\ -13.105 \\ -5.037 \end{bmatrix}, \qquad C_{vr} = \begin{bmatrix} 7.883 & -0.488 & 12.752 \end{bmatrix}. \tag{4.5.26}$$

For Controller-A, B_{fr} and C_{vr} matrices are obtained as described in section 2.4.1.

To verify the effectiveness of Controller-B in suppressing the spillover instability, a 9-mode ROM is constructed. In this example, the 9-mode ROM is constructed using the first 5 modes and the first 4 residual modes. All systems that will be referred in the sequel are summarized in Table. 4.2.

Table 4.2: Definition of various systems

ROM	Open-loop system	Closed-loop system formed with	
		Controller-A	Controller-B
5-mode ROM	OPEN-5	CLOSED-5A	CLOSED-5B
9-mode ROM	OPEN-9	CLOSED-9A	CLOSED-9B

Figure - 4.7 shows the responses of the open-loop system OPEN-5 and two closed-loop systems, i.e. CLOSED-5A and CLOSED-5B, subjected to a pulse force applied to the plate at the location shown in Figure - 4.6. The pulse force has an amplitude of 1 lb within a time interval of [0, 0.002] second. In Figure - 4.7, the displacement responses $U_z(t)$ measured at 4 randomly selected locations (as defined in Figure - 4.6) on the plate are compared. It can be seen that, both controllers are able to attenuate the vibration of the first 5 modes. The performance of the closed-loop system CLOSED-5B, which is formed by using Controller-B, is not as good as

(a) Responses at O_1

(b) Responses at O_2

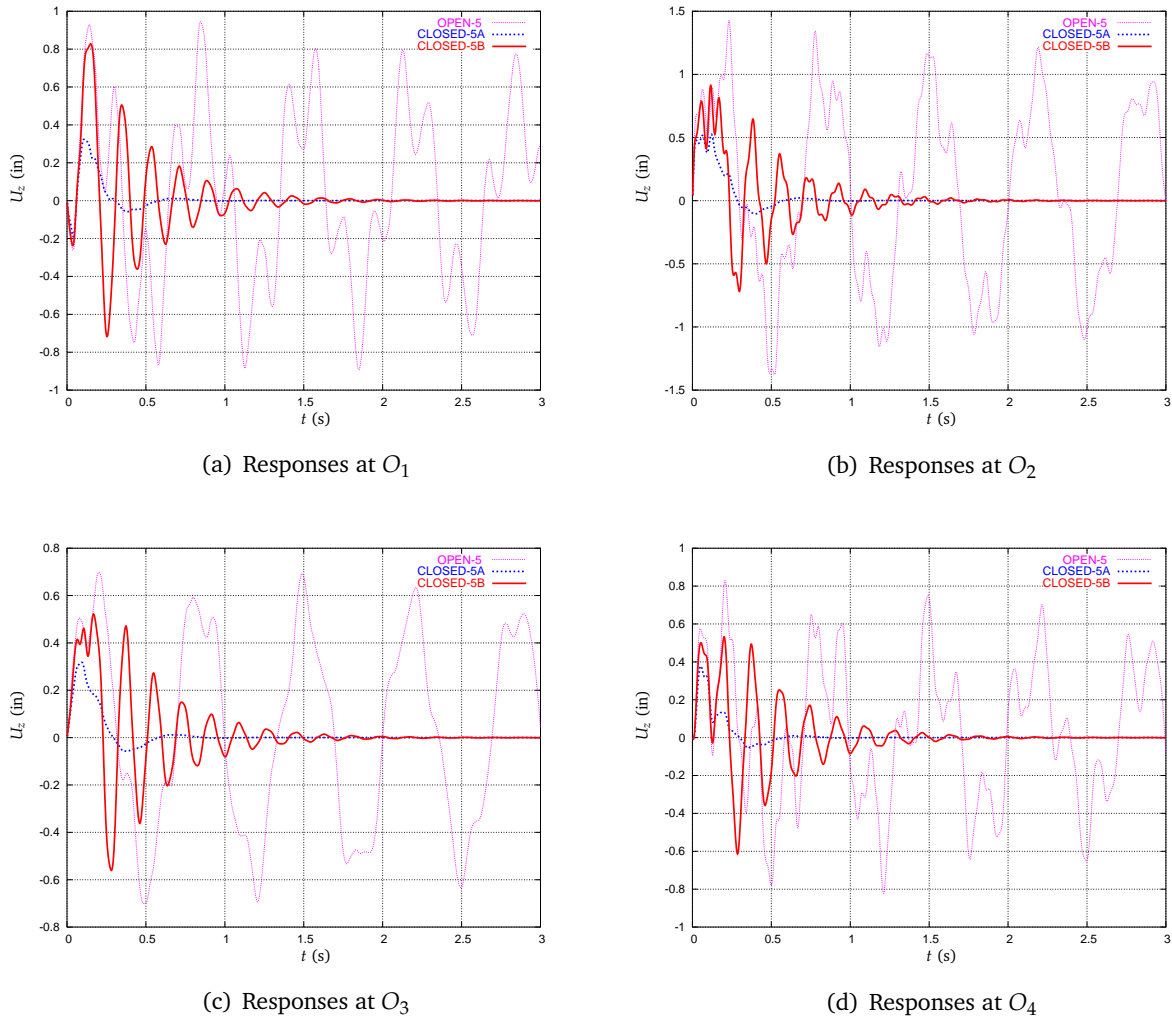(c) Responses at O_3

(d) Responses at O_4

Figure - 4.7: Comparison of responses of OPEN-5, CLOSED-5A and CLOSED-5B to a pulse force, where thin dashed lines denote OPEN-5, thick dashed lines denote CLOSED-5A, and thick solid lines denote CLOSED-5B.

CLOSED-5A, which is using a standard $\mathcal{H}_2$ controller. Both overshot and the settling time of CLOSED-5B are larger than that of CLOSED-5A.

One physical explanation for the reduced in-bandwidth performances of the system CLOSED-5B is that, because Controller-B was designed to avoid spillover instability, it has to reduce its control energy to avoid disturbing the residual modes, as a result, its ability to attenuate the in-bandwidth vibration is reduced correspondingly. Controller-A, however, was designed solely for

the 5-mode ROM, all its control efforts are addressed to attenuate the in-bandwidth vibration, therefore, it should outperform Controller-B when is used to the system it was designed for.

To determine if the spillover instability happens to the system CLOSED-9A using the criterion given in (4.4.16), the $\mathcal{H}_\infty$ norm of the residual dynamics and the system as shown in Figure - 4.8 are computed. In the system as shown in the figure, $G_r(s)$ is the 5-mode ROM, and $K(s)$
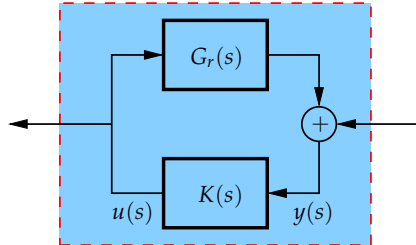

Figure - 4.8: The system used to determine the spillover instability.

represents Controller-A. The residual dynamics include the $6, 7, 8, 9$-th modes of the plate. As described previously in this chapter, the $\mathcal{H}_\infty$ norms of this system and that of residual dynamics determine whether or not the spillover instability happen to the closed-loop system CLOSED-9A. The $\mathcal{H}_\infty$ norm of the system shown in Figure - 4.8 is found to be -36.8dB. Using (4.4.20), the $\mathcal{H}_\infty$ norm of the residual dynamics is found to be 53.4dB, which is corresponding to the 6-th mode.

By (4.4.16), it is concluded that the spillover will cause instability to the closed-loop system CLOSED-9A. This conclusion can also be verified by looking at the eigenvalues of the system matrix of CLOSED-9A. In Table. 4.3, eigenvalues of the three systems, i.e. OPEN-9, CLOSED-9A and CLOSED-9B, are listed. It can be seen from the table that, the locations of the eigenvalues of the residual modes were displaced in CLOSED-9A by Controller-A. Among the 4 residual modes considered here, eigenvalue corresponding to the 6-th vibration mode was moved to the right-half-plane due to the spillover, and as a result, this mode was unstable in the closed-loop system CLOSED-9A, as predicted using the criterion (4.4.16). For CLOSED-9B, because the controller was designed to block spillover on the 4 residual modes, the eigenvalues corresponding to these residual modes were therefore not disturbed by the controller, as can be seen from the table by comparing the values inside the two shaded boxes. Because the residual modes are originally stable, the spillover instability will not happen to a closed-loop as long as they are not perturbed

Table 4.3: Comparison of eigenvalues of closed-loop systems using standard $\mathcal{H}_2$ controller and the proposed approach

Mode	OPEN-9		CLOSED-9A		CLOSED-9B	
	$\mathrm{Re}(\lambda_i)$	$\mathrm{Im}(\lambda_i)$	$\mathrm{Re}(\lambda_i)$	$\mathrm{Im}(\lambda_i)$	$\mathrm{Re}(\lambda_i)$	$\mathrm{Im}(\lambda_i)$
1	-0.047	± 9.369	-5.426	± 10.843	-12.674	± 26.452
2	-0.174	± 34.842	-13.822	± 32.264	-2.731	± 35.007
3	-0.292	± 58.438	-6.816	± 58.308	-18.232	± 51.971
4	-0.578	± 115.665	-9.800	± 115.714	-2.331	± 115.585
5	-0.819	± 163.702	-4.023	± 163.798	-12.840	± 162.334
6	-0.924	± 184.760	3.121	± 178.214	-0.924	± 184.760
7	-1.159	± 231.713	-2.290	± 231.528	-1.159	± 231.713
8	-1.356	± 271.124	-0.360	± 271.248	-1.356	± 271.124
9	-1.704	± 340.714	-5.129	± 340.331	-1.704	± 340.714

by the controller, which was guaranteed by Controller-B.

Figure - 4.9 compares the responses of the two closed-loop systems, i.e. CLOSED-9A and CLOSED-9B, to the pulse force defined previously. The responses shown in the figure are measured at the 4 randomly selected locations as defined in Figure - 4.6. Because the first residual modes is unstable in the system CLOSED-9A, the response from this closed-loop system explodes rapidly. However in the system CLOSED-9B, all residual modes are not disturbed by the cotroller with the spillover-suppression capability, the whole system is kept stable. As can be seen from the figure, the spillover instability didn't happen, and the responses of the system CLOSED-9B gradually decayed to zero.

It should be noted that, because the residual modes are not perturbed by the controller in CLOSED-9B, the vibration components caused by the 4 residual modes are not attenuated by the controller. They are decayed naturally due to the material damping. Figure - 4.10 compares the responses of the systems CLOSED-5B and CLOSED-9B. It can be seen from the figure that, there are some high frequency components exist in the responses obtained from CLOSED-9B.

(a) Responses at O_1

(b) Responses at O_2
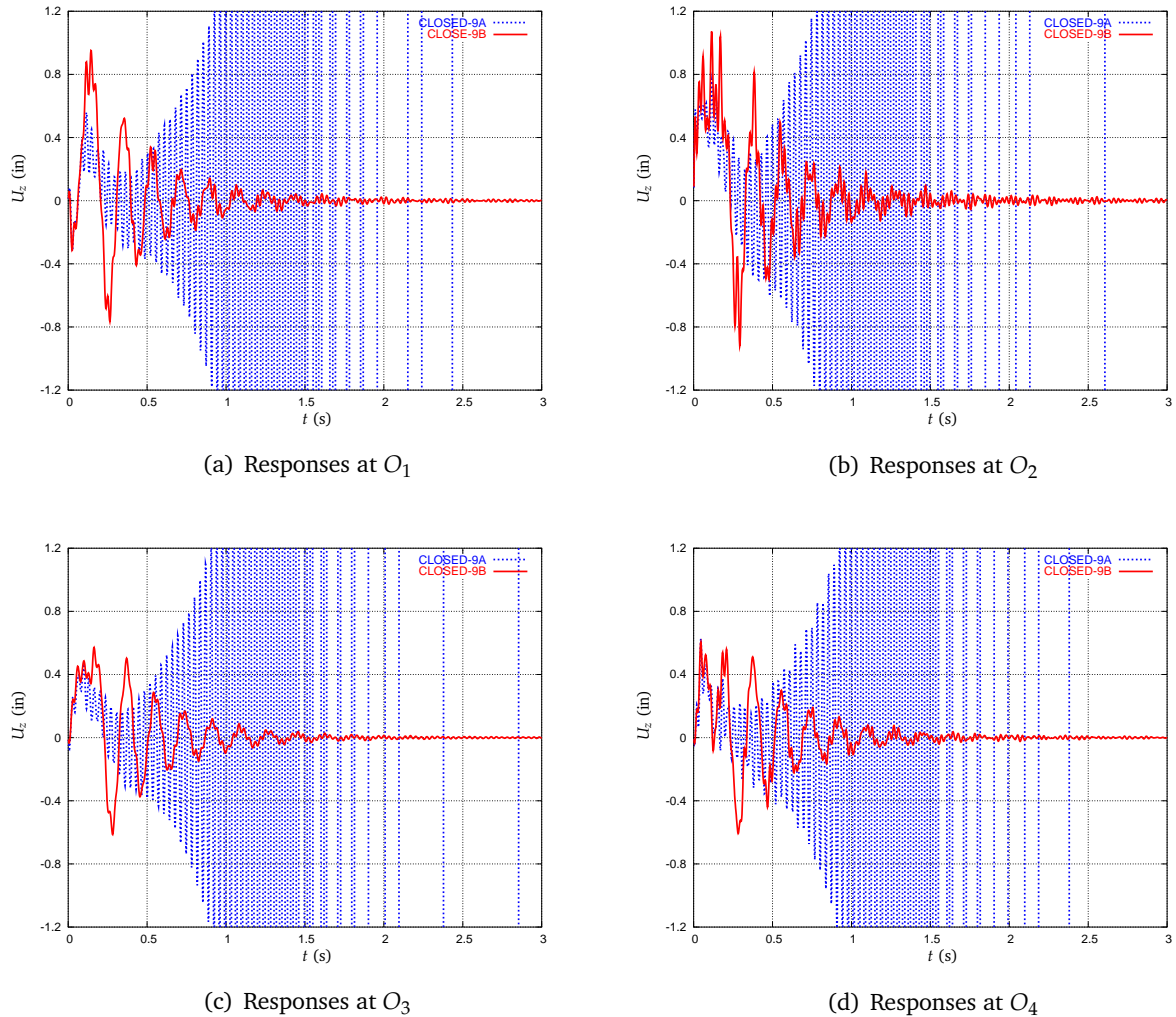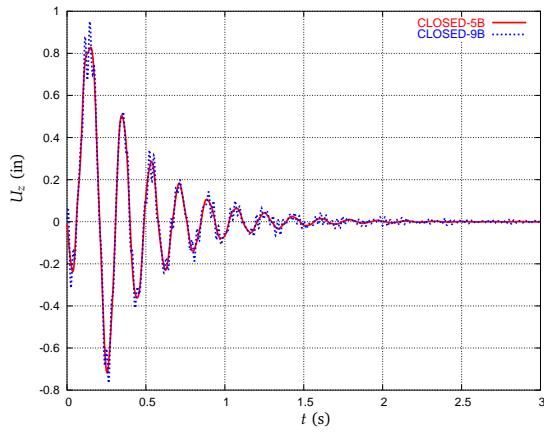

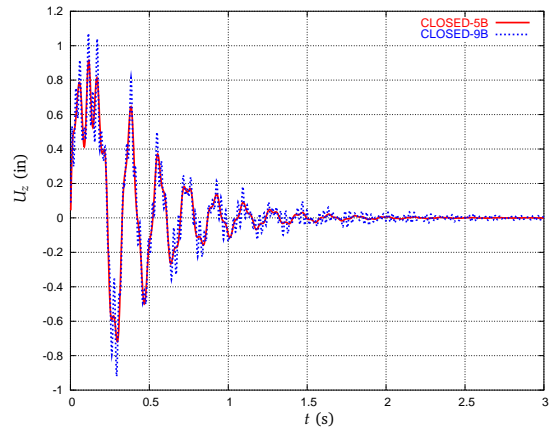
(c) Responses at O_3

(d) Responses at O_4

Figure - 4.9: Comparison of responses of CLOSED-9A and CLOSED-9B to the pulse force, where thick dashed lines denote CLOSED-9A, and thick solid lines denote CLOSED-9B.

As reflected in Table. 4.3, Controller-B is able to attenuate the in-bandwidth vibrations without disturbing the residual dynamics. Vibrations due to the uncontrolled residual modes are superposed to the attenuated in-bandwidth responses, and as a result, some high frequency components are observed in the responses obtained from the system CLOSED-9B. Because the residual modes are stable in CLOSED-9B, these high frequency vibrations decays to zero eventually as shown in Figure - 4.10 due to the structural damping.
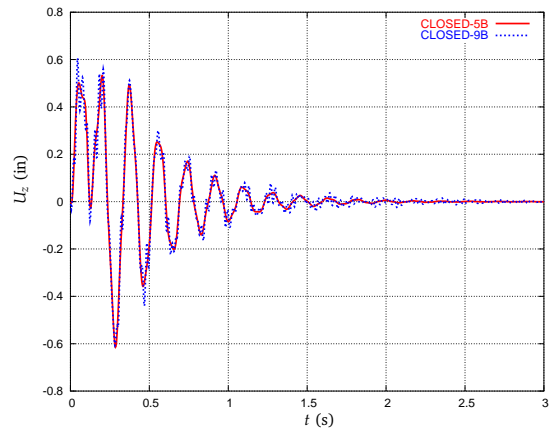
(a) Responses at O_1

(b) Responses at O_2
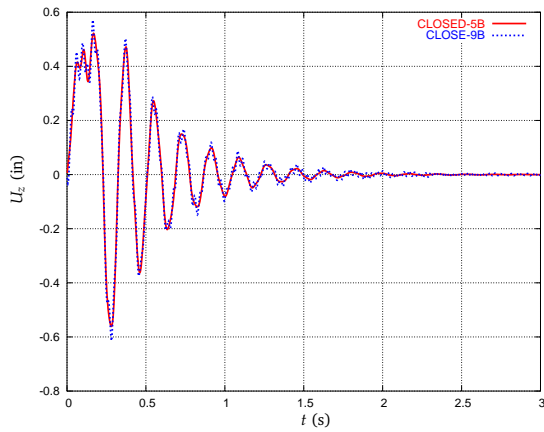
(c) Responses at O_3

(d) Responses at O_4

Figure - 4.10: Comparison of responses of CLOSED-5B and CLOSED-9B to the pulse force, where dashed lines denote CLOSED-9B, and thick solid lines denote CLOSED-5B.

4.6 Summary

In this chapter, the spillover phenomenon was studied in a SVC system, and a method to suppress the spillover instability was developed. Through an analysis on the mechanism of spillover, it was showed that the spillover instability was attributed to the control spillover and the observation spillover. Blocking any one of them, the spillover instability can be avoided. Although blocking the spillover for all residual modes of a SVC system using limited number of pointwise

actuators and sensors is impossible, this can be done for some selected residual modes. Based on this observation, the proposed method was developed to construct an input and an output matrices that are orthogonal to a space spanned by some selected residual modes that tend to be unstable under the spillover. The number of residual modes for which the spillover instability can be avoided is dependent on the number of actuators and sensors used in a control system.

Based on the small gain theorem, a criterion that can be used to determine whether or not the spillover instability happen to a SVC system was proposed. The proposed criterion can also be used to identify the residual modes that tend to be unstable under the spillover. In this case, however, the criterion can only provide a sufficient condition.

The proposed method was verified via a numerical study of vibration control of a cantilever plate. Responses obtained from the two closed-loop systems, which was form by a standard $\mathcal{H}_2$ controller and a controller with the spillover-suppression capability, were simulated and compared. Simulation results verified that the controller designed from the proposed method was able to suppress the spillover instability.

CHAPTER 5

Optimal Locations of Sensors/Actuators

5.1 Introduction

For a SVC system with given number of sensors and actuators (SAs), the system performance can be affected significantly by the locations of the SAs. In order to achieve the highest performance-expanse ratio, finding the optimal locations of SAs is desired. For a structure with simple geometry and smaller number of DOF's, experience and a trail-and-error approach may suffice to find optimal locations for SAs. While, for a large scale structure, a systematic and efficient methodology is needed to solve this optimization problem. Moreover, the performance index used in finding the optimal locations is another important factor that affects the performance that can be achieved by a closed-loop system.

In this chapter, the method to find the optimal locations for sensors and actuators (OLSA) used in a SVC system for large scale structures is studied. In this study, the OLSA problem is formulated as an optimization problem with given number of sensors and actuators. To solve such a multi-variable nonlinear optimization problem, a GA method is used, because traditional gradient-based optimization methods may suffer from the slow convergence speed in finding a global optimal solution. In solving a large scale nonlinear optimization problem, e.g. the OLSA problem at hand, a GA method is efficient because no Jacobian matrix needs to be evaluated in its solving process. Furthermore, a GA method solves an optimization problem using a random-

search-like strategy, a global optimal solution may be easier to obtain. Because a spatial $\mathcal{H}_2$ norm [44, 45] is able to provide a more comprehensive index measuring the characteristics of a structural system, it is used as the performance index in solving the OLSA problem.

The first part of this chapter introduces the spatial $\mathcal{H}_2$ norm and the controller design based based on the spatial $\mathcal{H}_2$ norm. Then the OLSA problem is formulated, and the numerical algorithm based a GA method is developed to solve the obtained OLSA problem. Finally, the developed algorithm is verified through a numerical example.

5.2   Spatial $\mathcal{H}_2$ Norm

The concept of the spatial $\mathcal{H}_2$ norm was proposed by Moheimani and Fu [44, 45] to describe the input-output characteristics of a distributed system, e.g. structural system. Based on this concept, the spatial $\mathcal{H}_2$ controller was developed by the same authors. In this section, the spatial $\mathcal{H}_2$ norm and the spatial $\mathcal{H}_2$ controller design will be introduced.

Consider a n-DOF structural system as defined in (2.4.34), the state space equations of the system is given by

$$\dot{x} = Ax + Bu,$$
$$y = Cx. \tag{5.2.1}$$

Assume there are p inputs and q outputs associated with the above system, i.e. the transfer function of the system is a $q \times p$ complex matrix, which can be written as follows,

$$G(s) = \sum_{i=1}^{m} G_i(s) = \sum_{i=1}^{n} \frac{(C_{di} + C_{vi}s)B_i}{s^2 + 2\zeta_i\omega_i s + \omega_i^2}, \tag{5.2.2}$$

where $G_i(s)$ is the modal transfer matrix of the i-th mode, B_i is the i-th row of the matrix $\boldsymbol{\phi}^T B_u$, which was defined in section 2.4.1, C_{di} and C_{vi} are i-th column of the matrices $C_d\boldsymbol{\phi}$ and $C_v\boldsymbol{\phi}$ (see section 2.4.1 for definition), respectively. When the output from the system is pointwise, the transfer matrix of the system is a complex function dependent only on the frequency.

The spatial $\mathcal{H}_2$ norm concept was introduced by Moheimani and Fu [44] to a system with a distributed output. In this case, the system is given by

$$\dot{x} = Ax + Bu,$$
$$y(t, \xi) = C(\xi)x(t), \tag{5.2.3}$$

where the distributed output $y(t, \xi) : \mathbb{R}^t \times \mathcal{R} \to \mathbb{R}^\ell$ is measured on ℓ spatial domains $\mathcal{R}_i$ with $i = 1, \ldots, \ell$, $\xi \in \{\mathcal{R}_i\}$ is the spatial coordinate (for 2D structure, $\xi \in \mathbb{R}^2$), $C(\xi) \in (C^1)^{\ell \times n}$ is the output matrix of the state variable $x(t) \in \mathbb{R}^n$ on each of the ℓ spatial domains. Similarly, the transfer matrix of the system can be decomposed by modes as follows

$$G(s, \xi) = \sum_{i=1}^{m} \frac{C_i(\xi)}{s^2 + 2\zeta_i \omega_i s + \omega_i^2} B_i, \tag{5.2.4}$$

in which, $C_i(\xi) \in (C^1)^{q \times 1}$ is the projection of $C(\xi)$ into the i-th mode of the system. The spatial $\mathcal{H}_2$ norm of the transfer matrix $G(s, \xi)$ is then defined by

$$\langle\!\langle G \rangle\!\rangle_2^2 = \frac{1}{2\pi} \int_{-\infty}^{\infty} \int_{\mathcal{R}} \text{Trace}\{G(j\omega, \xi)G^*(j\omega, \xi)\} d\xi d\omega, \tag{5.2.5}$$

where the superscript $(^*)$ denotes the complex conjugate operator. As seen in the above definition, the spatial $\mathcal{H}_2$ norm is different from the standard $\mathcal{H}_2$ norm (see (2.4.56)) in the sense that it introduces an additional average operation over the spatial domain $\mathcal{R}$. It represents the characteristics between a set of discrete inputs and a set of distributed outputs of a system. This property makes it suitable to be a performance index in structural vibration control, where the performance is usually required over a continuous area on the structure being controlled, instead of on some isolated points.

It has been proved [44, 45] that the spatial $\mathcal{H}_2$ norm of the system G in (5.2.4) is equal to the standard $\mathcal{H}_2$ norm of another system $\hat{G}$, i.e.

$$\langle\!\langle G(s, \xi) \rangle\!\rangle_2^2 = \|\hat{G}(s)\|_2^2 , \tag{5.2.6}$$

where $\hat{G}(s)$ is the transfer matrix of the following pointwise system

$$\hat{G}(s) = \Gamma(sI - A)^{-1}B , \tag{5.2.7}$$

and Γ is a matrix satisfying

$$\Gamma^T \Gamma = \int_{\mathcal{R}} C(\xi)^T C(\xi) d\xi . \tag{5.2.8}$$

The $\mathcal{H}_2$ norm of the transfer matrix $\hat{G}(s)$ can be obtained using the method described in section 3.2.1.

Based on the relationship as described in (5.2.6), the optimal spatial $\mathcal{H}_2$ controller for the system $G(s, \xi)$ is therefore a standard optimal $\mathcal{H}_2$ controller for the system $\hat{G}(s)$. Consider the
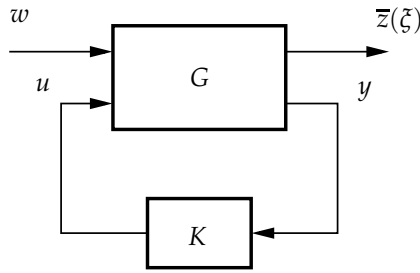
Figure -5.1: Block diagram for the optimal spatial $\mathcal{H}_2$ controller design

optimal spatial $\mathcal{H}_2$ controller design problem for the system shown in Figure - 5.1. The plant G has the following state space representation,

$$\dot{x} = Ax + B_1 w + B_2 u,$$
$$\overline{z}(\xi) = C_1'(\xi)x + D_{12}u, \tag{5.2.9}$$
$$y = C_2 x + D_{21}w,$$

where w is the disturbance vector, $\overline{z}(\xi)$ is the distributed controlled output defined on a spatial domain Ξ, y is the measurement output from sensors. $C_1'(\xi)$ is the matrix consisting of modal shape functions. If the controlled outputs $\overline{z}(\xi)$ are displacements, then

$$C_1'(\xi) = \begin{bmatrix} \phi_1(\xi) & 0 & \phi_2(\xi) & 0 & \dots & \phi_m(\xi) & 0 \end{bmatrix}. \tag{5.2.10}$$

Denote the optimal spatial $\mathcal{H}_2$ norm of the transfer matrix $T_{\overline{z}w}$ from the disturbance w to the distributed controlled output $\overline{z}(\xi)$ by $\langle\!\langle T_{\overline{z}w}(\xi) \rangle\!\rangle_2$, then the controller K minimizing the $\langle\!\langle T_{\overline{z}w}(\xi) \rangle\!\rangle_2$ is thus the standard optimal $\mathcal{H}_2$ controller for the following system,

$$\dot{x} = Ax + B_1 w + B_2 u,$$
$$z = C_1 x + D_{12}u, \tag{5.2.11}$$
$$y = C_2 x + D_{21}w,$$

where C_1 is a matrix satisfying

$$C_1^T C_1 = \int_{\Xi} C_1'(\xi)^T C_1'(\xi) d\xi. \tag{5.2.12}$$

In a special case when Ξ is the spatial domain of the entire structure, by using the orthogonal

93

property of the modal shape functions, the following simplified relation can be obtained,

$$C_1^T C_1 = \int_\Xi C_1'(\xi)^T C_1'(\xi) d\xi = \mathrm{diag}(E_i),$$

$$E_i = \begin{bmatrix} \int_\Xi \phi_i(\xi)^T \phi_i(\xi) d\xi & 0 \\ 0 & 0 \end{bmatrix}.$$

(5.2.13)

In this case, C_1 can be chosen as follows,

$$C_1 = \mathrm{diag}\left(\begin{bmatrix} \sqrt{\int_\Xi \phi_i(\xi)^T \phi_i(\xi) d\xi} & 0 \\ 0 & 0 \end{bmatrix} \right).$$

(5.2.14)

Following the standard $\mathcal{H}_2$ controller design procedure as described in section 2.4.3, an optimal $\mathcal{H}_2$ controller can be obtained for the system (5.2.11). The obtained controller minimizes the $\|T_{zw}\|_2$ for the system (5.2.11), or equivalently, minimizes the spatial $\mathcal{H}_2$ norm of the closed-loop transfer function $T_{\bar{z}w}$ of the original system (5.2.9), i.e. $\lang\!\langle T_{\bar{z}w} \rangle\!\rangle_2$ is minimized. The minimum achieved by the controller was shown [69] to be

$$\min\left\{ \langle\!\langle T_{\bar{z}w} \rangle\!\rangle_2^2 \right\} = \min\left\{ \|T_{zw}\|_2^2 \right\}.$$

(5.2.15)

From the minimal $\mathcal{H}_2$ norm (see (2.4.68)) that can be achieved, it is seen that $\min\left\{ \langle\!\langle T_{\bar{z}w} \rangle\!\rangle_2^2 \right\}$ is indirectly dependent on both the actuator locations (i.e. B_2 matrix) and the sensor locations (i.e. C_2 matrix). By appropriately changing the SA locations, or equivalently adjusting the parameters of the B_2 and C_2 matrices, a smaller $\min\left\{ \langle\!\langle T_{\bar{z}w} \rangle\!\rangle_2^2 \right\}$ can be found. The smaller $\langle\!\langle T_{\bar{z}w} \rangle\!\rangle_2$, the stronger ability the closed-loop system has in rejecting the disturbance, which in turn implies better performance.

5.3 Dominant Modes and Reduced Order Model

In section 3.4.1, the dominant modes of a structural system were found using an index that measures the contribution of a mode to the whole system in terms of a standard $\mathcal{H}_2$ norm. Based on the relationship that exists between the $\mathcal{H}_2$ norm and the spatial $\mathcal{H}_2$ norm as described in (5.2.6), the index used in measuring the importance of a mode in a structural system can be re-defined in terms of the spatial $\mathcal{H}_2$ norm.

Because the spatial $\mathcal{H}_2$ controller as introduced above minimizes the spatial $\mathcal{H}_2$ norm of the closed-loop transfer matrix relating the disturbance to the controlled output, it make sense to use the spatial $\mathcal{H}_2$ norm of the same transfer matrix in finding the dominant modes for the system. For simplicity, the transfer matrix used in here is evaluated in the open-loop system.

For a system as given in (5.2.9), by ignoring the path from the control input u to the measurement output y, the subsystem relating the disturbance w to the controlled output z can be written in a form as given in (5.2.3). The dominant modes mentioned here are then defined using the spatial $\mathcal{H}_2$ norm of the open-loop transfer function of this system.

For a lightly damped system, the spatial $\mathcal{H}_2$ norm can be decomposed by modes as introduced in section 3.4.1 (or in [44, 45] as well), i.e.

$$\langle\!\langle\, G\,\rangle\!\rangle_2^2 = \sum_{i=1}^{m} \|\widehat{G}_i\|_2^2, \tag{5.3.16}$$

where $\widehat{G}_i$ is the equivalent modal transfer matrix associated with the i-th mode given by

$$\widehat{G}_i(s) = \frac{C'_{di} + C'_{vi}s}{s^2 + 2\zeta_i\omega_i s + \omega_i^2}B_i \,, \tag{5.3.17}$$

where B_i is the i-th row of the matrix $\boldsymbol{\Phi}^T B_u$ (see section 2.4.1 for definition), C'_{di} and C'_{vo} are the matrices satisfying

$$
\begin{aligned}
C'_{di}{C'_{di}}^T &= \int_{\mathcal{R}} C_{di}(\xi)C_{di}^T(\xi)d\xi \,, \\
C'_{vi}{C'_{vi}}^T &= \int_{\mathcal{R}} C_{vi}(\xi)C_{vi}^T(\xi)d\xi \,,
\end{aligned}
\tag{5.3.18}
$$

in which $C_{di}, C_{vi} \in \mathbb{R}^{r\times 1}$ are the i-th columns of the matrices $C_d\boldsymbol{\Phi}$, $C_v\boldsymbol{\Phi}$ (see section 2.4.1 for definition), respectively. From (5.3.18), it follows that

$$
\begin{aligned}
C'_{di} &= C_{di}R, \quad C'_{vi} = C_{vi}R \,, \\
R &= \sqrt{\int_{\mathcal{R}} \boldsymbol{\phi}_i(\xi)\boldsymbol{\phi}_i^T(\xi)d\xi} \,,
\end{aligned}
\tag{5.3.19}
$$

where $\boldsymbol{\phi}_i(\xi)$ is the eigenfunction (mode shape vector) corresponding to the i-th mode.

In terms of the spatial $\mathcal{H}_2$ norm, the contribution of the i-th mode, or alternatively, the importance level of the mode, can be described by the following nondimensional quantity r_i,

$$r_i = \frac{\|\widehat{G}_i\|_2}{\langle\!\langle\, G\,\rangle\!\rangle_2}. \tag{5.3.20}$$

The larger the r_i, the more important the i-th mode in terms of the system's spatial $\mathcal{H}_2$ norm. A mode is considered neglectable if the corresponding r_i is less than a predefined threshold value.

Using the above defined index, dominants modes of a system with distributed output can be found. The obtained dominant modes can then be used to construct a ROM respresenting the original system using the traditional modal truncation method, or the model reduction method developed in Chapter 3. For simplicity, the ROM used in this chapter is constructed using the traditional modal truncation methods.

5.4   GA Method for the OLSA Problem

Using the spatial $\mathcal{H}_2$ norm as the performance index, the OLSA problem can be formulated as an optimization problem as follows: For a structural system as given in (5.2.9) with a distributed controlled output, find the locations for sensors and actuators such that the spatial $\mathcal{H}_2$ norm of the closed-loop transfer matrix $T_{\bar{z}w}$ is minimized. Because the locations of sensors and actuators are represented by the measurement output matrix C_2 and the input matrix B_2, respectively, the above optimization problem can be mathematically represented by

$$(B_2, C_2) = \underset{B_2, C_2}{\operatorname{argmin}} \{ \langle\!\langle\, T_{\bar{z}w} \,\rangle\!\rangle_2 \}. \qquad (5.4.21)$$

In the above defined optimization probelm, the number of sensors and actuators are given, i.e. B_2 and C_2 matrices have given dimensions.

To solve the OLSA problem using a GA method (Appendix C), the locations of the sensors and actuators are indexed by a set of integer numbers. Each of them corresponds to a unique location on the structure, and is encoded in a binary string, which is known as *chromosome* in the GA method. Assume there are p actuators and q sensors, then $p + q$ of chromosomes constitute a *population member*, several of population members make a *population* in a GA method. Figure - 5.2 shows a typical chromosome used in the OLSA problem, where each of q binary-strings represents a location index of a sensor, and each of p strings represents a location of an actuator.

The length of binary encoded string depends on the size of the searching space. For the problem at hand, the size of the searching space is the number of nodes on the FEM mesh excluding the constrained nodes and the vibration nodes of the selected modes. The fitness value of a population member is determined by its chromosome. For convenience of implementation,
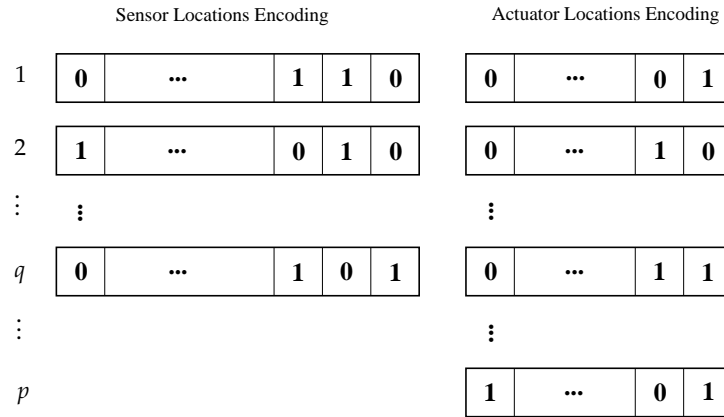
Figure - 5.2: A typical chromosome used in an OLSA problem with q sensors and p actuators

in each GA iteration step, the size of the population is kept same. An outline of using the GA process in the OLSA problem is given as follows:

Algorithm for the GA process in OLSA Problem:

1. Given q sensors and p actuators, randomly generate the initial population of N members.

2. Design an optimal spatial $\mathcal{H}_2$ controller, and evaluate $\langle\!\langle T_{\bar{z}w} \rangle\!\rangle_2$ for each member of the population.

3. Generate N new population members by repeating following steps:

   (a) Randomly select two members from the current population to be the parents. The probability that a member is selected is determined by its fitness value.

   (b) Generate a child by applying the crossover with certain probability (known as *crossover rate*) on the selected parents.

   (c) Mutate one or two bits of the child's chromosome with certain probability (known as *mutation rate*).

   (d) Fill the new population with the newly generated child.

4. Evaluate the fitness value for each member of the new population, and find the optimal one.

5. If the predefined end-condition is satisfied, the GA iteration is stopped, and return the best solution in current population.

6. Otherwise, go back to the step 2.

The GA iteration is terminated either when a certain number of iterations have been reached, or when the required accuracy is achieved. For the problem at hand, the ending condition of the GA is chosen to be the number of iterations.

It is worth noting that the results obtained from a GA process with the limited number of iterations might be a suboptimal solution. To ensure a solution be a global optimal one, sufficient number of iterations have to be done before the GA process can be terminated. Due to the random nature of a GA method, the number of iterations that need to obtain a global optimal solution is difficult to determine. In this research, the GA program will be run several times such that a solution *good enough* can be found.

5.5 Numerical Example

In this section, the numerical scheme proposed above is used to solve an OLSA problem for a fixed-fixed supported plate as shown in Figure - 5.3. The plate has dimension of 36 in × 18 in ×
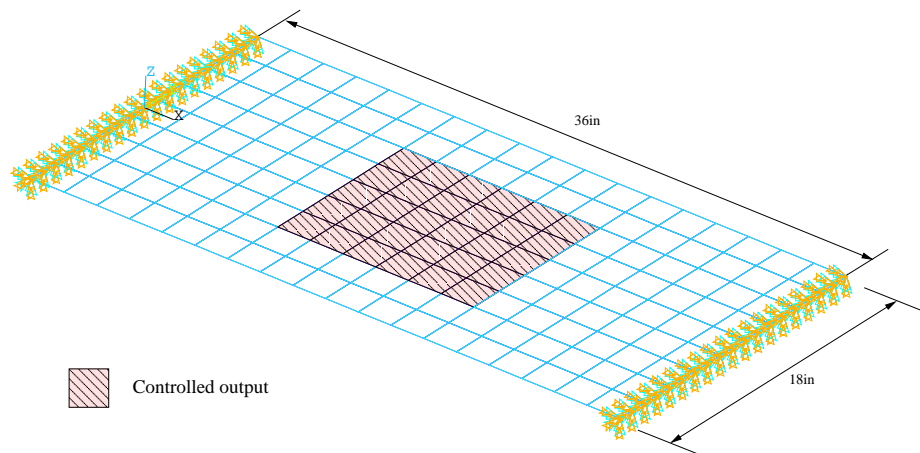
Figure -5.3: A fixed-fixed plate. Solid dots denote the locations where the disturbances are applied, shaded area denotes the region on the plate where the distributed displacement output is attenuated.

0.05 in, and is discretized using the 8-node plate elements. The plate is made of a material with the Young's modulus $E = 30 \times 10^6$ psi, the Poisson's ratio $\mu = 0.27$ and the mass density $\rho = 0.0009218$ lb/in^3. A modal damping ratio of 0.005 is assumed. The Cartesian coordinate used in sequel is shown as Figure - 5.3.

The objective is to find the locations for the 4 sensors and 4 actuators such that, for the given disturbances, the distributed displacement response measured on the shaded region as shown in Figure - 5.3 is attenuated as much as possible.

The disturbance considered here is a 2D Gaussian disturbance given by

$$D(x,y,t) = \frac{W_D(t)C_g}{2\pi\sigma_x\sigma_y} \exp\left[-\frac{1}{2}\left(\frac{x - \mu_x}{\sigma_x}\right)^2 - \frac{1}{2}\left(\frac{y - \mu_y}{\sigma_y}\right)^2\right], \qquad (5.5.22)$$

where μ_x and μ_y define the center location of the Gaussian disturbance on the plate, σ_x and σ_y define the shape of the disturbance. $W_D(t)$ is a time-dependent magnitude of the force, and C_g is a normalization coefficient. In the following simulation, $W_D(t)$ is chosen as

$$W_D(t) = \begin{cases} W_c = \text{const} & \text{for } 0 \leq t \leq 0.01 \\ 0 & \text{otherwise.} \end{cases} \qquad (5.5.23)$$

To excite as many vibration modes as possible, the center of the 2D Gaussian disturbance is chosen at a location away from the center of the plate. Figure - 5.4 shows the load $D(x,y,t)$ for $0 \leq t \leq 0.01$ with $\mu_x = 12$ in, $\mu_y = -5$ in, $\sigma_x = 6$ in and $\sigma_y = 4$ in, $W_c = 10$ lb, and $C_g = 105.8$ (is chosen such that the peak value of $D(x,y,t)$ is 10 lb/in^2).

The natural frequencies and the modal shapes of the plate are obtained through a modal analysis. Figure - 5.5 shows the modal shapes and natural frequencies of the first 6 modes.

A ROM is then constructed using the dominant modes of the structural system defined above. For this purpose, the dominance indices r_i as defined in (5.3.20) are calculated for the first 40 modes. As explained previously, the subsystem relating the disturbance to the controlled output is used to evaluate these indices. Figure - 5.6 shows r_i's for the first 40 modes of the plate.

It is observed that, for the given disturbance, the contribution from the i-th mode is getting smaller with increase of i. Starting from the 23rd mode, the index σ_i is less then 10^{-6}, which is considered sufficiently small and can be neglected. Therefore, the ROM containing the first 22 modes is used in the following analysis to represent the original structural system.
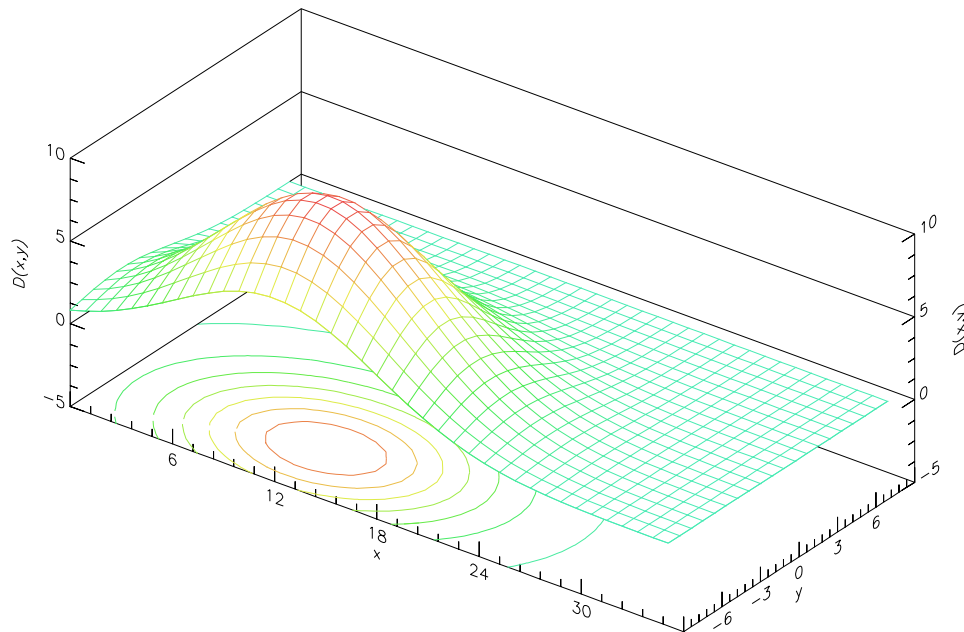
Figure - 5.4: The 2D Gaussian disturbance applied on the plate, centered at ($x = 12$, $y = -5$) with peak value $D(12, -5, t) = 10$ lb/in^2 for $0 \leq t \leq 0.01$.
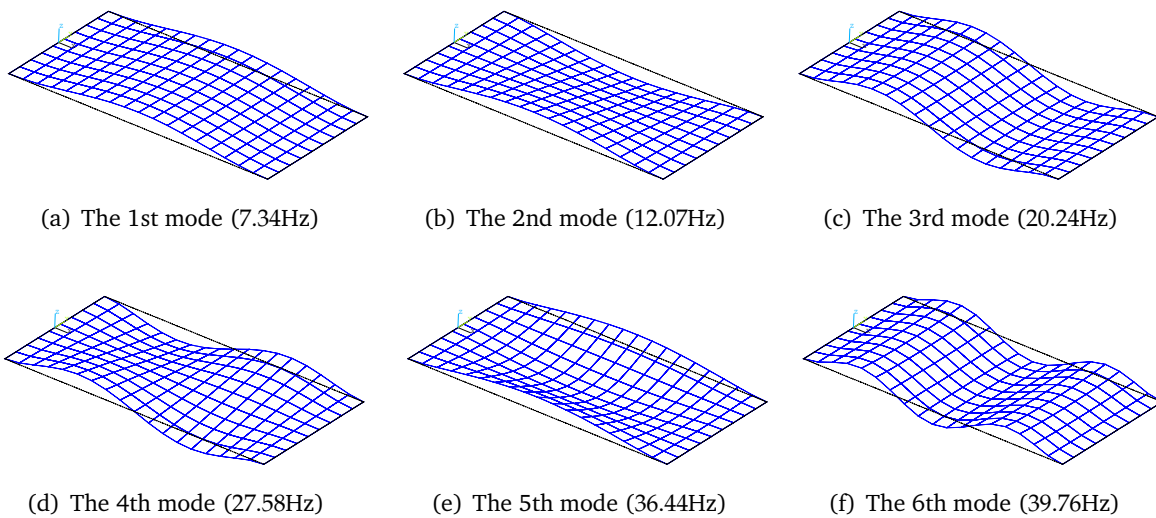

(a) The 1st mode (7.34Hz) (b) The 2nd mode (12.07Hz) (c) The 3rd mode (20.24Hz)

(d) The 4th mode (27.58Hz) (e) The 5th mode (36.44Hz) (f) The 6th mode (39.76Hz)

Figure -5.5: The first six mode shapes of the plate

To solve the OLSA problem using the GA method, the searching space, which defines the admissible locations for the sensors and actuators, has to be defined. There are 541 nodes in the FEM mesh of the plate. Excluding the 38 constrained nodes and the nodes where the mode shape

100
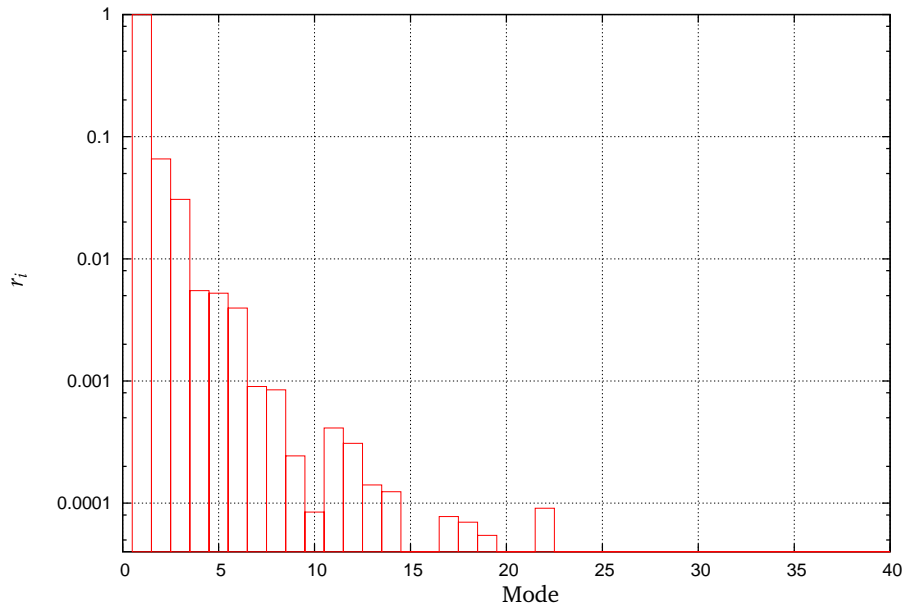
Figure - 5.6: The mode importance index of the plate

values are zero for the first 22 modes, there are 460 candidate nodes that can be used to place sensors and actuators. These 460 nodes define the searching space for the GA process, which is visualized in Figure - 5.7. In this plot, the area corresponding $T(x, y) = 1.0$ are admissible for placing a sensor or an actuator. The nodes (of the FEM mesh of the plate) fall inside this area are then numbered from 1 to 460, and encoded in a binary string, whose length is 9 bits ($2^8 < 460 < 2^9$).

The GA method is then simulated with a population size of 50, a crossover rate of 95%, and a mutation rate of 10%. The GA process is terminated upon the finish of 1000 iterations. Figure - 5.8 shows the variation of the performance index, i.e. $\langle\langle T_{\bar{z}w} \rangle\rangle_2$ of the closed-loop system, vs the GA's iteration steps in the five runs of the simulation (each takes 4h20min on an 930MHz PC). The minimum performance index achieved by these runs is found to be 4.47×10^6. For a randomly selected SA set, this performance index is generally between 7.5×10^8 and 8.0×10^6. A simple algebra shows that the solution found by the GA process improves the closed-loop system performance by 40% to 50% in terms of the spatial $\mathcal{H}_2$ norm. The optimal locations for the SA are shown in Figure - 5.9(a).

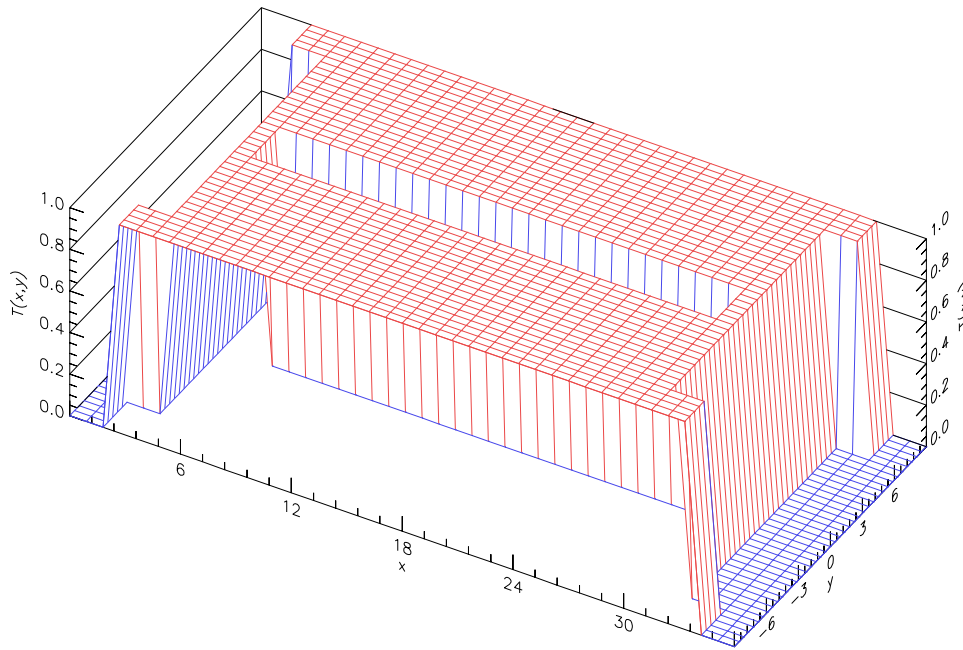To demonstrate the performance improvement, two closed-loop systems are formed. One of

101

Figure - 5.7: The searching space for the OLSA problem. All nodes corresponding to $T(x,y) = 1$ define the searching space for the optimization.
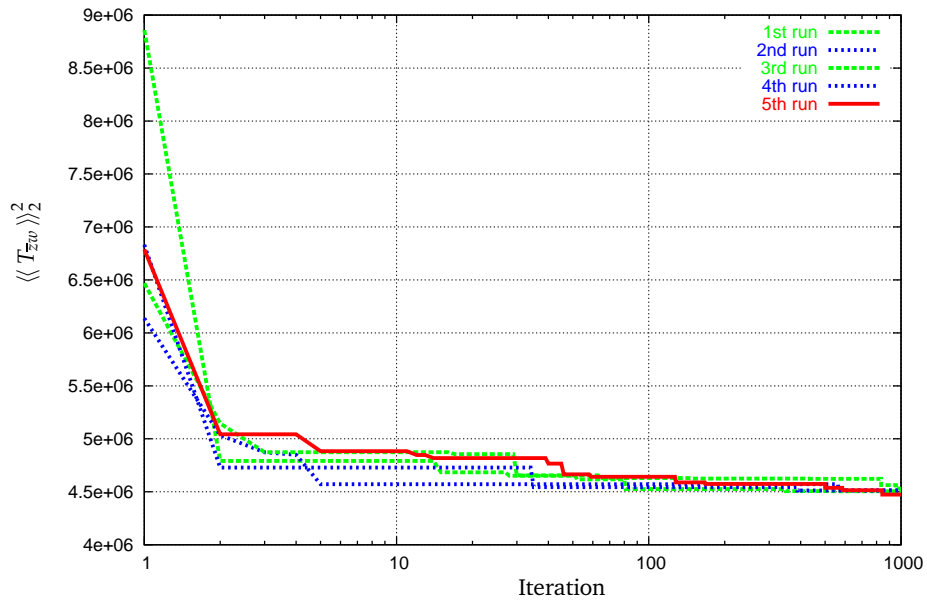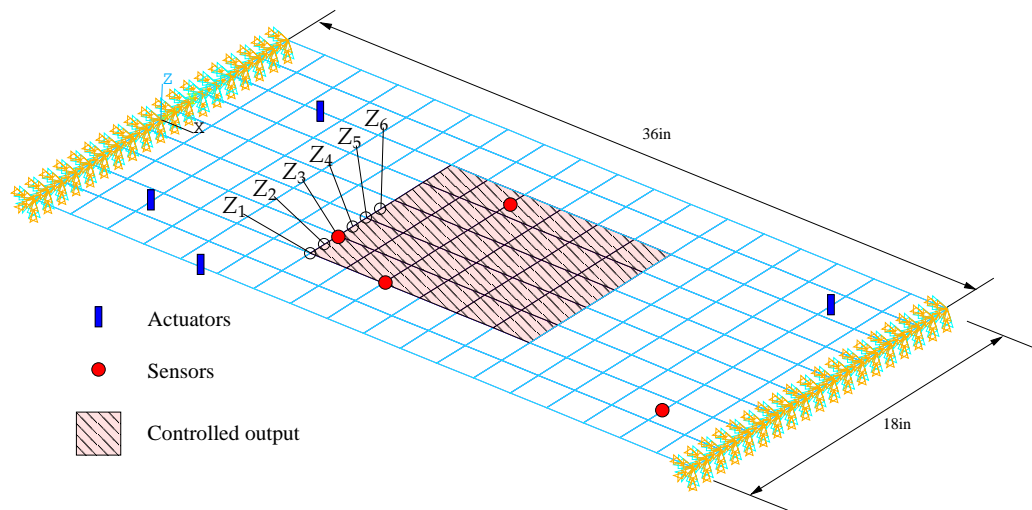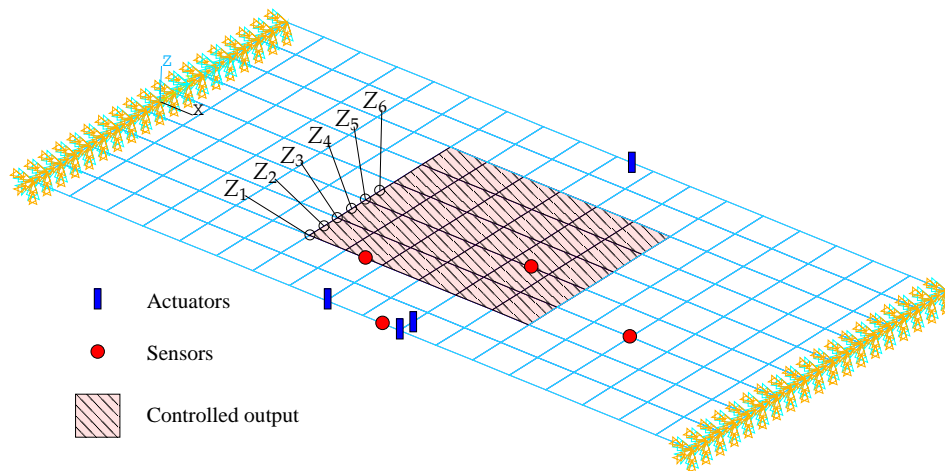

Figure - 5.8: The performance index v.s. the GA iteration steps.

(a) SA with the randomly selected locations (SYS-RND)

(b) SA with the optimal locations (SYS-OPT)

Figure -5.9: Sensor and actuator locations of (a) the SYS-RND, and (b) the SYS-OPT

them, which is denoted by SYS-OPT, is formed by the structural model and a controller using the SAs with the optimal locations. Another one, which is denoted by SYS-RND, is formed by a controller using the same number of SAs with randomly selected locations as shown in the Figure - 5.9(b). The open-loop system is denoted by the SYS-OPN.

(a) Location Z_1

(b) Location Z_2

(c) Location Z_3

(d) Location Z_4

(e) Location Z_5
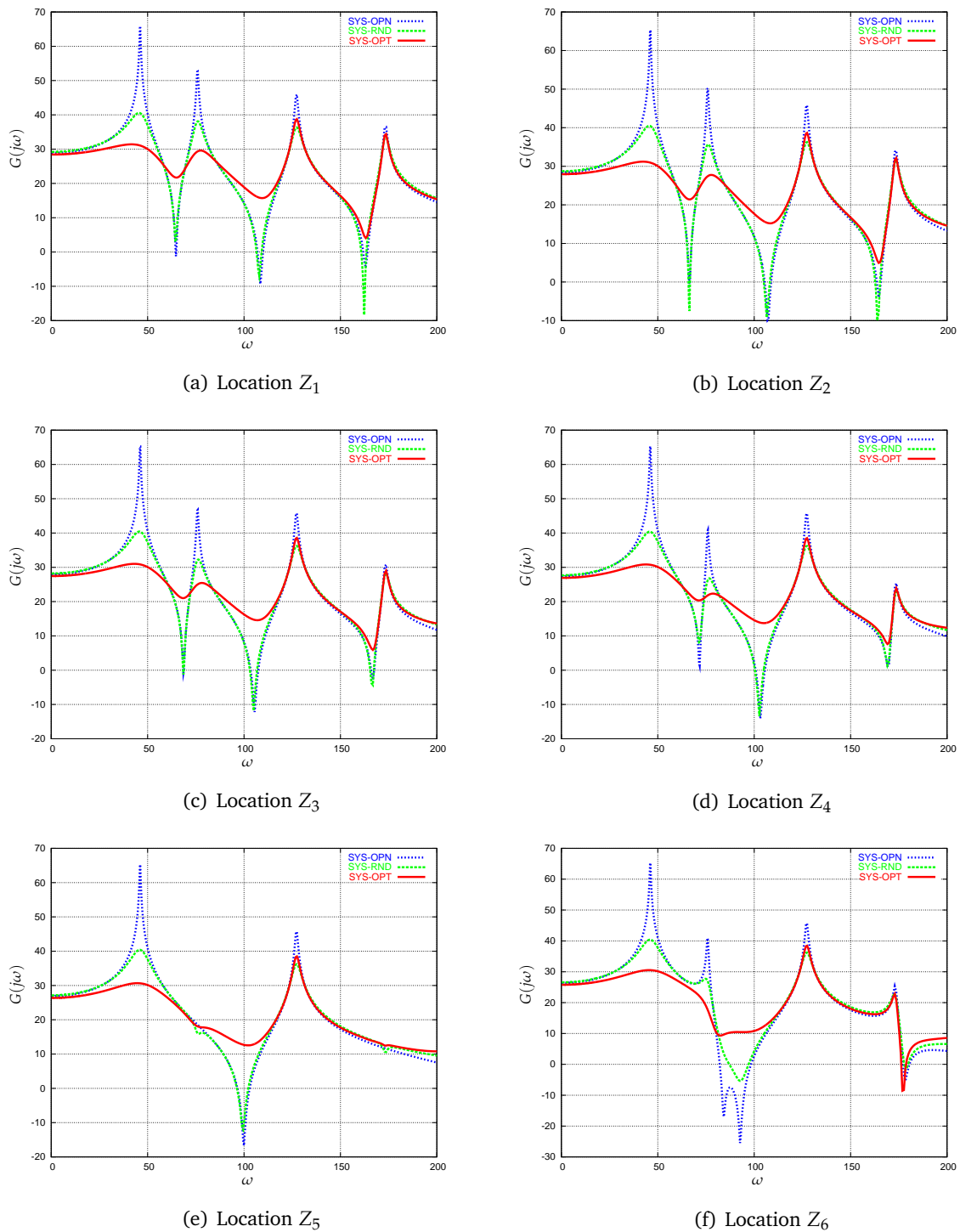
(f) Location Z_6

Figure - 5.10: Comparison of the frequency response functions of the three systems from the disturbance to the outputs measured at the locations Z_1 to Z_6 (see Figure - 5.9).

Firstly, the frequency domain characteristics of the systems defined above are compared in Figure - 5.10, where the singular values of the transfer matrices from the disturbance to the displacement outputs measured at the locations $Z1$ to $Z6$ (see Figure - 5.9) are plotted. For these randomly selected input-output pairs, the SYS-OPT shows the smallest value compared with the other two systems at the first two resonant peaks. Because these two modes are among the most dominant ones, suppressing the vibration for these modes has a significant effect on improving the overall performance. This means that the controller using the SAs with the optimal locations (as shown in Figure - 5.9(a)) is able to achieve the best result among the three systems in attenuating the vibration caused by the disturbance defined previously.

As a more comprehensive index, an *averaged* singular value, which is obtained by averaging all that over the shaded area (as defined in Figure - 5.3) at the first 4 resonant frequencies, is used to compare the performances of the systems. The results are listed in the Table. 5.1. From the table it is seen that, at the first resonant frequency, SYS-OPT can achieve about 35dB

Table 5.1: Comparison of singular values between the three systems

| i-th mode	ω_i (rad/s)	SYS-OPN (dB)	SYS-OPT (dB)	SYS-RND (dB)
1	46.1	66.5	31.6	41.7
2	75.9	46.0	25.5	32.6
3	127.2	38.5	32.4	29.6
4	173.3	22.4	21.3	20.5

reduction on the response, as compared 25dB reduction from the SYS-RND. At the third and the fourth resonant frequencies, although the reduction achieved by SYS-RND is little bit better than achieved SYS-OPT, SYS-OPT outperformances SYS-RND over the whole frequency range.

Performances of these systems are compared in the time domain as well. First, the displacement responses are compared in Figure - 5.11. The displacement curves plotted in Figure - 5.11 are measured at the same locations as those used in Figure - 5.10. It is seen that the response from the system SYS-OPT decays in a faster speed than the other two systems.
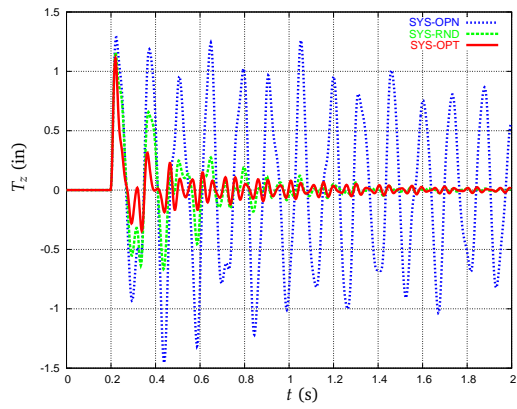
Secondly, the vibration energy are compared among the systems. The total vibration energy
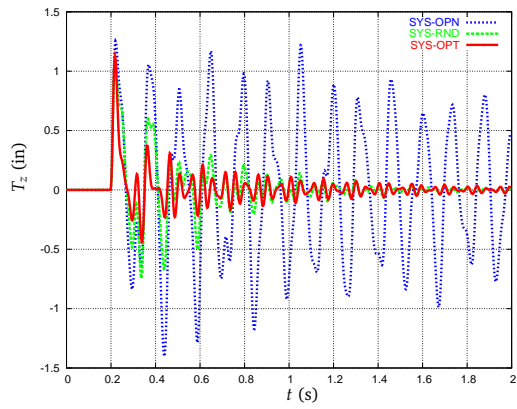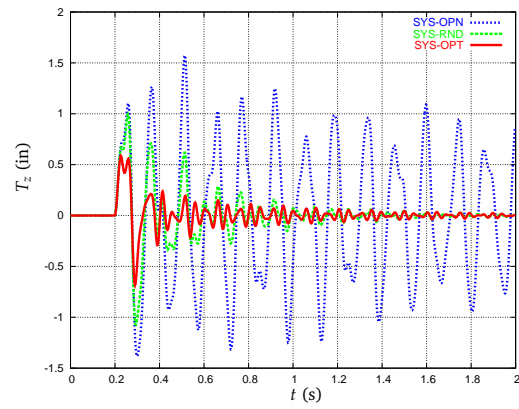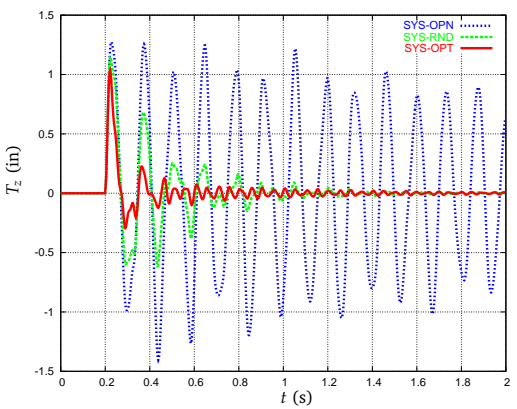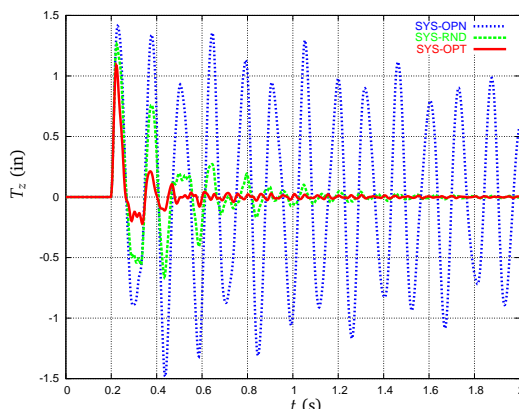
(a) Location Z_1
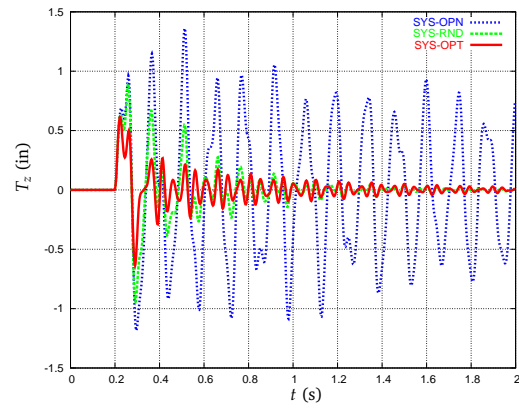
(b) Location Z_2

(c) Location Z_3

(d) Location Z_4

(e) Location Z_5

(f) Location Z_6

Figure - 5.11: Comparison of the displacement responses at the locations Z_1 to Z_6 (see Figure - 5.9) of the three systems

$E(t)$ of the structural system at certain time instant t, is defined as the summation of the potential energy and the kinetic energy, i.e.

$$E^2(t) = \frac{1}{2}\left(\dot{\boldsymbol{d}}^T(t)\boldsymbol{M}\dot{\boldsymbol{d}}(t) + \boldsymbol{d}^T(t)\boldsymbol{K}\boldsymbol{d}(t)\right) \approx \frac{1}{2}\sum_{i=1}^{m}\begin{bmatrix} a_i(t) & \dot{a}_i(t) \end{bmatrix}\begin{bmatrix} \omega_i^2 & 0 \\ 0 & 1 \end{bmatrix}\begin{bmatrix} a_i(t) \\ \dot{a}_i(t) \end{bmatrix}, \qquad (5.5.24)$$

where $\boldsymbol{M}$ and $\boldsymbol{K}$ are mass and stiffness matrices of the structure, respectively, $\boldsymbol{d}$ and $\dot{\boldsymbol{d}}$ are displacement and velocity vectors, respectively, q_i and $\dot{q}_i$ are *modal* displacement and velocity of the i-th mode, respectively. ω_i is the natural frequency of the i-th mode. Figure - 5.12 shows the time history of $E(t)$ obtained from the three systems subjected to the disturbance. It can be seen
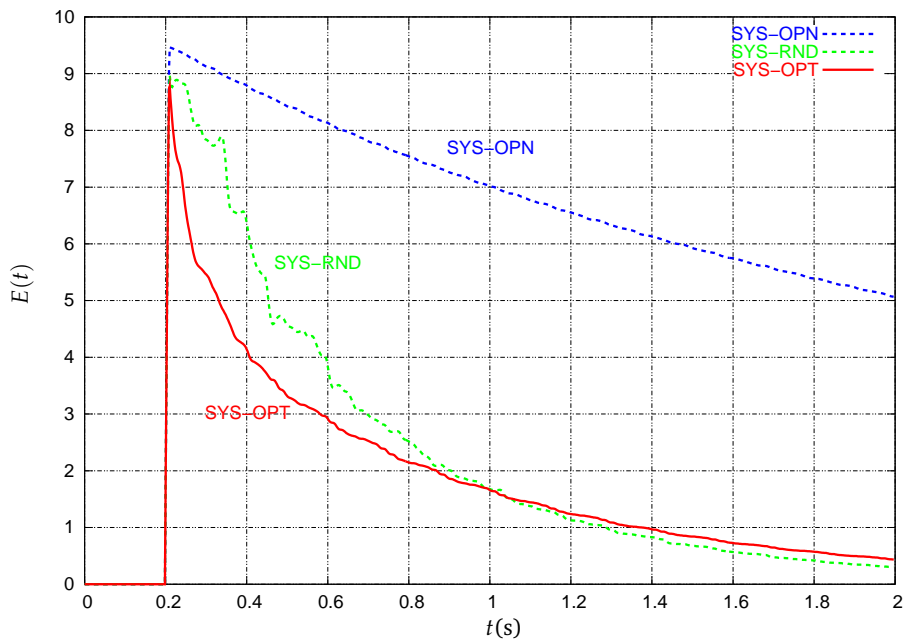

Figure - 5.12: Comparison of the vibrating energy vs time.

that the SYS-OPT demonstrates the fastest energy-decay rate among the three systems. In other words, the SYS-OPT demonstrates the best performance not only in a local but also in a global sense.

To compare the effect of the optimization index used in the OLSA problem on the performance of the final closed-loop system, the standard $\mathcal{H}_2$ norm is used in solving the OLSA problem (see [71] for details). In this OLSA problem, the optimization index is defined as the $\mathcal{H}_2$ norm the closed-loop transfer matrix relating the disturbance, which is same as the one used in the above analysis, to the displacement outputs measured at the four corners and center point

of the shaded region as shown in Figure - 5.13. The method as described in [71] is then used
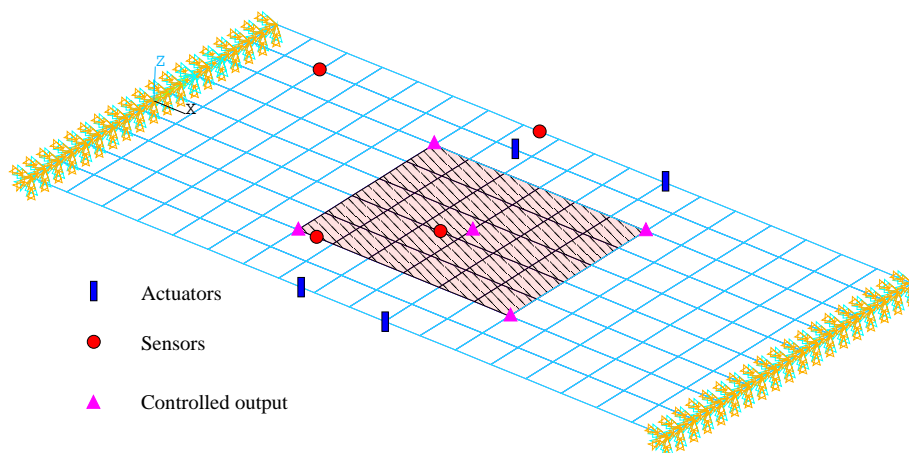

Figure - 5.13: Controlled output and SA locations of SYS3. The point controlled outputs are shown by the solid triangles. Solid rectangular and circles show the optimal locations for the actuators and the sensors, respectively.

to solve this OLSA problem, and a set of the optimal locations of the SAs are found as shown in Figure - 5.13. A standard optimal $\mathcal{H}_2$ controller is then designed, and a new closed-loop system, which is denoted by SYS-PH2, is formed. The vibration energy of the above obtained closed-loop system is then compared with that of SYS-OPT and SYS-OPN. The comparison is shown in Figure - 5.14. It is observed that the vibration of the SYS-PH2 decays slower than that of both SYS-RND and SYS-OPT. Because the standard $\mathcal{H}_2$ norm describes pointwise input-output characteristics of a system, it has inherent limitation on describing the overall dynamical behavior of a distributed system. As a comparison, the spatial $\mathcal{H}_2$ norm overcomes the limitation by introducing an additional averaging over the spatial domain, it is therefore a more comprehensive performance index for a structural system. As a result, when a spatial $\mathcal{H}_2$ norm is used as an optimization index in an OLSA problem, the obtained optimal locations of SAs is able to result a better closed-loop performance when they are used to design a controller. Simulation results shown in Figure - 5.14 demonstrate the benefits that one may get by using a spatial-$\mathcal{H}_2$-norm based performance index in solving an OLSA problem for a distributed system.

In this numerical example, a distributed impulse load as defined in (5.5.22) is used, and
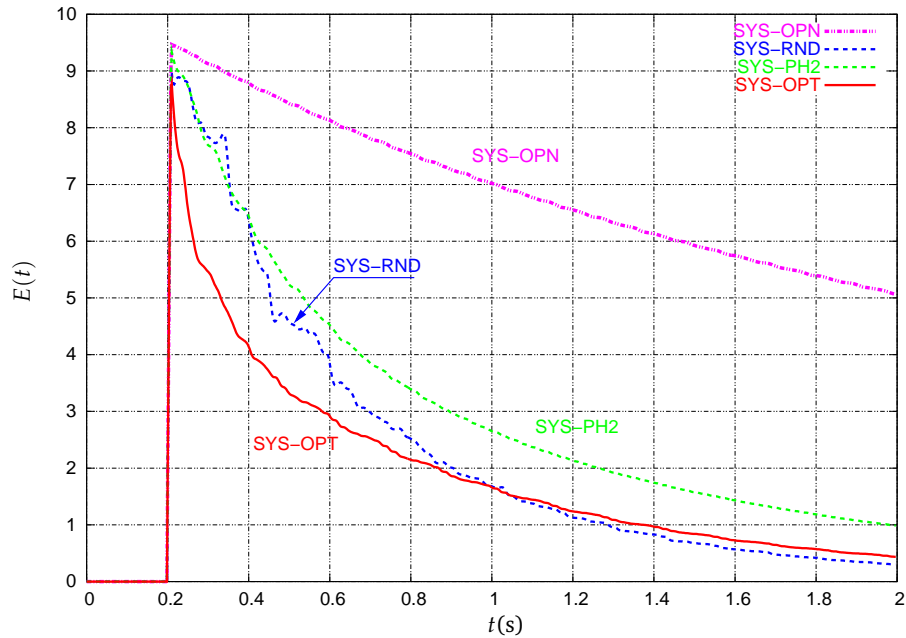
Figure - 5.14: Comparison of vibrating energy vs time of the four systems.

it should be noted that for this example, the obtained optimal locations for the SA's are *not* dependent on time (i.e. $W_D(t)$ in (5.5.22)) but dependent on the spatial distribution of the applied load. When $W_D(t)$ is not an impulse function, to obtain a time-independent solution to the OLSA problem, the frequency information (if available) has to be absorbed into the system. In this case, the optimal locations for SA's are dependent on time *indirectly*.

5.6   Summary

The problem of optimal locations for sensors and actuators in a SVC system was studied in this chapter. Based on a brief introduction of the spatial $\mathcal{H}_2$ norm and the spatial $\mathcal{H}_2$ controller design, a numerical scheme using the spatial $\mathcal{H}_2$ norm as the performance index was proposed to find the optimal locations for the sensors and actuators in a SVC system. A GA method was used in solving the OLSA optimization problem. The effectiveness of the proposed scheme was illustrated via extensive numerical simulation studies on the vibration control of a plate structure. The simulation results showed that the scheme was effective in finding optimal sensor and actuator locations. A controller using the SAs with the locations found by the proposed scheme, is

109

able to improve the performance of the resultant closed-loop substantially. Additionally, the spatial $\mathcal{H}_2$ norm was shown to be a better performance index to be used in the structural vibration control when the vibration reduction is required over a continuous area on the structure.

CHAPTER 6

Modeling of MR Dampers and Applications

6.1 Introduction

The MR fluids typically consist of microsized, magnetically polarizeable particles (such as iron particles) dispersed in a carrier medium. An applied magnetic field can turns the MR fluids into a semi-solid in a few milliseconds [2]. This phase change increases the yield stress of the MR fluids dramatically. Various devices have been developed to utilize this special material property demonstared by the MR fluids. Because the deformation of the MR fluids resembles that of yielding, the force provided by a MR device is always dissipative, as a result, MR devices are also known as MR *dampers*. A schematic of a typical MR damper is shown in Figure - 6.1. As shown in this figure, the MR fluids are contained inside of a sealed channel. The piston can move back and forth along the channel with valves on the piston. There is a coil inside the piston that can generate a magnetic field inside the channel when the electric current flows inside the coil through the wire. The magnetic field around the MR fluids can be regulated by altering the intensity of the current flowing through the coil, and as a result, the material property, i.e. the yielding stress, of the MR fluids can be controlled.

A MR damper can be operated in a wide temperature range (-40$°$C to 150$°$C), and can provide up to tons of damping force using a battery power supply (as low as 20 $\sim$ 50 watts). These properties make MR dampers an powerful and reliable devices that can be used in various appli-
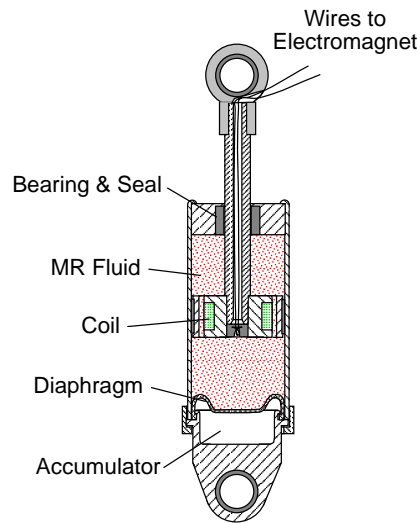
Figure - 6.1: A schematic of a typical MR damper

cations, such as vibration control of bridges [46–48], buildings [49–51], and vehicle suspension system [52], etc.

In this chapter, hysteresis behavior of MR dampers and the their applications to structural vibration control are studied. Mathematical model of a MR damper and the corresponding control algorithm that will be used in this research are determined through a comparison study on various MR models and control algorithms available in the literature. Using the determined MR model and control algorithm, passive control and semi-active control of large scale structures using MR dampers are studied. In this chapter, emphasis will be put on the application aspect and the related numerical simulations.

6.2 Modeling of MR Fluids Damper

In this section, several widely used models of MR dampers are briefly introduced and their abilities to reproduce the hysteresis behavior of MR dampers are compared. The comparison study presented in this section are mainly based on the experimental study reported by Spencer Jr. et al. [54].

6.2.1 Binham Model

The stress-strain behavior of the Bingham viscoplastic model [53] is often used to describe the behavior of MR fluids. In this model, the plastic viscosity is defined as the slope of the measured shear stress versus shear strain rate. For positive values of the shear rate $\dot{\gamma}$, total stress is given by

$$\tau = \tau_y \operatorname{sgn}(\dot{\gamma}) + \eta \dot{\gamma},$$ (6.2.1)

where τ_y is the yield stress induced by magnetic field; and η is viscosity of the MR fluids. Based on this model, Stanway et al. [72] proposed an idealized mechanical model for a controllable fluid damper, which is applicable to MR dampers. The schematic of this model is shown in Figure - 6.2.
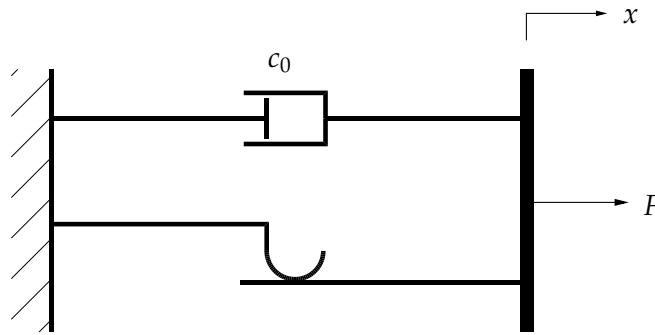

Figure - 6.2: Bingham model

In this model, the force generated by the device is given by

$$F = f_c \operatorname{sgn}(\dot{x}) + c_0 \dot{x}$$ (6.2.2)

where c_0 is damping coefficient; f_c is friction force related to fluid yield stress.

6.2.2 Extended Bingham Model

Gamota and Filisko [73] proposed a model predicting the behavior of the ER material, which has similar hysteresis behavior as the MR fluids, based on the Bingham model. As shown in Figure - 6.3, this model is an extension of the Bingham model, and consists of the Bingham model and a standard model of linear solid. The governing equation of this model is given by
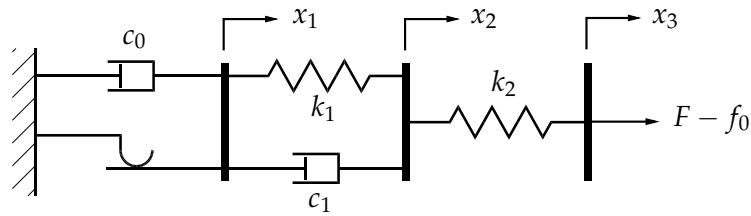
Figure -6.3: Extended Bingham model [73]

$$F = \begin{cases} \begin{aligned} &k_1(x_2 - x_3) + c_1(\dot{x}_2 - \dot{x}_1) + c_0\dot{x}_1 + \\ &f_c\,\mathrm{sgn}(\dot{x}_1) + f_0 + k_2(x_3 - x_2) \end{aligned} & \text{for } |F| > f_c, \\[1em] k_1(x_2 - x_3) + c_1\dot{x}_2 + f_0 + k_2(x_3 - x_2) & \text{for } |F| < f_c. \end{cases} \tag{6.2.3}$$

For this model, it was experimentally observed [74] that the decrease in the damping coefficient c_1 can produce nonlinear roll-off in the measured force-velocity relationship as the velocity approaches zero. A problem associated with this model is that much smaller time steps are needed to simulate the system [75].

6.2.3 Bouc-Wen Model

One model that is numerically tractable and has been used extensively for modeling hysteretic systems is the Bouc-Wen model [1]. The Bouc-Wen model is extremely versatile, and can be used to simulate a variety of hysteretic behaviors. A schematic of this model is shown in Figure - 6.4.
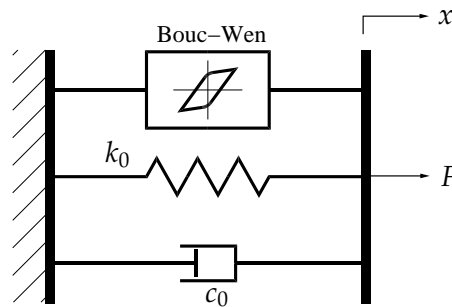

Figure -6.4: Bouc-Wen model [1]

The force in this model is governed by

$$F = c_0\dot{x} + k_0(x - x_0) + \alpha z, \tag{6.2.4}$$

114

where z is an hidden variable governed by

$$\dot{z} = -\gamma |\dot{x}| z |z|^{n-1} - \beta \dot{x} |z|^n + A\dot{x}. \qquad (6.2.5)$$

By tuning the parameters γ, β and A, this model is able to simulate a variety of hysteretic materials. According to Spencer Jr. et al. [54], main problem for this model is that its force-velocity relation within the low velocity range does not closely reproduce the measurement results obtained from a typical MR damper used in their research.

6.2.4 Modified Bouc-Wen Model

From the above investigation it can be seen that, there are various problems associated with the models introduced above. Based on extensive experiments, Spencer Jr. et al. [54] proposed a modified Bouc-Wen model, which avoided most of the problems observed in the other models. This model was able to maintain all advantages exhibited by the Bouc-Wen model. The schematic of this model is shown in Figure - 6.5.
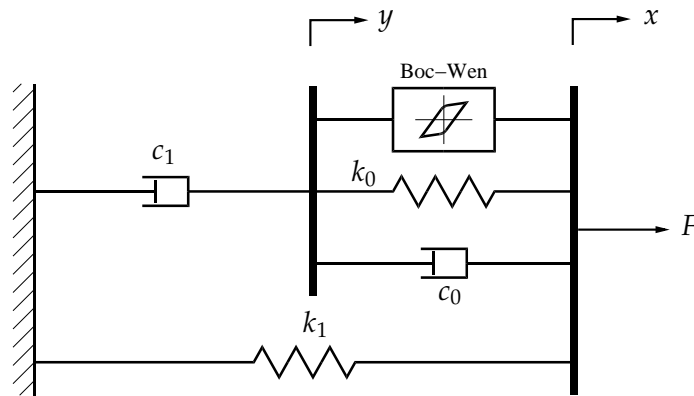
PSfrag replacements

Figure - 6.5: Modified Bingham model [54].

In this model, the damping force f_d produced by the MR device is given by

$$f_d = c_1 \dot{y} + k_1 (x - x_0), \qquad (6.2.6)$$

where y is governed by the following equations

$$\dot{y} = \frac{1}{(c_0 + c_1)} \{ \alpha z + c_0 \dot{x} + k_0 (x - y) \} \qquad (6.2.7)$$

$$\dot{z} = -\gamma |\dot{x} - \dot{y}| z |z|^{n-1} - \beta (\dot{x} - \dot{y}) |z|^n + A(\dot{x} - \dot{y}).$$

In the above equations, parameters α, c_1 and c_0 are directly related to the voltage u applied to the MR damper in a manner shown below,

$$
\begin{aligned}
\alpha &= \alpha(u) = \alpha_a + \alpha_b u, \\
c_1 &= c_1(u) = c_{1a} + c_{1b} u, \\
c_0 &= c_0(u) = c_{0a} + c_{0b} u,
\end{aligned}
\qquad (6.2.8)
$$

where u is given as the output from a first-order filter as follows

$$
\dot{u} = -\eta(u - u_c),
$$

in which, u_c is the command voltage signal sent to the current driver. The parameters associated with this model were found through matching the simulated data with experimental data obtained in a variety tests [54]. The obtained parameters are shown in the following table. As reported in [54], the mathematical model described in (6.2.6) and (6.2.7) with the above

Table 6.1: Parameters of the MR damper used in simulation

Parameter	Value	Parameter	Value
c_{0a}	$20.2\ N \cdot sec/cm$	α_a	44.9
c_{0b}	$2.68\ N \cdot sec/cm \cdot V$	α_b	$638\ V^{-1}$
k_0	$15.0\ N/cm$	γ	$39.3\ cm^{-2}$
c_{1a}	$350\ N \cdot sec/cm$	β	$39.3\ cm^{-2}$
c_{1b}	$70.7\ N \cdot sec/cm \cdot V$	A	47.2
k_1	$5.37\ N/cm$	n	2
x_0	$18.4\ cm$	η	$251\ sec^{-1}$

parameters was able to match experimental results satisfactorily. Therefore, this model and the corresponding parameters shown in Table. 6.1 will be used in this research.

Using this model, the responses of the MR damper due to a 2.5Hz sinusoidal excitation with an amplitude of 1.5cm are shown in Figure - 6.6. It can be seen from this figure that, at 0V input voltage, the MR damper behaves like a viscous damper, i.e. the force-displacement relation is approximately elliptical, and the force is almost linearly proportion to the velocity.
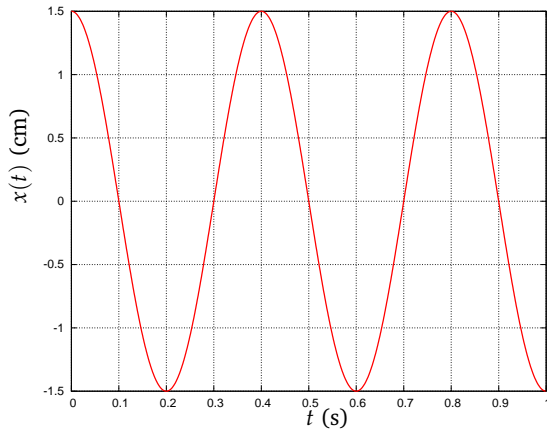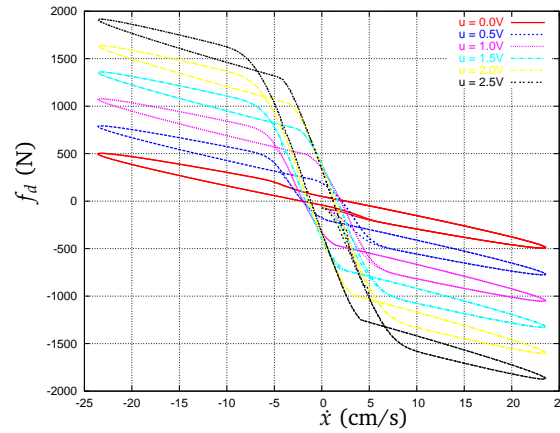
(a) Excitation signal
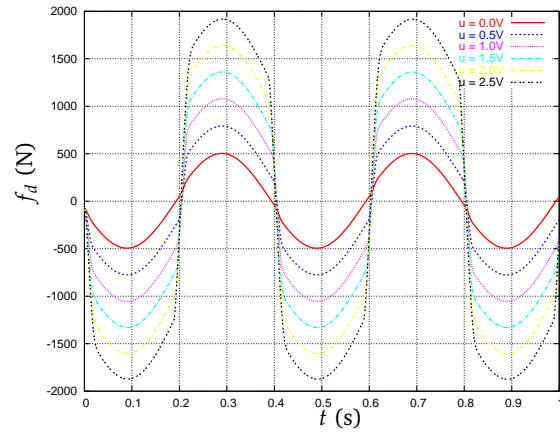
(b) MR damping force
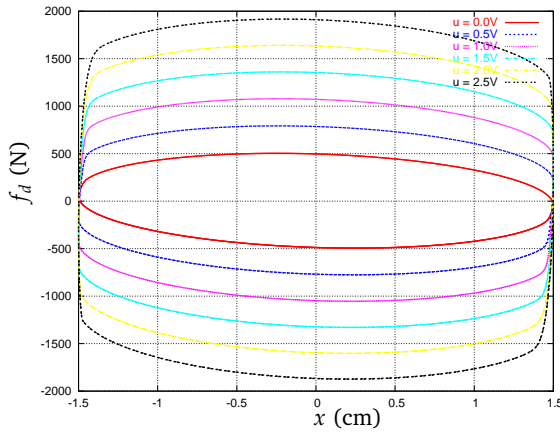
(c) Damping force v.s. displacement

(d) Damping force v.s. velocity

Figure - 6.6: Simulated MR damper force for a 2.5Hz sinusoidal excitation with an amplitude of 1.5cm by using the modified Bouc-Wen model. Four different input voltages are used.

With the increasing of the applied voltage, the force needed to yield the material increase, and the amount of energy dissipated within one cycle, which is measured by the area circled by the curve as shown in Figure - 6.6(c), increases correspondingly.
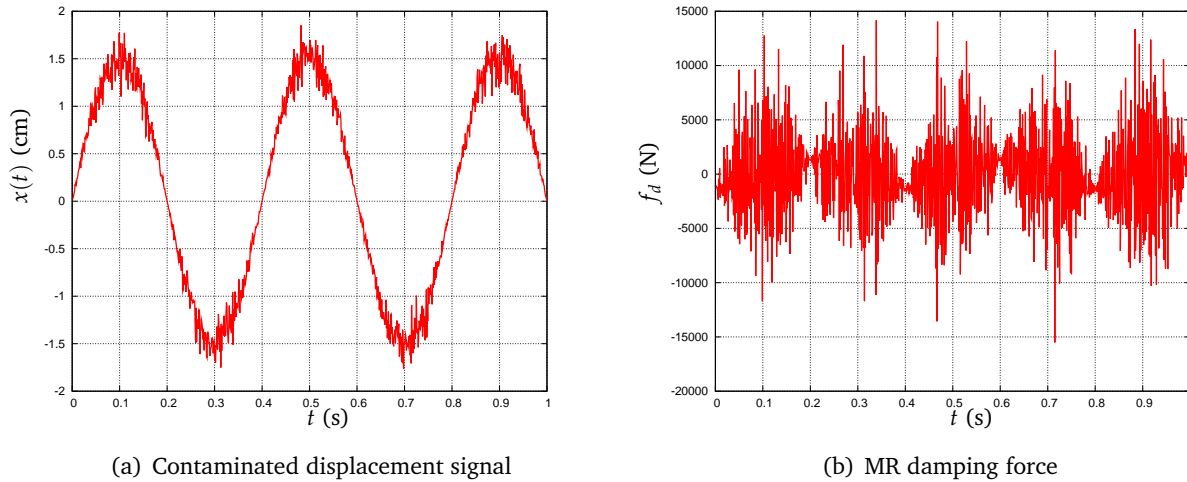
(a) Contaminated displacement signal

(b) MR damping force

Figure - 6.7: Response of the MR damper to a noisy displacement excitation.

6.2.5 Improvement of the Numerical Property

Through numerical experiment of the MR model described above, it was observed that the response of the model is extremely sensitive to the change of the velocity. High frequency components in the velocity not only cause the trouble in solving the model, but also make the model losing its desired hysteretic behavior as shown in the following example.

Consider a case where the MR model is excited by the following sinusoidal displacement signal contaminated by noise,

$$x(t) = 1.5 A_n \sin(5\pi t), \qquad (6.2.9)$$

where $A_n = N(0, 0.01)$ is a zero-mean Gaussian white noise. Figure - 6.7(a) shows the time history of this displacement signal, and Figure - 6.7(b) gives the MR force obtained from the above model. It can be seen that desired hysteretic behavior as shown in Figure - 6.6 is destroyed by the noise inside the displacement signal.

Through numerical experiments, it is observed that the response from the MR model given in (6.2.7) is dominated by the input velocity $\dot{x}$, and is sensitive to the change in the velocity. This property causes the model behave erratically when there are sudden changes in the velocity, which is the case when the velocity is evaluated numerically from the displacement. In many numerical simulations, evaluation of the velocity from noisy displacement data is inevitable. Therefore, it is desirable to take necessary measure to improve the numerical property of the

MR model.

To this end, a low-pass filter (LPF) is added to the MR model (6.2.7) in order to improve the ability of the model in dealing with noisy displacement data. The dynamics of the MR model with a LPF thus becomes

$$
\begin{aligned}
\dot{y} &= \frac{1}{(c_0 + c_1)}\{\alpha z + c_0 v + k_0(x - y)\}, \\
\dot{z} &= -\gamma|v - \dot{y}|z|z|^{n-1} - \beta(v - \dot{y})|z|^n + A(v - \dot{y}), \\
\dot{w} &= A_f w + B_f \dot{x}, \\
v &= C_f w,
\end{aligned}
\tag{6.2.10}
$$

where A_f, B_f and C_f are system matrices of the low-pass filter, w is the state of the filter, and v is the filtered velocity. The damping force of the MR damper is still given by (6.2.6). The system matrices associated of a 2nd order LPF are given as follows

$$
A_f = \begin{bmatrix} 0 & 1 \\ -\omega_c^2 & -\sqrt{2}\omega_c \end{bmatrix}, \quad B = \begin{bmatrix} 0 \\ 1 \end{bmatrix}, \quad C = \begin{bmatrix} \omega_c^2 & 0 \end{bmatrix},
\tag{6.2.11}
$$

where ω_c is the cutoff frequency of the filter. Figure - 6.8 shows the damping force obtained from the improved model (6.2.10) subjected to the noisy displacement given in Figure - 6.7(a). The MR damping force showed in Figure - 6.8 is obtained by setting the cutoff frequency of
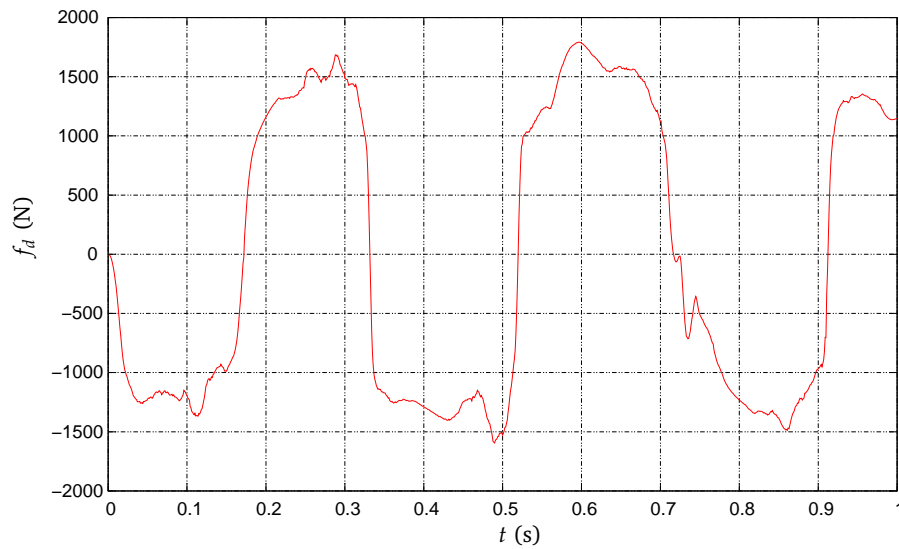

Figure - 6.8: Response of the improved MR model to a noisy displacement excitation.

119

the LPF to 15 Hz. Because the frequency of the primary component of the excitation is 5 Hz, therefore, the LPF allows the pass of this main component, and all higher frequency components are rejected. As a result, the desired hysteretic behavior of the MR damper is retained as shown in Figure - 6.8.

6.3 Structural Vibration Control Using MR Dampers

To attenuate vibration of a structure, MR damper can be used either in a passive or a semi-active way. In the passive way, a MR damper is used as a normal damping device, whose natural hysteretic behavior helps to dissipate the vibration energy through its interaction with the structure to which it is attached. In this case, an appropriate input voltage to the MR damper is chosen and kept constant throughout its working cycle. In the semi-active way, the controllable hysteretic behavior of the MR damper is used to achieve a better vibration attenuation. In this case, the input voltage to the MR damper changes in a way such that the damping force provided by the MR damper follows a command signal, which is usually generated by a feedback controller according to the measured response of the structure. In the semi-active control, a MR damper is used in a way more like an actuator with additional controllable damping capability.

Passive control is simple to implement and robust to uncertainties. Semi-active control may achieve better performance at the expense of a more complicated design and analysis. In this section, issues related to the analysis of passive and semi-active control of a structure using MR damper will be discussed.

6.3.1 Passive Control

Given a n-DOF structure and m MR dampers, the equations of motion of the system can be expressed as follows,

$$M\ddot{x} + C\dot{x} + Kx = B_m f_d(x, \dot{x}) + f, \tag{6.3.12}$$

where $M, C, K \in \mathbb{R}^{n \times n}$ are mass, damping and stiffness matrices of the structure, respectively, $x \in \mathbb{R}^n$ is the displacement vector, $B_m \in \mathbb{R}^{n \times m}$ is a matrix specifying the locations of the m MR dampers, $f_d \in \mathbb{R}^m$ and $f \in \mathbb{R}^n$ are MR damping force and external force vectors, respectively.

Because the MR damping force vector f_d is a function of the unknown displacement x and velocity $\dot{x}$, (6.3.12) represents a set of nonlinear equations.

Two approaches can be used to solve the above nonlinear equations. One approach is to use a linear solver, e.g. the Newmark method as introduced in Appendix A, by treating (6.3.12) as a piecewise-linear system, computing the MR damping force $f_d(x)$ from the displacement at the previous time step, and treating it as constant in each time step. In this approach, MR dampers actually acts like active devices providing additional excitation to the system. Numerical experiment showed that, this approach can not produce an accurate results, and even worse, could lead to an unstable solution. To obtain an stable and accurate solution, the integration time step needs to be sufficiently small. Another approach is to transform the above second order ODE into a set of first order ODE's (or state space form), and solve the obtained first order system using a Runge-Kutta method. Because each MR damper has 4 states (2 internal states and 2 filter states), the obtained the first order ODE has totally $2n + 4m$ states. For a large scale structure with multiple MR dampers, numerical simulation on such a big system is a difficult task.

To facilitate the numerical simulation in this research, an efficient method to solve (6.3.12) is developed. The propposed numerical scheme is based on the Newmark method, and the unconditionally-stable property of the Newmark method is preserved. To deal with the nonlinearity, the proposed scheme finds the solution through iteration within each integration step.

Assume the solution to (6.3.12) have been obtained at time t, to find the solution at time $t + \triangle t$, the MR force f_d at time instant $t + \triangle t$ is first expressed by the known values at the previous time instant t. The error introduced by the above approximation calls for the iteration within each time step. The solution at the i-th iteration step is obtained by solving,

$$M\ddot{x}^{(i)}_{t+\triangle t} + C\dot{x}^{(i)}_{t+\triangle t} + Kx^{(i)}_{t+\triangle t} = B_m f_d(x^{(i-1)}_{t+\triangle t}, \dot{x}^{(i-1)}_{t+\triangle t}) + f_{t+\triangle t}. \tag{6.3.13}$$

The solution at $i + 1$-th iteration step is obtained as follows

$$x^{(i+1)}_{t+\triangle t} = \delta x^{(i)}_{t+\triangle t} + x^{(i)}_{t+\triangle t}, \quad \dot{x}^{(i+1)}_{t+\triangle t} = \frac{3}{\triangle t}\delta x^{(i)}_{t+\triangle t} + \dot{x}^{(i)}_{t+\triangle t}, \quad \ddot{x}^{(i+1)}_{t+\triangle t} = \frac{6}{\triangle t^2}\delta x^{(i)}_{t+\triangle t} + \ddot{x}^{(i)}_{t+\triangle t}. \tag{6.3.14}$$

The coefficients used in the above equations are obtained from the assumptions of the Newmark method (see Appendix A). $\delta x^{(i)}_{t+\triangle t}$ is obtained by solving the following linear equations,

$$-\left[\frac{6}{\triangle t^2}M + \frac{3}{\triangle t}C + K\right]\delta x^{(i)}_{t+\triangle t} = M\ddot{x}^{(i)}_{t+\triangle t} + C\dot{x}^{(i)}_{t+\triangle t} + Kx^{(i)}_{t+\triangle t}$$

121

$$- B_m \boldsymbol{f_d}(\boldsymbol{x}_{t+\triangle t}^{(i)}, \dot{\boldsymbol{x}}_{t-\triangle t}^{(i)}, u_{t+\triangle t}) + \boldsymbol{f}_{t+\triangle t}. \qquad (6.3.15)$$

Above iteration steps will be terminated when $\|\boldsymbol{\delta x}_{t+\triangle t}^{(i)}\| \leq \varepsilon$ has been satisfied, where ε is an accuracy tolerance.

The method proposed above solves (6.3.12) without transforming to a state space form. Because the symmetric property of the mass, damping and stiffness matrices can be utilized, the method can be implemented efficiently for a large scale structure.

6.3.2   Semi-Active Control

In a semi-active control system, the desired control force (i.e. command signal) is calculated by a controller based on the measured response of the structure, and MR damper is used as an actuator to apply the control force to the structure. Because a MR damper is a passive device, a force can only exist in its interaction with the structure. In other words, the force developed by a MR damper is determined by the displacement, velocity as well as the input voltage to the MR damper as shown in (6.2.10). As a result, the MR force can not be totally controlled by changing the input voltage.

To instruct a MR damper to follow a given command signal, some researchers (Chang and Roschke [57], Hidaka et al. [58]) proposed to use a neural networks to represent the inverse-dynamics of the MR damper, such that the desired input voltage to the MR damper can be found by an off-line-trained neural network. Numerical experiments showed that an off-line-trained neural network can not generate an acceptable output when the inputs are different in nature from the that used in the training process. In this research, a control algorithm based a clipped-optimal control algorithm [62] is used to find an appropriate input voltage for a MR damper, such that the force developed by the MR damper can follow the command signal. The block diagram of a semi-active control system using MR damper is shown in Figure - 6.9. In the system showed in the figure, the controller can be any linear controller. The command signal f_u is generated by the controller from the measured structural response $x, \dot{x}$. The 'control law' acts like a secondary controller, which is designed to produce an output u, which is the input voltage to the MR damper, such that the difference between the actual MR damping force f_d and the command signal f_u is as small as possible. The clipped-optimal control algorithm uses the
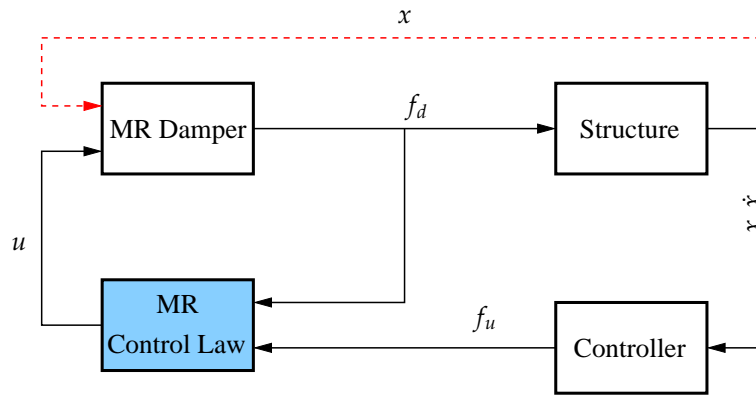
Figure - 6.9: Block diagram of a semi-active control system using MR damper.

following bang-bang type control strategy to determine the input voltage u to the MR damper,

$$u = u_{max}H\left[f_d \times (f_u - f_d)\right],\tag{6.3.16}$$

where $H(\cdot)$ is the Heaviside function. Essentially, this control law switches the voltage to its maximum allowed value u_{max} whenever the MR force is in the same direction as the command signal f_u and smaller than f_u.

6.4 Numerical Example

Vibration control of a plate using the MR dampers is considered here. The plate has a dimension of $30 \times 20 \times 0.01$in, and is made of a material with Young's modulus $E = 30 \times 10^6$ psi, Poisson's ratio $v = 0.27$ and mass density $\rho = 0.0009218$ psi. The modal damping ratio is assumed be 0.005. The finite element mesh of the plate is shown in Figure - 6.10. A single point excitation force is applied to the plate at the location as shown in the figure. Passive and semi-active vibration control using 3 MR dampers, whose locations are randomly selected as specified in the figure, are considered for two different excitation cases: impulse and Gaussian white noise excitations. The impulse force has a magnitude of 10 lb and lasts for 0.01 s. The Gaussian white noise excitation has an intensity of 0.05 lb^2/s with zero mean.

The MR dampers used in the following simulation are based on the model whose parameters are specified in Table. 6.1. Because the MR defined by these parameters is too stiff for the plate structure considered here, the MR force calculated from this MR model is scaled by a factor of
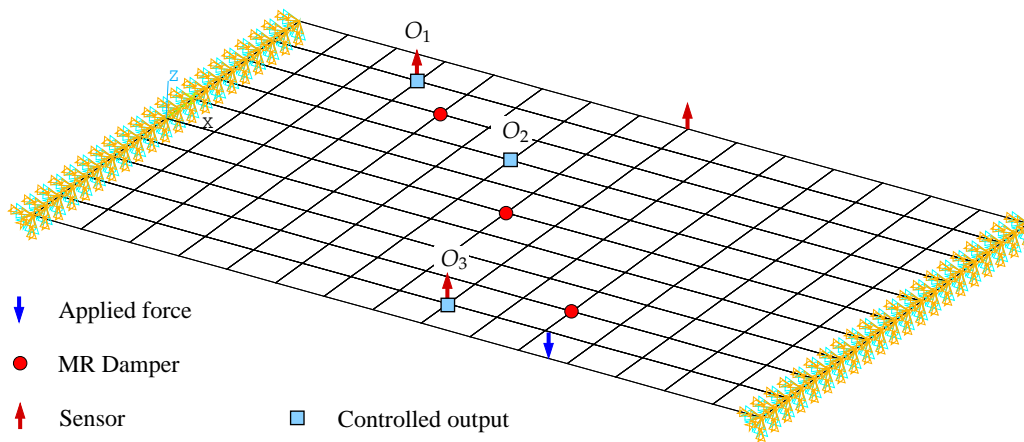
123

Figure - 6.10: Finite element mesh of a plate.

0.002.

For comparison purpose, the displacement responses at the three randomly selected locations, i.e. O_1, O_2 and O_3 as shown in Figure - 6.10, are computed for each cases. As a global performance index, the vibration energy of the plate is also computed and compared between the passive and the semi-active control strategies. The vibration energy of the plate was defined (5.5.24) (on pp.107).

6.4.1 Passive Control

In this case, a constant voltage $u = 0.05$ V is applied to all 3 MR dampers. Figure - 6.11 shows the responses of the plate with and without MR dampers due to the impulse excitation. From the displacement responses plotted in Figure - 6.11(a)-(c), it is seen that the displacement response is quickly decayed to zero when the MR dampers are used. In terms of the energy index, over 99% of the vibration energy is drained from the plate by the MR dampers at $t = 3$ s.

Figure - 6.12 compares the the responses of the plate subjected to the white noise excitation for the cases with and without MR dampers. At the three randomly selected locations, it is seen from Figure - 6.12(a)-(c) that the displacement responses are reduced apparently by using the MR dampers. The RMS responses at these locations are compared in the Table.6.2. From the results listed in the table, it is observed that the largest reduction appears at O_2, which is close to the two of 3 MR dampers. O_1 is very close to one of the MR dampers, and therefore achieves

(a) Displacement at O_1

(b) Displacement at O_2
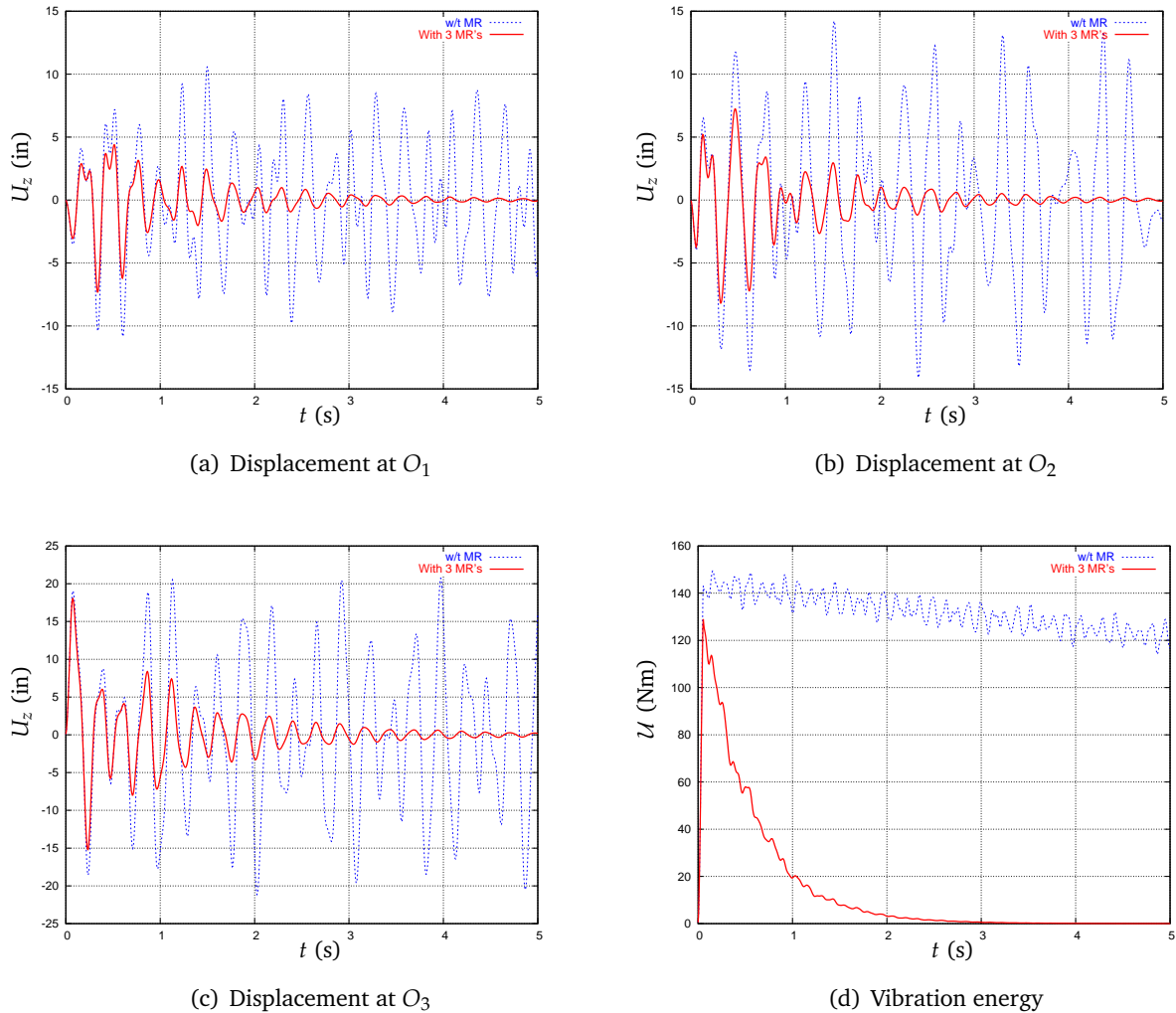
(c) Displacement at O_3

(d) Vibration energy

Figure - 6.11: Passive vibration control using MR dampers of a plate subjected to an impulse excitation.

the second best reduction. The distance between the location O_3 and any one of the three MR dampers are much larger than other locations, and as a result, the effects of the MR dampers experienced at this location is the smallest among the three locations. From this analysis, it is observed that, reduction of vibration measured at any specific location depends on its distance from the MR dampers, and therefore varies across the structure. In terms of the vibration energy, the passive control using MR dampers definitely achieves significant overall vibration reduction as shown in Figure - 6.12(d).
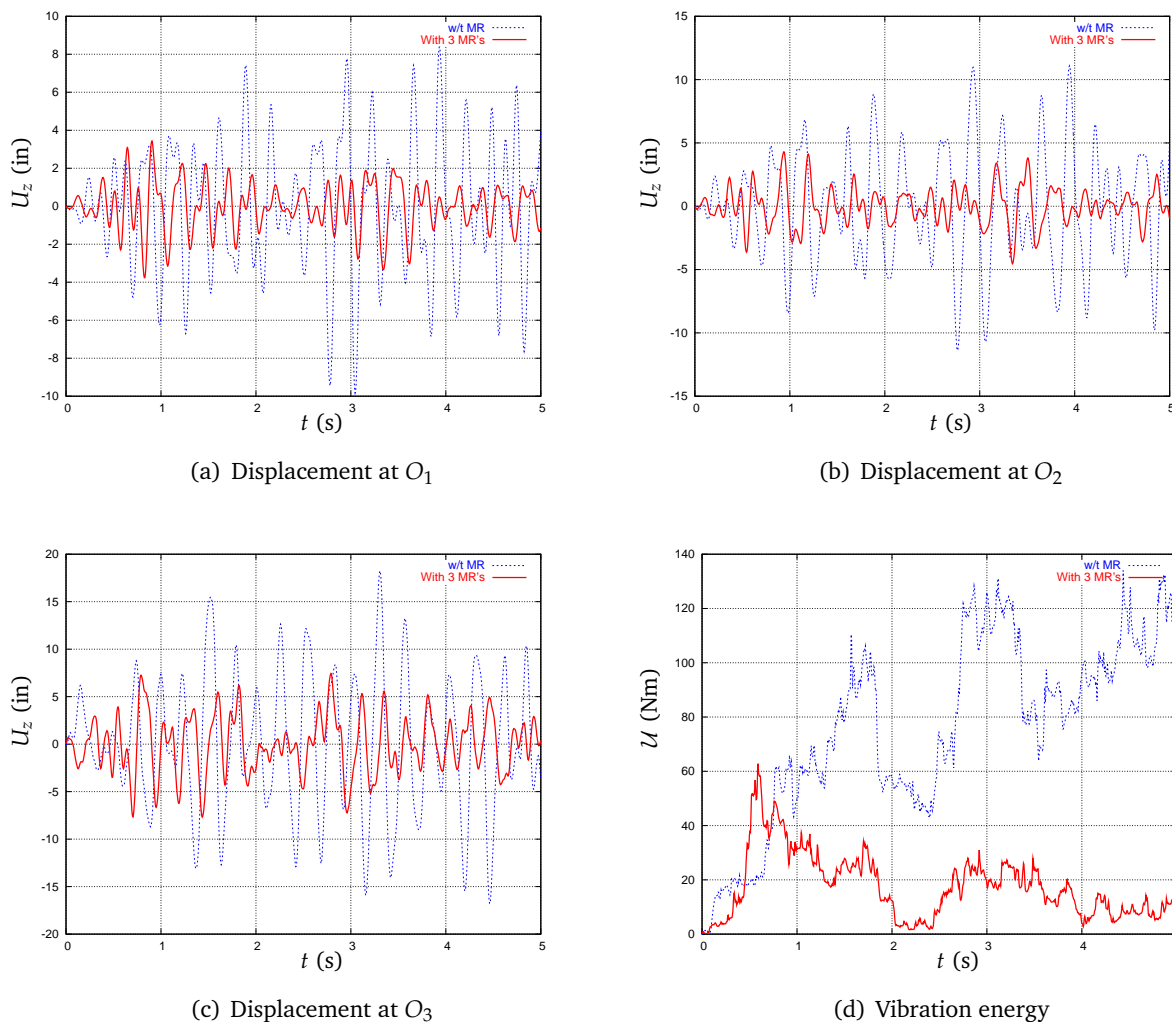
(a) Displacement at O_1

(b) Displacement at O_2

(c) Displacement at O_3

(d) Vibration energy

Figure - 6.12: Passive vibration control using MR dampers of a plate subjected to a white noise excitation (intensity 0.05).

6.4.2 Semi-Active Control

In this section, a semi-active control system using the MR dampers is designed for the vibration control of the plate. A $\mathcal{H}_2$ controller with 3 velocity sensors, whose locations are shown as in Figure - 6.10, is first designed. The controlled output of the controller are displacements measured at the locations as shown in Figure - 6.10. The input voltages to the MR dampers are determined using the control law as described in (6.3.16).

The $\mathcal{H}_2$ controller is designed to attenuate the first 4 modes of the structure. The weighting

Table 6.2: Comparison of the RMS responses

| Locations	Without MR damper (in)	With MR dampers (in)	Reduction (%)
O_1	3.54	1.19	66%
O_2	4.93	1.44	71%
O_3	7.18	3.11	57%

coefficient matrix C_1 (see (2.4.53) and (2.4.54)) for the controlled outputs is chosen as identity matrix. Following the standard procedure as outlined in Chapter 2, the $\mathcal{H}_2$ controller used in the semi-active control system is obtained. In this example, the obtained controller has 3 measurement inputs from the velocity sensors, and 3 outputs, which are command signals for the 3 MR dampers. Figure - 6.13 compares the Bode plots of the transfer matrices relating the disturbance to the controlled outputs of the open-loop and closed-loop systems. It can be seen that using $\mathcal{H}_2$ controller reduces the responses by $20 - 50$dB at the resonant frequencies in the controlled output channels. By using the clipped optimal control algorithm, it is expected the control force provided by the MR dampers be able to follow the ideal control force generated by the controller, such that the desired vibration reduction can be achieved.

For the comparison purpose, the same impulse and white noise excitations as being used in the passive control case are used here. Figure - 6.14 shows the response of the controlled plate subjected to the impulse excitation applied at the location shown in Figure - 6.10. The displacement responses of the three controlled outputs are compared between the passive and semi-active cases in Figure - 6.14(a)-(c). It is seen that the semi-active control scheme achieves more fast vibration decay speed than the passive one does. At the three controlled outputs locations, the displacements settle down at about 1.5s in the semi-active control scheme, which is 4s faster than in the passive control case. Figure - 6.14(d) compares the variation of the energy v.s. time between the two control strategies. In the semi-active case, 99% of the vibration energy is dissipated in 1s, as compared 3.5 s in the passive control system.
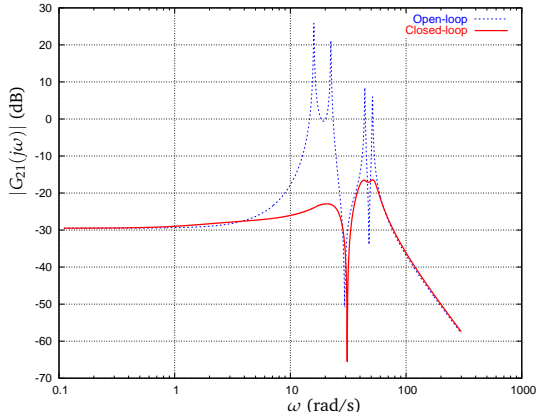
For the white noise excitation, semi-active control also outperforms the passive control as shown in Figure - 6.15, where (a)-(c) compares the displacement responses measured at the
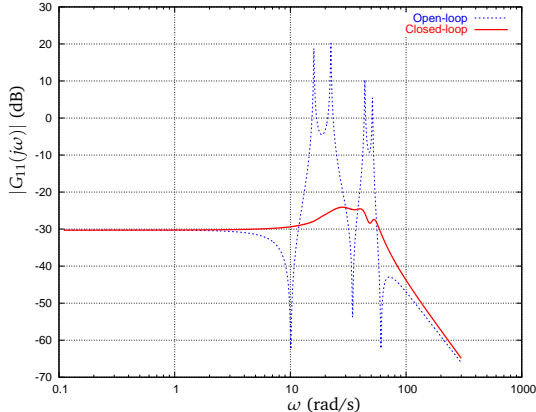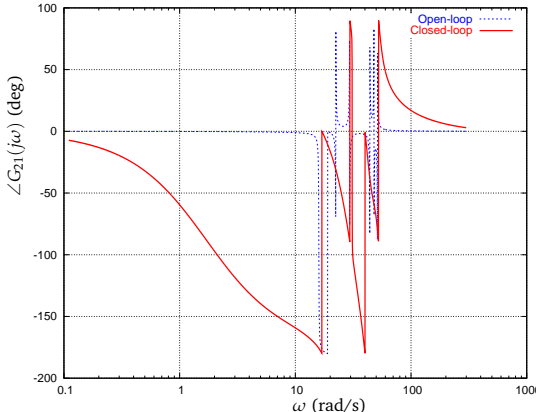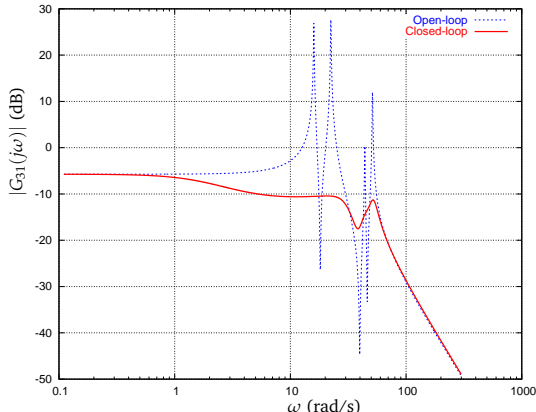
(a) Magnitude of $G_{11}(j\omega)$
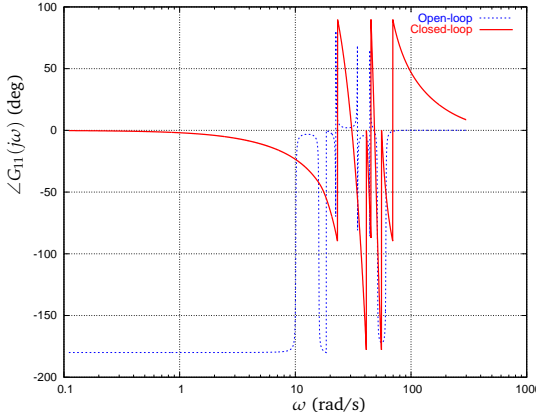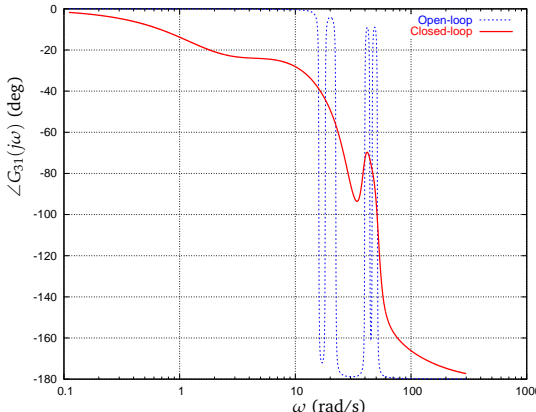
(b) Phase angle of $G_{11}(j\omega)$

(c) Magnitude of $G_{21}(j\omega)$

(d) Phase angle of $G_{21}(j\omega)$

(e) Magnitude of $G_{31}(j\omega)$

(f) Phase angle of $G_{31}(j\omega)$

Figure - 6.13: Comparison of the Bode plots of the open-loop and closed-loop systems.

(a) Displacement at O_1

(b) Displacement at O_2
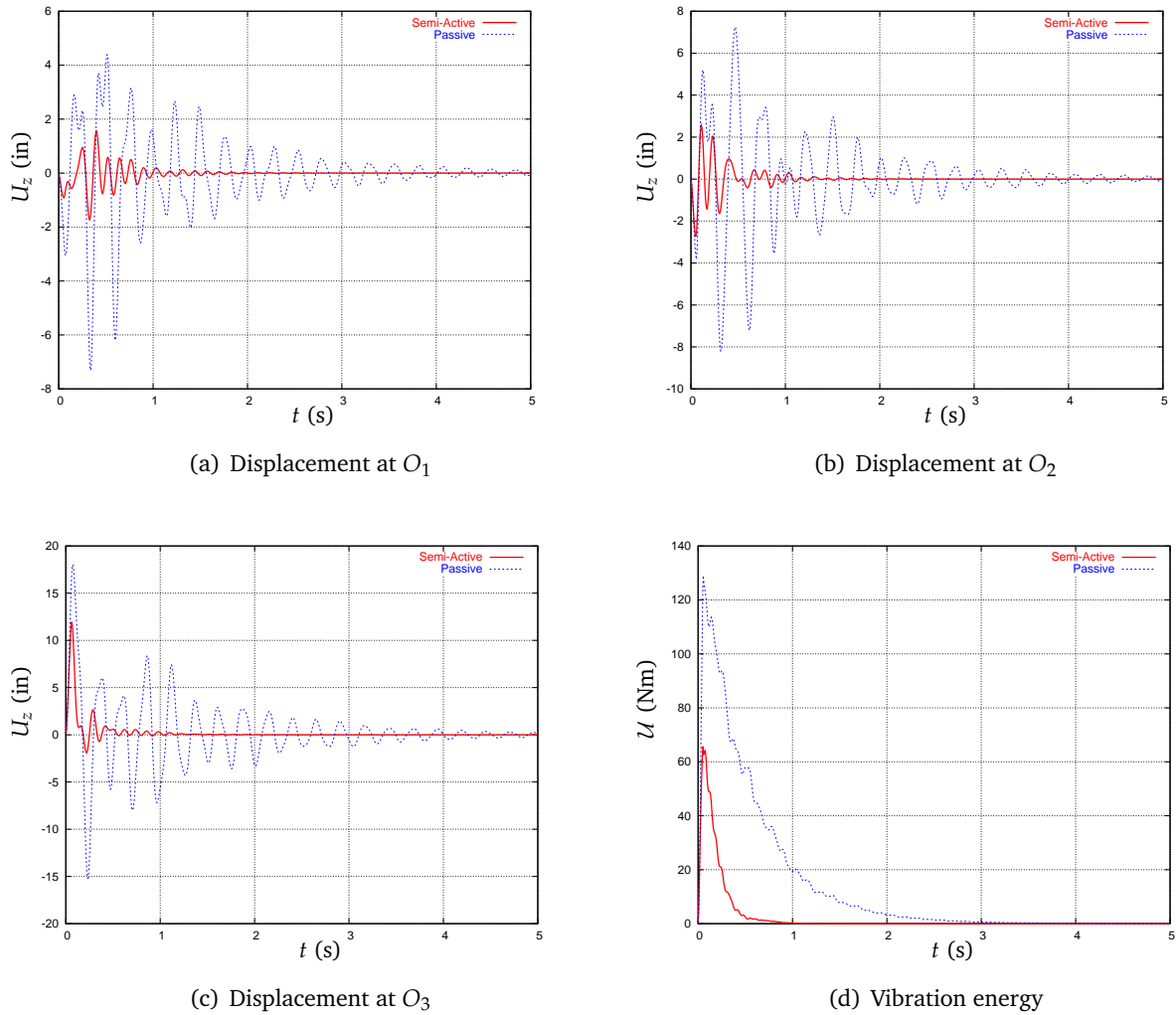
(c) Displacement at O_3

(d) Vibration energy

Figure - 6.14: Respose comparison of the plate with passive and semi-active control using MR dampers (Impulse excitation).

three controlled output locations between the passive and semi-active control schemes. It is seen that the response obtained from the semi-active control system is much smaller than that from the passive control system. Table.6.3 summarizes the RMS responses obtained from the passive and semi-active control systems. From the results listed in Table.6.3 it can be seen that, in terms of the RMS response, the semi-active control system achieves a much better performance than the passive one does.
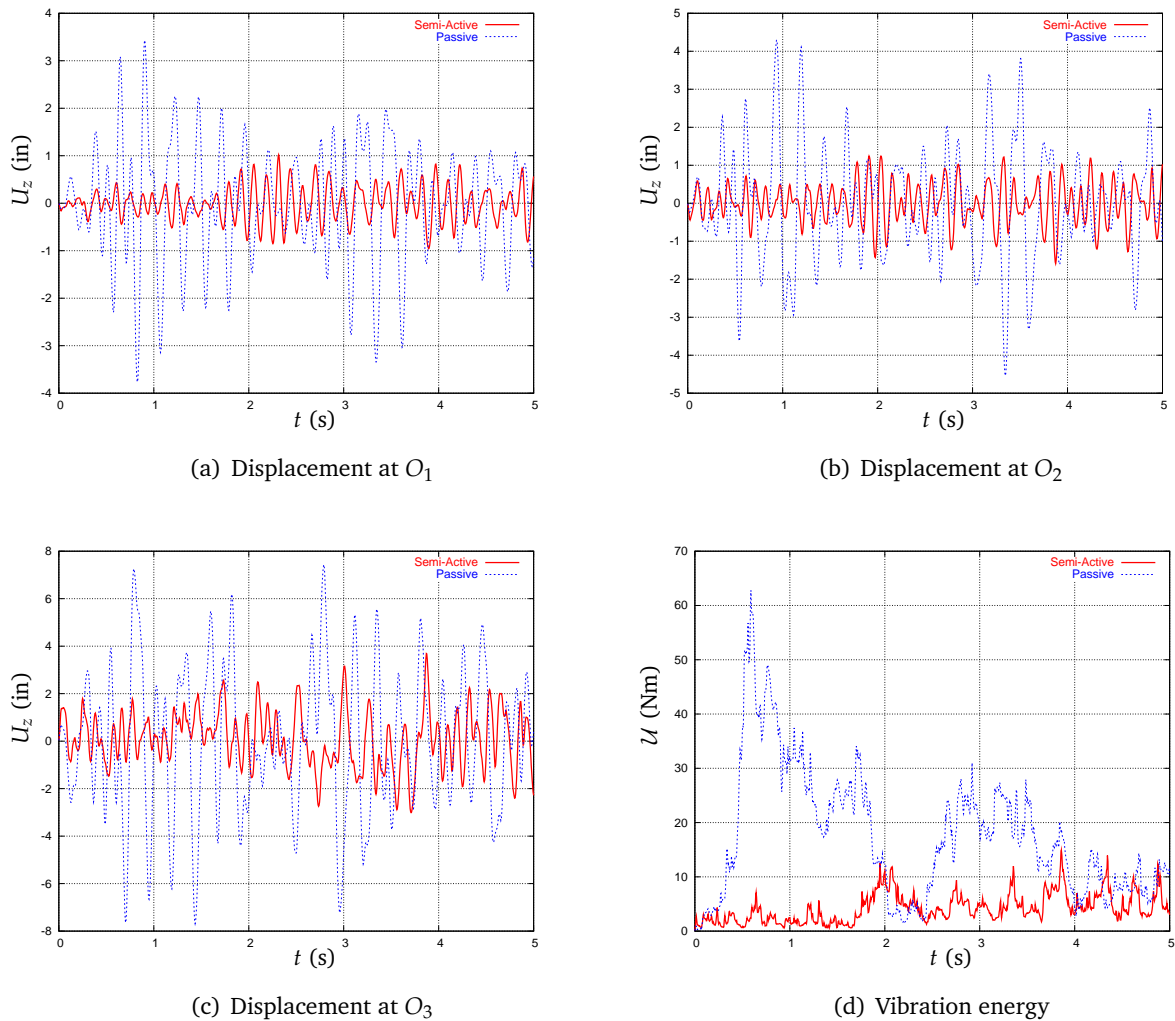
PSfrag replacements

PSfrag replacements

(a) Displacement at O_1

(b) Displacement at O_2

(c) Displacement at O_3

(d) Vibration energy

Figure - 6.15: Respose comparison of the plate with passive and semi-active control using MR dampers (white noise excitation).

6.5 Summary

In this chapter, the hysteretic behavior of a MR damper and the its application to structural vibration control were studied.

First, several existant models used to simulate the nonlinear dynamics of MR damper were briefly introduced and compared. Based on the research and experiments conducted by Spencer Jr. et al. [54], a modified Bouc-Wen MR model was used in this research.

Numerical experiments on the modified Bouc-Wen model showed that the desired hysteretic

Table 6.3: Comparison of the RMS responses

Locations	Passive (in)	Semi-Active (in)	Reduction (%)
O_1	1.19	0.37	69%
O_2	1.44	0.58	60%
O_3	3.11	1.32	58%

behavior of the model was dominated by the variation of the input velocity. Although this characteristic of the model is essential to produce the desired hysteretic behavior, it makes the model extremely sensitive to the noise that exists in the displacement signal. This sensitivity makes the desired hysteretic behavior of the MR model vulnerable to the noise. To improve the numerical robustness of the MR model in dealing with noisy data, the MR model was modified to include a LPF such that the modified MR model can preserve its hysteretic behaviors in various numerical simulations. A simple example verified that this modification improved the numerical stability, and preserved the desired hysteretic behavior of the original MR model.

A Newmark method based iteration technique was suggested to solve the nonlinear differential equations encountered in a structural system with MR dampers. By iterating inside each integration step, an accurate and stable solution can be obtained.

The improved MR model and the proposed solution method were verified through a numerical example, where the vibration control of a plate structure was considered. Simulation results showed that both passive and semi-active control systems using MR dampers were able to effectively attenuate the structure vibration both locally and globally. Compared with the passive control, semi-active control using the clipped-optimal control algorithm was able to achieve a better performance. For the impulse excitation case, the semi-active control system was able to bring the structure to rest more faster than the passive control system. For the white noise excitation, smaller RMS displacement response was achieved by the semi-active control system.

Vibration Control of a Roof Structure

In the previous chapters, some key issues involved in the design of a SVC system for large scale structures using the MR dampers were studied, and the methodologies used to address these issues were developed. In this chapter, these methodologies are used to design a SVC system for an industrial roof structure subjected to wind loading. Through the work presented in this chapter, the methodologies developed in the previous chapters will be further verified by applying them to a large scale structure. From application point of view, this work also has impact on improving the performance and safety of the similar roof structures.

For a roof structure, one of the most commonly encountered structural damages is caused by wind load. Under a stormy weather condition, such as typhoon, hurricanes, etc., strong wind may cause severe damage to roof structures. Although less strong wind may not cause an instant damage to a roof, but the wind-induced structural vibration has potentials to develop fatigue damage to the structural components of the roof, and as a result, reduce the possibility for the roof structure to survive in the coming storms. A SVC system is able to reduce the wind-induced vibration, and as result, reduce the deterioration rate of a roof structure due to fatigue, and improve the life span of the structure.

In this chapter, structural vibration control for an industrial roof structure using MR dampers will be studied by using the methodologies developed in the previous chapters. The FEM model of the roof structure is first built. A transient and a modal analysis are performed on the ob-

tained FEM model, and a critical area, in which larger response appears, on the roof structure is identified. Through an analysis on the wind load data, a wind filter is designed. A passive and a semi-active SVC systems are designed for the roof structure. The performances of the SVC systems are then analyzed and compared.

7.1 Dynamic Response Analysis of Roof Structure

Figure - 7.1 shows a sketch of the real industrial roof structure[1] considered in this study. Each of the fasteners and the clips as shown in the figure represents a fixed support on the roof structure. The weight of roof panel is 1.23 psf (mass density is 0.0009218 lb/in^3). Material properties are the Poisson's ratio $\nu = 0.3$, the elasticity modulus $E = 30000$ ksi, yield stress $\sigma_y = 50$ ksi. A modal damping ratio of 0.005 is assumed.

7.1.1 Wind Load

To determine the distribution of the wind load on the roof under typical territory conditions, a wind tunnel experiment was conducted on a scaled-down roof model by the researchers in the university of Western Ontario[2]. The wind pressures were measured through 714 taps distributed on the test model at a time interval of 0.0299 second. The measurement was lasted for 344.563 seconds.

The wind pressure data used in this research were provided by the FM Global®, and applicable to the real roof structure. Figure - 7.2 shows the locations where the wind presure data were provided. Each rectangular box as shown in the figure represents an area with which the provided data were associated. The number shown inside each box is an index used to identify the data. Figure - 7.3 plots two time histories of the wind pressure corresponding to the locations 1003 and 1207 (denoted in Figure - 7.2 by two dark boxes).

The given wind pressure data are analyzed both in the time domain and the frequency domain. From Figure - 7.3 it can be seen that, in the time domain, the wind pressure at any given location can be viewed as a random process, and therefore, the associated statistical properties,

---

[1]The model of the roof structure and all wind loading data were provided by the FM Global®
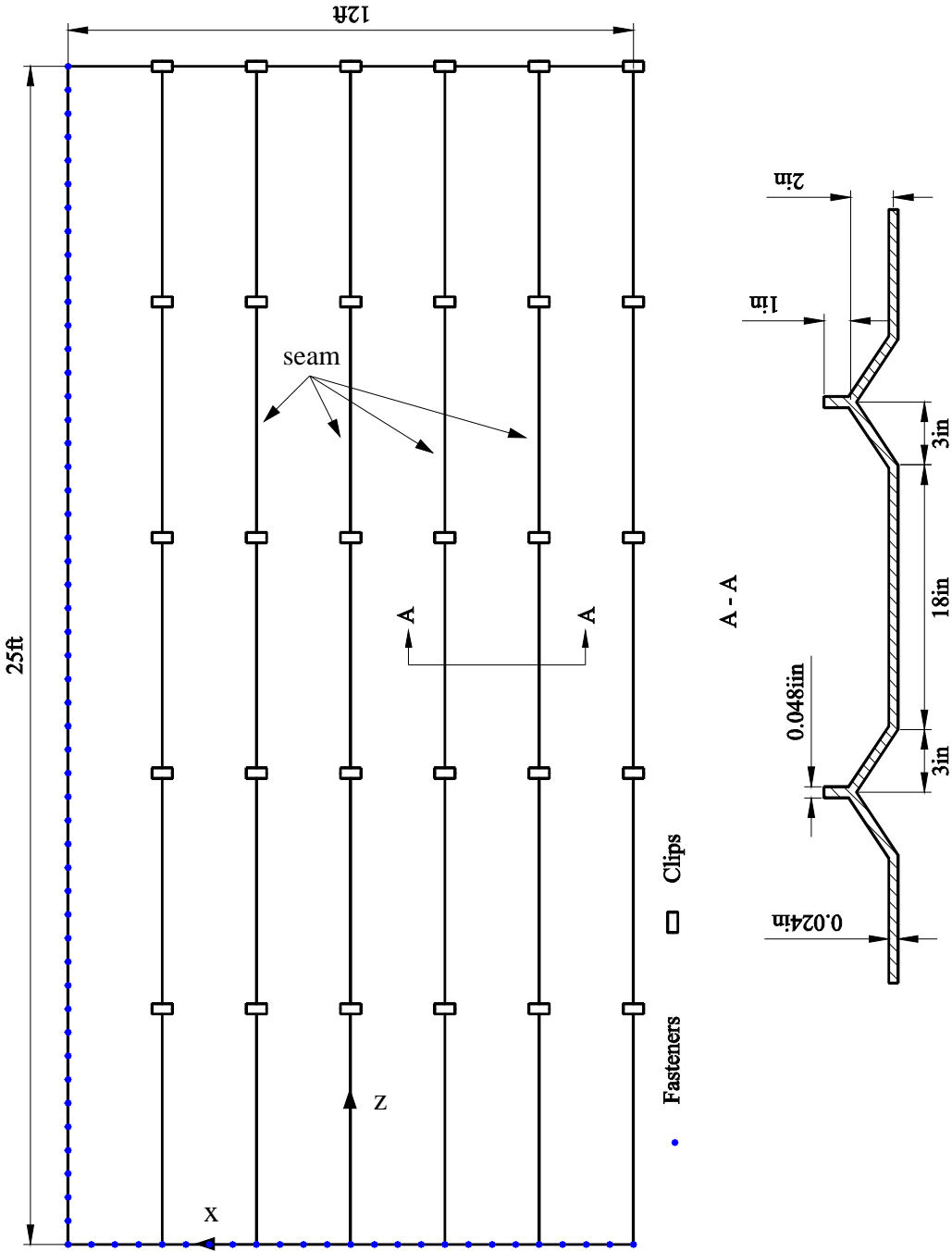
[2]The experiment was sponsored by the FM Global®

Figure - 7.1: An industrial roof structure.

i.e. the mean value and the standard variation, can be obtained. Figure - 7.4 plots the mean and standard deviation of the wind pressure over the whole roof structure.

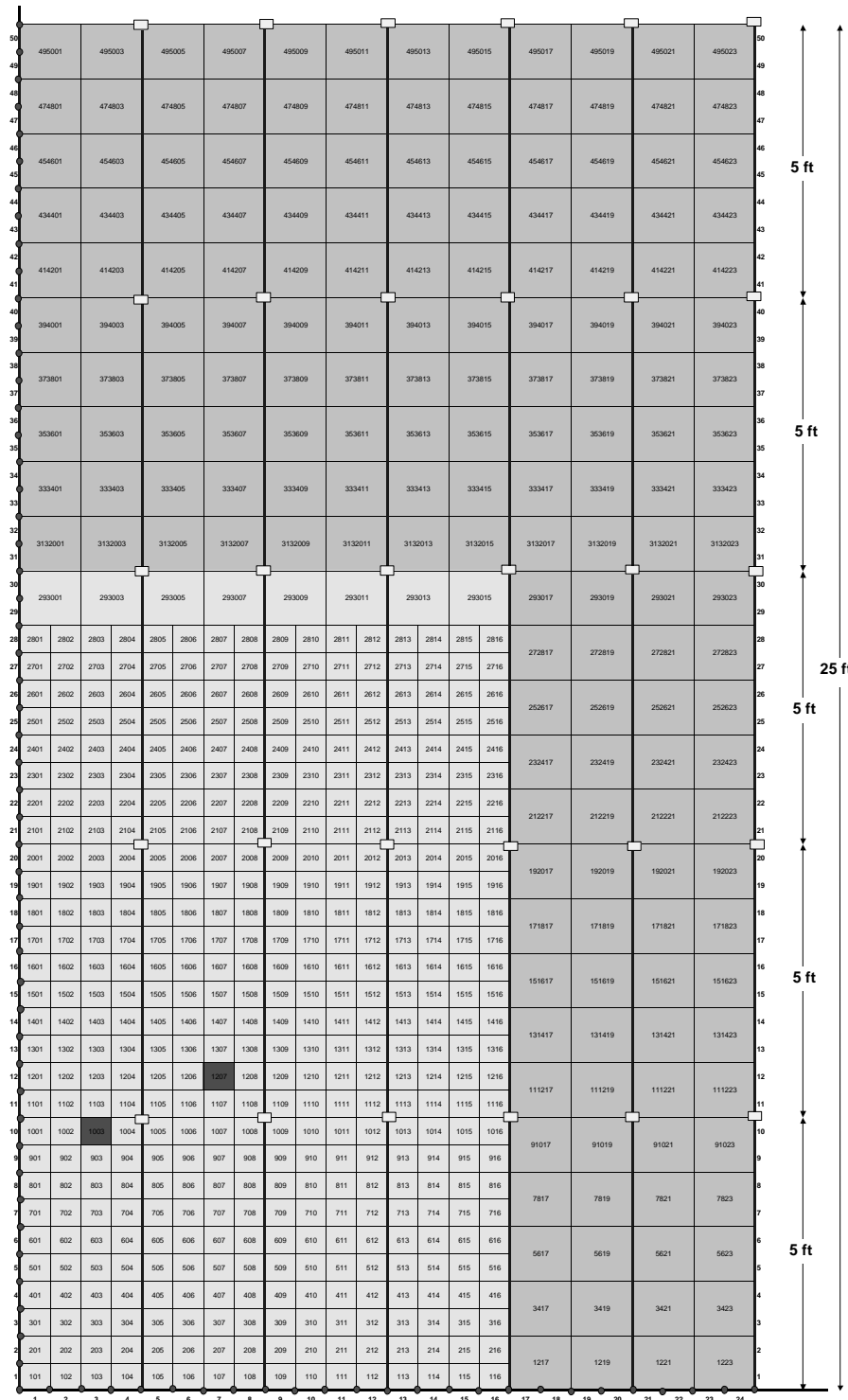Because the wind pressure P at a typical location can be decomposed into a static part P_s

Figure 7.2: Wind tunnel measurement locations on the prototype roof model.
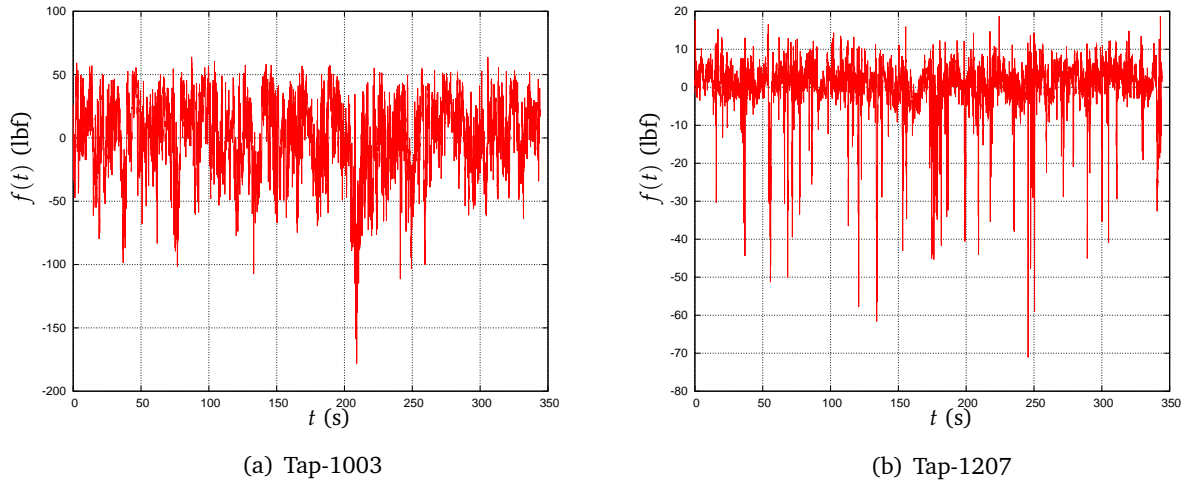
(a) Tap-1003

(b) Tap-1207

Figure - 7.3: Wind loading at the two typical locations on the roof.

and dynamic part P_t with zero mean as follows,

$$P = P_s + P_t. \tag{7.1.1}$$

When the structure is linear, static and dynamic part of the wind loading can be considered separately. The static part of the wind pressue causes a static deformation of the roof structure. In the SVC system design, the main concern is the structural vibration caused by the dynamic part of the wind loads. In the frequency domain, the frequency contents of the wind pressure is of interest in the following analysis. In Figure - 7.5, the spectrum of the wind pressure at a typical location is plotted (solid line). Through a series spectral analyses on the dynamic part of the wind pressure data, it was found that the spectra of the wind pressure given at different locations on the of structure were highly consistent. Therefore, in this study, an upper envelope of the spectra will be used to represent the spectrum of the wind pressure at any given locations. The envelope was shown in Figure - 7.5 by the dashed line. The bump that appears around 10.4 Hz was thought due to the some errors in the raw data. Futhemore, because the magnitudes around the bump are small, this bump will be ignored in the following analysis.

Based on the spectra envelope obtained above, a wind filter is designed for controller design purpose. The filter is able to produce a dynamical output of the same spectrum as the spectra envelope of the wind pressure when excited by a Gaussian white noise. Assume the transfer
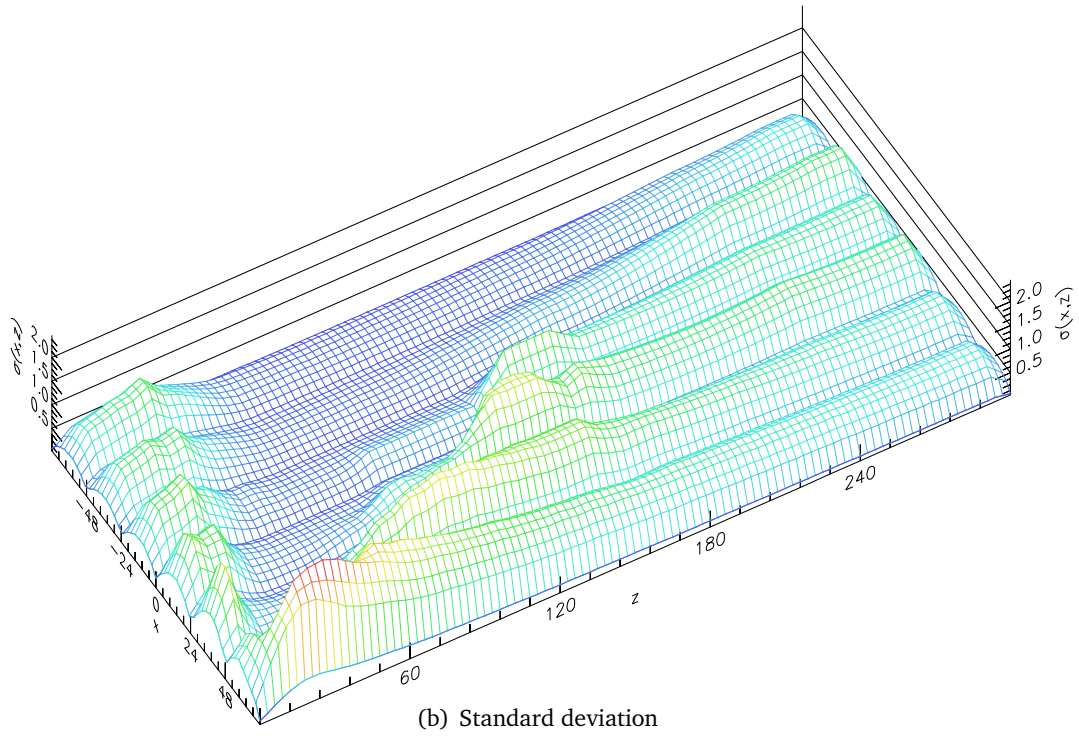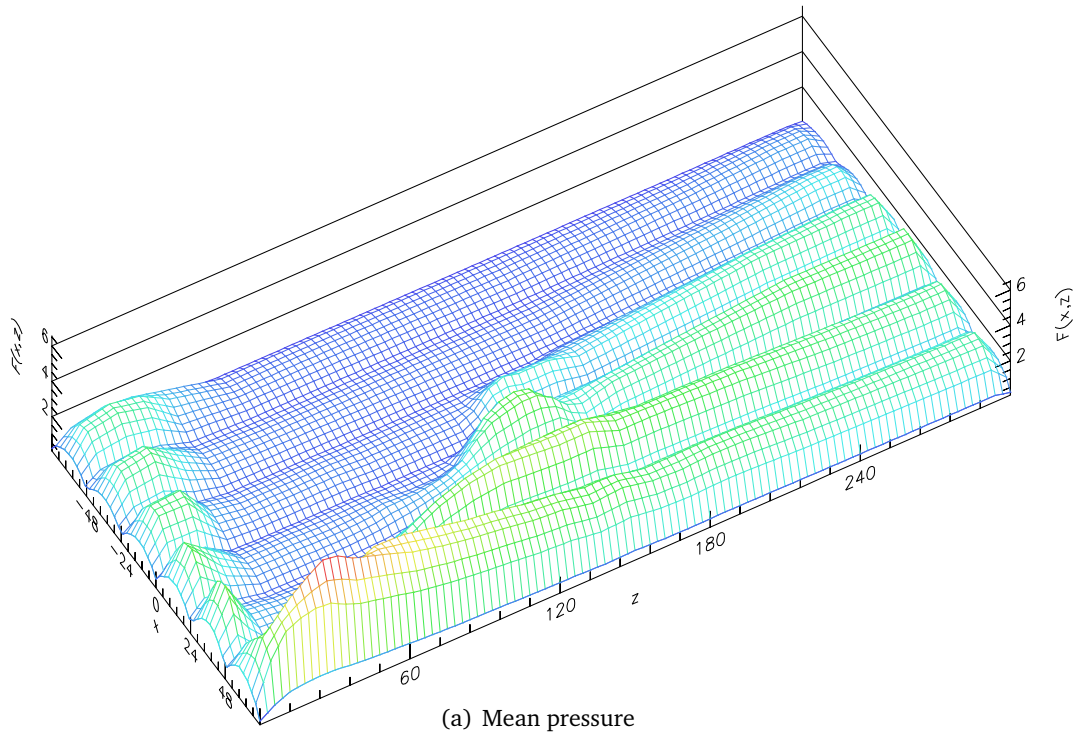
(a) Mean pressure

(b) Standard deviation

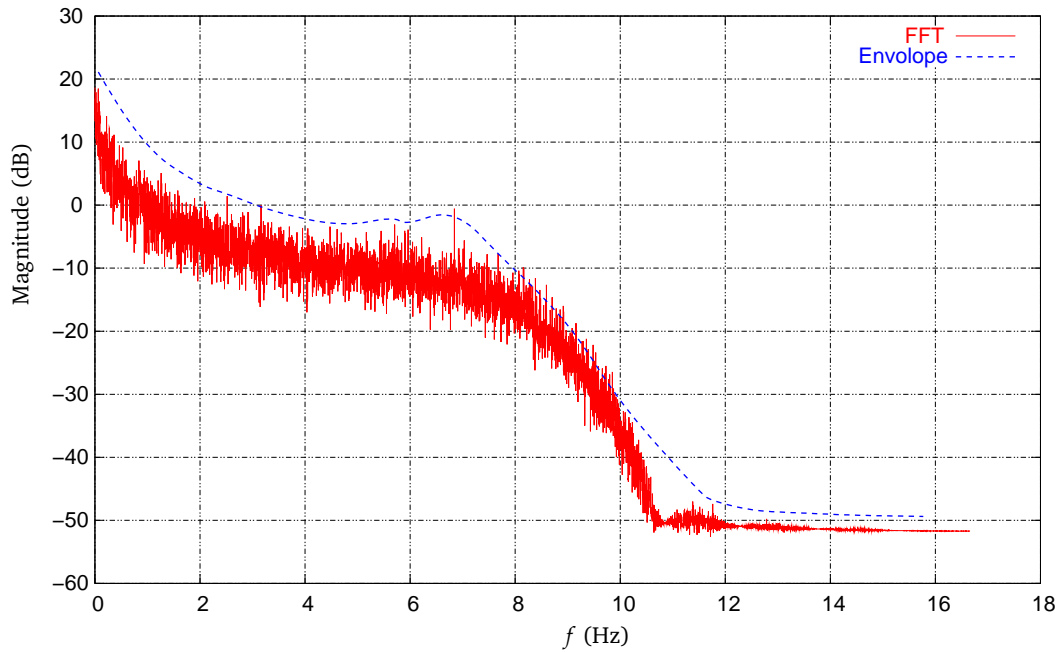Figure - 7.4: Statistical properties of the wind loading.

137

Figure - 7.5: Frequency components of the wind loading. Dashed line shows the envelope obtained from the numerical analysis of the wind data.

function of the filter is of the following form,

$$T_w(s) = \frac{a_0 + a_1 s + a_2 s^2 + \cdots + a_{n-1} s^{n-1}}{b_0 + b_1 s + b_2 s^2 + \cdots + b_n s^n}, \tag{7.1.2}$$

where a_i, $i = 0, 1, \ldots, n-1$, b_i, $i = 0, 1, \ldots, n$ are unknown parameters to be determined. These parameters are determined such that the spectrum of $T_w(s)$ is the best approximation of the wind spectrum envelope as shown in Figure - 7.5. Denote the wind spectrum envelope by $S(f)$, which is a function of frequency f, the wind filter can be found by minimizing the following error index J,

$$J = \| S(f) - |T_w(f)| \|_w, \tag{7.1.3}$$

where $\| \cdot \|_w$ is a norm defined in a frequency interval $[f_1, f_2]$ as follows,

$$\| g(f) \|_w = \int_{f_1}^{f_2} g^2(f) df. \tag{7.1.4}$$

For the problem at hand, f_1 and f_2 are set to 0.07Hz and 10Hz, respectively. To ensure a stable filter, the optimization subject to the following constraints,

$$\mathrm{Re}(\lambda_i) < 0, \quad i = 1, 2, n, \tag{7.1.5}$$

where λ_i is the i-th pole of the filter's transfer function $T_w(s)$. Because the order of the filter is unknown, three cases with $n = 2, 3, 4$ were tried. It was found that the error index J took the minimal value when $n = 3$, and the corresponding optimal wind filter was given by

$$T_w(s) = \frac{-19.27s^2 - 0.5151s + 2.07}{-0.1597s^3 - 1.72s^2 - 1.855s - 0.4117}. \qquad (7.1.6)$$

Figure - 7.6 shows the comparison of the optimal wind filter and the spectrum envelope of the wind loading. It is seen that the obtained filter matches the objective envelope spectrum satis-
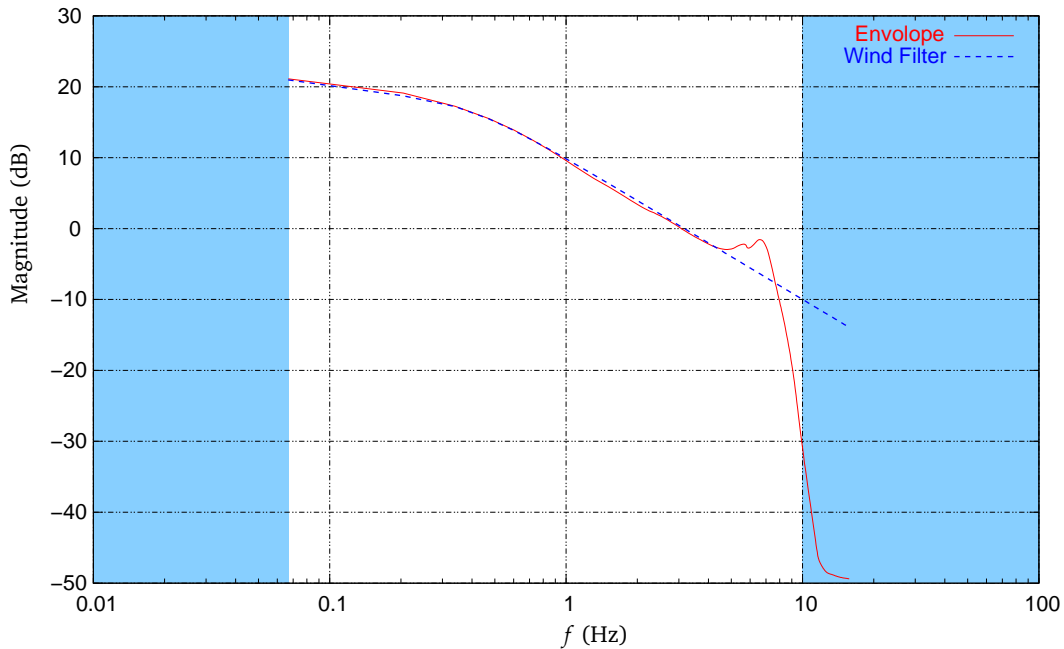
PSfrag replacements

Figure - 7.6: An optimal 3rd order wind filter.

factorily in most part of the frequency band $[0.07, 10]$ Hz. The bump appeared on the spectrum envelope curve at 6Hz was caused by the error that existed in the raw data of the wind pressure, and therefore can be ignored.

The obtained wind filter will be incorporated with the structural model of the roof in the controller design. In the dynamical response analysis presented in the next section, the real wind pressure data will be used.

7.1.2   Response of the Roof to the Wind Excitation

The response of the roof structure subjected to the wind excitation was first studied experimentally[3]. The wind load measured from the wind tunnel test were scaled to drive an array of magnets attached to a 1 : 1 scale roof structure to simulate the response of the structure under the wind loading. In this work, however, the dynamical responses of the roof structure excited by the wind load will be studied numerically through a transient finite element analysis using the commercial software ANSYS®.

To this end, a FEM model was built by discretizing the roof structure using the 8-node shell elements. The FEM model is shown in Figure - 7.7. In this model, there are totally 1850 ele-
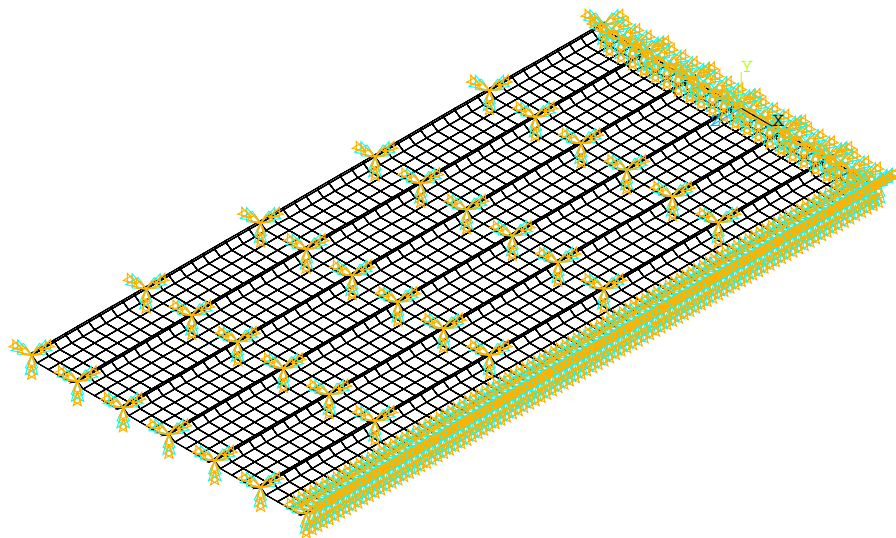

Figure - 7.7: Finite element model of the roof structure.

ments, 5725 nodes and 28625DOF's.

The wind pressure at a given location (as shown in Figure - 7.2) was transformed to the corresponding element of the FEM model as a pressure applied in the y direction, which is defined in Figure - 7.1. Then a full transient analysis was performed with a time step of 0.0299 second, which is same as the sampling resolution of the wind pressure data. The simulation started at 0 second and ended at 344.563 second. Figure - 7.8 gives the y-displacement responses at 2 randomly selected locations on the roof.   Figure - 7.9 gives 6 snap-shoots of the contour plots

---

[3]The experimental study was performed by the researchers in the Mississippi state University
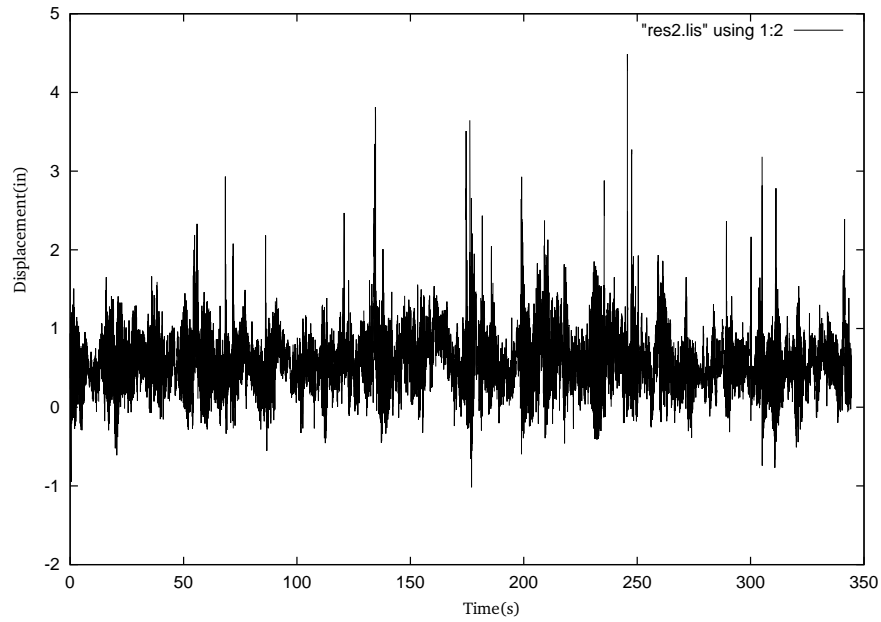
(a) Node 765
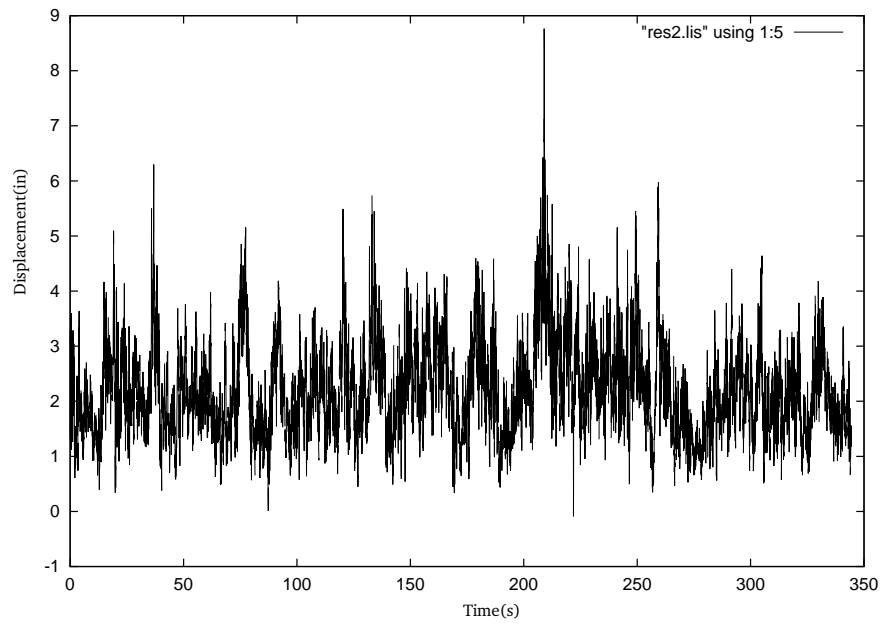
(b) Node 934

Figure -7.8: U_y displacement response at 2 randomly selected locations.

141
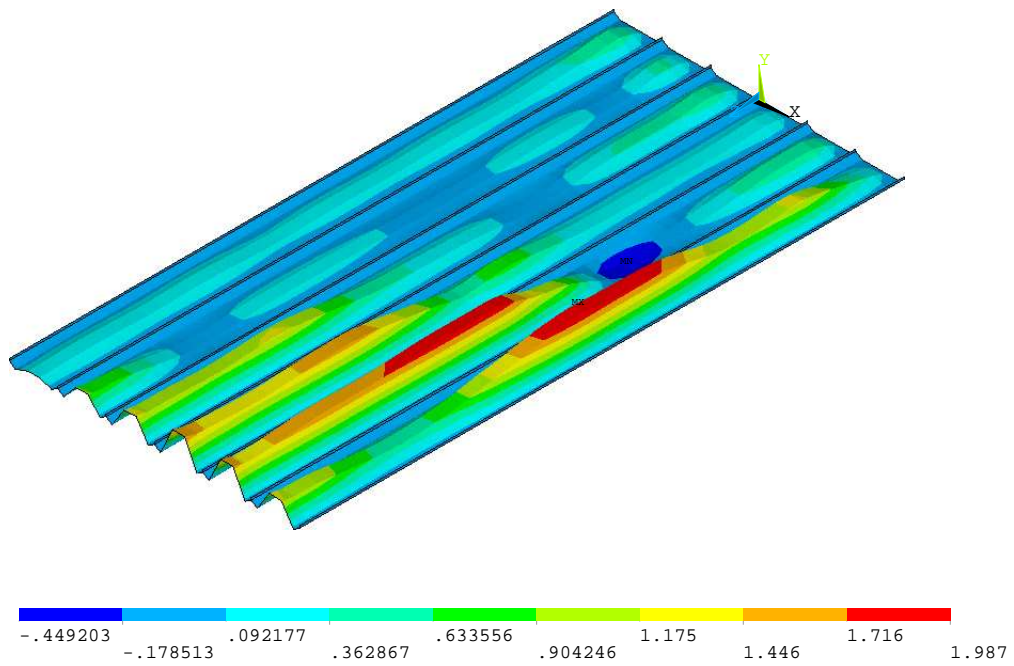
(a) Displacement U_y at time = 20s
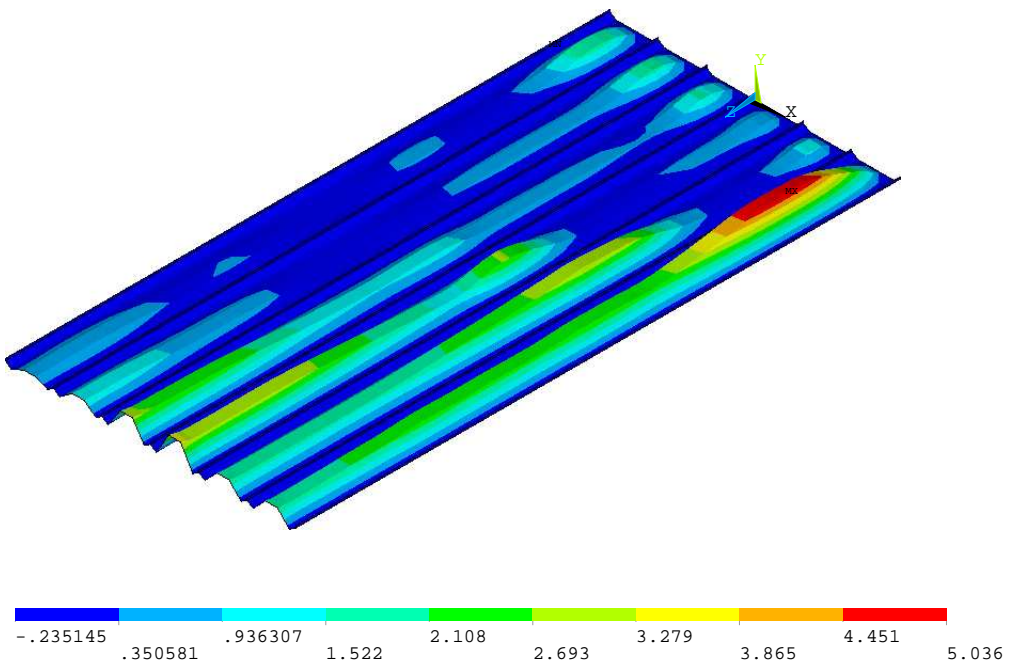
(b) Displacement U_y at time = 50s
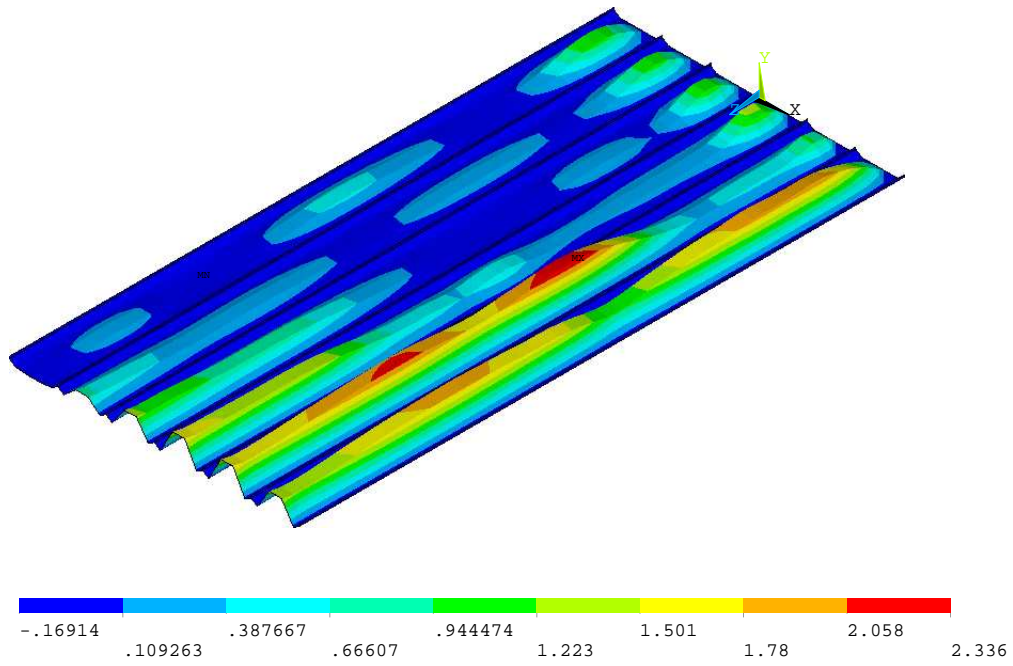
(c) Displacement U_y at time = 100s
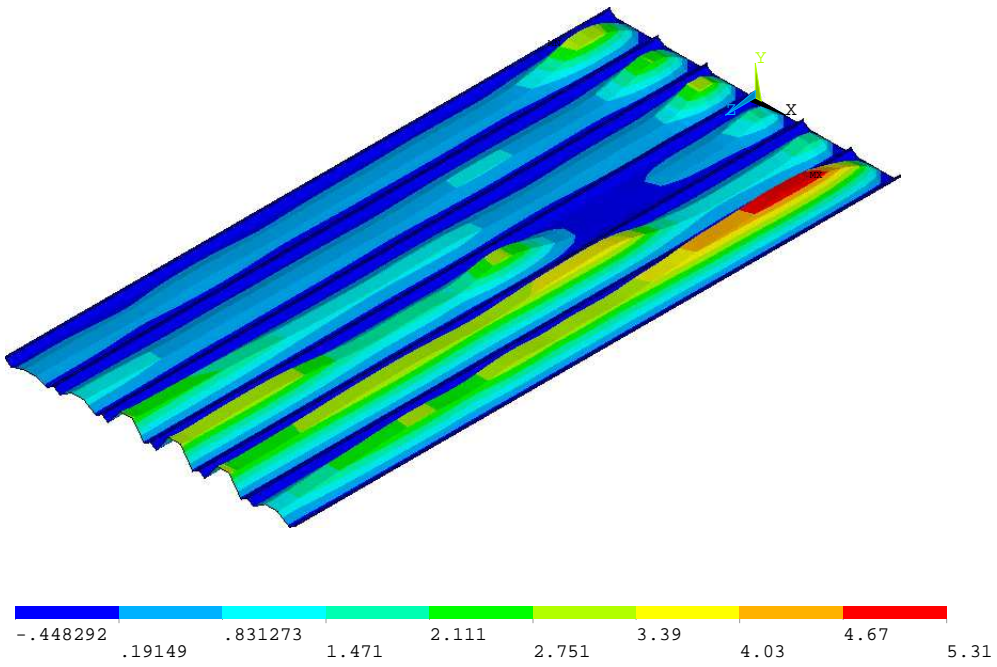
(d) Displacement U_y at time = 150s

143
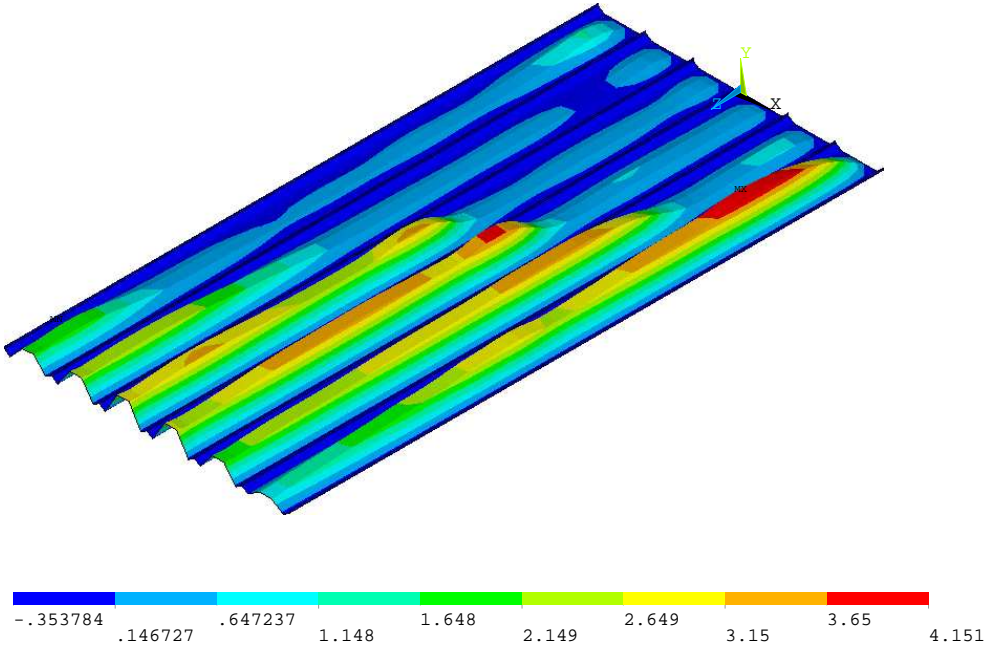
(e) Displacement U_y at time = 250s
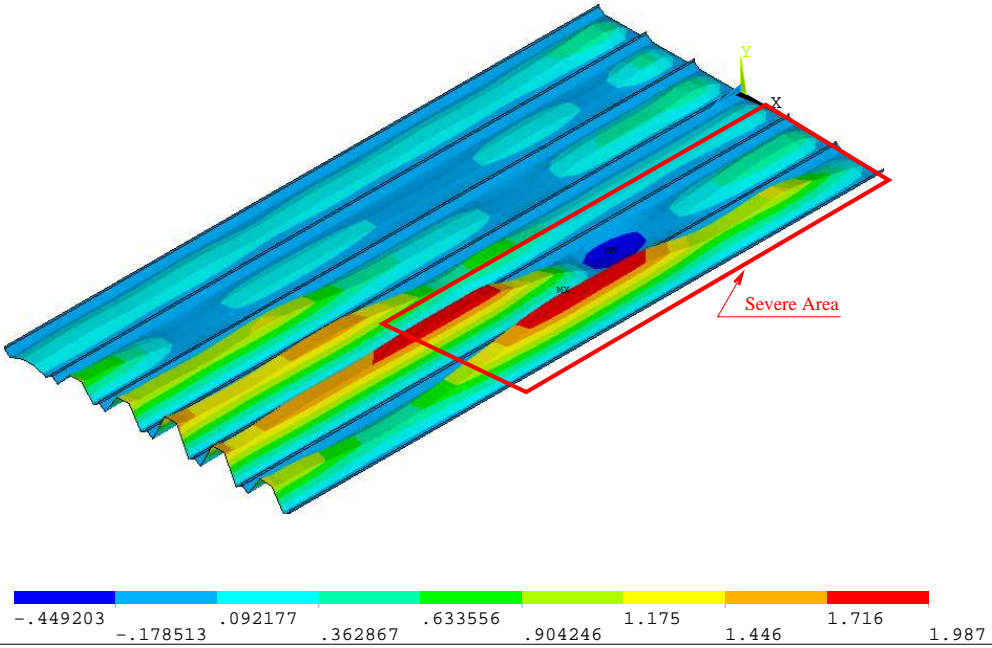
(f) Displacement U_y at time = 340s

Figure-7.9: Snap shots of displacement response (y direction) of the roof structure to the distributed wind loads at some time instants.

of the y displacement taken at $t = 20$, 50, 100, 150, 250, 340 second, respectively.

Through analyzing the obtained transient responses, it was found that a larger average displacement response appeared inside the area defined by $\{(x, z)|24 \leq x \leq 72,\ 0 \leq z \leq 170\}$ on the roof as shown in Figure - 7.9(f). This area is therefore a critical area in which the vibration should be attenuated. The maximum y-displacement response of 13 in also appeared inside this area.

7.2 Modal Analysis of the Roof Structure

To investigate the dynamic characteristics of the roof structure, a modal analysis was performed, and the natural frequencies and the mode shapes of the roof structure were obtained. Figure - 7.10 shows the variation of the natural frequencies of the first 2500 modes. It is observed that
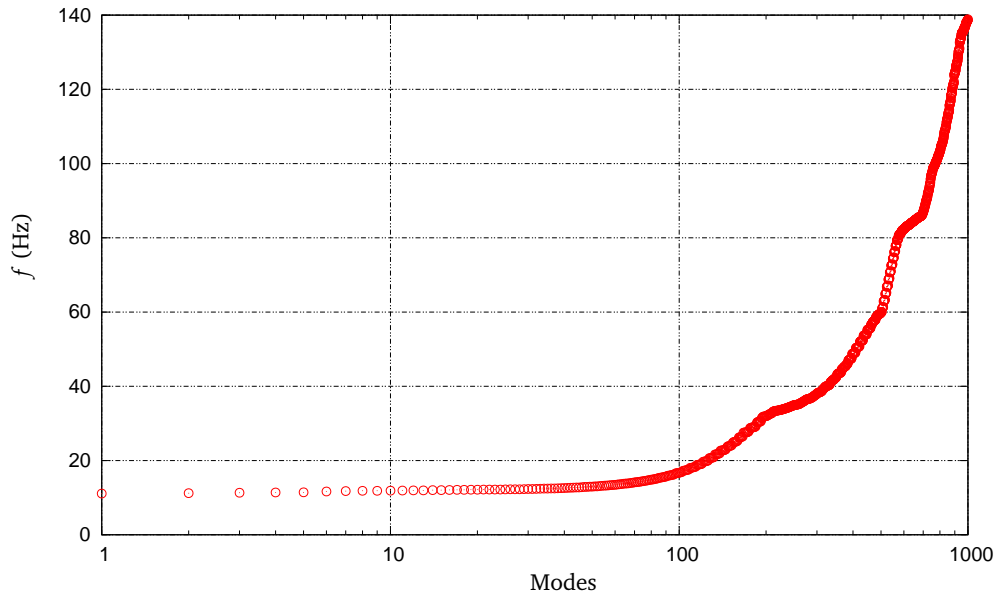
Figure - 7.10: Variation of natural frequencies of the roof structure (Fully constrained case).

the natural frequencies are densely distributed, especially at the lower frequency range. Figure - 7.11 gives the mode shapes of the first 6 modes. These figures reveal another characteristics of the roof structure, i.e. the vibration modes are isolated by the seams along the longer direction of the roof as shown in Figure - 7.1, and each mode can only affect a small part of the roof statue. This is due to the stronger stiffness of the seams (compared to the roof panels between

(a) 1st mode (11.194 Hz)

(b) 2nd mode (11.31 Hz)

(c) 3rd mode (11.413 Hz)

(d) 4th mode (11.492 Hz)

(e) 5th mode (11.534 Hz)

(f) 6th mode (11.88 Hz)

Figure - 7.11: Mode shapes of the first 6 modes of the roof structure.

them) and the supports (i.e. clips as shown in Figure - 7.1) that are uniformly distributed on the seams.

7.3 Modeling of the Roof Structure

In this section, the modeling of the roof structure for the purpose of designing the SVC systems for the roof structure using the MR dampers are studied. The optimal locations of the actuators (i.e. the MR dampers) and sensors will be found using the numerical scheme developed in Chapter 5. The optimal locations of the actuators found in this section will be used in designing both the passive and the semi-active SVC systems that will be discussed later in this chapter.

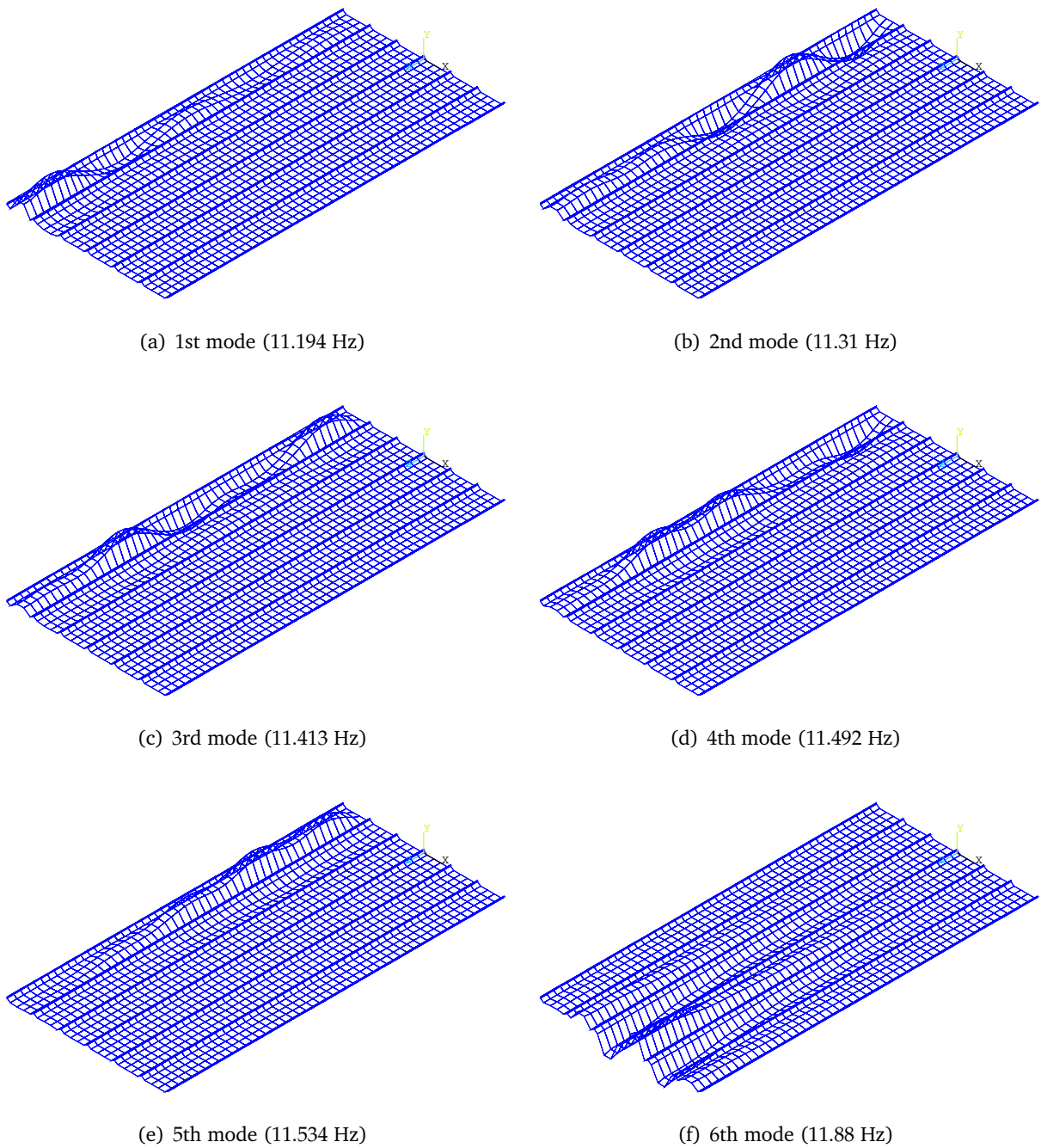From the spectral analysis of the wind pressure, it was observed that most part of the excitation energy were concentrated in a frequency band of $[0.07, 10]$Hz. This observation makes it possible to ignore a lot of the vibration modes in the following design. The 50-th natural frequency of the roof structure is 13 Hz, which is already beyond the frequency band of the excitation, therefore, the first 50 modes are considered adequate to represent the dynamics of the roof structure as involved in the following analysis. The 50-mode model is already a reduced order model for the roof structure, for the verification purpose, however, the model reduction method developed in Chapter 3 will be used to obtain a further reduced ROM that will be used in the semi-active SVC system design.

As pointed out in the previous section, because the vibration modes, especially the first few modes, of the roof structure were found confined within a localized area due to the special natures of the roof structure, it would be very difficult for both a passive and a semi-active SVC systems to achieve an effective vibration reduction over the whole roof structure. Considering the structural vibration inside the critical area are more severe than in other region, both the passive and the semi-active SVC systems will be designed to attenuate the vibration inside this critical area, such that the RMS response would be reduced. The modeling of the roof structure will be discussed with this objective in mind.

7.3.1 Admissible Actuator/Sensor Locations

To find the optimal locations for the sensors and the actuators using the algorithm developed in Chapter 5, a searching space, i.e. admissible locations for placing the sensors and the actuators, has to be found first.

The admissible locations consist of those being able to ensure the controllability and the ob-

servability of the structural system. To avoid an uncontrollable (undetectable) system, locations that are the vibration nodes of the modes being controlled should be excluded from the searching space. Additionally, it is favorable to place an actuator (sensor) at a location where the *modal influence factor*[4] associated to the mode takes the maximum value, because the mode can be controlled (sensed) with a minimum effort by placing an actuator (sensor) at this location. For a structure with multiple modes, it is rare that the best location for a mode is also the best for other modes. Therefore, an index measuring the 'goodness' of a location should be defined to find the admissible locations. This index will be referred as *modal sensitivity index* in sequel. Assume the modal matrix of the roof structure is given by

$$\boldsymbol{\Phi} = \begin{bmatrix} \boldsymbol{\phi}_1 & \boldsymbol{\phi}_2 & \cdots & \boldsymbol{\phi}_k \end{bmatrix} \in \mathbb{R}^{N_n \times k}, \tag{7.3.7}$$

where N_n is the number of DOF's and k is number of the modes considered, $\boldsymbol{\phi}_i \in \mathcal{R}^{N_n}$, $i = 1, \ldots, k$ is the mode shape vector of the i-th mode. $\boldsymbol{\phi}_{ij}$ will be used in the sequel to denote the j-th value of $\boldsymbol{\phi}_i$ vector. It should be noted that the modal matrix given above includes only the DOF's corresponding to the y-displacement. Therefore, N_n is actually the number of the nodes of the FEM model of the roof structure.

Given the above notations, the modal sensitivity index mentioned above is computed as follows:

1. First, the mode shape vectors are normalized by dividing the maximum absolute value of that vector, i.e.

$$\boldsymbol{\phi}_i = \frac{\boldsymbol{\phi}_i}{\max\{s \mid s = |\boldsymbol{\phi}_{ij}|, \ j = 1, 2, \ldots, N_n\}}, \quad i = 1, 2, \ldots, k \tag{7.3.8}$$

2. Compute the number of modes can be sensed at node j, i.e. compute

$$N_j = \sum_{i=1}^{k} H\left(|\boldsymbol{\phi}_{ij}| - \epsilon\right), \tag{7.3.9}$$

where $H(\cdot)$ is the Heaviside function, ϵ is a predefined threshold value such that, location j is a vibration node of the i-th mode if $|\boldsymbol{\phi}_{ji}| < \epsilon$.

---

[4]Referred to the value in a mode shape vector corresponding to certain location.

3. The modal sensitivity index S_j associated with the location j is then defined as

$$S_j = \alpha \sum_{i=1}^{k} |\boldsymbol{\phi}_{ji}| + (1 - \alpha)N_j, \quad j = 1, 2, \ldots, N_n, \tag{7.3.10}$$

where $0 \leq \alpha \leq 1$ is weight coefficient.

From the above definition it can be seen that, if an actuator is placed at a location j, the modal sensitivity index S_j associated with this location is a combined index measuring: ① the number of the modes that can be controlled and, ② how effectively these modes can be controlled at this location. In (7.3.10), the parameter α is used as a weighting factor to make a tradeoff between these two indices. The larger the sensitivity index S_j, the better the location j.

For the roof structure, the searching space consists of the nodes inside the critical area whose nodes indices are specified by the following set,

$$S = \{j \mid N_j > 30, \ S_j > 0.1, \ 1 \leq j \leq n\}. \tag{7.3.11}$$

Figure - 7.12 shows the modal sensitivity indices, number of sensable modes and the positions of the obtained admissible locations obtained by using $k = 50$, $\epsilon = 10^{-4}$ and $\alpha = 0.1$. Inside the critical area, there are 1175 nodes and only 506 of them are admissible according to (7.3.11). Their sensitivity indices varies from 14 to 0.1 (Figure - 7.12(a)). More than 43 modes can be sensed at 70% of the addmissiable locations (see Figure - 7.12(b)). The distribution of these locations is shown in Figure - 7.12(c).

7.3.2 Optimal Locations of Actuators and Sensors

In the previous section, searching space used for solving an OLSA problem has been found. In this section, the optimal locations of 3 actuators and 4 velocity sensors will be found by solving the OLSA problem using the algorithm developed in Chapter 5.

As defined at the beginning of this section, the SVC systems will be designed to reduce the RMS response inside the critical area on the roof structure. In solving the OLSA problem, the spatial $\mathcal{H}_2$ norm of the closed-loop transfer matrix relating the disturbance (i.e. the wind load) to the distributed controlled out (i.e. the displacement response inside the critical area) will be used as the optimization index. Because the closed-loop will be involved in the course of solving the OLSA problem, it is necessary to elaborate a little bit on the controller design.

(a) Modal sensitivity indices

(b) Number of modes sensable at found locations

(c) Distribution of admissible locations
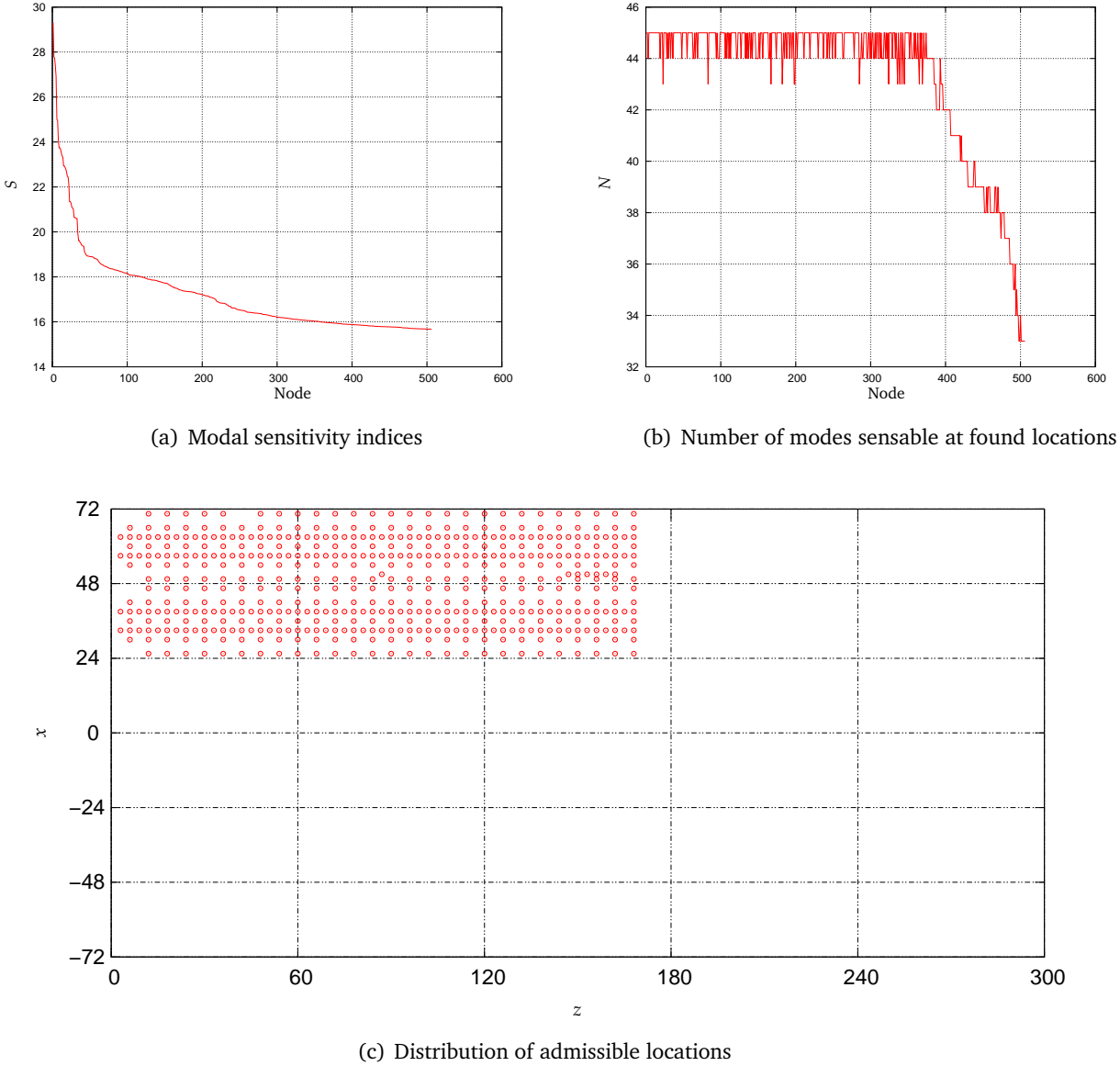
Figure - 7.12: Admissible locations for actuator and sensor placement.

When design a controller for the roof structure, the distributed wind loads are treated as the process noises. It can be shown that these process noises can be modeled as the Gaussian white noises. Through the modal transformation, the distributed wind loads enter the structural system as disturbances applied to each mode. Denote the wind load at node i by $F_w^{(i)}$, $i = 1, 2, \ldots, N_n$ where N_n is the total number of nodes in the FEM model of the roof structure, then

the modal disturbance W_j applied to the j-th mode due to the wind loads is given by

$$W_j(t) = \sum_{i=1}^{N_n} \boldsymbol{\phi}_{ij} F_w^{(i)}, \qquad (7.3.12)$$

where $\boldsymbol{\phi}_{ij}$ denotes the modal influence factor of the j-th mode at node i. By the central limit theorem, W_j has a limiting cumulative distribution function which approaches to a normal distribution. Therefore, the process noises are Gaussian. The variance of the process noises can be found as follows. Assume $F_w^{(1)}, F_w^{(2)}, \ldots, F_w^{(N_n)}(t)$ are independent with each other, i.e.

$$E\{F_w^{(i)} F_w^{(j)}\} = 0 \quad \text{when } i \neq j, \qquad (7.3.13)$$

and each has zero-mean and variance σ_i^2. Then, the variance of the modal disturbance can be calculated as follows,

$$\text{Var}(W_j) = \sum_{i=1}^{N_n} \boldsymbol{\phi}_{ji}^2 \sigma_i^2. \qquad (7.3.14)$$

Using the above relationship and the variance σ_i^2 of the wind load at the node i, the variances of the process noises corresponding to the first 50 modes are obtained and plotted in Figure - 7.13. The obtained variances will be used to construct B_1 matrix used in a $\mathcal{H}_2$ controller design.
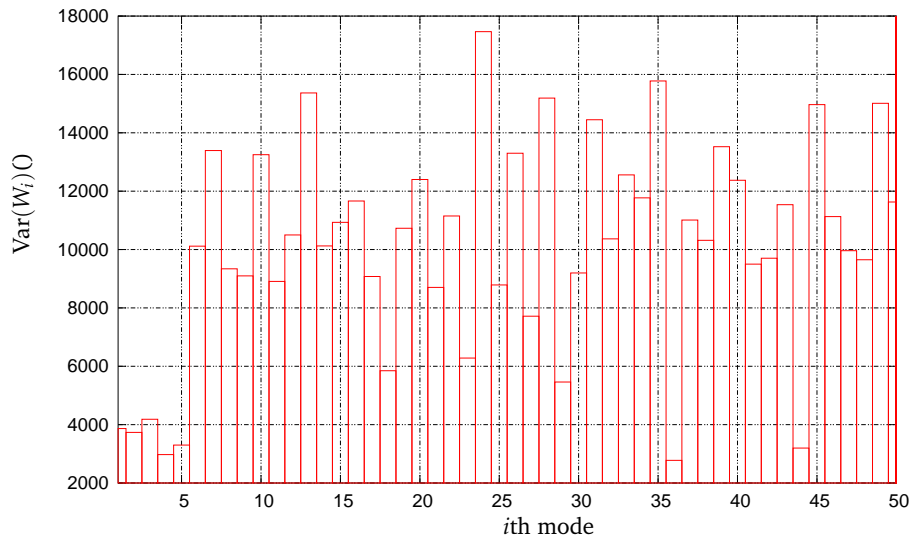

Figure -7.13: Variance of the modal disturbance for the first 50 modes.

Moreover, by incorporating the wind filter given in (7.1.6) in the structural model, the process noises can be treated as the Gaussian white noises. The augmented structural system by including the wind filter is shown in Figure - 7.14, where w denotes the disturbances to the sys-
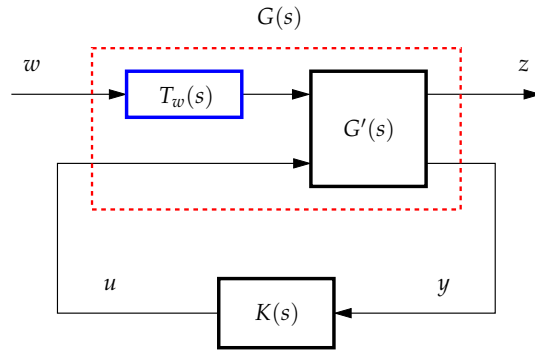
PSfrag replacements

Figure -7.14: Block diagram of the roof structure system.

tem, which includes both the process and measurement noises, z is the controlled output, u and y are control input and sensor output, respectively, $T_w(s)$ is the wind filter given in (7.1.6), $G'(s)$ represents the structure model, which is a ROM constructed from the first 50 modes, $K(s)$ is a controller. By incorporating the wind filter into the structure model, an augmented plant $G(s)$ (denoted by the dashed box in Figure - 7.14) is formed. Assume the original structural system is

$$G'(s) = \left[\begin{array}{c|cc} A' & B'_1 & B'_2 \\ \hline C'_1 & 0 & D'_{12} \\ C'_2 & D'_{21} & 0 \end{array} \right],$$ (7.3.15)

and the realization of the wind filter $T_w(s)$ is given by

$$T_w(s) = \left[\begin{array}{c|c} A_w & B_w \\ \hline C_w & 0 \end{array} \right],$$ (7.3.16)

then the augmented plant $G(s)$ can be written as follows,

$$G(s) = \left[\begin{array}{cc|cc|c} A' & B'_1 C_w & 0 & 0 & B'_2 \\ 0 & A_w & B_w & 0 & 0 \\ \hline C'_1 & 0 & 0 & 0 & I \\ \hline C'_2 & 0 & 0 & I & 0 \end{array} \right] = \left[\begin{array}{c|cc} A & B_1 & B_2 \\ \hline C_1 & 0 & D_{12} \\ C_2 & D_{21} & 0 \end{array} \right].$$ (7.3.17)

Let T_{zw} be the closed-loop transfer matrix relating the disturbance w to the distributed controlled out z, then the OLSA problem is solved with $\langle\!\langle T_{zw} \rangle\!\rangle_2$ being the optimization index.

To solve the OLSA problem, 506 locations in the searching space as shown in Figure - 7.12 are indexed sequentially using integers $1 \sim 506$. Therefore, any member in the searching space
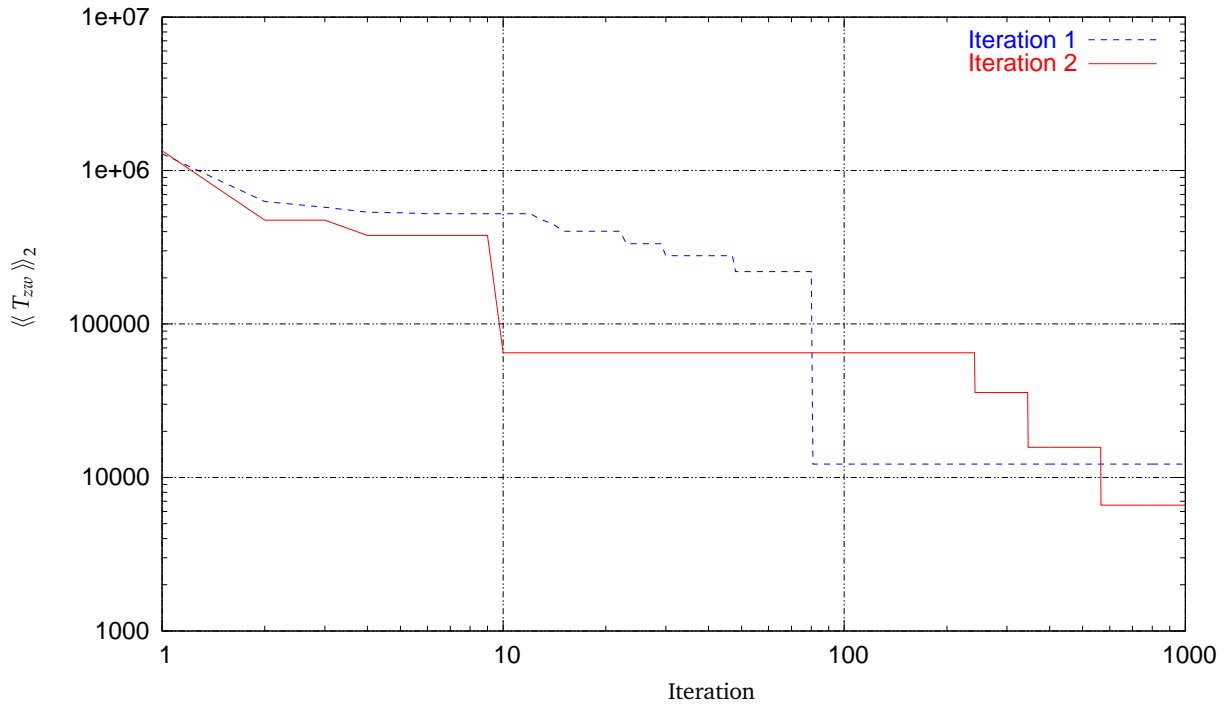
Figure - 7.15: GA iteration history.

can be represented by a chromosome that has a length of 9 bits ($2^8 < 506 < 2^9$) in the GA method. In the GA simulation, the population size of 50, the crossover rate 95% and mutation rate 10% are used. The simulation was runed for 2 times, and both of them were terminated when 1000 iterations have been reached.

Figure - 7.15 shows the variation of the performance index with respect to the iteration steps in the two runs of the GA simulations. The minimal performance index obtained from these simulations was 6592.7. For randomly selected actuator/sensor locations, the typical performance index is in the level of 10^6. Therefore, the the performance of the closed-loop system has been improved significantly. Figure - 7.16 plots the optimal locations for the actuators (denoted by S_i, $i = 1, 2, 3$) and sensors (denoted by O_i, $i = 1, \ldots, 4$). The coordinates of the found optimal locations are listed in the Table. 7.1

7.3.3 Reduced Order Model

As motioned previously, for the roof structure subjected to the wind loads, a ROM constructed from the first 50 modes can reproduce the dynamics of the original structure. For the verifica-
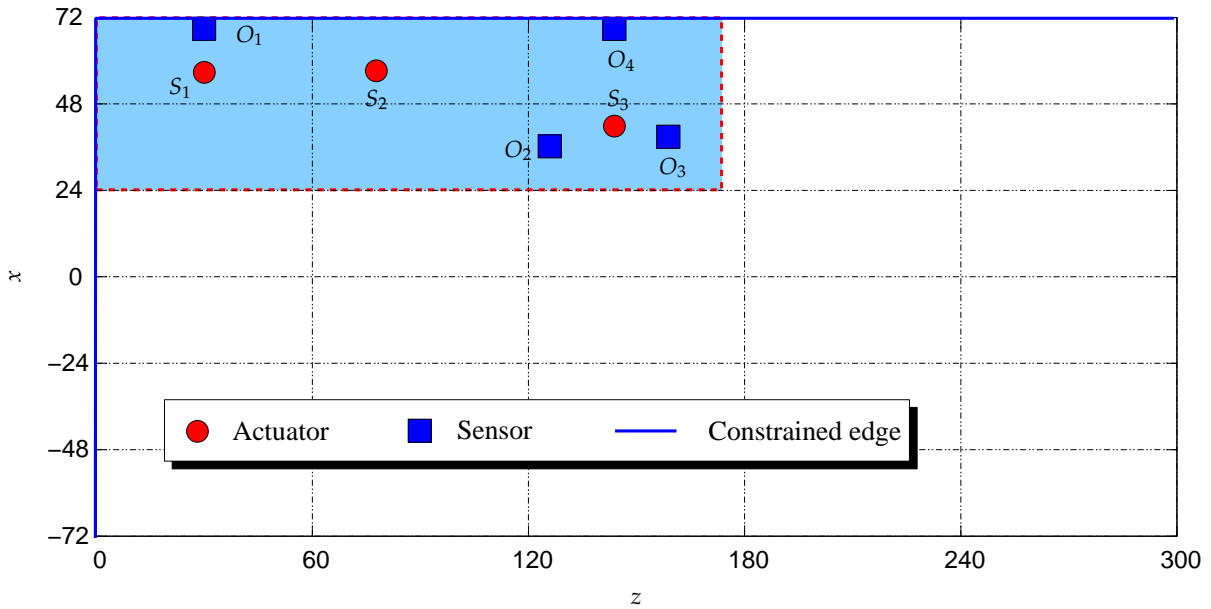
Figure - 7.16: The optimal locations of the actuators/sensors, where the shaded area inside the dashed box denotes the critical area.

Table 7.1: Coordinates of the optimal locations for the actuators and sensors

Actuator/Sensor	Node Index	x (in)	y (in)	z (in)
S_1	912	57	0	30
S_2	2055	57	0	78
S_3	2092	42	0	144
O_1	986	70.5	0	30
O_2	2889	36	0	126
O_3	2910	39	0	159
O_4	3090	70.5	0	144

tion purpose, however, the method developed in Chapter 3 is used here to construct a further reduced ROM containing only the first 20 modes. This lower order ROM will be used to design a controller for the semi-active SVC system. In the sequel, the 50-mode ROM with be denoted

154

by "ROM50", and the 20-mode ROM will be denoted by "ROM20".

In construction of ROM20, the objective dynamics of the structural system is represented by the transfer matrix of ROM50 with the 3 actuators and 4 velocity sensors. The locations of the actuators and sensors are those shown in Figure - 7.16. The objective dynamics used in the model reduction is described by the following 4×3 transfer matrix, i.e.

$$G(s) = \begin{bmatrix} G_{11}(s) & G_{12}(s) & G_{13}(s) \\ G_{21}(s) & G_{22}(s) & G_{23}(s) \\ G_{31}(s) & G_{32}(s) & G_{33}(s) \\ G_{41}(s) & G_{42}(s) & G_{43}(s) \end{bmatrix}, \tag{7.3.18}$$

where $G_{ij}(s)$ ($i = 1, \ldots, 4$ and $j = 1, 2, 3$) denotes the transfer function from the j-th input (i.e. actuators) to the i-th output (i.e. sensors). Each G_{ij} is a summation of the corresponding modal transfer functions of the first 50 modes. ROM20 is found using the method developed in Chapter 3 such that, its transfer matrix is an optimal approximation of $G(s)$ given in (7.3.18) in the sense that the zero shift due to modal truncation is minimized.

Figure - 7.17 plots the frequency response functions of ROM20 (thick solid lines), ROM50 (thick dashed lines) and the 20-mode model (thin dashed lines) obtained from the direct modal truncation. It is seen that the truncation errors in each input-output channel have been significantly reduced. For G_{1i} $i = 1, \ldots, 3$, G_{21} and G_{42} channels, although the original truncation errors were very large, the model reduction method developed in Chapter 3 still can find the transfer functions sufficiently close to the objectives. For the channel G_{21}, the average improvement reaches 45dB. Because the natural frequencies of the roof structure are densely distributed, there is only one notable peak appears in the transfer function curves shown in Figure - 7.17. It should be noted that, although the zero shift can not be observed in these curves, the model reduction method developed in Chapter 3 is still able to reduce the errors due to the modal truncation. The effectiveness of the method is therefore further verified on the roof structure.

7.4   Passive Control Using MR Damper

In this section, a passive SVC system using 3 MR dampers is designed. The locations of these MR dampers were obtained in section 7.3.2. To check the effect of the MR dampers on reducing
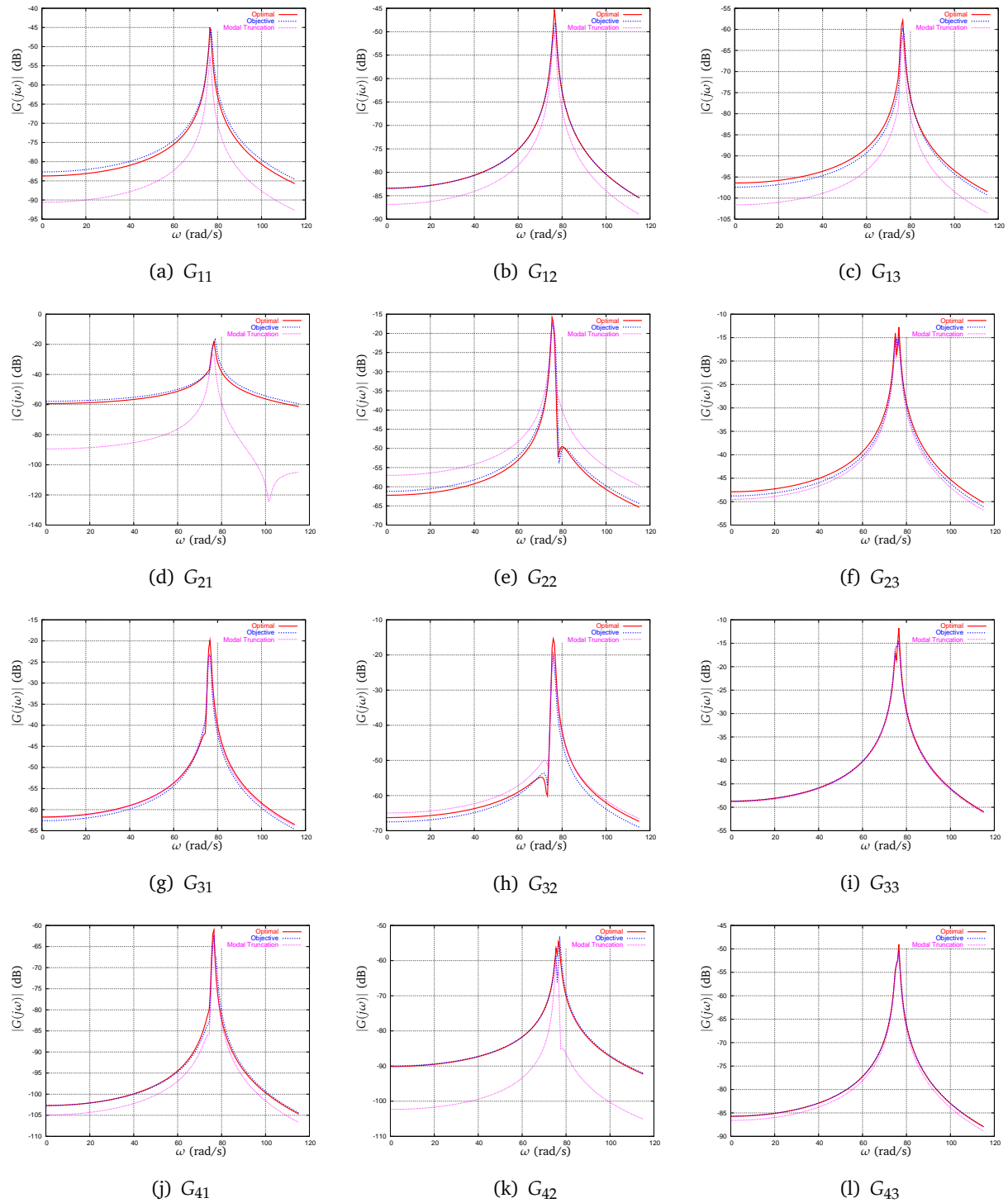
(a) G_{11}

(b) G_{12}

(c) G_{13}

(d) G_{21}

(e) G_{22}

(f) G_{23}

(g) G_{31}

(h) G_{32}

(i) G_{33}

(j) G_{41}

(k) G_{42}

(l) G_{43}

Figure -7.17: The Optimal reduced order model of the roof structure.

the responses, four locations (denoted by p_i, $i = 1, \ldots, 4$) as shown in Figure - 7.18 are selected to read the displacement responses.
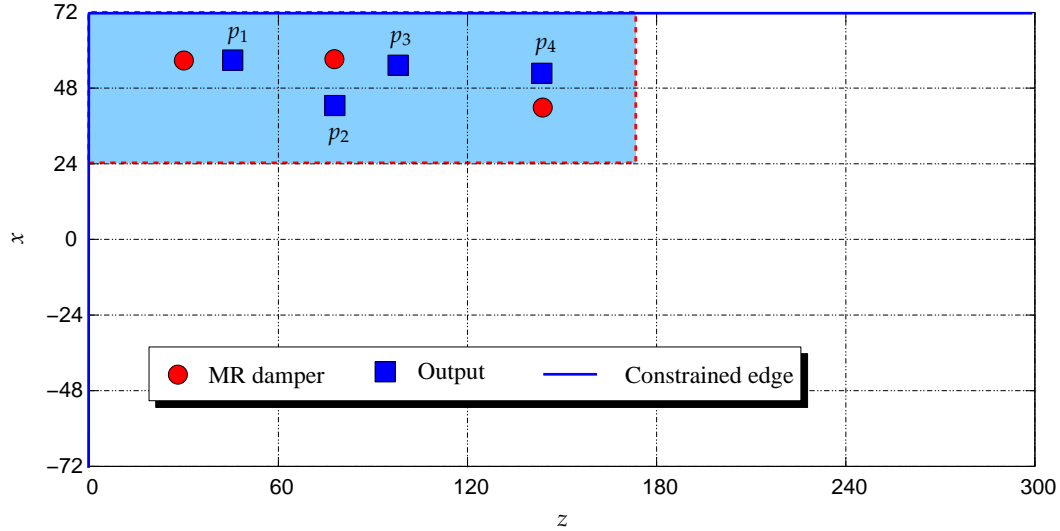

Figure - 7.18: Locations of the MR dampers and outputs on the roof structure.

In the simulation, ROM50 is used to represent the roof structure. Because the real wind loads are used, the wind filter is not used in this simulation. The voltages applied to the MR dampers are 0.5 V and kept constants throughout the simulation. The MR forces are calculated based on the parameters defined in Table. 6.1. As explained in section 6.4, the obtained MR forces are scaled-down by a factor in order to match the local stiffness of the structure to which the MR dampers are attached. If a MR damper is too stiff for a structure, i.e. the MR damping force is too big compared with the (local) stiffness of the structure, it would behave more like a support instead of a damper, which it is supposed to be, and as a result, the damping effects of the MR damper is compromised. In this simulation, a scale factor of 0.05 is used for each of the MR dampers.

The simulation starts at 0 second and is terminated at 10 second. The wind load is applied to the structure between $t = 0$ s and $t = 3$ s, such that both the responses of the forced vibration and the free vibration can be obtained. If assume that the wind loads are stationary random processes, the RMS response obtained from the period of the first 3 seconds is adequate to represent that would be obtained from a simulation lasting for 300 seconds. Figure - 7.19 shows the comparison of the displacement responses measured at p_1, p_2, p_3 and p_4 locations

157

(see Figure - 7.18). From the results shown in the figure, it is seen that at a location close to the

(a) Transverse displacement at p_1

(b) Transverse displacement at p_2

(c) Transverse displacement at p_3
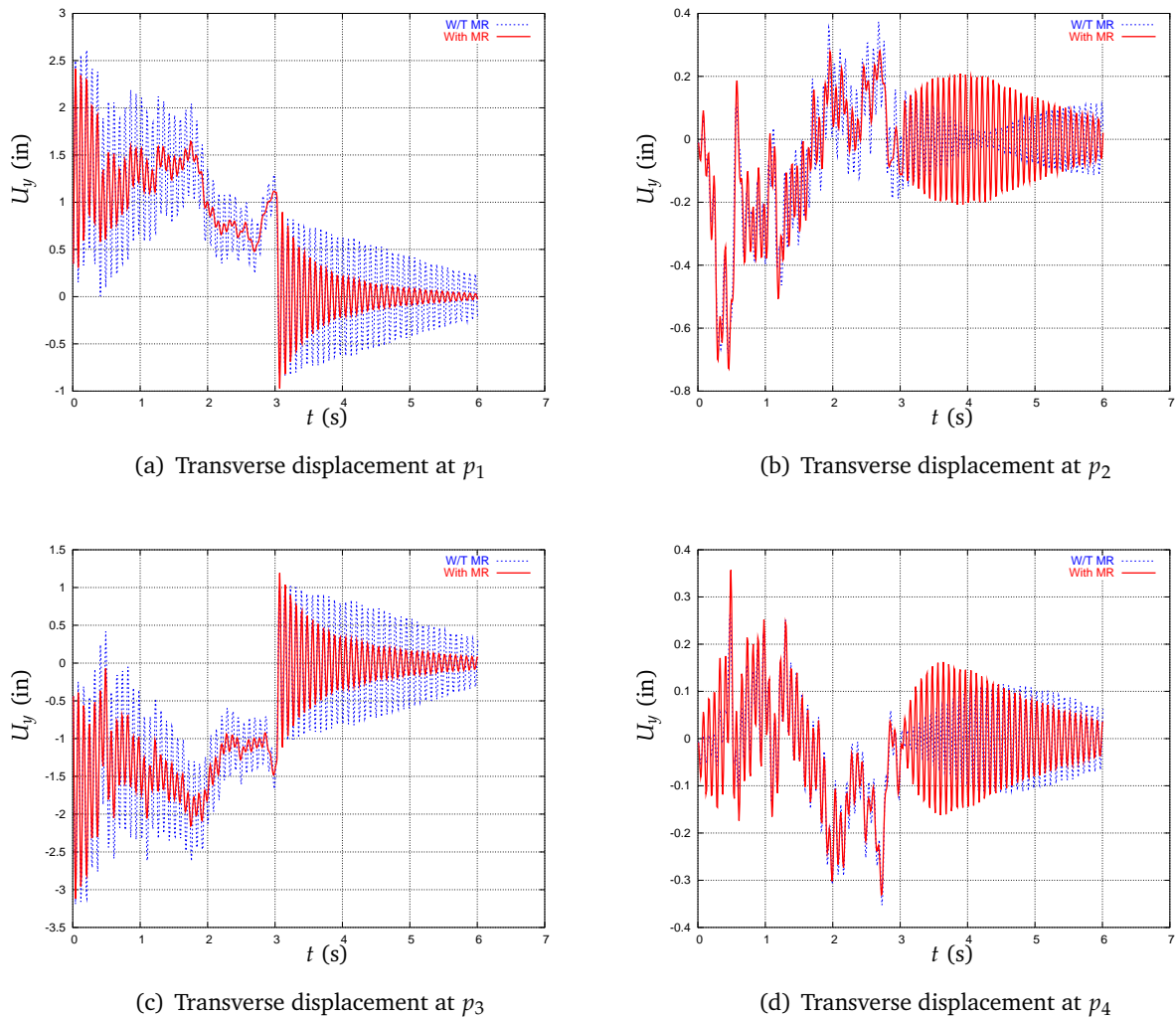
(d) Transverse displacement at p_4

Figure - 7.19: Comparison of the displacement responses at 4 randomly picked locations. Dashed line for the case without MR dampers, solid line for the case with MR dampers.

MR dampers, such as p_1 or p_3, the displacement responses of both the forced vibration ($t \leq 3$ s) and free vibration ($t > 3$ s) were reduced consistently. The maximum reduction factor of the displacement response varies between $2 - 3$ times as shown in Figure - 7.19(a)(c). While for the locations p_2 and p_4, which are separated from the MR dampers by a seam, the response reduction was barely observed as shown in Figure - 7.19(b)(d). From the previous modal analysis,

it was observed that the vibration modes of the roof structure are isolated by the seams on the roof. This is due to the presence of the relatively strong seams and the supports on these reams. Compared with these reams, the roof panels between the two adjacent seams are much softer. Therefore, most of the flexible modes can only be observed in the areas between the reams. As a result, any vibration control efforts can only have a limited influence area. This explains the results observed in Figure - 7.19(b)(d).

For the whole structure, the effect of the passive vibration control using the MR dampers can be evaluated by the vibration energy. Figure - 7.20 shows the vibration energies of the roof structure with and without the MR dampers. It is seen that, the vibration energy of the system
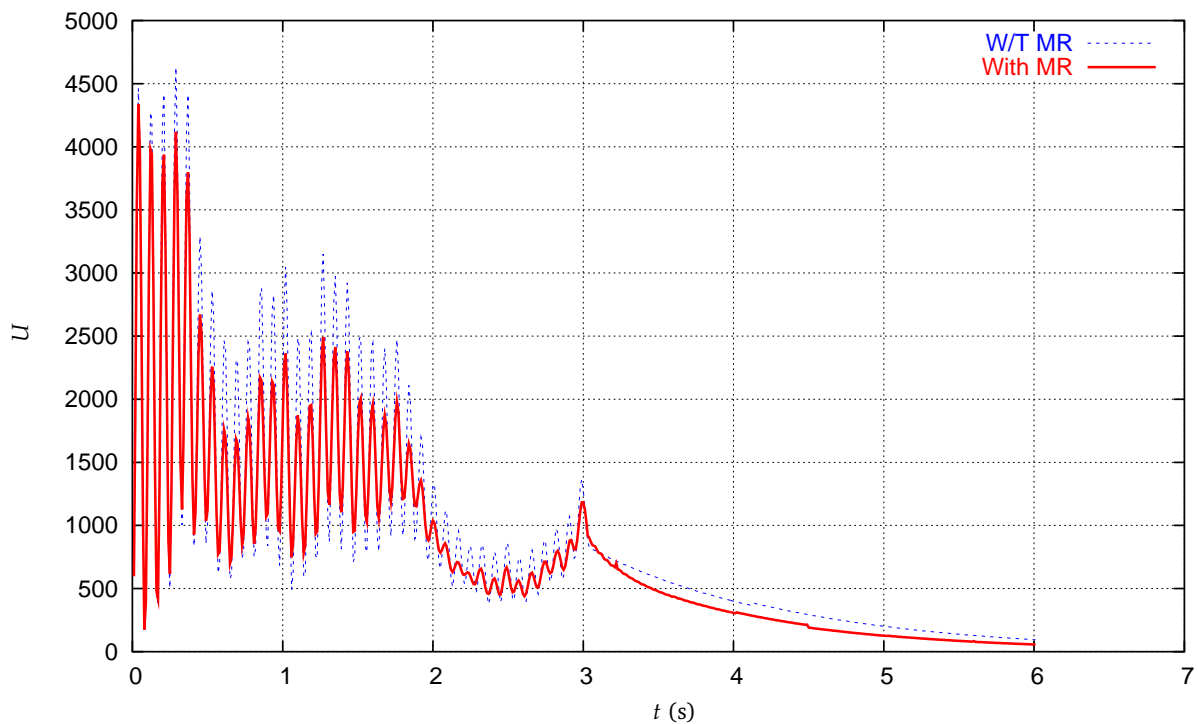

Figure - 7.20: Comparison of the vibration energy for the cases with and w/t MR dampers.

is dissipated by the MR dampers. When the MR dampers are used, the decay of the vibration energy is faster than the case without MR dampers. Although the influence of the MR dampers

are limited to local area due to the special configuration of the roof structure, from the energy point of view, usage of MR dampers does help in reducing the structural vibration.

Figure - 7.21 shows the contour plots of a *normalized RMS response* obtained from the two cases, i.e. without MR dampers and with MR dampers. The normalized RMS response at a location on the roof is obtained by dividing the RMS response at this location by the maximal RMS response found on the whole roof in the first case (without MR damper). Therefore, the value read from the contour plots is actually a non-dimensional ratio, not a real RMS response, but for a concise statement sake, *normalized RMS response* is used to refer this ratio. Because a limited number of MR dampers were used inside the critical area, the effect of the MR dampers may not be clearly seen from these plots.

To evaluate the effect of the MR dampers, an averaged index are defined for the critical area and the region outside of the critical area. The averaged index of an area is obtained by an algebraic averag on all the normalized RMS responses calculated inside the area. Using the index defined above, the effect of the MR dampers can be evaluated quantitatively for an region of interst. Table. 7.2 compares the averaged indices of the critical area and the other part on the roof. It can be seen that, outside the critical area, the average reduction of the RMS response is

Table 7.2: Comparison of average normalized RMS responses.

Region	Without MR Dampers	With MR Dampers	Reduction
Outside the Critical Area	0.1291	0.1179	8%
Inside the Critical Area	0.1114	0.0944	18%

8% as compared 18% reduction inside the critical area. Because the special nature of the roof structure as observed in the modal analysis, and the limited number of the MR dampers, the absolute reduction on the roof structure's response due to the usage of the MR dampers is not as good as it was obtained on the plate structure used in the previous chapter. The effect of the MR dampers on reducing the vibration would be more clearly exemplified or observed by changing the roof structure design such that the influence area of a vibration mode can cover a larger potion of the roof.
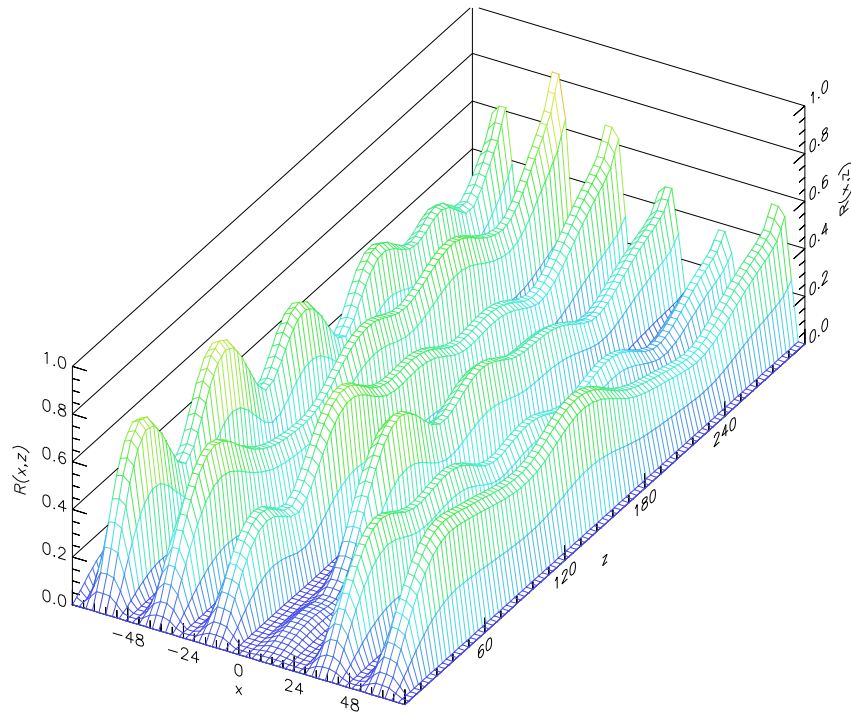
(a) Without MR dampers
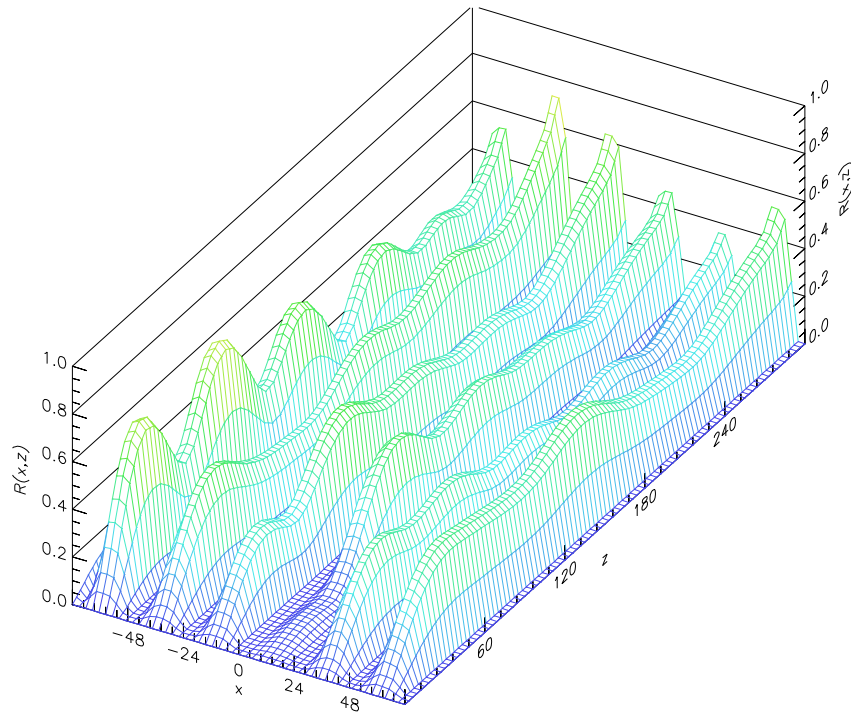
(b) With MR dampers

Figure -7.21: Normalized RMS response of the roof structure.

161

7.5 Semi-Active control Using MR Damper

Using the reduced order model ROM20 obtained in section 7.3.3, a semi-active SVC system using a spatial $\mathcal{H}_2$ controller is designed to attenuate the structural vibration inside the critical area. The controller is designed with the 3 MR actuators and 4 velocity sensors that are placed at the locations found in section 7.3.2. The locations of the MR dampers, sensors and the 4 outputs (denoted by p_i, $i = 1, \ldots, 4$) are shown in Figure - 7.22.
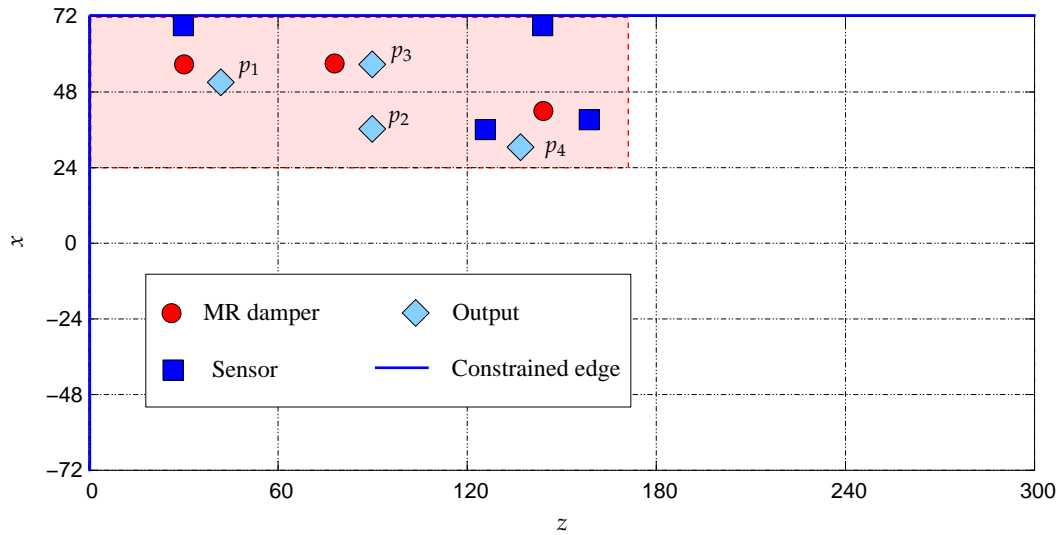

Figure - 7.22: Locations of MR dampers and outputs on the roof structure.

To analyze the performance of the obtained semi-active SVC system, the spatial $\mathcal{H}_2$ controller is used to ROM50, and the closed-loop system is simulated. The excitation used in this simulation is same as that was used in the previous section, i.e. the distributed wind load are applied to the roof structure during the time interval of $0 \leq t \leq 3$ second. Figure - 7.23 compares the displacement responses of the passive and the semi-active SVC systems at the 4 output locations. In this figure, the dashed and solid lines denote the responses obtained from the passive and the semi-active SVC systems, respectively. It is observed that except at the location p_4, almost same responses between the passive and the semi-active SVC systems are observed at other three locations.

Using the response obtained from the semi-active system in the time interval of $[0, 3]$s, the averaged RMS response (as defined in section 7.4) inside the critical area obtained from the

(a) Transverse displacement at p_1

(b) Transverse displacement at p_2

(c) Transverse displacement at p_3
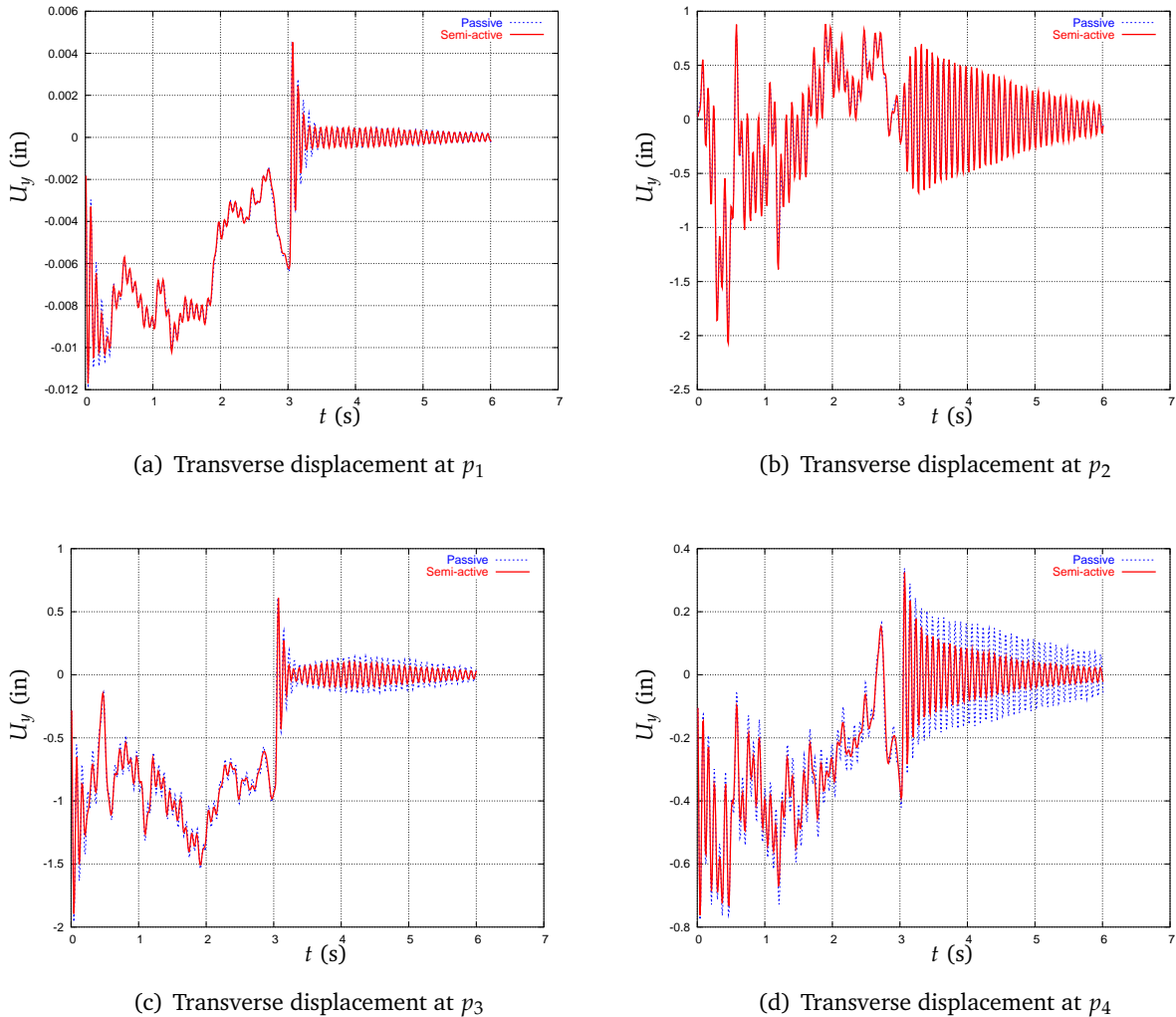

(d) Transverse displacement at p_4

Figure - 7.23: Comparison of the displacement responses of the passive and the semi-active SVC systems.

semi-active system are calculated. Table. 7.3 compares the average normalized RMS responses reduction between passive and semi-active control. The results show that the semi-active control using the MR dampers has the limited advantage over the passive control in reducing the RMS response inside the critical area.

The results observed above does not agree with that obtained in the previous chapter. This disagreement was due to the special characteristics of the roof structure as revealed through the modal analysis. Due to the stiffness difference between the seams and the roof planels, the mode

Table 7.3: Comparison of the averaged RMS responses reduction between the passive and semi-active SVC systems.

Location	Passive Control	Semi-active Control	Reduction
Outside Critical Area	0.1179	0.1179	0%
Inside Critical Area	0.0944	0.0907	4%

shapes of the roof structure were isolated with each other by the seams. Because the interior supports distributed on the seams make the stiffness difference even bigger, it is getting more difficult for a control system to achieve a global vibration reduction. As a result, the advantage of a semi-active control system that would be observed otherwise is compromised.

7.6 Less Constrained Roof Structure

To verify that it is the special characteristics of the roof structure be responsible for the limited performance improvement of the semi-active SVC system, in this chapter, a passive and a semi-active SVC systems for a less constrained roof structure are designed and analyzed. The less constrained roof structure is obtained by removing all the interior supprots originally distributed on the seams. By removing these supports, the stiffness difference between the seams and the roof panels is reduced, and the isolation level of the mode shapes will be lowered correspondingly. It is expected that the characteristics of thus modified roof structure allow a more effective vibration reduction using a semi-active SVC system.

First, the modal analysis is performed on the modified roof structure. Figure - 7.24 gives the mode shapes of the first 6 modes. It is seen that the area affected by a mode is expanded significantly, at least for the first 6 modes as shown in the figure. This change is favorable to improve the efficiency of a control system. The natural frequencies of the first 1000 modes are plotted in Figure - 7.25. By removing the interior supprots, the stiffness of the structure is reduced. As a result, the first natural frequency drops to 4.38 Hz, and the first 15 modes move into the frequency band of the wind excitation. These 15 modes should be considered in the design and analysis of control system. In this case, the roof structure is represented by its first
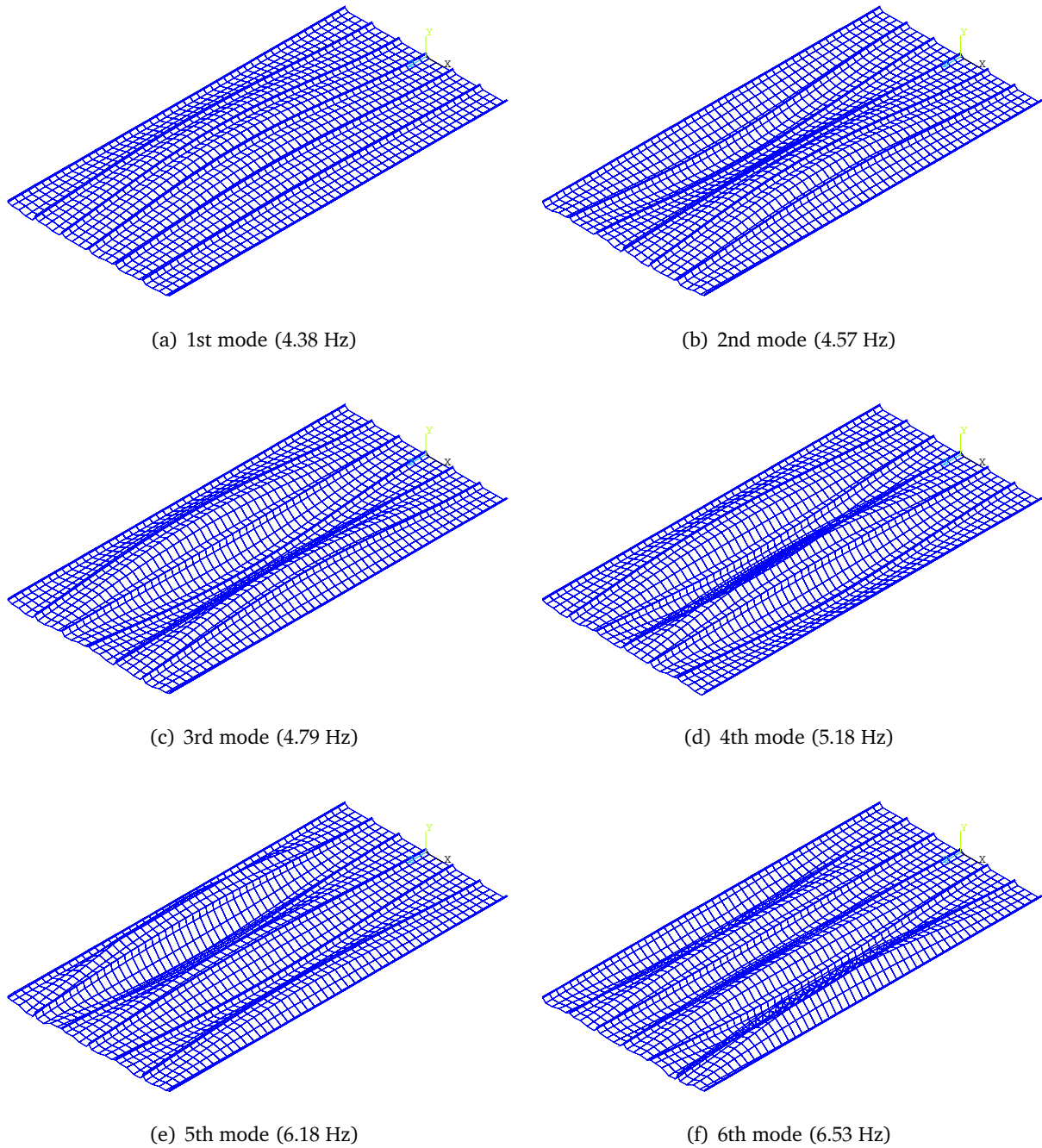
164

(a) 1st mode (4.38 Hz)

(b) 2nd mode (4.57 Hz)

(c) 3rd mode (4.79 Hz)

(d) 4th mode (5.18 Hz)

(e) 5th mode (6.18 Hz)

(f) 6th mode (6.53 Hz)

Figure - 7.24: Mode shapes of the first 6 modes of the modified roof structure.

20 modes.

In the following analysis, it is assumed that the modification on the roof structure does not change the wind loads distribution on the roof structure. For the comparison purpose, the SVC
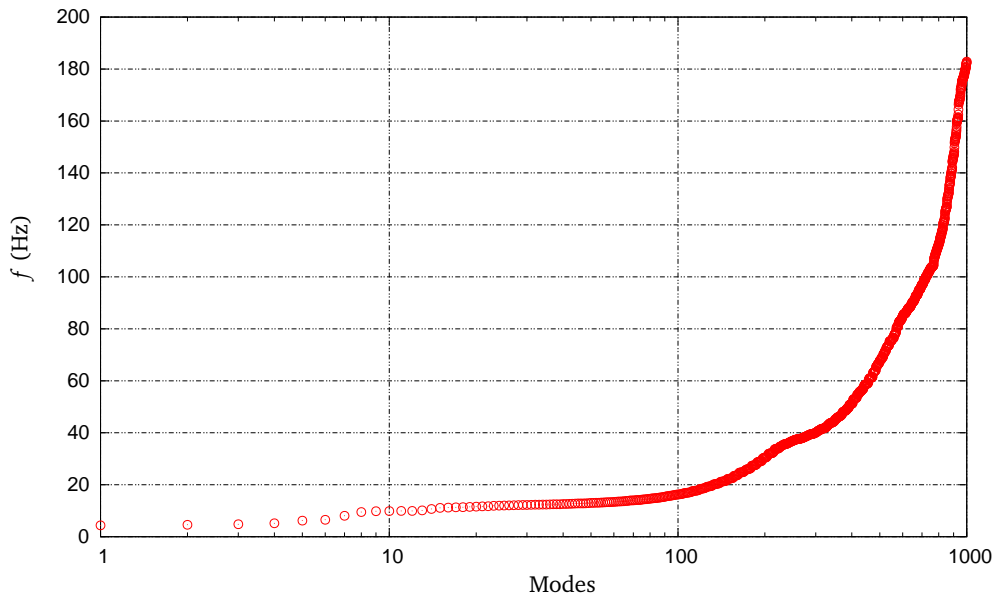
Figure - 7.25: Natural frequencies of the modified roof structure.

system is designed to attenuate the vibration of the same critical area. Furthermore, the number and locations of the actuators and the sensors are same as those used in the previous chapter.
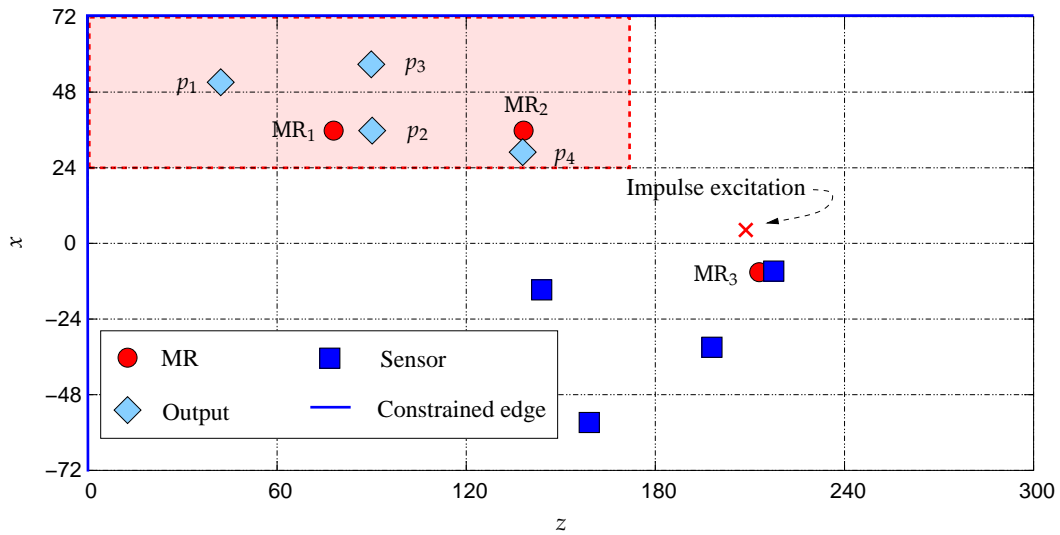
First, the optimal locations of the sensors and the actuators used in the passive and the semi-active SVC systems for the modified roof structure need to be found. In this case, the searching space for the OLSA problem is defined as follows,

$$S = \{j \mid N_j \geq 19, \ S_j > 0.1, \ 1 \leq j \leq n\}. \tag{7.6.19}$$

The symbols used in the above expression are same as those defined in section 7.3.1. Using the same procedure as described in section 7.3.1, 1200 admissible locations for the actuators and sensors are found for $k = 20$, $\epsilon = 10^{-4}$ and $\alpha = 0.1$, and their positions are shown in Figure - 7.26(a). Same as did in section 7.3.1, the spatial $\mathcal{H}_2$ norm the closed-loop transfer matrix is used as the optimization index in solving the OLSA problem. For the modified roof structure, the optimal locations of the actuators and sensors are found as shown in Figure - 7.26(b). It can be seen that, although vibration reduction is required in the same critical area as defined before, optimal locations for 4 sensors and 1 actuator are found outside that critical area. Because the mode shapes of the modified roof structure have been expanded significantly by removing the interior supports, an actuator (sensor) is able to have a more large influence area when is used to control (sense) a mode. Therefore, to attenuate the vibration in the critical area, the optimal
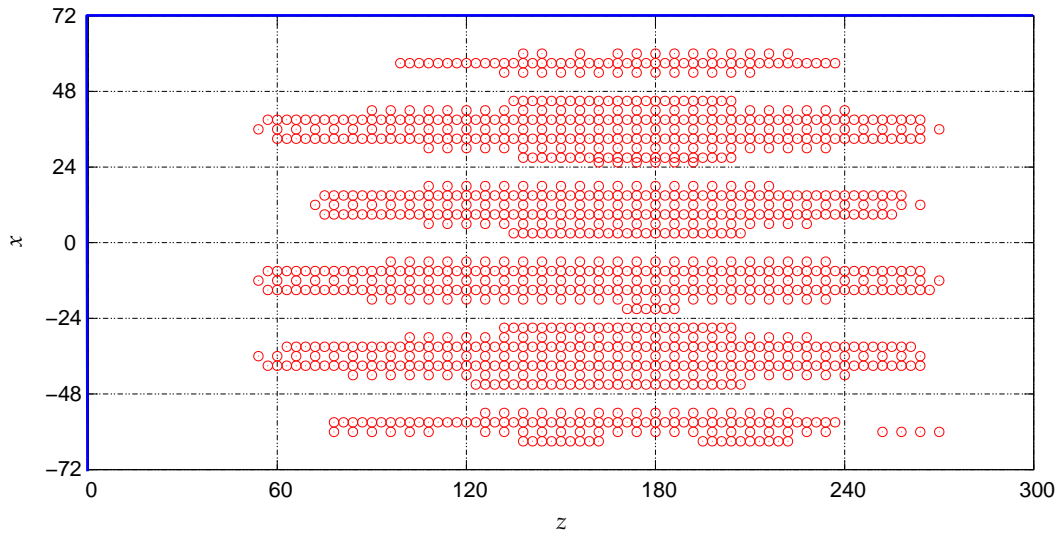
(a) 1200 candidate locations for actuators/sensors

(b) Optimal locations for actuators/sensors

Figure -7.26: Admissible and optimal locations for the actuators and sensors (less constrained case).

locations of the actuators and sensors do not necessarily be inside that area.

After the optimal locations of the sensors and actuators are found, the passive and the semi-active SVC systems can be designed for the modified roof structure using the exactly same

167

procedure as described in the previous section. Therefore, details of the SVC systems design are skipped. In the rest part of the section, the performances of the passive and the semi-active SVC systems are compared for an impulse excitation case, where the impulse force, whose magnitude is 100 lb and lasting for 0.01 second, is applied to the roof at the location shown in Figure - 7.26(b).

Figure - 7.27 shows the displacement responses at the 4 output locations $p_1 \sim p_4$ (defined in Figure - 7.26) for the case with and without MR dampers. From the results shown in the figure, it is seen that responses at all the 4 output locations are reduced by using the MR dampers. Although p_1 and p_3 are separated from the MR dampers by the seams, their responses are still reduced.

Figure - 7.28 compares the responses obtained from the the semi-active control and the passive control systems. From the plots it can be seen that, different from the results observed in the original fully constrained roof structure, responses obtained from the semi-active control are found much better than that obtained from the passive control. In the semi-active control, all MR dampers are working cooperatively to achieve the best vibration attenuation over the whole critical area. At the location p_2, although the response from the semi-active control is a little bit larger than that from the passive control, globally, the responses are significantly reduced. This can be seen from the comparison of the vibration energy as shown in Figure - 7.29. The semi-active control achieves much faster energy decay. At $t = 1$s, semi-active dissipates 73% of the total energy, while passive control dissipates 43% of the total energy. At $t = 6$s, 99.1% of energy is disspipated by semi-active control v.s. 93% by passive control.

Figure - 7.30 plots the command voltages applied to the MR dampers. This figure also compares the actual MR forces with the desired control forces calculated by the spatial $\mathcal{H}_2$ controller. The command voltages as showed in the figure demonstrates that the clipped-optimal control algorithm used in this research is indeed a bang-bang type control. When it is used to control a MR damper, it is expected to drive the MR damper follow the desired control force as quick as possible with the maximum available control input, which is the input voltage in this case. From the comparison of the forces, it is found that MR forces can follow the trend of the control forces, but can not exactly follow the desired control forces. This is because the force developed by a MR damper can not be directly controlled by the input voltage. The force provided by a
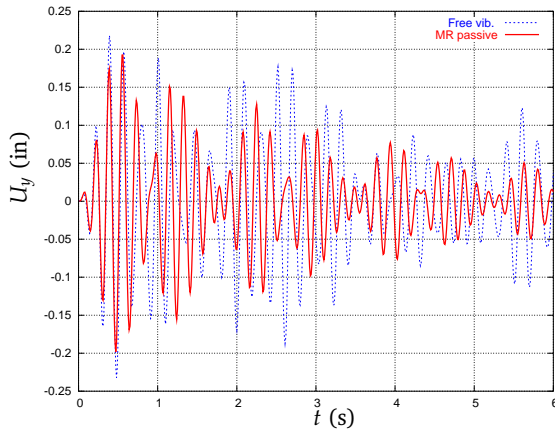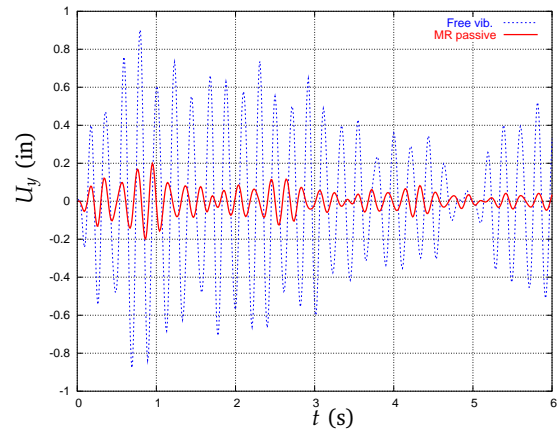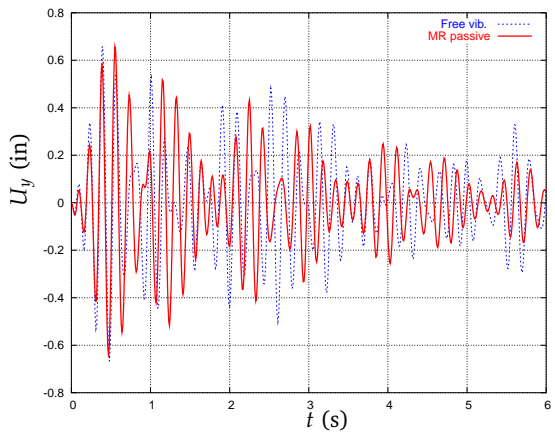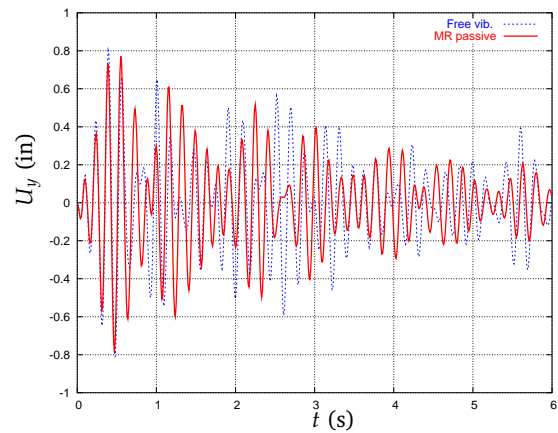
(a) Transverse displacement at p_1

(b) Transverse displacement at p_2

(c) Transverse displacement at p_3

(d) Transverse displacement at p_4

Figure -7.27: Comparison of the displacement responses at 4 randomly picked locations in the original critical area. Dashed line for the case without MR dampers, solid line for the case with MR dampers.

MR damper is also dependent on the displacement and velocity at the location to which the MR damper is attached. Changing the input voltage only has an indirect effect on the force generated by a MR damper. In a semi-active control system, by changing the input voltage, the damping effect of a MR damper is changed in a way such that the vibration can be attenuated more efficiently. Therefore, although the MR forces did not follow the desired control forces, semi-active control system was still able to outperform the passive control system.

(a) Transverse displacement at p_1

(b) Transverse displacement at p_2

(c) Transverse displacement at p_3
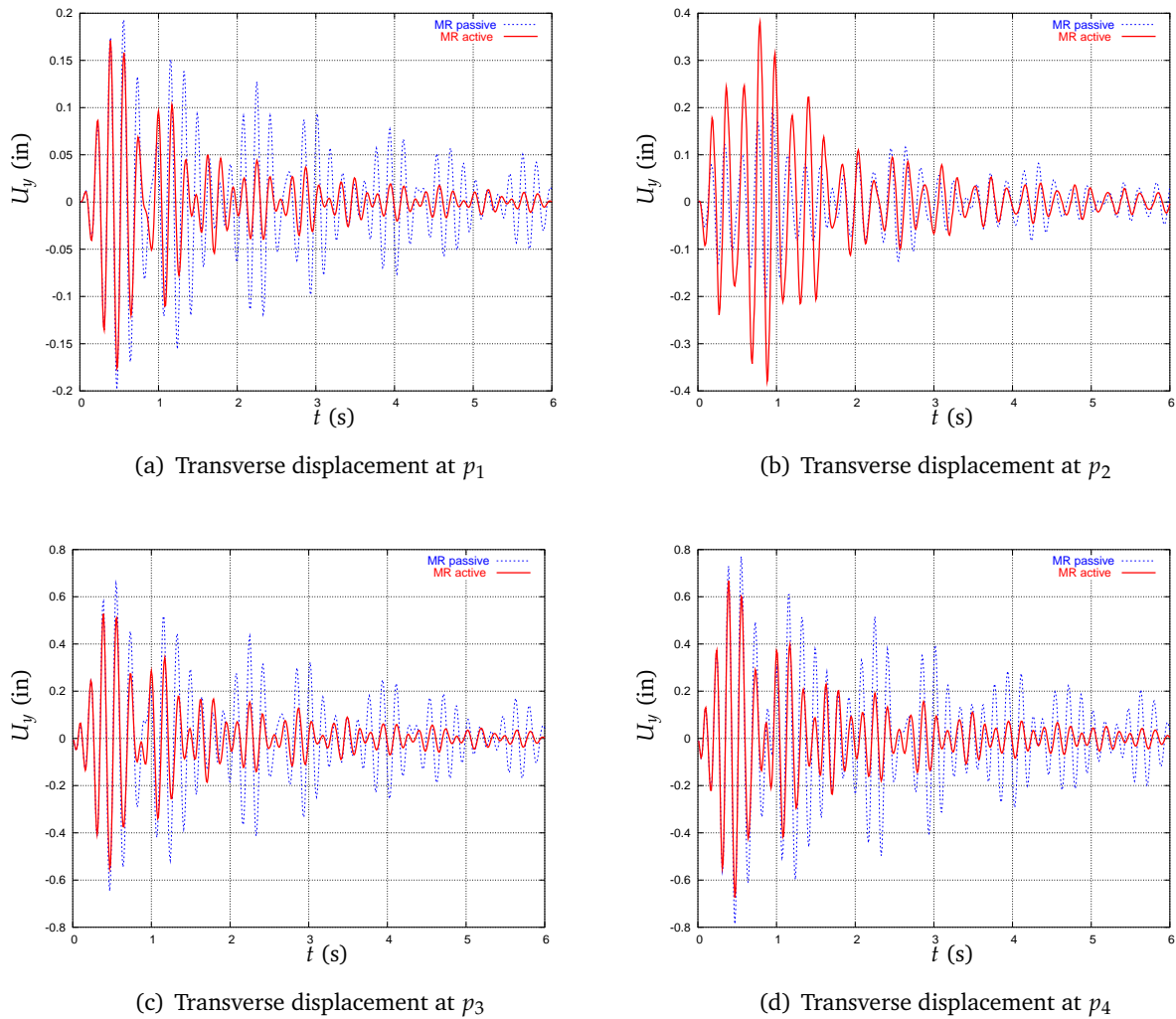

(d) Transverse displacement at p_4

Figure - 7.28: Comparison of the displacement responses at 4 output locations in the original critical area. Dashed line for the case of passive control, solid line for the case of semi-active control.

Figure - 7.31 shows the hysteretic curves of the 3 MR dampers used in the semi-active control system. The force-displacement curves illustrates the amount of energy dissipated through the MR dampers. The larger the area enclosed by a curve during a cycle, the more vibration energy is absorbed by the corresponding MR damper. Changing the input voltages to the MR dampers will change the area enclosed by the force-displacement curve. The typical force-velocity relationship as demonstrated by a MR damper (see Figure - 6.6(d)) can also be observed in this figure.
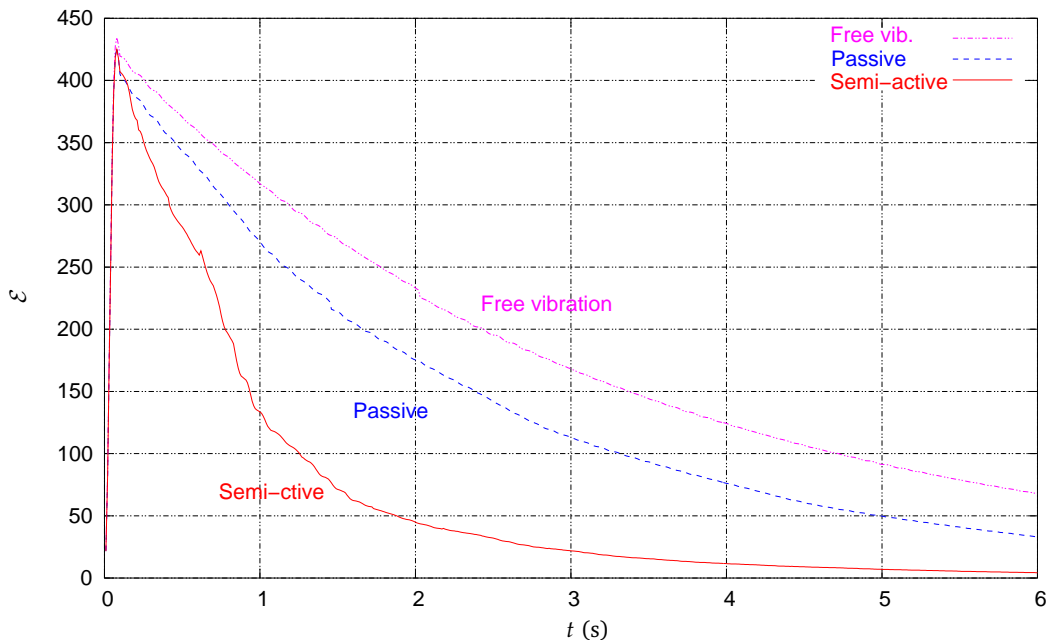
Figure - 7.29: Comparison of the vibration energy.

The analyses presented in this section showed that, on the modified roof structure, a semi-active SVC system is able to achieve a better vibration reduction result than a passive SVC. This is because by removing the supports from the original roof structure, the influence area of a vibration mode has been significantly expanded, as a result, the advantages inherent in a semi-active control system are able to exemplify themselves.

7.7   Summary

In this chapter, structural vibration control of an industrial roof structure subjected to a wind excitation was studied. The methodologies developed in the previous chapters were verified through designing a passive and a semi-active SVC systems for the roof structure.

Based on a spectral analysis of the wind loading, an optimal wind filter was obtained to be used in the semi-active control system design. A critical area on the roof structure was identified through a transient analysis of the roof structure subjected to the wind loads. Through a modal analysis of the roof structure, it was found that for the given wind excitation, a ROM consisted of the first 50 modes was adequate to represent the dynamics of the roof structure used for
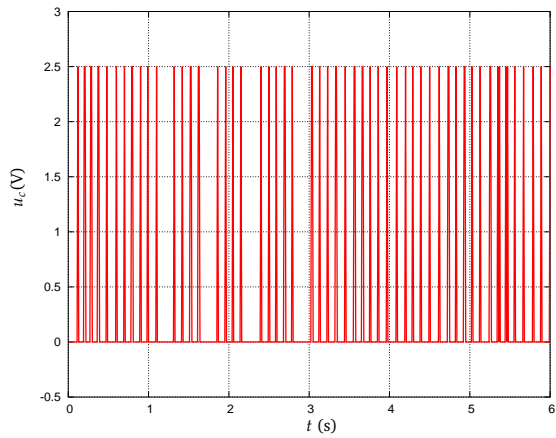
(a) Command voltage for MR$_1$
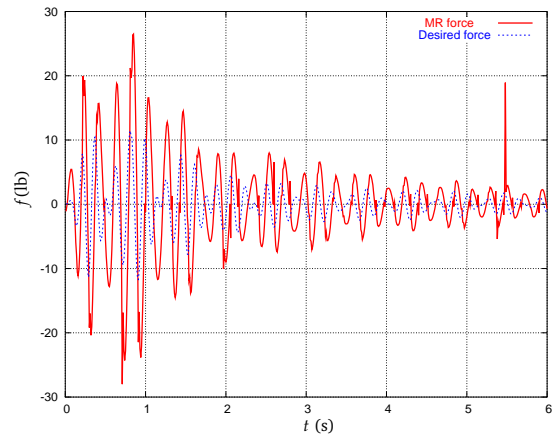
(b) Desired and actual force for MR$_1$
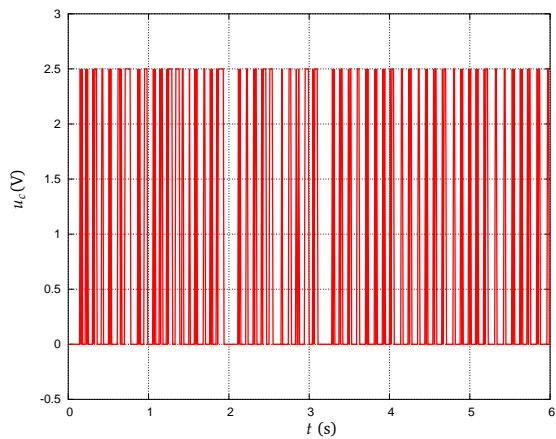
(c) Command voltage for MR$_2$
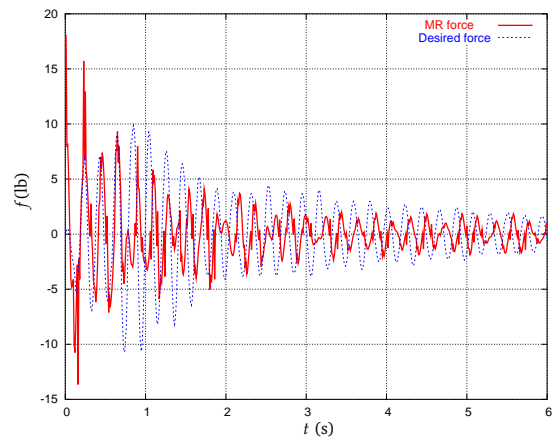
(d) Desired and actual force for MR$_2$
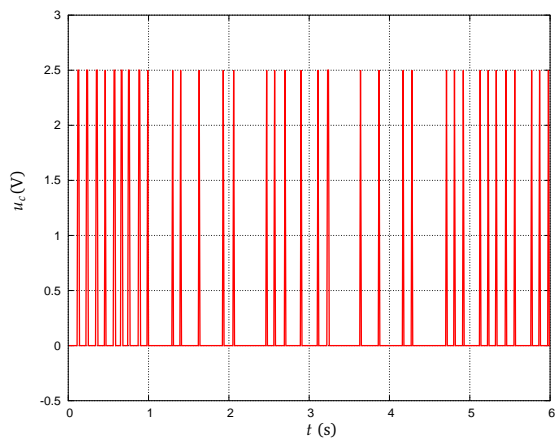
(e) Command voltage for MR$_3$
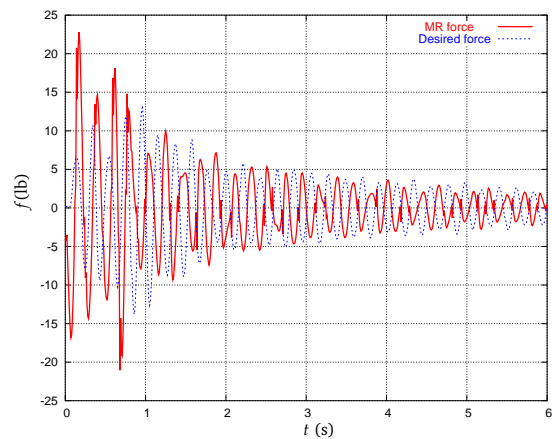
(f) Desired and actual force for MR$_3$

Figure - 7.30: Command voltages, MR forces and the desired control forces
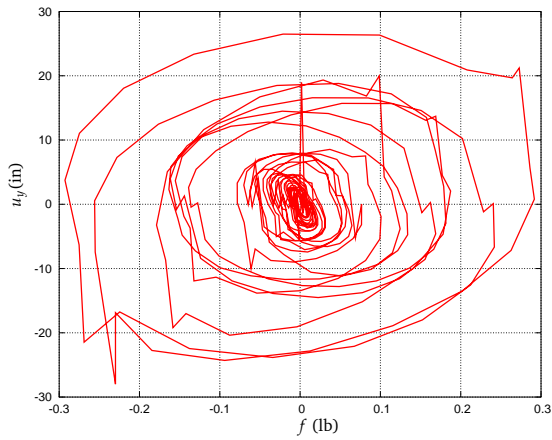
(a) MR$_1$ force v.s. displacement
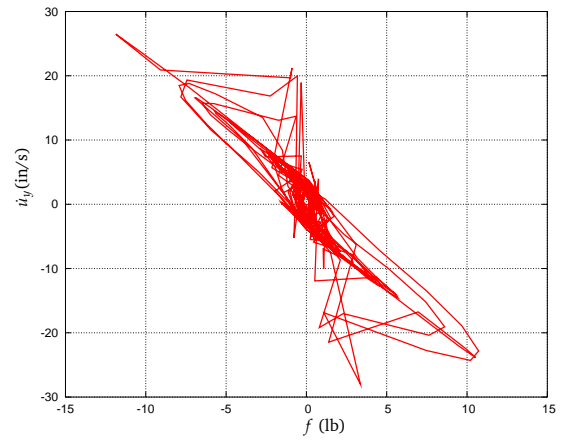
(b) MR$_1$ force v.s. velocity
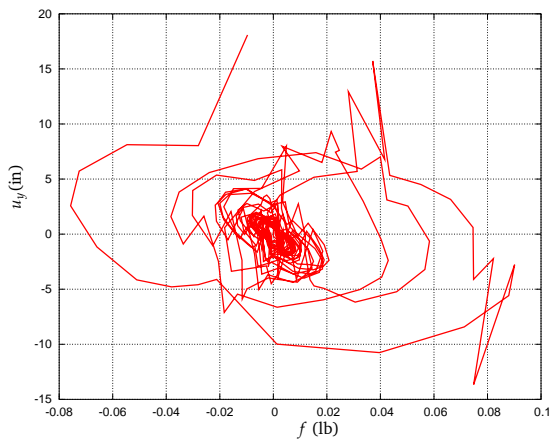
(c) MR$_2$ force v.s. displacement
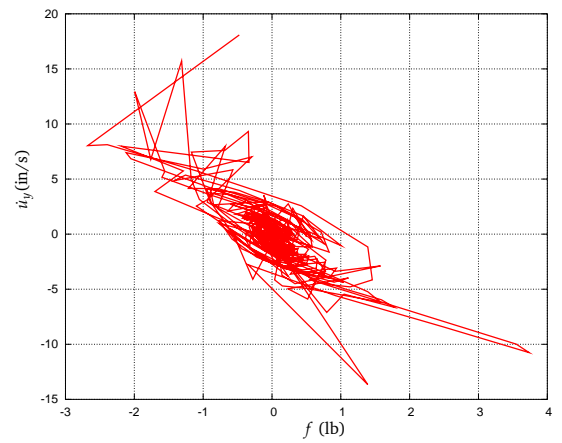
(d) MR$_2$ force v.s. velocity
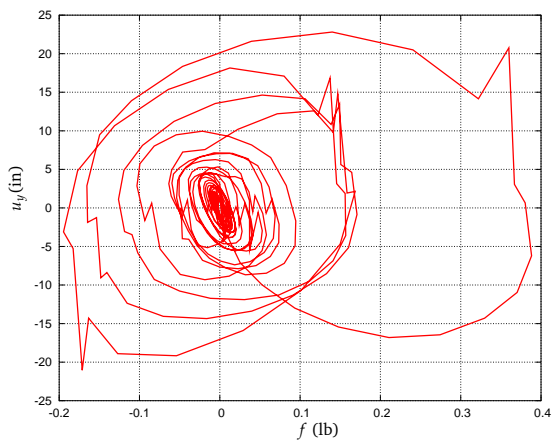
(e) MR$_3$ force v.s. displacement
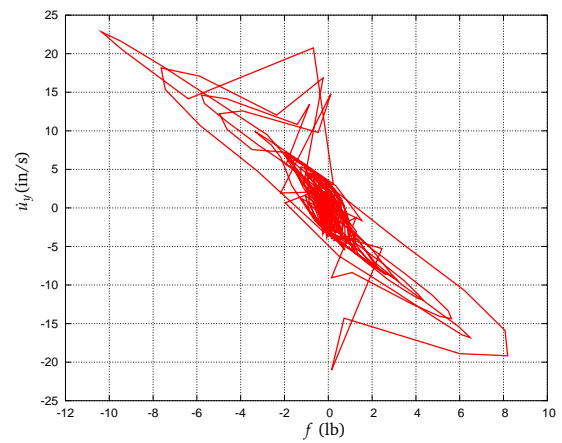
(f) MR$_3$ force v.s. velocity

Figure -7.31: Hysteretic curves of the MR dampers in the semi-active control system

the SVC systems design. Based on the 50-mode ROM, an OLSA problem was solved using the method developed in Chapter 5. For the verification purpose, a 20-mode ROM was obtained using the model reduction method developed in Chapter 3. A spatial $\mathcal{H}_2$ controller was then designed using this 20-mode ROM, and used in a semi-active SVC system. The passive and the semi-active SVC systems were used to the roof structure to attenuate the wind-induced vibration inside the critical area. It was found that the average RMS responses inside the critical area were reduced by 18% by using the passive SVC system, and the semi-active SVc system achieved 4% more reduction than the passive SVC system. The limited performance improvement observed in the semi-active SVC system as compared with the passive one, was attributed to the special charcateristics demonstrated by the roof structure due to its special structural configuration and the suppots on the seams. This observation was verified by an analysis on a modified roof structure, where a semi-active SVC system was demonstrated be able to achieve much better performance than the passive one. Finally, it should be noted that, due to the dissipative natures of MR dampers, the ROM based semi-active control system didn't cause the spillover instability problem when it was used to control a higher order structural system. Therefore, the spillover problem was not involved in this chapter.

CHAPTER 8

Concluding Remarks

8.1   Summary of the Work

This dissertation was devoted to the vibration control of large scale flexible structures using the MR dampers. Altough the structural vibration control has been extensively studied for decades, its application to large scale structures is still a task full of challenge, and many issues need to be addressed. As reviewed in the first chapter of this dissertation, the methods developed in the previous works aimed at addressing these issues have more or less limitations, and some these limitations prevent them from being efficiently used for large scale structures. These issues were therefore revisited in this work, such that more efficient new methods or the improved methods can be developed to enable an efficient application of the structural vibration control technology for large scale structures.

The issues addressed in this research and the work done on these issues are summarized as follows:

1. **Modeling of Flexible Structures and Controller Design**: As one of the most commonly encountered structural members in various flexible structures, plate structures were used in this research. The procedure of modeling the plate structures was introduced. The Mindlin plate theory was briefly reviewed and the equations of motion of thick plate were derived. Finite element formulation of an 8-node plate element was introduced. Two nu-

merical methods commonly used for dynamical analysis of linear MDOF systems, i.e. the Newmark direct integration method and the modal superposition method, were also reviewed. Finally, the LQG and $\mathcal{H}_2$ controller design methods were introduced, and the differences and relationships between these two methods were outlined. Because the $\mathcal{H}_2$ controller design method deals with a more general system, $\mathcal{H}_2$ controller was selected to be used in this research.

2. **Model Reduction**: In order to get an implementable controller for large scale structures, model reduction is an essential issue that needs to be addressed. In this part, minimizing the truncation error of a reduced order model obtained from the modal truncation was studied. Through a parametric study on the modal truncation method, it was found that by adjusting the modal parameters of the in-bandwidth modes, the truncation error can be reduced. Based on this observation, an algorithm to minimize the in-bandwidth truncation error was developed. The proposed algorithm could be used to find an optimal ROM with minimized truncation error from a ROM obtained from the direct modal truncation method, and can be used to both SISO and MIMO systems. Finally, the proposed method was verified through a numerical example.

3. **Suppression of Spillover Instability**: When a ROM based controller is used to control the original structure from which the ROM was obtained, spillover is inevitable. Spillover not only degrade the system performance, for a lightly damped structure, it may also destabilize the system. In this part, the mechanism of the spillover was studied, and the method to suppress spillover instability in a SVC system was developed. A criterion to check if the spillover instability will happen to a closed-loop system was proposed. It was found that the spillover instability could be avoided by blocking either the control spillover or the observation spillover in a closed-loop system. The proposed method suppresses the spillover instability by constructing a controller that lies in a null space spanned by several selected residual modes. Vibration control of a plate structure showed that the proposed method was able to effectively suppress the spillover instability that would happen otherwise.

4. **Optimal Locations of Sensors/Actuators**: For the vibration control of a large scale structure, selecting the optimal locations for actuators and sensors is not only a problem that

should be addressed from the economical point of view, but also there is a need to be able to achieve the best performance. In this research, the spatial $\mathcal{H}_2$ norm of a SVC system was used as the performance index in finding the optimal locations for actuators and sensors. The GA method was used to solve this optimization problem. It is found that the optimal locations for actuators and sensors found by using the spatial $\mathcal{H}_2$ norm as the optimization index, can achieve better closed-loop system performance than other commonly used indices (such as controlability, observability, $\mathcal{H}_2$ and $\mathcal{H}_\infty$ norms, etc.).

5. **Modling of MR Dampers and Applications**: Several hysteresis models for the MR dampers reported in the literature were compared, and a modified Bouc-Wen model due to Spencer Jr. et al. [54] was selected to be used in this research. It was found that the hysteretic behavior of this model was extremely sensitive to the change of the velocityand this characteristic could lead to the loss of the desired hysteretic behavior when noisy data were used. In this research, the MR model was modified to include a low-pass filter in the model, such that the hysteretic behavior of the MR model could be preserved when noisy data were used. Application of the MR dampers in the structural vibration control was then studied. A passive and semi-active SVC systems using 3 MR dampers and 4 velocity sensors were designed. In the passive control analysis, a Newmark based numerical scheme was developed to solve the resultant nonlinear differential equations. In the semi-active control system, the clipped-optimal control algorithm [62] was used to find the appropriate input voltages for the MR dampers.

6. **Vibration Control of a Roof Structure**: For verification purpose, the methodologies developed in this work were finally used to design a passive and a semi-active SVC systems for an industrial roof structure subjected to wind loading. An optimal wind filter was designed based on a spectrum analysis of the wind loads. Through a full scale transient analysis of the roof structure, a critical area on the roof was identified. A passive and a semi-active SVC systems using 3 MR dampers and 4 velocity sensors were then designed to attenuate the vibration inside the critical area on the roof structure. The method developed in Chapter 5 was used to find the optimal locations for the MR dampers and the sensors. A ROM containing the first 20 modes was constructed using the model reduction method

developed in this work for the semi-active control system design. Through numerical simulation, it was found that the average RMS response in the critical area could be reduced by 18% using the passive control system, and the semi-active control system achieved 4% more reduction. The stiffness difference between the structural members of the roof, and interior constraints were attributed to the limited improvement on the performance of the semi-active control system over the passive one. To support this observation, a less constrained roof structure with all interior supports being removed was analyzed. Simulation results showed that the semi-active control system achieved a much better performance than the passive one on the less constrained roof.

8.2   Main Contributions

✳— A new model reduction method was developed. The proposed method is able to minimize the truncation error of a modal-truncation based ROM, such that the shift of zeroes in the transfer function of the ROM is compensated. The proposed method does not add a feed-through term to the ROM, as a result, the difficulty of an infinite $\mathcal{H}_2$ norm as encountered in the method reported by Halim and Moheomani [20] can be avoided. Because the developed method was based on the GA method, it can be efficiently implemented for large scale structures. The method can be used for both SISO and MIMO systems. A state space realization of thus obtained ROM could be obtained using either the balanced realization method, or the Eigensystem Realization Algorithm (ERA). To the best of the author's knowledge, this work was the first of its kind.

✳— An innovative method to suppress spillover instability in a SVC system was developed. A criterion used to determine whether or not the spillover instability will happen to a closed-loop system was proposed. Compared with the distributed sensing method [25] and orthogonal filter methods [32, 33], the proposed method uses a set of point actuators and sensors to achieve the suppression of the spillover instability. When used for a large scale structure, the proposed method eliminates the need on the expensive hardwares as required by the other methods reviewed in the first chapter of this dissertation, and therefore is cheaper and easier to implement for large scale structures.

✳— A new numerical scheme to find the optimal locations for sensors and actuators for a SVC system was proposed. Different from the existing works, the spatial $\mathcal{H}_2$ norm was used as the performance index in the optimization process. The optimization problem was solved using a GA algorithm. It was verified numerically that the locations of sensors and actuators obtained by using the spatial $\mathcal{H}_2$ norm as the optimization index can achieve better performance than using the standard $\mathcal{H}_2$ norm.

✳— An improved MR model based on a modified Bouc-Wen MR model [54] was developed. The improved MR model proposed in this study was able to deal with noisy input data and still maintain the hysteretic behavior. Numerical analysis showed that the modified MR model was able to reproduce the dynamics of the original MR model in both normal and noisy situations.

✳— A Newmark based iteration scheme was proposed to solve the nonlinear differential equations aroused from using the MR dampers in a large scale linear structural system. Because the symmetric properties of the structural mass, stiffness and damping matrices can be utilized, this method can be used to analyze large scale structure. Furthermore, the proposed method was based on the Newmark direct integration method, numerical instability problem is avoided.

✳— A passive and a semi-active SVC system using the MR dampers were designed for an industrial roof structure. In this study, an optimal wind filter was designed for the controller design purpose. A critical area on the roof was identified through the transient analysis of the roof structure subjected the wind load. The optimal locations for the actuators (i.e. MR dampers) and sensors were found using the algorithm developed in this work. Using the passive control system, it was found that an average RMS response in the critical area can be reduced by 18%. The cause of a limited performance improvement for the semi-active control system was analyzed. It was concluded that the special characterstic of the roof structure prevented the improvement of the performance of a semi-active control system. The observation was verified through an analysis performed on a less constrained roof structure, where a semi-active control achieved a much better vibration reduction over the passive counterpart.

8.3   Recommendations for Future Work

There are several ways in which the work presented in this dissertation could be advanced. A few possible extensions to the current work are suggested as follows:

1. **Model Reduction**: From the development of the proposed model reduction method it is seen that, the nature of the method was to compensate the truncation error through modifying the mode shapes of the in-bandwidth modes. The present algorithm modifies the modal influence parameters on the locations where point actuators and sensors are presented. Considering the distributed nature of a structure, it could be extended to allow the distributed inputs and outputs.

2. **Optimal Locations for Actuators/Sensors**: In this research, a set of locations for the actuators and sensors are optimal in the sense of the spatial $\mathcal{H}_2$ norm of the closed-loop transfer function is minimized. Because the locations of actuators and sensors also affect the spillover, the algorithm could be improved by including the index measuring the spillover instability. This can be done by combining the OLSA algorithm with the method to suppress the spillover instability.

3. **Control of MR Damper**: The clipped-optimal control algorithm proposed by Dyke et al. [62] was used in this work to design a semi-active control system using MR damper. The algorithm used a bang-bang type control strategy to find an input voltage to a MR damper, such that the MR force follow the desired control force. Using the clipped optimal control algorithm allows a linear controller be used control a nonlinear actuator – MR damper, and therefore simplifies the control system design. However, from the simulation results presented, it was observed that the clipped-optimal control algorithm could not guarantee an exact match between the MR force and the desired control force. Due to the dissipative nature of MR dampers, this mismatch did not cause the instability to the closed-loop system, and achieved satisfactory results in attenuating vibrations. However, it destroys the optimality of the original linear controller. It is reasonable to believe that the performance of the semi-active control system could be further improved by reducing the mismatch. Including the inverse dynamics of a MR damper into a semi-active control loop is one of the possible solutions to this problem. Because the inverse dynamics of a MR damper is

difficult to find, some researchers (Hidaka et al. [58] and Chang and Zhou [59]) proposed to use a Neural Networks (NN) to represent the inverse dynamics of MR damper. However, in most cases, the NN representation of the inverse dynamics of MR damper is only good for the data for which the NN was trained, and therefore is not robust to the change of the inputs. Suppout Vector Machine (SVM) [76] is an another method developed after the NN and used in pattern recognition and artificial intelligence. It is based on structural risk minimization principle to find an optimal approximation to a given set of data, such that the obtained SVM is able to produce good approximation for both training and unseen samples. Therefore, a trained SVM is able to represent a process in a statistically optimal sense. Using SVM to represent the inverse dynamics of a MR damper could be able to produce a good result over a wide range of inputs.

4. **Modeling of Roof Structure**: The characteristic of a set of densely distributed vibration modes demonstrated by the roof structure studied here, may pose a challenge for a SVC system design. Fortunately, because the spectrum of the wind load does not have much overlap with that of the roof structure, this characteristic did not cause much trouble in our research. In an unfortunate case, there could be hundreds of modes fall into a frequency band that need to be considered. In this case, one possible solution is to construct a new model for the controller design. The new model contains several number of 'modes', each of them is a 'lumped' mode which includes the contributions from a number of original modes within a certain frequency band. In some optimal sense, each one of these lumped modes should be able to reproduce the overall dynamics of the modes from which it was constructed within certain frequency band. By this way, hundreds of modes piled inside a relatively narrow frequency band could be represented by few of these lumped modes, and as a result, a controller with a smaller order could be designed. The stability problem aroused from applying thus obtained controller to the original structure should also be addressed.

APPENDIX A

Newmark Direct Integration Algorithm

The Newmark method is one of the most extensively used direct integration method in the dynamical FEM analysis. It was developed to solve a system of the 2nd order linear ordinary differential equations as given in (2.3.16). In this study, the Newmark method and its related assumptions was used in Chapter 6 in deriving (6.3.14).

Newmark direct integration procedure is an extension of the linear acceleration method, which assumes that the acceleration vary linearly inside each time step. In the Newmark method, this assumption can be summarized as follows,

$$\dot{d}_{t+\Delta t} = \dot{d}_t + [(1-\delta)\ddot{d}_t + \delta\ddot{d}_{t+\Delta t}]\Delta t, \tag{A-1}$$

$$d_{t+\Delta t} = d_t + \dot{d}_t\Delta t + \left[\left(\frac{1}{2} - \alpha\right)\ddot{d}_t + \alpha\ddot{d}_{t+\Delta t}\right]\Delta t^2, \tag{A-2}$$

where α and δ are two constant parameters determined by the accuracy and stability requirements. Solving for the acceleration $\ddot{d}_{t+\Delta t}$ from (A-2) gives

$$\ddot{d}_{t+\Delta t} = \frac{1}{\alpha\Delta t^2}(d_{t+\Delta t} - d_t) - \frac{1}{\alpha\Delta t}\dot{d}_t - \left(\frac{1}{2\alpha} - 1\right)\ddot{d}_t. \tag{A-3}$$

Then the velocity $\dot{d}_{t+\Delta t}$ can be obtained by substituting (A-3) into (A-1). The displacement $d_{t+\Delta t}$ is obtained by enforcing the dynamical equation at the time instant $t + \Delta t$, i.e.

$$M\ddot{d}_{t+\Delta t} + C\dot{d}_{t+\Delta t} + Kd_{t+\Delta t} = f_{t+\Delta t}. \tag{A-4}$$

From the above equations, the displacement can be obtained by solving the following linear system equations,

$$\left(K + \frac{1}{\alpha \Delta t^2} M + \frac{\delta}{\alpha \Delta t} C\right) d_{t+\Delta t} = f_{t+\Delta t} + M\left[\frac{1}{\alpha \Delta t^2} d_t + \frac{1}{\alpha \Delta t}\dot{d}_t + \left(\frac{1}{2\alpha} - 1\right)\ddot{d}_t\right]$$

$$+ c\left[\frac{\delta}{\alpha \Delta t} d_t + \left(\frac{\delta}{\alpha} - 1\right)\dot{d}_t + \left(\frac{\delta}{2\alpha} - 1\right)\Delta t \ddot{d}_t\right]. \qquad \text{(A-5)}$$

The procedure of the Newmark method can be summarized as follows:

1. Compute the stiffness matrix K, the mass matrix M and the damping matrix C;

2. Set the initial values d_0, $\dot{d}_0$ and $\ddot{d}_0$;

3. Set the time step Δt, the integration parameters α and δ, and compute

$$c_0 = \frac{1}{\alpha \Delta t^2}, \quad c_1 = \frac{\delta}{\alpha \Delta t}, \quad c_2 = \frac{1}{\alpha \Delta t}, \quad c_3 = \frac{1}{2\alpha} - 1,$$

$$c_4 = \frac{\delta}{\alpha} - 1, \quad c_5 = \frac{\Delta t}{2}\left(\frac{\delta}{\alpha} - 2\right), \quad c_6 = \Delta t(1 - \delta), \quad c_7 = \delta \Delta t;$$

4. Compute the effective stiffness matrix $\hat{K} = K + c_0 M + c_1 C$;

5. Perform LDL decomposition of the effective stiffness matrix $\hat{K} = LDL^T$;

6. For each time step,

   (a) compute the affective load vector at time instant $t + \Delta t$,

   $$\hat{f}_{t+\Delta t} = f_{t+\Delta t} + M(c_0 d_t + c_2 \dot{d}_t + c_3 \ddot{d}_t) + C(c_1 d_t + c_4 \dot{d}_t + c_5 \ddot{d}_t);$$

   (b) solve for the displacement at time instant $t + \Delta t$ using the following equation

   $$LDL^T d_{t+\Delta t} = \hat{f}_{t+\Delta t};$$

   (c) compute the acceleration and velocity using

   $$\ddot{d}_{t+\Delta t} = c_0(d_{t+\Delta t} - d_t) - c_2 \dot{d}_t - c_3 \ddot{d}_t,$$

   $$\dot{d}_{t+\Delta t} = \dot{d}_t + c_6 \ddot{d}_t + c_7 \ddot{d}_{t+\Delta t}.$$

The Newmark method has been proved unconditional stable when the two integration parameters satisfythe following conditions,

$$\delta \geq 0.5 \quad \text{and} \quad \alpha \geq 0.25(0.5 + \delta)^2. \tag{A-6}$$

In this case, the time step used in the Newmark procedure is determined by the accuracy requirement. A larger time step will not cause the numerical instability problem, but may reduce the accuracy of the obtained solutions. Generally, the time step should be at least 2 times smaller than the smallest period of the interested modes.

Eigensystem Realization Algorithm

The Eigensystem Realization Algorithm (ERA) is usually used to find a state space realization for a MIMO transfer matrix. In this research, a ROM obtained by using the model reduction method as introduced in Chapter 3 is in a transfer matrix form. ERA method can be used to find a state space realization for a thus obtained ROM.

For a $p \times q$ MIMO system, its transfer matrix $G(s) \in \mathbb{C}^{p \times q}$ can be considered in the form of the ratio of a matrix numerator polynomial $B(s) \in \mathbb{C}^{p \times q}$, and a n-th order scale polynomial $a(s)$, i.e.

$$G(s) = \frac{B(s)}{a(s)} \tag{B-1}$$

where

$$B(s) = B_0 + B_1 s + \cdots + B_n s^n \tag{B-2}$$

$$a(s) = a_0 + a_1 s + \cdots + a_n s^n \tag{B-3}$$

and $B_i \in \mathbb{R}^{p \times q}$, $i = 0, 1, \ldots, n$. By dividing $a(s)$ into $B(s)$, one can obtain the Markov parameter sequence $\{H_i\}$ as follows,

$$\frac{B(s)}{a(s)} = \sum_{i=0}^{\infty} H_i s^i. \tag{B-4}$$

Expanding the above equation gives

$$B_0 + B_1 s + \cdots + B_n s^n = (a_0 + a_1 s + \cdots + a_n s^n) \sum_{i=0}^{\infty} H_i s^i. \tag{B-5}$$

185

By equating the first N powers of s in the above equation, one can obtain a system of equations that are used to solve for the Markov parameters $H_i \in \mathbb{R}^{p \times q}$. It can be shown that the Markov parameters are given by the following recursive formula,

$$H_0 = B_0, \tag{B-6}$$

$$H_k = B_k - \sum_{j=1}^{k} a_j H_{k-j}, \quad k = 1, 2, \ldots, n, \tag{B-7}$$

$$H_k = - \sum_{j=1}^{n} a_j H_{k-j}, \quad k = n+1, n+2, \ldots, N. \tag{B-8}$$

Then choose any r and s such that $r + s \leq N$ and $\min(r, s) \geq n$, and form the following Hankel type matrices $H(0)$ and $H(1)$

$$H(0) = \begin{bmatrix} H_1 & H_2 & \ldots & H_s \\ H_2 & H_3 & \ldots & H_{s+1} \\ \vdots & \vdots & \ddots & \vdots \\ H_r & H_{r+1} & \ldots & H_{r+s-1} \end{bmatrix}, \quad H(1) = \begin{bmatrix} H_2 & H_3 & \ldots & H_{s+1} \\ H_3 & H_4 & \ldots & H_{s+2} \\ \vdots & \vdots & \ddots & \vdots \\ H_{r+1} & H_{r+2} & \ldots & H_{r+s} \end{bmatrix}. \tag{B-9}$$

A Balanced state space realization of the given transfer function then can be found using the ERA algorithm as follows,

1. Compute the singular value decomposition of $H(0)$,

$$H(0) = U \Sigma V^T \tag{B-10}$$

   where $\mu = \min(r \cdot q, s \cdot p)$, $U \in \mathbb{R}^{(r \cdot p) \times \mu}$, $V \in \mathbb{R}^{(s \cdot q) \times \mu}$, $\Sigma = \mathrm{diag}(\sigma_1, \ldots, \sigma_\mu)$, and the singular values are ordered such that $\sigma_i \geq \sigma_{i+1}$, $i = 1, \ldots, \mu - 1$.

2. Set a threshold value δ, find m such that $\sigma_i > \delta$ for $i = m+1, \ldots, \mu$.

3. Then a m-th order state space realization of G is given by

$$\begin{aligned} \dot{x} &= Ax + Bu, \\ y &= Cx + Du, \end{aligned} \tag{B-11}$$

   where

$$\begin{aligned} A &= \Sigma_m^{-1/2} U_m^T H(1) V_m \Sigma_q^{-1/2}, \quad B = \Sigma_m^{1/2} V_m^T E_u, \\ C &= E_y^T U_m \sigma_m^{1/2}, \quad D = H(0). \end{aligned} \tag{B-12}$$

186

and

$$E_y^T = \begin{bmatrix} I_{p \times q} & 0 \end{bmatrix} \in \mathbb{R}^{p \times (r \cdot p)}, \quad E_u^T = \begin{bmatrix} I_{q \times q} & 0 \end{bmatrix} \in \mathbb{R}^{q \times (s \cdot q)}. \tag{B-13}$$

In above equations, U_m and V_m are submatrices formed by the first m columns of the matrices U and V, respectively.

APPENDIX C

Genetic Algorithm

A Genetic Algorithm (GA), which was first proposed by Holland [70], is a heuristic procedure used as an effective numerical method to find a global optimal (or sub-optimal) solution for a complicated multi-parameter optimization problem. It starts with a certain number of randomly generated solution candidates, which is known as a *generation*, and advances towards better solutions by applying the so-called *genetic operators*, i.e. *crossover* and *mutation*, mimicking a natural genetic selection and evolution process. After the applications of these operators, a new generation of the same sizer is obtained. The objective function is used in evaluating the quality of a member in a generation. In each generation, the better solutions pass on to the next generation with a higher probability than the bad ones. In this way, GA operations make the new generation acquire better properties and more suitability. Iterating the above process till the solutions converge or the maximum number of iterations has been reached. The best solution of these generations is chosen as the final solution.

In a GA method, the variables of the optimization problem can be either represented by real numbers, called *real-coded* GA, or by strings of binary numbers, called *binary-coded* GA. In this work, the binary-coded GA was used, i.e. the optimization variables were encoded in the form of binary strings, which is known as *chromosome*. Each chromosome consists of several binary bits (0 or 1) as shown in Figure - C.1. The number of binary bits in a chromosome defines the resolution of the optimization variables. In each iteration step, GA operations are performed on
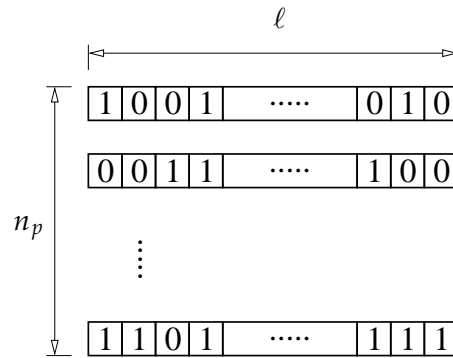
$$\ell$$

PSfrag replacements n_p

Figure - C.1: Chromosomes of a binary-coded GA.

a group of chromosomes, which is known as the *population*. The size of the population n_p is determined empirically by user, and kept constant through the GA iteration.

GA operations are performed on the two members selected from the current population, which are known as the *parents*. Selection of parents from the current population involves the evaluation the *fitness values* of the current population. The fitness value of a member is defined by the objective function of the optimization problem. Without loss of generality, consider a optimization problem finding a solution maximizing a function. Then the fitness value of a member, i.e. a set of optimization variables, is just the value of the objective function evaluated using these variables. In this case, the bigger the fitness value, the higher probability the corresponding member be selected to be one of the parents. Foe example, assume there are 4 members (or chromosomes) in the current population, and their fitness values are 1.0, 2.1, 0.6 and 0.3 respectively. The probability for each of them being selected can be obtained by dividing the fitness value by the summation of all fitness values. In this example, the summation of the fitness values is 4.0. Then the probability associated with these chromosomes are 1/4, 2.1/4, 0.06/4 and 0.3/4, respectively. By following this rule, the members corresponding to good fitness values have better chance to pass their properties (i.e. making objective function take larger value) to the new generation. After a pair of parents are selected, the GA operations can be applied.

The first GA operation is *crossover*. For each pair of parents obtained by the above selection process, the crossover combines their binary codes to produce a new chromosome with certain probability, which is known as the *crossover rate*. The binary codes of the new chromosome consist of segments of codes from its parents. Generally, to preserve the good characteristics

189

from the parents, one party of the parents corresponding to a better fitness value contributes more its code to the new chromosome than another one. The binary strings of the parents are randomly divided into several segments, then the codes of these segments are copied to the new chromosome from either one of the two parents according to the criterion mentioned above. Note that the chromosome generated by the crossover operation has the same length as their parents'. When the crossover does not happen, the new chromosome is just the copy of one of the parents, usually the one corresponding to a better fitness.

The second operation is *mutation*, which is performed on the chromosomes produced by the crossover operation. The mutation operation happens with certain probability as well. This probability is known as the *mutation rate*. When the mutation happens, some randomly selected bits of the chromosome are mutated, i.e. flip the bit from 1 to 0 or 0 to 1. When it does not happen, the chromosome produced from the crossover is kept untouched. The chromosome obtained through the above two GA operations is known as a *child*. The above two GA operations are iterated until the population that consists of the newly generated children reaches the same size as the old population. The above GA operations are illustrated in Figure - C.2.
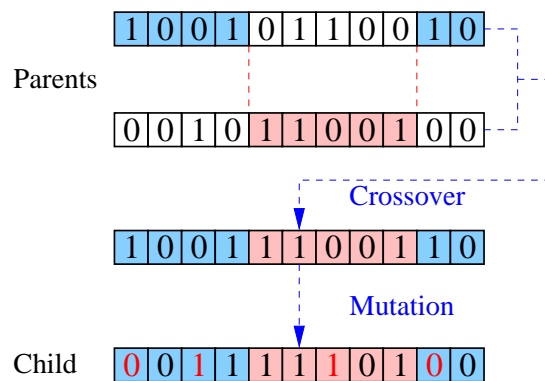
Figure - C.2: GA operations.

The essential mechanism of emulating the evolution process is implemented through the operations introduced above. Among these two GA operations, the crossover ensures that the good characteristics of one generation be able to pass to the next generation. The convergence property of a GA method is dominated by the crossover operation. For this reason, the crossover rate is usually very high, e.g. 90% or higher. The mutation operation introduces diversity to the GA iteration to prevent the GA iteration converge to a local extrema. For a complicated

nonlinear optimization problem, where exists many local extrema, the mutation operation is critical to find a global optimal solution. Generally, the mutation rate is less than 10%.

An overall view of GA process is shown in Figure - C.3. It is seen that the new generation is
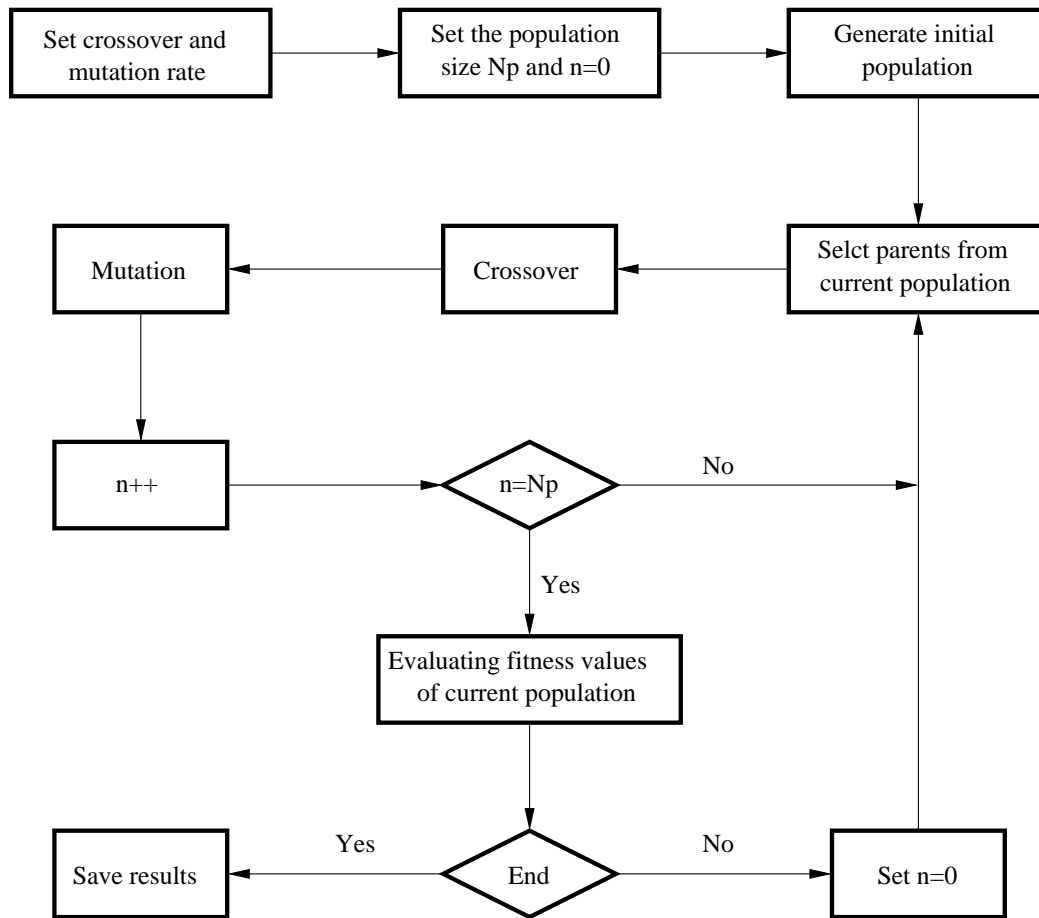
Figure - C.3: Flow chart of a GA method.

produced by applying the GA operations on the current population. After the new generation is obtained, the original one is replaced by the new population. The fitness value of each member of the current population is then evaluated. The GA iteration continues until either the solution is converged or, a maximum number of iterations has been reached. Upon the ending of the GA iteration, the best solution in the current population is the final optimal solution.

BIBLIOGRAPHY

[1] W. M. Winslow. Method and means for translating electrical impulses into mechanical force. US Patent No.2.417.850, 1947.

[2] K. D. Weiss, J. D. Carlson, and D. A. Nixon. Viscoelastic properties of magneto- and electrorheological fluids. *Journal of Intelligent Material Systems and Structures*, 5:772–775, 1994.

[3] L. M. Jansen and S. J. Dyke. Semi-active control strategies for mr dampers: A comparative study. *Journal of Engineering Mechanics*, 126(8):795–803, 1995.

[4] M.D. Symans, M.C. Constantinou, D.P. Taylor, and K.D. Garnjost. Semi-active fluid viscous dampers for seismic response control. In *Proceedings of the First World Conference on Structural Control*, pages FA4(3–12), Los Angeles, California, 3-5 August 1994.

[5] Andre Preumont. Vibration control of active structures: An introduction. Kluwer Academic Print, Dordrecht, 2002.

[6] M. J. Balas. Feedback control of flexible systems. *IEEE Transactions on Automatic Control*, AC-23:673–679, August 1978.

[7] A. C. Antoulas, D. C. Sorensen, and S. Gugercin. A survey of model reduction methods for large-scale systems. In Vadim Olshevsky (Georgia State University), editor, *Structured Matrices in Mathematics, Computer Science, and Engineering*, volume 1 of *Contemporary Mathematics*. American Mathematical Society, 2001.

[8] B. C. Moore. Principal component analysis in linear systems: controllability, observability, and model reduction. *IEEE Trans. Auto. Contr.*, 26(2), 1981.

[9] D. Enns. *Model Reduction for Control System Design*. PhD thesis, Stanford University, Stanford, California, 1984.

[10] K. Zhou, J. C. Doyle, and K. Glover. Robust and optimal control. Prentice Hall, New Jersey 07458, 1995.

[11] P. V. Kokotovic, R. E. O'Malley, and P. Sannuti. Singular perturbations and order reduction in control theory - an overview. *Automatica*, 12:123–132, 1976.

[12] Y. Liu and B. D. O. Anderson. Singular perturbation approximation of balanced systems. *International Journal of Control*, 50:1379–1405, 1989.

[13] R. J. Guyan. Reduction of stiffness and mass matrices. *AIAA Journal*, 3(2):380, 1965.

[14] M. I. Friswell, S. D. Garvey, and J. E. T. Penny. Model reduction using dynamic and iterated irs techniques. *Journal of Sound and Vibration*, 186(2):311–323, 1995.

[15] R. R. Craig and M. C. Bampton. Coupling of substructures for dynamic analyses. *AIAA Journal*, 6(7):1313–1319, 1968.

[16] M. A. Blair, Camino T. S., and J. M. Dickens. An iteration approach to a reduced mass matrix. In *Proceedings of the 99th International Modal Analysis Conference*, pages 621–626, Florence, Italy, April 1991.

[17] R. L. Clark. Accounting for out-of-bandwidth modes in the assumed modes approach: implications on collocated output feedback control. *Transactions of the ASME, Journal of Dynamics Systems, Measurement, and Control*, 119:390–395, 1997.

[18] S. O. R. Moheinami. Minimizing the effect of out-of-bandwidth dynamics in the models of reverberant systems that arise in modal analysis: implications on spatial $\mathcal{H}_\infty$ control. *Automatica*, 36:1023–1031, 2000.

[19] R. L. Bisplinghoff and H. Ashley. Principles of aeroelasticity. Dover, New York, 1975.

[20] Dunant Halim and S. O. Reza Moheomani. Reducing the effect of truncation error in spatial and pointwise models of resonant systems with damping. *Mechanical Systems and Signal Processing*, 18:291–315, 2004.

[21] S. O. R. Moheimani. Minimizing the effect of out of bandwidth modes in truncated structure models. *ASME Journal of Dynamic Systems, Measurement, and Control*, 122:237–239, 2000.

[22] Dunant Halim and S. O. Reza Moheimani. Spatial $\mathcal{H}_2$ control of a piezoelectric laminate beam: Experimental implementation. *IEEE Tansactions on Control Systems Technology*, 10 (4):533–546, 2002.

[23] M. Balas. Modal control of certain flexible dynamic systems. *SIAM Journal of Control and Optimization*, 1978.

[24] Y. Chait and C. J. Radcliffe. Control of flexible structures with spillover using an augmented observer. *Journal of Guidance, Control, and Dynamics*, 12(2):155–161, 1989.

[25] S. P. Nagarkatti, C. D. Rahn, D. M. Dawson, and E. Zergeroglu. Observer-based modal control of flexible systems using distributed sensing. In *Proceedings of the 40th IEEE Conference on Decision and Control*, pages 4268–4273, Orlando, Florida USA, December 2001. FrM04-4.

[26] M. H. Kim and Inman D. J. Spillover reduction in vibration control of flexible structures using sliding mode observer. *Journal of Vibration and Control*, 7:1087–1105, 2001.

[27] C. P. Smyser and K. Chandrashekhara. Robust vibration control of composite beams using piezoelectric devices and neural networks. *Smart Materials and Structures*, 6:178–189, 1997.

[28] W. Chang, S. V. Gopinathan, and V. K. Varadan, V. V. Varadan. Design of robust vibration controller for a smart panel using finite element model. *ASME Journal of Vibration and Acoustics*, 124:265–276, 2002.

[29] J. H. Kim, S. B. Choi, C. C. Cheong, S. S. Han, and J. K. Lee. H_∞ control of structure-borne

noise of a plate featuring piezoceramic actuators. *Smart Materials and Structures*, 8:1–12, 1999.

[30] A. Baz. Robust control of active layer damping. *Journal of sound and Vibration*, 221(3): 467–480, 1998.

[31] I. N. Kar, T. Miyakura, and T. Seto. Bending and torsional vibration control of a flexible plate structure using H_∞-based robust control law. *IEEE Transactions on Control systems Technology*, 8(3):545–553, 2000.

[32] R. E. Skelton and P. W. Likins. Orthogonal filters for model error compensation in the control of nonrigid spacecraft. *Journal of Guidance, Control, and Dynamics*, 1:41–49, Jan. 1978.

[33] H. S. Tzou and J. J. Hollkamp. Collocated independent modal control with self-sensing orthogonal piezoelectric actuators (theory and experiment). *Smart Materials and Structures*, 3(3):277–284, 1994.

[34] K. B. Lim. Method for optimal actuator and sensor placement for large flexible structures. *Journal of Guidance, Control, and Dynamics*, 15:59–57, 1992.

[35] W. Gawronski. Actuator and sensor placement for structural testing and control. *Journal of Sound and Vibration*, 208(1):101–109, 1997.

[36] R. E. Skelton and M. L. DeLorenzo. Selection of noisy actuators and sensors in linear stochastic systems. *Journal of Large scale Systems*, 4:109–136, 1983.

[37] R. E. Skelton and M. L. DeLorenzo. Space structure control design by variance assignment. *Journal of Guidance, Control, and Dynamics*, 8:454–462, 1985.

[38] F. Fahroo and M. A. Demetriou. Optimal location of sensors and actuators for an active noise control problem. *Journal of Computational and Applied Mathematics*, 114(1):137–158, 2000.

[39] M. A. Demetriou. Integrated actuator/sensor placement and hybrid controller design of flexible structures under worst case spatiotemporal disturbance variations. *Journal of Intelligent Material Systems and Structures*, 2004(to appear).

[40] Q. S. Li, D. K. Liu, J. Tang, N. Zhang, and C. M. Tam. Combinatorial optimal design of number and positions of actuators in actively controlled structures using genetic algorithms. *Journal of Sound and Vibration*, 270(4-5):611–624, 2004.

[41] A. Arabyan and S. Chemishkian. H_∞-optimal mapping of actuators and sensors in flexible structures. In *Proceedings of the 37th IEEE Conference on Decision and control*, pages 821–826 (Vol.1), 16-18 Dec. 1998.

[42] S. Chemishkian and A. Arabyan. Intelligent algorithms for H_∞-optimal placement of actuators and sensors in structural control. In *Proceedings of the 1999 American Control Conference*, pages 1812–1816, 2-4 June 1999.

[43] Dunant Halim and S. O. Reza Moheomani. An optimization approach to optimal placement of collocated piezoelectric actuators and sensors on a thin plate. *Mechatronics*, 13:27–47, 2003.

[44] S. O. R. Moheimani and M. Fu. Considerations in placement of piezoceramic actuators that are used in structural vibration control. In *Proceedings of the 37th IEEE Conference on Decision and Control*, pages 3623–3624, Tampa, FL, USA, December 1998.

[45] S. O. R. Moheimani and M. Fu. Considerations in placement of piezoceramic actuators that are used in structural vibration control. In *Proceedings of the 38th IEEE Conference on Decision and Control*, pages 1118–1123, Phoenix, AZ, USA, December 1999.

[46] W. J. Wu, C. S. Cai, and S. R. Chen. Experiments on reduction of cable vibration using MR dampers. In *Proceedings of 17th ASCE Engineering Mechanics Conference*, Newark, DE, June13-16 2004.

[47] Q. Feng and M. Shinozuka. Use of a variable damper for hybrid control of bridge response under earthquake. In *Proc. U.S. Nat. Workshop on Struct. Control Res.*, pages 107–112, University of southern California, Los Angeles, 1990. USC Publ. No. CE-9013.

[48] F. Gordaninejad, M. Saiidi, B. C. Hansen, and F. K. Chang. Magnetorheological fluid dampers for control of bridges. In *Proc. of the Second World Conference on Structural Control*, Kyoto, Japan, 1999.

[49] S. J. Dyke, B. F. Spencer Jr., M. K. Sain, and J. D. Carlson. Modeling and control of magnetorheological dampers for seismic response reduction. *Smart Materials and Structures*, 5: 565–575, 1996.

[50] B. F. Spencer Jr. and M. K. Sain. Controlling buildings: A new frontier in feedback. *IEEE Control Systems Magazine: Special Issue on Emerging Technologies*, 17(6):19–35, 1997.

[51] N. Markris, S. A. Burton, d. Hill, and M. Jordan. analysis and design of an ER damper for seismic protection of structures. *Journal of Engineering Mechanics ASCE*, 122(10):1003–1011, 1996.

[52] w. H. Liao. Semiactive vibration control of train suspension systems via magnetorheological dampers. *Journal of Intelligent Material, Systems and Structures*, 14(3):161–172, 2003.

[53] I. H. Shames and F. A. Cozzarelli. *Elastic and Inelastic Stress Analysis*. Prentice Hall Inc., Englewood Cliffs, NJ, 1992.

[54] B. F. Spencer Jr., S. J. Dyke, M. K. Sain, and J. D. Carlson. Phenomenological model for magnetorheological dampers. *Journal of Engineering Mechanics*, 123(3):230–238, 1997.

[55] Y. K. Wen. Method of random vibration of hysteretic systems. *J. Engrg. Mech. Div. ASCE*, 102(2):249–263, 1976.

[56] G. Cybenko. Approximation by superpositions of a sigmoidal function. *Mathematics Control, Signals, Systems*, 2:303–314, 1989.

[57] C. C. Chang and P. Roschke. Neural network modeling of a magnetorheological damper. *Journal of Intelligent Materials, System and Structure*, 9:755–764, 1998.

[58] S. Hidaka, Y. K. and, and s. Morishita. Adaptive vibration control by a variable-damping dynamic absorber using ER fluid. *Journal of Vibration and Acoustic*, 121(3):373–378, 1999.

[59] C. C. Chang and L Zhou. Neural network emulation of inverse dynamics for a magnetorheological damper. *Journal of Structural Engineering*, 128(2):231–239, 2002.

[60] M. Yokoyama, J. Hedrick, and S. Toyama. A model following sliding mode controller for semi-active suspension system with MR dampers. In *Proceedings of the American Control Conference*, pages 2652–2657, 2001.

[61] N. H. McClamroch and H. P. Gavin. Closed loop structural control using electrorheological dampers. In *Proceedings of the American control Conference*, pages 4173–4177, Seattle, washington, 1995.

[62] S. J. Dyke, B. F. Spencer Jr., M. K. Sain, and J. D. Carlson. Experimental verification of semiactive structural control strategies using acceleration feedback. In *Proc., 3rd Int. Conf. on Motion and Vibration Control*, pages 291–296, Tokyo, Japan, 1996. Japan Society of Mechanical Engineers.

[63] S. P. Timoshenko and S. Woinowsky-Krieger. Theory of plates and shells. McGraw-Hill, New York, 1961. Cited from MR-44.

[64] J. S. Rao. Dynamics of plate. Narosa Publishing House, New Delhi, India, 1999.

[65] E. Reissener. The effect of transverse shear deformation on the bending of elastic plates. *Journal of Applied Mechanics*, 12:A69–A77, 1945.

[66] R. D. Mindlin. Influence of rotaory inertia and shear on flexural motions of isotropic, elastic plates. *Trans. ASME Journal of Applied Mechanics*, 18:31–38, 1951.

[67] Wodek K. Gawronski. Advanced structural dynamics and active control of structures. Springer-Verlag, New York, 2004.

[68] B. D. O. Anderson and J. B. Moore. Optimal control. Prentice Hall, Englewood Cliffs, NJ, 1990.

[69] K. M. Zhou and J. C. Doyle. Essentials of robust control. Prentice Hall, New Jersey, 1998.

[70] J. H. Holland. Adaption in natural and artificial systems. University of Michigan Press, Ann Arbor, MI, 1975.

[71] Wei Liu, Zhikun Hou, and Michael A. Demetriou. Optimal sensor/actuator locations for vibration control of structures. In *The Proceedings of the 17th Engineering Mechanics Conference (CD)*, University of Delware, Newark, DE, June 13-16 2004. American Society of Civil Engineers.

[72] R. Stanway, J. L. Sposton, and N. G. Stevens. Non-linear modelling of an electro-rheological vibration damper. *Journal of Electrostatics*, 20:167–184, 1987.

[73] D. R. Gamota and F. E. Filisko. Dynamic mechanical studies of electrorheological materials: moderate frequencies. *Journal of Rheology*, 35:399–425, 1991.

[74] B. F. Spencer, S. J. Dyke, M. K. Sain, and J. D. Carlson. Phenomenological model for magnetorheological dampers. *Journal of Engineering Mechanics*, 123(3), 1997.

[75] R. C. Ehrgott and S. F. Masri. Structural control applications of an electrorheological device. In *Proceedings of International Workshop on Structure Control*, number CE-9311, pages 115–129, University of Southern California, Los Angeles, 1994. USC Publication.

[76] C. J. C. Burges. A tutorial on support vector machines. *Data Mining and Knowledge Discovery*, 2(2), 1998.